

**EXTRUSION OF ALUMINA PARTICULATE REINFORCED
METAL MATRIX COMPOSITES**

By

WEI CHANG CHEN

B. A. Sc.	Beijing University of Iron and Steel Technology	1983
M. Sc.	University of Science and Technology Beijing	1986
M. A. Sc.	University of British Columbia	1991

**A THESIS SUBMITTED IN PARTIAL FULFILLMENT
OF THE REQUIREMENT FOR THE DEGREE OF
DOCTOR OF PHILOSOPHY**

in

**THE FACULTY OF GRADUATE STUDIES
METALS AND MATERIALS ENGINEERING**

**We accept this thesis as conforming
to the required standard**

THE UNIVERSITY OF BRITISH COLUMBIA

December 1994

© Wei Chang Chen, 1994

In presenting this thesis in partial fulfilment of the requirements for an advanced degree at the University of British Columbia, I agree that the Library shall make it freely available for reference and study. I further agree that permission for extensive copying of this thesis for scholarly purposes may be granted by the head of my department or by his or her representatives. It is understood that copying or publication of this thesis for financial gain shall not be allowed without my written permission.

(Signature)

Department of METALS & MATERIALS ENG.

The University of British Columbia
Vancouver, Canada

Date Feb. 24, 95

ABSTRACT

Alumina particulate reinforced metal matrix composite is a new kind of material, which has wide potential applications in automobile industry. The study of its physical nature during extrusion process is essential to optimize the process which may improve its mechanical properties and increase its productivity to finally reduce its cost and make it more competitive to other materials.

Constitutive equations were developed for the alumina particulate reinforced metal matrix composites (Duralcan materials) based on the hot deformation tests on a 'Gleeble 1500' machine. Plant trials were conducted for the same materials in both a laboratory extrusion device at Kingston R & D Center (KRDC), and an industrial extrusion press at Universal Alloy Corporation, California. Different temperatures and extrusion ratios with different ram speeds were adopted during extrusion. Low speed cracking was observed at the front end of some extrudates, which has not been observed with the unreinforced aluminum alloy (AA6061). Microstructure change with particle fracture and particle distribution was studied using an optical microscope and an image analyzer in the deformation zone of a billet and the extrudates from the plant trials.

The extrusion processes have been simulated with the aid of a finite element model. The plant trial data were used to validate the model predictions. The model predictions at both a macroscopic and a microscopic level were correlated with microstructural changes. Extrusion limit diagrams for both composites of 6061/Al₂O₃/10p and 6061/Al₂O₃/20p were developed with low speed cracking boundaries included for the press at UAC. The mechanism of the low speed cracking was proposed based on the FEM and SEM analysis.

Although low-speed cracking was proposed to be associated with void formation in the surface layer of the extrudates, the voids were not significant to the effect of tensile properties, because the elastic modulus, the yield stress and the ultimate tensile strength measured from extrudates of the plant trials at KRDC did not decline at extrusion ratios from 10 to about 30. Minimization of void formation in the composites was discussed and recommendations have been provided for optimization of the extrusion of the alumina particulate reinforced MMCs.

This page left blank intentionally

TABLE OF CONTENTS

ABSTRACT	ii
TABLE OF CONTENTS	v
TABLE OF TABLES	xi
TABLE OF FIGURES	xiii
NOMENCLATURE	xix
ACKNOWLEDGEMENTS	xxii
DEDICATION	xxiii
Chapter 1 INTRODUCTION	1
1.1 Characteristics of Metal Matrix Composites	1
1.2 Fabrication of Particulate Reinforced Metal Matrix Composites	3
1.3 Processing and Applications of Particulate Reinforced MMCs	4
1.3.1 Secondary Deformation Processing	4
1.3.2 Applications	5
Chapter 2 LITERATURE REVIEW	6
2.1 Extrusion Process	6
2.2 Extrusion Related Defects of Particulate Reinforced MMCs (PRMMCs)	8
2.2.1 Extrusion Related Defects	9
2.2.2 Hot Workability of PRMMCs	14
2.3 Development of Extrusion Limit Diagrams	17
2.3.1 Peak Pressure	18
2.3.2 Temperature Rise	19
2.4 Finite Element Analysis of An Extrusion Process	21
2.4.1 Finite Element Analysis of an Extrusion Process	21
2.4.2 Development of an Extrusion Limit Diagram Using FEM	22

2.4.3 Fracture Criteria for Monolithic Metals	24
2.5 Finite Element Analysis of the PRMMC	25
2.5.1 Multilevel Finite Element Method	29
2.5.2 Particle Fracture Model during Deformation	31
2.5.3 Microscopic Analysis of PRMMCs under Larger Deformation	33
Chapter 3 SCOPE AND OBJECTIVES	34
3.1 Scope and Objectives	34
3.2 Methodology	35
Chapter 4 EXPERIMENTAL	37
4.1 Gleeble Tests	37
4.2 Plant Trials at UAC, Anaheim	40
4.2.1 Extrusion Procedure	40
4.2.2 Extrusion Data	44
4.3 Pilot Extrusion at KRDC, Kingston	50
4.3.1 Extrusion Procedure	50
4.3.2 Extrusion Data	52
4.4 Extrusion Surface Defects	55
4.5 Effect of Extrusion Conditions on the Mechanical Properties	58
4.5.1 Tensile Tests	58
4.5.2 Property Changes after Extrusion	58
Chapter 5 MODELING EXTRUSION OF THE PRMMCs	64
5.1 Mathematical Model of the Extrusion Process	64
5.1.1 Finite Element Model	64
5.1.1.1 Flow Formulation	64
5.1.1.2 Boundary Conditions	68
5.1.2 Input Data	70
5.1.3 Finite Element Solution	70

5.2 Sensitivity Analysis of the Model	72
5.3 Extrusion Process Simulation	75
5.3.1 Processing Conditions	75
5.3.2 Model Predictions	76
5.3.2.1 Deformation Behavior	76
5.3.2.2 Temperature Distribution	84
5.3.2.3 Comparison of Predictions with Measured Data	86
5.4 Validation of Model Predictions	89
5.5 Summary	92
Chapter 6 MICROMECHANICAL ANALYSIS OF THE PRMMC DURING LARGE DEFORMATION	94
6.1 Obstacles and Challenges of Micromechanical Analysis of the PRMMCs	94
6.1.1 Particle Phenomena	94
6.1.2 Matrix Phenomena	95
6.1.3 Modeling Constraints	95
6.2 Micromechanical Analysis during Plane Strain Compression	96
6.2.1 Twin-Particle Model	98
6.2.2 Multiple-Particle Model	104
6.3 Micromechanical Analysis during Cylindrical Compression	106
6.3.1 Single-Particle Model	107
6.3.1.1 Material Flow of a Cylindrical Specimen Containing a Particle	109
6.3.1.2 Effect of Particle Shape	115
6.3.2 Twin-Particle Model	120
6.3.2.1 Effect of Reduction	121
6.3.2.2 Effect of Particle Spacing	121
6.4 Model Validation	126
6.5 Conclusions	126

Chapter 7 PARTICLE FRACTURE OF THE PRMMC DURING EXTRUSION	128
7.1 Specimen Preparation for the PRMMCs	129
7.2 Macroscopic Examination of Metal Flow in the Deformation Zone	130
7.3 Particle Fracture during Extrusion	134
7.3.1 Qualitative Microstructure Analysis	134
7.3.1.1 Particle Deformation Behavior in the Deformation Zone	134
7.3.1.2 Microstructure Analysis of the Extrudates	140
A. Comparison of Microstructure in Longitudinal and Transverse Sections	141
B. Comparison of Microstructure for 6061/Al ₂ O ₃ /20p and 6061/Al ₂ O ₃ /10p	143
7.3.2 Image Analysis of Particle Distribution in Extrudates	146
7.3.2.1 Homogeneity of Particle Distribution	146
7.3.2.2 Particle Size	149
7.3.2.3 Aspect Ratio of Particles	154
7.3.2.4 Particle Orientation	156
7.4 Modeling Particle Fracture during Extrusion	157
7.4.1 Particle Fracture Probability at High Temperature	157
7.4.2 Particle Fracture Model during Extrusion	158
7.4.3 Application of the Model	160
7.5 Discussion	162
7.5.1 Microstructure Comparison before and after Extrusion	163
7.5.1.1 Comparison of Particle Distribution before and after Extrusion	163
7.5.1.2 Particle Size Refinement after Extrusion	168
7.5.2 Particle Fracture Modes during Extrusion	168
7.5.3 Correlation between Particle Fracture and Bulk Deformation Behavior	170
7.6 Summary	173
Chapter 8 ORIGIN OF LOW SPEED CRACKING DURING EXTRUSION OF THE PRMMCs	177

8.1 Microstructure Examination of Low-speed Cracks	177
8.2 Particle Behavior and Microscopic Damage	180
8.2.1 Particle Fracture	180
8.2.2 Void Formation	183
8.3 Effect of Processing Parameters on Low Speed Cracking	186
Effect of Ram Speed	189
Effect of Billet Temperature	193
Effect of Die Temperature	197
Effect of Friction at Die Interface	198
Effect of Extrusion Ratio	200
Effect of Volume Fraction of the Composites	202
8.4 Mechanism of Low Speed Cracking	204
8.5 A Preliminary Criteria for Low Speed Cracking	206
Chapter 9 EXTRUSION OF THE PRMMCs	210
9.1 Development of Extrusion Limit Diagram	211
9.1.1 Using Empirical Equations	211
9.1.2 Using Finite Element Method	215
9.1.2.1 Application of the Finite Element Model	215
9.1.2.2 Comparison of Extrusion Limit Diagrams	217
9.2 Extrusion Limit Diagram with Low Speed Cracking Boundary	220
9.2.1 Low Speed Cracking Boundary	220
9.2.2 Effect of Extrusion Ratios	222
9.2.3 Extrusion Limit Diagram with Low Speed Cracking Boundary	223
9.3 Extrusion of the PRMMCs	224
9.3.1 Minimization of Microstructural Damage during Extrusion	225
9.3.2 Improvement in Particle Distribution and Size Refinement	229
9.3.3 Quality and Productivity of the PRMMCs	231

Chapter 10 CONCLUDING REMARKS	234
10.1 Summary and Conclusions	234
10.2 Future Work	236
REFERENCES	237

TABLE OF TABLES

Table 1.1	Illustration of the principle factors linked with the aspect ratio	2
Table 2.1	Microstructure observed in the particulate reinforced composite before and after extrusion	13
Table 4.1	Material constants for the constitutive equation of the Composites	40
Table 4.2	Extrusion programs for the 7" press at UAC	41
Table 4.3	Billet temperatures immediately prior to extrusion at UAC	43
Table 4.4	Plant trial conditions at KRDC	51
Table 4.5	Billet dimensions of each test at KRDC	53
Table 4.6	Measured test data of the plant trials at KRDC	53
Table 4.7	Extrudate data from plant trials at UAC	57
Table 4.8	Tensile test results of extrudates from the plant trials at KRDC	59
Table 5.1	Some data for sensitivity analysis of the FEM model	72
Table 5.2	Processing Conditions for Two Simulations	76
Table 6.1	Simulation conditions for plane strain deformation	97
Table 6.2	Simulation conditions for cylindrical compression test	107
Table 6.3	Particle sizes studied	109
Table 6.4	Comparison of model predictions with measured data	126
Table 7.1	Polishing procedure for Duralcan materials at KRDC	129
Table 7.2	Polishing procedure used at UBC for Duralcan materials	130
Table 7.3	Extrusion conditions of the Trial S92-3 of 6061/Al ₂ O ₃ /20p	131
Table 7.4	List of examined extrudates with two different cross-sections	141
Table 7.5	Statistical results for volume fraction distribution of the two composites	147
Table 7.6	Statistical results for the quantitative metallography	153
Table 7.7	Average number of parts fractured from a single particle in 6061/Al ₂ O ₃ /20p	159
Table 7.8	Comparison of model predictions with measured data	162
Table 8.1	Tensile stress in particles and matrix at different reductions	182

Table 8.2	Standard conditions for parametric study	188
Table 9.1	Constants in Eq. (9.1) for the composites	211
Table 9.2	Extrusion conditions for the specimens examined under an SEM	225

TABLE OF FIGURES

Figure 2.1	Schematic of a forward extrusion process	7
Figure 2.2	Tensile elongation to fracture against strength for A356 alloy and its composites with different volume fractions of SiCp before and after extrusion at different extrusion temperatures of 400°C and 600°C	10
Figure 2.3	Strain dependence of fractured particle of 6061/SiCp MMCs	15
Figure 2.4	A schematic extrusion limit diagram	18
Figure 2.5	Schematic extrusion limit diagram with low speed cracking	23
Figure 2.6	Finite element model used by Aradhya <i>et al</i>	26
Figure 2.7	Master mesh for generating different microscopic morphologies	27
Figure 2.8	The crack morphologies generated by the FEM study for different overall fraction of the angular ZrO ₂ with transformation	29
Figure 2.9	(a) FEM mesh with local refinement during a plane-strain upsetting; (b) Stress distribution along the line PQ ($\epsilon_x=1\%$ calculated with ABAQUS) ^l	30
Figure 3.1	Methodology for the extrusion of alumina particulate reinforced MMCs	36
Figure 4.1	Schematic of the Gleeble test set-up	38
Figure 4.2	Schematic of extrusion setup for Duralcan trials	42
Figure 4.3	Typical load-stroke curve with variation of ram speed (S92-3)	45
Figure 4.4	Die temperature increase during extrusion (S92-3)	46
Figure 4.5	Effect of homogenization on extrusion force (S92-3 and S92-4)	46
Figure 4.6	A weak correlation of increasing ram speed with increasing die temperature during extrusion (S92-5)	47
Figure 4.7	Effect of billet temperature on extrusion force (S92-5 and S92-6)	47
Figure 4.8	Effect of billet length on extrusion force during extrusion (S92-3 and J94-12)	48
Figure 4.9	Effect of volume fraction on extrusion force during extrusion (6061/Al ₂ O ₃ /10p: J94-3, and 6061/Al ₂ O ₃ /20p: J94-7)	48
Figure 4.10	Effect of extrusion ratio on extrusion force (J94-4, J94-10, J94-15)	49
Figure 4.11	Schematic drawing of the extrusion press at KRDC	52
Figure 4.12	Typical load-stroke curve during extrusion at KRDC (K-7)	54
Figure 4.13	Variation of ram speed at the press pressure limit (K-11)	55
Figure 4.14	Low speed cracking at the front end of two extrudates	56
Figure 4.15	Schematic of a tensile test specimen	58
Figure 4.16	Tensile property under different extrusion ratios	60
Figure 4.17	Elongation of the composites as a function of extrusion ratio	61
Figure 4.18	(a) Tensile property change of 6061/Al ₂ O ₃ /10p for different extrusion ratios	62

with a true volume fraction from 7.0% to 7.4%; (b) Tensile property change of 6061/Al₂O₃/20p for different extrusion ratios with a true volume fraction from 19.2% to 19.8%

Figure 4.19	Corresponding elongation values at different extrusion ratios for both composites	63
Figure 5.1	Schematic of an extrusion press	65
Figure 5.2	Initial finite element mesh for the billet and its surrounding tools	68
Figure 5.3	Sensitivity of load stroke curve to the number of elements in the billet	74
Figure 5.4	Sensitivity of the maximum temperature to the number of elements in the billet	74
Figure 5.5	Material flow near the end of upsetting stage	78
Figure 5.6	Effective strain distribution near the end of upsetting stage	78
Figure 5.7	Velocity distribution in the billet after a ram displacement of 40.7 mm in the large extrusion press; length of arrow is proportional to velocity	79
Figure 5.8	Velocity distribution in the billet after a ram displacement of 26.7 mm in a small extrusion press; length of arrow is proportional to velocity	79
Figure 5.9	Mean stress distribution in the billet at a ram displacement of 40.7 mm in the large extrusion press (negative values denote compressive stresses)	81
Figure 5.10	Mean stress distribution in the billet at a ram displacement of 26.7mm in the small extrusion press (negative values denote compressive stresses)	82
Figure 5.11	Effective strain distribution of the billet in the small press	83
Figure 5.12	Effective strain rate distribution of the billet in the small press	84
Figure 5.13	Temperature distribution in the large extrusion press	85
Figure 5.14	Temperature distribution in the small extrusion press	85
Figure 5.15	Comparison of predicted force with measured data (large press)	87
Figure 5.16	Comparison of predicted force with measured data (small press)	87
Figure 5.17	Comparison of predicted temperature with measured data (large press)	88
Figure 5.18	Comparison of FEM force with measured data corrected for extrusion press compliance according to Eq. (5.26); large press	91
Figure 5.19	Comparison of FEM force with measured data corrected for extrusion press compliance according to Eq. (5.26); small press	91
Figure 6.1	Initial finite element meshes for each object of plane strain deformation	97
Figure 6.2	Initial finite element mesh around two particles	98
Figure 6.3	Effective strain distribution at a reduction of 49%	100
Figure 6.4	Localized effective strain distribution around two particles at different reduction	102

Figure 6.5	Effective stress in the particles at different reductions	103
Figure 6.6	Localized effective strain distribution at a reduction of 1%	105
Figure 6.7	Localized effective stress distribution at a reduction of 1%	105
Figure 6.8	Localized mean stress distribution at a reduction of 1%	106
Figure 6.9	Initial mesh and location of a particle in a cylindrical specimen	108
Figure 6.10	Effective strain distribution in the cylindrical specimen with and without a particle at a reduction of 65%	110
Figure 6.11	Effective strain distribution around the particle at a reduction of 65%	111
Figure 6.12	Effective strain distribution along the center line of the specimen under different reductions	112
Figure 6.13	Effective stress distribution in the cylindrical specimen with and without a particle at a reduction of 65%	112
Figure 6.14	Effective stress in the matrix and in the particle at a reduction of 65%	113
Figure 6.15	Mean stress distribution in the cylindrical specimen with and without a particle at a reduction of 65%	114
Figure 6.16	Mean stress distribution both in the matrix and in the particle at a reduction of 65%	115
Figure 6.17	Effect of particle shape on damage factor at a reduction of 65%	118
Figure 6.18	Effect of particle shape on strain distribution at a reduction of 65%	119
Figure 6.19	Effect of particle shape on effective stress variation during compression	120
Figure 6.20	Effective strain distribution under different reductions with an initial particle spacing of 120 μm	122
Figure 6.21	Mean stress distribution in the matrix and in the two particles under different reductions with the initial particle spacing of 120 μm	123
Figure 6.22	Effect of particle spacing on strain distribution at a reduction of 65%	125
Figure 6.23	Comparison of predicted value with measured data	125
Figure 7.1	Metal flow of a billet in a container	131
Figure 7.2	Schematic positions for the pictures taken with low magnification	132
Figure 7.3	Metal flow in the deformation zone during extrusion	133
Figure 7.4	Schematic positions for the pictures taken for micro examination	134
Figure 7.5	Typical particle distribution in the Locations 1 - 9	137
Figure 7.6	Schematic of examined extrudate specimen	141
Figure 7.7	Typical characteristics of particles after extrusion of 6061/ Al_2O_3 /20p at an extrusion ratio of 34	142
Figure 7.8	Typical characteristics of particles after extrusion of 6061/ Al_2O_3 /10p at an extrusion ratio of 34	144

Figure 7.9	Histogram of volume fraction for 6061/Al ₂ O ₃ /10p	148
Figure 7.10	Histogram of volume fraction for 6061/Al ₂ O ₃ /20p	148
Figure 7.11	Histogram of the particle diameter for Sample B3 of 6061/Al ₂ O ₃ /20p	150
Figure 7.12	Histogram of the particle diameter for Sample B6 of 6061/Al ₂ O ₃ /10p	151
Figure 7.13	Histogram of the particle area for Sample B3 of 6061/Al ₂ O ₃ /20p	152
Figure 7.14	Histogram of the particle area for Sample B6 of 6061/Al ₂ O ₃ /10p	152
Figure 7.15	Histogram of the aspect ratio for Sample B3 of 6061/Al ₂ O ₃ /20p	155
Figure 7.16	Histogram of the aspect ratio for Specimen B6 of 6061/Al ₂ O ₃ /10p	155
Figure 7.17	Histogram of orientation of the particles with respect to extrusion direction for the Sample B3 of 6061/Al ₂ O ₃ /20p	156
Figure 7.18	Histogram of orientation of the particles with respect to extrusion direction for the Sample B6 of 6061/Al ₂ O ₃ /10p	157
Figure 7.19	Fracture probability variation in the deformation zone	161
Figure 7.20	Particle size reduction during extrusion	162
Figure 7.21	Microstructure of 6061/Al ₂ O ₃ /10p before and after extrusion	164
Figure 7.22	Microstructure of 6061/Al ₂ O ₃ /20p before and after extrusion	165
Figure 7.23	Variation of maximum and minimum alumina particle dimension	166
Figure 7.24	Aspect ratio of alumina particles of 6061/Al ₂ O ₃ /20p in back end of a billet and in extrudate	167
Figure 7.25	Orientation of alumina particles of 6061/Al ₂ O ₃ /20p in back end of a billet and in extrudate	167
Figure 7.26	A schematic diagram for three particle-fracture modes during extrusion	170
Figure 7.27	Effective strain rate distribution in the deformation zone	171
Figure 7.28	Mean stress distribution in the deformation zone	171
Figure 7.29	Shear stress distribution during extrusion	173
Figure 8.1	Void formation near a low speed crack tip of J94-14 of 6061/Al ₂ O ₃ /20p in longitudinal section	179
Figure 8.2	Void formation near a low speed crack tip of J94-11B of 6061/Al ₂ O ₃ /10p in longitudinal section	179
Figure 8.3	Tensile stress in a particle under plane strain condition at a reduction of 10%	182
Figure 8.4	Tensile stress distribution in the matrix and around particles	185
Figure 8.5	Tensile stress distribution in the monolithic material at a reduction of 10% under plane strain condition	185
Figure 8.6	Temperature distribution of billet and die at steady state extrusion	187
Figure 8.7	Tensile stress (σ_z) distribution at the die interface zone	188
Figure 8.8	Effect of ram speed: (a) Maximum temperature in the die land zone during	190

	extrusion; (b) Maximum tensile stress in the die land zone during extrusion	
Figure 8.9	Temperature distribution on both side of the die interface at a ram displacement of 30mm	191
Figure 8.10	Effect of ram speed on strain distribution through radius direction	192
Figure 8.11	Effect of ram speed on stress distribution (σ_z) through radius direction	192
Figure 8.12	Effect of ram speed on effective strain rate variation in extrudate	193
Figure 8.13	Effect of initial billet temperature:(a) Max. temperature in the die land zone during extrusion; (b) Max. tensile stress in the die land zone	194
Figure 8.14	Thermal gradient on both sides of the die interface under different billet temperature	195
Figure 8.15	Effect of initial die temperature: (a) Maximum temperature in the die land zone during extrusion; (b) Maximum tensile stress in the die land zone during extrusion	196
Figure 8.16	Thermal gradient on both sides of the die interface under different initial die temperatures	197
Figure 8.17	Effect of friction condition at die interface: (a) Maximum temperature in the die land zone during extrusion; (b) Maximum tensile stress in the die land zone during extrusion	199
Figure 8.18	Thermal gradient on both sides of the die interface under different friction condition at die interface	200
Figure 8.19	Effect of extrusion ratio (a) Maximum temperature in the die land zone during extrusion; (b) Maximum tensile stress in the die land zone during extrusion	201
Figure 8.20	Thermal gradient on both sides of the die interface under different extrusion ratios	202
Figure 8.21	Effect of volume fraction: (a) Maximum temperature in the die land zone during extrusion; (b) Maximum tensile stress in the die land zone during extrusion	203
Figure 8.22	Thermal gradient on both sides of the die interface under different volume fraction	204
Figure 8.23	Variation of E value during different conditions but same extrusion ratio	208
Figure 8.24	Variation of E value during extrusion at different extrusion ratios	208
Figure 9.1	Extrusion limit diagram at an extrusion ratio of 28 for 6061/Al ₂ O ₃ /20p for the press at KRDC	213
Figure 9.2	Extrusion limit diagram at a ram speed of 12.5mm/s for 6061/Al ₂ O ₃ /20p for the press at KRDC	213

Figure 9.3	Extrusion limit diagram for 6061/Al ₂ O ₃ /20p at an extrusion ratio of 34 for the large press at UAC	214
Figure 9.4	Extrusion limit diagram for 6061/Al ₂ O ₃ /10p at an extrusion ratio of 34 for the large press at UAC	214
Figure 9.5	Extrusion limit diagram for 6061/Al ₂ O ₃ /20p for the press at KRDC	216
Figure 9.6	The limit diagram for 6061/Al ₂ O ₃ /20p for the press at UAC	217
Figure 9.7	Comparison of the extrusion limit diagram for 6061/Al ₂ O ₃ /20p for the press at KRDC using different techniques	218
Figure 9.8	Comparison of the extrusion limit diagram for 6061/Al ₂ O ₃ /20p for the press at UAC using different techniques	219
Figure 9.9	The extrusion limit diagram for both 6061/Al ₂ O ₃ /10p and 6061/Al ₂ O ₃ /20p using the empirical equation technique	219
Figure 9.10	Low speed cracking boundary for the extrudate of 6061/Al ₂ O ₃ /20p at an extrusion ratio of 13	221
Figure 9.11	Low speed cracking boundary for the extrudate of 6061/Al ₂ O ₃ /20p at an extrusion ratio of 34	221
Figure 9.12	Low speed cracking boundary for the extrudate of 6061/Al ₂ O ₃ /20p at an extrusion ratio of 52	222
Figure 9.13	Effect on extrusion ratios on low speed cracking boundary during extrusion of 6061/Al ₂ O ₃ /20p	223
Figure 9.14	Extrusion limit diagram of 6061/Al ₂ O ₃ /20p for the press at UAC with low-speed cracking boundaries	224
Figure 9.15	Voids in the surface layer of an extrudate of 6061/Al ₂ O ₃ /20p at an extrusion ratio of about 34 without low speed surface cracking (front end of J94-14)	227
Figure 9.16	Voids in the surface layer of an extrudate of 6061/Al ₂ O ₃ /10p at an extrusion ratio of about 28 with low speed surface cracking (front end of K-6)	228
Figure 9.17	SEM image observed in the surface layer of the extrudate at an extrusion ratio of about 34 without low speed surface cracking (back end of J94-14)	230

NOMENCLATURE

A, B, C, E,	Experimental constants
F, a, b	
A_b	Cross section of a billet area, m^2
$C_1(t), C_2(t)$	Time-dependent constant in temperature analysis
C_F	Product of fracture stress and fracture strain of a material, MPa
c_p	specific heat, J/kg-K
[C]	Heat capacity matrix
d	Diffusion distance, m
D	Volume equivalent particle diameter, μm
\bar{D}_1	Mean refined volume equivalent particle diameter, μm
D_B	Initial billet diameter, m
D_C	Inside diameter of a container, m
D_E	Extrudate diameter, m
E, E_0	Elastic modulus of a solid phase, GPa
E_0	Overall stiffness of a press, kN/mm
E	Product of max. tensile stress and max. effective strain during extrusion
F_i	Surface traction on velocity boundary
{f}	Residual of the nodal point force vector
h_0	Initial width of the gap between two cracked particles, μm
J	Mechanical equivalent of heat
k	Thermal conductivity, $W/m^{-0} K$
K, K_1, K_2	Penalty constant, and material constants
[K_S], [K_C]	Stiffens matrix, and heat capacity matrix
L_0	Initial billet length, m
l_b, L	Instantaneous length of a billet measured from the dead metal zone, m
l_1	Die land length, m
L_R	Length of a discard
n	Stress exponent

n	Average number of parts fractured from a single particle
N_f^b, N_f^t	Number of broken particles, and number of total particles
P	Extrusion load, N
P_f	Extrusion force at the end of stroke, kN
p	extrusion pressure, MPa
p_h	Pressure required for matrix intrusion into the gap of cracked particles, MPa
p_f	Particle fracture probability;
\bar{p}_f	Average particle fracture probability rate over cross section in deformation zone
P_0	Fraction of porosity in a solid phase
\dot{q}	Heat generation rate, W/m^3
Q	Hot deformation activation energy, J
Q_b, Q_v	Activation energies for surface and bulk diffusion
$\{Q\}$	Heat flux vector
R	Extrusion ratio
R	Gas constant, $J/mol \cdot ^\circ C$
R_1	Radius of cross section in deformation zone during extrusion
S	Surface area, m^2
S_a, S_m	Adjusted and measured ram stroke, respectively
S_T	Total ram stroke, m
t	Time, s
$T, \{T\}$	Temperature and the matrix of its nodal values, $^\circ K$
$T_{i,i}$	Summation of temperature differentiation with spatial coordinates
\dot{T}	Temperature differentiation with time
v_i, v_p, v_j	velocity component
v_B	Ram speed, m/s
V	Volume, m^3
x	Material constant depending on internal structure
Z	Zener-Holloman parameter, s^{-1}
$\Delta D/D$	Mean particle size reduction after extrusion

ΔT	Temperature rise in extruded product, $^{\circ}\text{K}$
ΔT_D	Initial temperature difference between the billet and the chamber or die, $^{\circ}\text{K}$
Δt	Time incremental, s
$\{\Delta v\}, \Delta v_I$	First-order correction of the velocity at previous step
α	Material constant, MPa^{-1} ; and particle aspect ratio;
β	Time integration factor
β, β_1	Constant in particle fracture model, μm^{-3}
ϵ	Strain
ϵ_F	Fracture strain of a material
$\epsilon_N, \epsilon_G, \epsilon_L$	Fracture strain of void nucleation, growth, and linkage
$\bar{\epsilon}_{\max}$	Maximum effective strain during extrusion
$\dot{\epsilon}, \bar{\dot{\epsilon}}, \dot{\epsilon}_V$	Strain rate, effective strain rate, and volume strain rate, s^{-1}
$\dot{\epsilon}_G$	Critical strain rate for dislocation accumulation in front a particle, s^{-1}
η	Heat generation efficiency
φ	Semi angle of extrusion; degree
ϕ	Angle of dead metal zone, degree
Φ	Functional for the deformation body
ρ	density, kg/m^3
σ, σ_y	Flow stress, yield stress, MPa
$\bar{\sigma}, \sigma_m, \sigma_1$	Effective stress, mean stress, and principle stress, MPa
σ_F	Fracture stress of the composites
σ_X, σ_Z	Tensile stress in X-direction in plane strain compression, and in the extrusion direction, MPa

Sub- and Superscripts:

s	denotes the steel for tools
c	denotes the composite for the billet
t	time

ACKNOWLEDGEMENTS

I would like to express my sincere appreciation to Drs. Indira Samarasekera, Keith Brimacombe, Bruce Hawbolt, and Chris Davies for their supervision throughout the whole course of this project. Without their support, my dream of obtaining a Ph.D. would never have come true. Appreciation is extended to Alcan International Ltd. for providing test specimens, technical help and discussions. Thanks to Mr. William (Bill) Dixon of Duralcan USA, and Dr. David Lloyd, and Mr. Chris Cabryel, of Alcan International Ltd. for their help with the extrusion trials. Thanks are also extended to Dr. Stuart MacEwen for his help and discussion of finite element modeling of the extrusion process. Thanks for financial support go to the industrial partners in the Metal Matrix Composite Pre-competitive Research Consortium: Alcan International Ltd., Ontario Hydro Ltd., Sherritt Gordon Ltd., Pratt and Whitney Canada Inc., Inco Ltd. and NSERC, and also to the Ontario Center for Materials Research, through whose auspices the consortium was set up. Thanks to Ms. Mary Mager for her assistance in using the SEM.

Thanks to Professor Tara Chandra from University of Wollongong for his interest to this project. A great help from Dr. Warren Poole in this department is very much appreciated. I would also like to thank all my fellow students in this department for their discussion and friendship.

Finally, I would like to take this opportunity to express my appreciation from the bottom of my heart to my mother, and my wife, Xiaoli (Shelly). Without their love and emotional support, this Ph. D. project could never be finished.

DEDICATION

To my mother

Chapter 1 INTRODUCTION

1.1 Characteristics of Metal Matrix Composites

Metal Matrix Composite (MMC) research was initiated in the 1960's. It is particularly attractive in applications when the following improvements over monolithic materials are required:

- Easily designed and tailor-made material;
- Improved strength/density ratio;
- Improved stiffness/density ratio;
- Improved wear resistance;
- Improved high temperature mechanical properties;
- Adjustable physical properties (coefficient of thermal expansion, diffusivity, elastic

modulus).

Among the important MMC systems, the following are of interest^[1]:

- Al₂O₃/Al and Al₂O₃/Mg;
- SiC/Al
- Boron/Aluminium;
- Carbon/Aluminium.

MMC research initially focused on continuous fiber reinforcements which give very high stiffness and strength. Most of the continuous reinforcements are very expensive and have low workability owing to fiber fracture; they have found applications primarily in aerospace and military. In order to avoid the problems of high cost and low ductility, there

has been considerable interest in discontinuous reinforcements such as short fibers, whiskers and particles. The advantages of discontinuous reinforcements over continuous reinforcements can be seen in Table 1.1^[2].

Since particulate reinforced MMCs can be processed by conventional metal working methods or techniques to produce all forms of semifinished products, they become more attractive from a cost perspective. Another decisive factor, especially for small industry, is that parts made of particulate reinforced MMCs behave almost isotropically, and are therefore much simpler to use in design. Although the strength and elastic modulus of particulate reinforced composites are inferior to those of continuously reinforced composites, the low cost, high workability and isotropic properties render them suitable for a wider range of applications, especially in automobile production.

Table 1.1 Illustration of the principle factors linked with the aspect ratio

(where '✓' denotes the advantage and '×' the disadvantage)

Advantages	Discontinuous Reinforcement	Continuous Reinforcement
Isotropy	✓	×
Orientable Properties	×	✓
Formability, Ductility	✓	×
Fabrication Costs	✓	×
Material Cost	✓	×
Recyclability	✓	×
Reinforcement Efficiency	×	✓

1.2 Fabrication of Particulate Reinforced Metal Matrix Composites

In discontinuously reinforced metal matrix composites, the reinforcements are generally ceramic in nature and can either be added to the matrix as discrete elements or formed in situ in the matrix. Reactivity with the matrix during fabrication and service, differences in coefficient of thermal expansion (CTE) between the matrix and reinforcements, and cost/performance in the finished product are the critical selection criteria used for the reinforcements. Alumina and silicon carbide powder (greater than 1 micron in size) have been chosen primarily for the reinforcement, as these materials represent a good compromise between density, property improvement, and cost. However, alumina is about 5-10 times cheaper than silicon carbide powder (SiCp) and 10-100 times cheaper than alumina or silicon carbide filaments^[3]. Moreover, alumina has a higher stability than silicon carbide in aluminum alloys, such as the 2xxx, 6xxx, and 7xxx series. Lower manufacturing cost provides a potential for large scale production of a competitively priced product. In fact, the MMC that is closest to a commercial breakthrough is an aluminum matrix composite with discontinuous, particulate ceramic reinforcements (SiC and Al₂O₃)^[4]. It is being fabricated in several different ways:

--- Foundry processes, where particles (or whiskers) are inserted into the molten metal by mechanical stirring, and the product is cast into an ingot of desired shape or size;

--- Powder metallurgy process, where metal powders and reinforcements are blended cold, compressed and bonded by diffusion;

--- Squeeze casting, where the molten metal is pressure infiltrated into a preform of fibers;

--- Spray deposition technique, where deposition of atomized liquid metal along with particulate is employed to fabricate MMC ingots.

The attraction of ingot casting is the potential for producing MMC billets suitable for utilization on the large scale equipment currently employed for fabrication of monolithic alloys. This approach will capture economies of scale, and is being used at Alcan International Limited, Canada, Duralcan, USA^[5], and Hydro Aluminium, Norway^[6]. Melt viscosity limits the volume fraction of the reinforcement to approximately 25 volume percent. Alcan Aluminium Ltd. has commissioned a 25 million lb/yr facility in Quebec for the production of composites for Duralcan in Canada in 1990^[5]. The scale-up of the casting process to larger sizes presents challenges related to: a) the effects of the solidification rate on the ingot cell size, and b) attendant particle-pushing to the last regions to freeze. A cast route which could have more homogeneous particle distribution in a cast product of particulate reinforced metal matrix composites is sought. In addition, since matrix-reinforcement reaction is a critical issue in some MMC systems, large ingots which have longer solidification times result in increased exposure of the reinforcement to the molten metal.

1.3 Processing and Applications of Particulate Reinforced MMCs

1.3.1 Secondary Deformation Processing

Many discontinuously reinforced metal composite products require subsequent deformation processing via rolling, extrusion, or forging to achieve the final shape, irrespective of how the primary ingot is produced. Dural Aluminium Composites Corporation (Duralcan), has developed necessary technologies to produce a range of ceramic particle reinforced MMCs by the molten metal route. Their products have been used to produce cast

shapes, forgings and a wide range of extruded solid and hollow shapes. The main thrust of their extrusion development has focused on 6061 and 2014 alloys, reinforced either with silicon carbide or alumina at 10 - 20 volume percentage. Significant improvements are achieved in the elastic modulus and strength, although ductility is reduced. The elastic modulus is increased by up to 40%, and the minimum increase in tensile strength is 20%^[7]. However, defects such as surface tearing are observed during extrusion, which affect the quality of the final MMC products. To improve the quality of MMC products^[5,7], a better understanding of how deformation processing influences the microstructure and properties in these materials is needed.

1.3.2 Applications

Metal matrix composites (MMCs) are now used in, or being considered for use in, a variety of applications in the military, aerospace, automotive, and other commercial areas. Automotive applications include automotive drive shafts, cylinder linings, brake rotors^[8]; other applications include bicycle frames and components, and tire studs^[9]. However, the introduction of the MMCs into actual applications is still sparse. No true high volume applications exist to date. To promote further use of MMCs, some fundamental changes must take place. The cost of the composites must be reduced, probably by improving the manufacturing processes. A better chemical and physical understanding of the MMCs must be developed so that designers can use the material with confidence.

Chapter 2 LITERATURE REVIEW

2.1 Extrusion Process

Extrusion is a forming technique widely used in the aluminium industry to produce shapes of complex cross section. The extrusion process can be classified into three broad categories^[10] depending on the direction of extruded material movement relative to the punch.

- i) Forward extrusion: material flows in the same direction as the motion of the punch;
- ii) Backward extrusion: material flows in a direction opposite to the motion of the punch;
- iii) Side extrusion: material flow is perpendicular to the direction of motion of the punch.

In the forward aluminium extrusion process, cylindrical billets are preheated to a temperature, between 300°C and 500°C, at which point they are transferred to the heated container of an extrusion press (Figure 2.1). The container is generally heated to a temperature, 30-50°C lower than the billet in order to compensate for cooling during billet transfer. A load is applied to one end of the billet via a ram and dummy block, forcing material through a die of a shape and size calculated to give the dimensions of the final cooled product. The die is also heated, and sits on top of a number of support components, collectively known as the stack. The die may be classified into shear or flat face die, conical, parabolic and streamlined types, the difference among them being the mathematical representation of the surface or material path lines. In a shear die, a dead metal zone exists and a shearing band is formed between the dead metal zone and the deformation zone. In a conical die, the material path line is a linear function; in the parabolic die (convex or concave) it is a parabolic function (second order equation); and in the streamlined die a cubic function has been used. The conical die, which is relatively easy to design and manufacture, is fairly

well known. In this case, material flow is more uniform than for the shear (or flat face) die. However, the conical die may induce some rigid body rotation near the die exit due to abrupt changes of material flow at that point. The parabolic die (convex type) has a smooth entry but the exit is sharp, creating rigid body rotation and discontinuities in the velocity distribution. Dies having both smooth entry and exit are referred to as streamlined dies with the implicit assumption that the material path lines coincide with the improved die surfaces. Streamlined dies have been shown to be suitable for processing "difficult to extrude" metal alloys^[10]. However, the shear die type is still widely used for the extrusion of aluminium and its alloys in industry, probably because of its simple design and low cost.

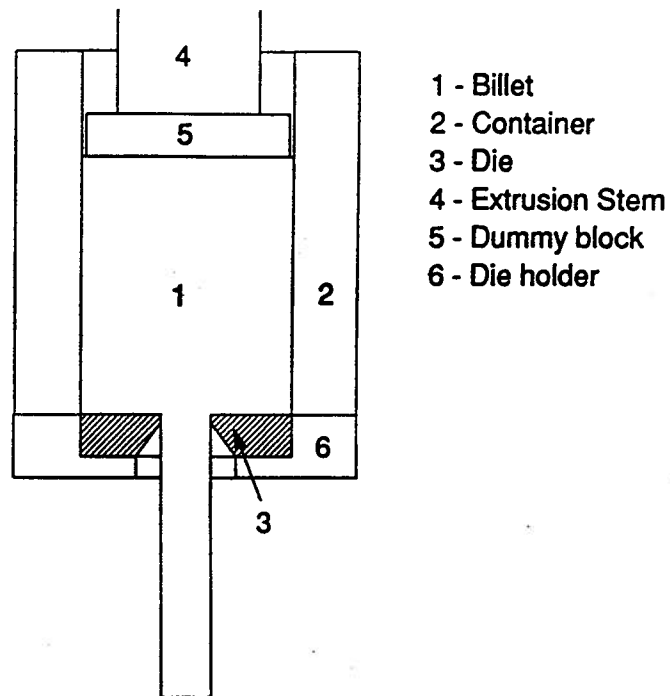


Figure 2.1 Schematic of a forward extrusion process

Press sizes range from lab scale- 200 ton maximum load, 60mm container / billet diameter- to industrial-size presses of up to and greater than 10,000 ton load capacity, with billet diameters of 250mm. Extrusion ratios (upset billet area to extrudate area) of between

10:1 and 200:1 are typical; associated extrusion speeds, measured at material exit, can range from less than 0.5m/min. to 10m/min. or greater. The process is stopped short of all the material exiting the die; the portion of billet remaining in the container is known as the discard, the extruded material as the extrudate. The extrudate may either be air cooled, or quenched with water sprays.

It is also important to note that hydrostatic extrusion is a nearly-ideal friction-free process. Low frictional forces in hydrostatic extrusion permit the use of lower die angles and high extrusion ratios, both of which lead to higher hydrostatic stress and therefore to conditions which suppress fracture^[11,12]. The uniform deformation near the surface, caused by low friction, reduces the danger of surface cracking and fracture can be suppressed by extruding at high fluid pressure. Therefore, brittle materials were the prime target for the application of the hydrostatic extrusion^[13]. Embury *et al.*^[11,12] have suggested application of the hydrostatic extrusion process for MMC processing to increase its formability. Unfortunately, the complexity of the production process leads to a higher cost of the product.

2.2 Extrusion Related Defects of Particulate Reinforced MMCs (PRMMCs)

There is a considerable interest in the forming of metal matrix composites (MMCs), in particular, for controlling the deformation parameters so as to avoid defects or microstructural damage. Of the various forming processes, extrusion has received considerable attention. Not only does the large compressive hydrostatic component of the stress facilitate the imposition of large strain, which homogenizes the particle distribution and heals particle fracture during the process, but it also causes axial alignment of discontinuous reinforcements.

DURALCAN[®] composites have been manufactured by hot, direct (forward) extrusion

[®] Owned by Alcan Aluminum Corporation

(lubricated and unlubricated) and also by hydrostatic extrusion. Hot direct extrusion with shear-face dies without lubrication is the simplest, the cheapest and the most widely used method. Alternative processes involving conical-entry dies, with or without lubrication, are not presently being considered, owing to the difficulty of obtaining a high-quality surface finish. In an exceptional study, using a conical die, Selseth and Lefstad^[4] found that when extruding the AA6061/SiCp (SiCw) MMCs produced by the powder metallurgy (P/M) route, the necessary extrusion force was about 30% higher compared to a shear-face die. The 'p' and 'w' notations stand for particle and whisker reinforcement, respectively.

2.2.1 Extrusion Related Defects

Although hot extrusion of casting products appears to homogenize the particle distribution, clustering (defined as the aggregation of particles) and banding are still evident due to an insufficient extrusion ratio^[54]. The study by Lloyd^[53] also indicated that although the tensile elongation of a permanent mould cast composite test bar (Cast A356 -15% SiC) is around 1%, which is much lower than the unreinforced alloy (Cast A356) as shown in Fig. 2.2. After extrusion at an extrusion ratio of 70:1 under different temperatures (e.g. at 400°C and 600°C for A356-10%SiC and A356-20%SiC), the composite elongation is comparable to or better than the unreinforced as-cast alloy (Cast A356). However, it is lower than the alloy in extruded conditions. During extrusion, surface defects such as surface tearing and cracking appear; some of these defects are known to occur during extrusion of unreinforced materials, while some others are specific features on the MMCs only. These defects will significantly affect the extrudability of particulate reinforced MMCs.

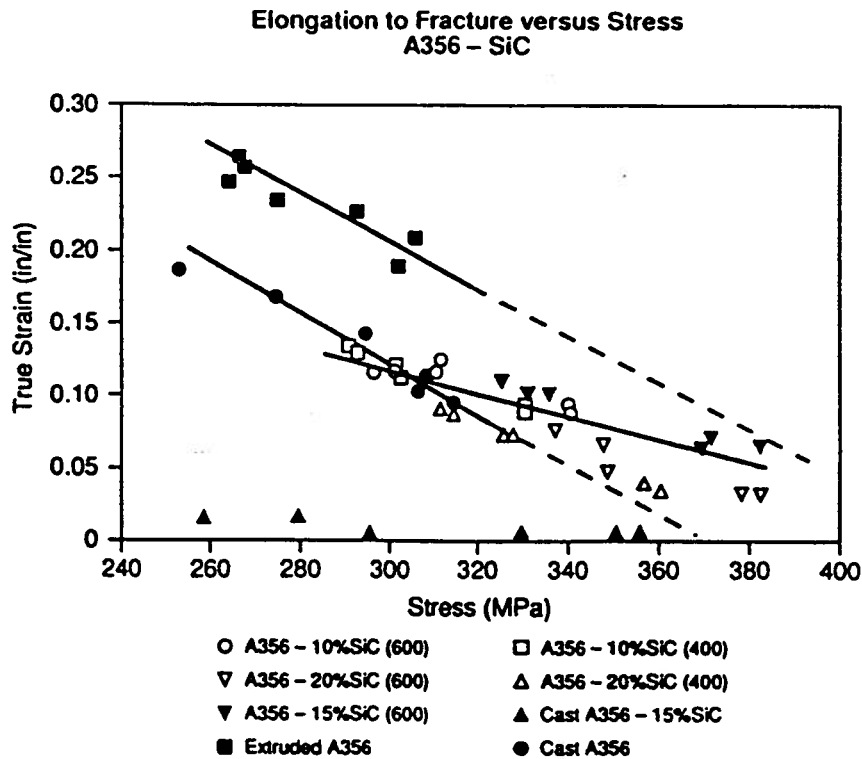


Figure 2.2 Tensile elongation to fracture against strength for A356 alloy and its composites with different volume fractions of SiCp before and after extrusion at different extrusion temperatures of 400°C and 600°C^[53]

Extrudability refers to the maximum attainable speed of the billet without surface defects occurring during extrusion. Based on the early extrusion trials done by Hains *et al.*^[7], it was found that: (i) two kinds of defects occurred during extrusion of 6061 and 2014 with alumina reinforced MMCs, and (ii) their behavior was very different from unreinforced alloys. Firstly, considerable surface tearing occurred at the front end of the extrusion at low extrusion speeds, which persisted over the entire extruded length. However, the intensity of tearing usually reduced with increasing extrusion speed, and on occasion, disappeared completely at intermediate speeds. Secondly, a further increase in speed resulted in the onset of edge and surface cracking which differed from the low speed cracking. These cracks were similar in appearance to a type commonly encountered with conventional aluminium extrusions. It was

reported that two types of crack mechanisms exist for speed-limiting cracking of Al-Mg-Si alloys. The first type initiated at the die/extrudate interface, and occurred because the matrix was not strong enough to withstand frictional force at the die. The second type initiated at subsurface weaknesses, and was assumed to be due to incipient melting. Obviously, both types of tearing mechanisms are temperature dependent and are initiated in a region close to the die/extrudate interface. Therefore, the temperature distribution resulting from heat losses and the temperature rise during extrusion needs to be examined. Although both types of high speed cracking occurred in both monolithic alloys and the MMCs, low speed tearing which should be designated as the third type, appeared only in the MMCs (Brusethaug *et al.*^[6]). This tearing was characterized by deep notches extending from the surface into the material. A probable explanation of the mechanism for the third type was given by Hains *et al.*^[7] as follows: In the initial stages of extrusion, the die was colder than the extrudate. Metal adhering to the die bearing land during this phase was immediately chilled and its flow stress increased. This may create conditions which were energetically favorable for subcutaneous fracturing, so that the material in contact with the bearing remained stationary, while the subsurface material continued its forward motion. Further increase in pressure broke the bond between the bearing and adhered material; this material then moved across the bearing surface. The entire periphery did not move in unison; different segments breaking away at different times. New material adhered to the die bearing land and consequently the extrudate surface retained this debris. The process was repeated in the classic stick-slip mode until conditions were energetically favorable for continuous movement of material across the bearing surface. This low speed tearing introduces a minimum extrusion speed for the MMCs.

Obviously, this mechanism needs to be refined, because it does not include the interaction between particles and matrix materials.

Another trial was conducted by Selseth and Lefstad^[4] in Europe for three different aluminium composites. They investigated the extrudability of discontinuously reinforced aluminium alloys. The composites were SiCp, SiCw and Al₂O₃p in an AlMgSi matrix. The silicon carbide particle (SiCp) reinforced MMC was fabricated by mixing AlMgSi powder (AA6061) and SiC particles of size 4µm, while the alumina particle (Al₂O₃p) reinforced MMC was fabricated by stirring the Al₂O₃p of size of 30µm into the molten AlMgSi (AA6082). The volume fractions of particles or whiskers were all 20%. In the tests, a conventional shear-face die was used, and the extrusion ratios were 22 and 39. In some of the experiments a disc of unreinforced material was clad in front of the billet. This markedly reduced the tendency towards high speed surface tearing, thus increasing the maximum extrusion speed. Their experimental results showed that the composite containing the finest SiC particles (4µm) could be extruded to solid rod at an extrusion speed of 250mm/s, while the alumina particle reinforced MMC was extruded at a speed of only 83mm/s. Because the matrix materials of AA6061 for SiC particles and AA6082 for Al₂O₃ particle reinforcement were quite similar, the relatively poorer extrudability for the alumina particle reinforced MMC was related to the difference of microstructure of the MMCs by Selseth and Lefstad^[4]. As described earlier, in Al₂O₃p reinforced MMCs, there were some particle clusters especially at lower volume fraction, such as 10vol% and 15vol%, which were not discovered in SiCp reinforced materials made by the P/M route. The material with the least clusters, yielded the best surface quality. This could be the reason for its poor extrudability. However, the effect of different particle

size for $\text{Al}_2\text{O}_3\text{p}$ ($30\mu\text{m}$) and SiCp ($4\mu\text{m}$) MMCs should also be considered, because it is also important to the deformation and fracture behavior.

Table 2.1 Microstructure observed in the particulate reinforced composite before and after extrusion

(where '✓' denotes the observation of the defect. * may not be taken as defects.)

Material State	Defects	MMCs	Unreinforced Matrix Alloy
As-cast	Porosity, voids	✓	✓
	Cluster, stringers	✓	
	Surface cracks	✓	✓
Deformed (Extruded)	Particle fracture	✓	
	Debonding at particle/matrix interface	✓	
	Near interface Matrix Fracture	✓	✓
	Low speed surface cracking	✓	
	High speed surface cracking: 1) at die/extrudate interface 2) at subsurface of billet	✓	✓
	Rotation and migration of particles*	✓	

Obviously, the ability of material to withstand high strain rates is vital to the extrudability of the composite. Higher strain rates may cause fracture of the extruded material at the extrudate surface and also result in an overheating in the low melting zone at the subsurface of the extrudate, giving hot shortness during extrusion. All the defects observed in as-cast and extruded materials are summarized in Table 2.1. Therefore, it is essential to analyze the process to establish the optimum operating conditions to produce defect-free products. It

is worth pointing out that the rotation and migration of particles during extrusion of MMCs produced by the melt-casting route will be beneficial to the particle distribution.

2.2.2 Hot Workability of PRMMCs

Hot workability relates to the ability of a metal or alloy to be deformed under conditions of high temperature ($T > 0.6T_M$), where T_M is the melting point of the material in Kelvin), and relatively high strain rates (0.1 to 1 s^{-1}) without forming cracks^[44]. The two characteristics that govern hot workability are strength and ductility. Since for a given material, different strains are attained prior to fracture depending on the process, workability of a material is affected by both the material itself and the external processing conditions, i.e.:

$$\text{Workability} = f_1(\text{material}) \times f_2(\text{process, friction}) \quad (2.1)$$

where f_1 is a function of the basic ductility of the metal and f_2 that of the external factors which modify the basic ductility. The formula clearly implies that the accumulation of internal damage which leads to fracture is closely related to the deformation and restoration processes operative during hot working.

In particulate reinforced metal-matrix composites, the aim has been to combine the beneficial stiffness of ceramics with the superior ductility and toughness of metals. However, this combination produces lower ductility and toughness in composites as compared to the matrix alloy. In order to maximize these properties, it is necessary to understand the local micromechanical failure modes and their relation to macroscopic toughness. As mentioned above, these local failure modes are also dependent on the processing details and, for the MMCs, on the matrix treatment and its effect on the interface. In general, the failure modes in the particulate reinforced MMCs can be due to one or more of the following:

--- Particle fracture;

--- Debonding at particle/matrix interface;
--- Near interface matrix fracture;
--- General fracture mechanism of the matrix of the MMCs as the same as that of the unreinforced matrix alloy^[52].

The study by Lloyd^[53] showed that, for the SiCp reinforcements, fracture occurs in the larger size fraction of the particulate population. Fig. 2.3 shows the strain dependence of fractured particles for 6061-10 and 20vol%SiCp at room temperature.

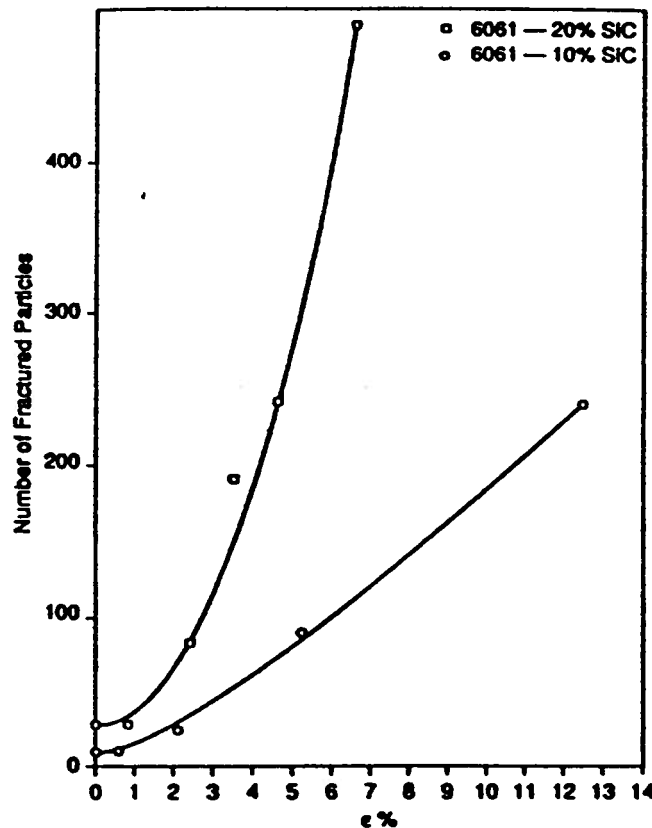


Figure 2.3 Strain dependence of fractured particle of 6061/SiCp MMCs^[53]

It is evident that the extent of particle cracking is lower in the 10vol%SiCp composite, which is not surprising considering the lower particle content in this composite. The rate of particle cracking with strain is also lower. It is interesting to note that less than 5% of the

total particle population has cracked at fracture of the composite. However, it is apparent that particle cracking is initiated at low strains. In spite of this, the voids created do not grow sufficiently during subsequent straining to affect the final fracture strain; the strain of fracture does not correspond to the strain for particle cracking. Similar behavior has also been observed in 6061/Al₂O₃ composites. This indicates that there is a critical amount of damage developed at large strains. The damage is in the form of voids associated with particle clusters, together with the occasional cracked particles. The voids have not grown extensively in the tensile stress direction. This is generally the case in unreinforced alloys. This also suggests that the growth strain is negligible in comparison with the nucleation strain, and that void nucleation is primarily a result of matrix failure within closely spaced particles. The reason for this behavior is related to the deformation response of the particle clustered region relative to the rest of the composite. Within clusters, the far field applied stresses are no longer controlling. Actually, higher-stiffness particles constrain the deformation of the matrix adjacent to them, and this results in a complex triaxial stress being developed in the matrix within the cluster. Obviously, the triaxial stresses are important because a triaxial tensile stress enhances both void nucleation and void growth. To consider the effect of the degree of the triaxial tensile stress, a ratio of mean stress to effective stress, $\sigma_m/\bar{\sigma}$ was adopted. Lloyd found that the unreinforced alloys have a significant loss in elongation with increasing triaxiality, while the composites are relatively unaffected. This is consistent with the idea that the fracture of the composite is controlled by the intrinsic triaxiality generated at particle clusters, and these dominate any imposed far field stress state. Zhao *et al*^[101] have reported that as the temperature increases the void formation due to interface debonding at the ends of particles in tensile direction becomes dominant comparing to particle fracture which is

dominant at low temperature. Lloyd^[53] also pointed out that due to the importance of particle size on the deformation and fracture behavior of the composite, particle size must be limited to maximize strength, and minimize fracture. It has been indicated that using particles of around 10 microns with a tight size distribution, reduces the propensity for particle fracture, which occurs most readily in coarse particles. However, a small particle size may result in more clusters which are harmful for the final properties of the MMCs.

2.3 Development of Extrusion Limit Diagrams

Modeling of extrusion has, at a practical level, been focused on the use of empirical equations and analytical solutions to predict optimum operating conditions^[55-65]. Consequently, the determination of extrudability has been based on extrusion press-side measurements and property / quality requirements^[66]. The extrusion process is governed by the imposed variables, temperature, strain rate (speed), and strain (reduction ratio) and their interaction with the characteristics of the material. The significance of each of these parameters will be determined by several factors, such as surface quality, minimum microstructural damage if there is any, excessive pressure requirement, etc.. Meadows and Cutler^[63] showed that the bounds of extrudability may be calculated theoretically, and demonstrate this on a diagram showing maximum tolerable extrusion pressures and surface incipient melting plotted on the axes of extrusion speed against temperature for a certain extrusion ratio, as schematically shown in Fig. 2.4. The constant pressure boundary line is determined by the extrusion press limit, but is a function of extrusion ratio, temperature and strain rate. The incipient melting boundary line is depicted according to the temperature at the die land interface, which is a function of initial extrusion temperature, extrusion ratio, ram speed, friction coefficient at interfaces, etc..

Such limit diagrams have been developed to include structural^[58,59] and property features^[55]. Sheppard^[56] reviewed these and other developments, and found that most prior research has been oriented to the prediction of a peak or maximum load required of the press, and the prediction of temperature rise due to extrusion deformation.

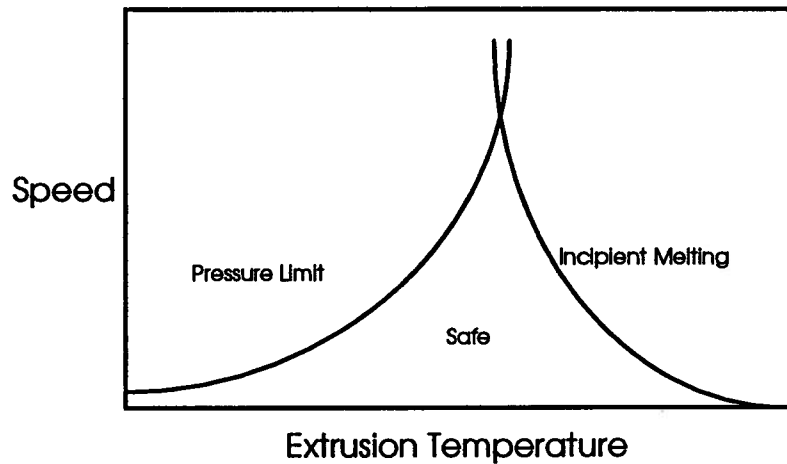


Figure 2.4 A schematic extrusion limit diagram

2.3.1 Peak Pressure

The simplest equation for estimation of peak pressure during extrusion is expressed as,

$$p = \sigma(a + b \ln R) \quad (2.2)$$

where σ is the flow stress of a material, R is the extrusion ratio, and a and b are constants.

The above equation needs to be modified to include friction effects; assuming that sticking friction condition prevails during extrusion which was widely adopted by researchers in aluminium extrusion industry^[55-65], the above equation is changed to,

$$p = \sigma \left[(a + b \ln R) + \frac{4L}{\sqrt{3}D_c} \right] \quad (2.3)$$

where L is an instantaneous length of the billet measured from the dead metal zone and D_c is the inside diameter of the container.

At high temperature, the flow stress of a material is a function of strain rate and temperature, and may be characterized by a hyperbolic sine equation,

$$Z = \dot{\epsilon} \exp\left(\frac{Q}{RT}\right) = A \sinh(\alpha\sigma)^n \quad (2.4)$$

where Z is Zener-Holloman parameter, and A , α , Q and n are material constants. Inserting Eq.(2.4) into Eq.(2.3), a general equation for peak pressure during extrusion can be derived:

$$p = \frac{1}{\alpha n} \left\{ B + C \ln R + E \ln \frac{Z}{A} + F \left(\ln \frac{Z}{A} \right) \left(\frac{L}{D_c} \right) \right\} \quad (2.5)$$

where B , C , E , F are constants for a specific press. The mean strain rate formula adopted in this study is expressed as,

$$\bar{\dot{\epsilon}} = \frac{4v_B D_B^2 \tan \phi}{(D_B D_E)^{3/2}} \quad (2.6)$$

where D_B and D_E are diameters of the billet and the extrudate, respectively, v_B is the ram speed and ϕ is the semi angle of the deformation zone outlined by the shear zone in unlubricated shear die extrusion, expressed as^[62],

$$\phi = 54.1 + 3.45 \ln R \quad (2.7)$$

Based on some plant trials, the above four constants for the extrusion press can be estimated, and the constant pressure boundary line in a limit diagram can be delineated using Eq.(2.5).

2.3.2 Temperature Rise

A general analytical equation for temperature rise during extrusion was derived by Castle and Sheppard^[65] based on a thermal analysis including the billet, and the surrounding tools.

$$\Delta T = (0.9 P v_B t - \Delta T_D C_2(t)) / C_1(t) \quad (2.8)$$

where P is the extrusion force, ΔT_D is the initial temperature difference between the billet and the container or die, $C_1(t)$, and $C_2(t)$ are heat flow coefficients and t denotes extrusion time. Sheppard^[67] claimed that '*for high conductivity aluminum alloys, this form of temperature increase may be sufficiently accurate for practical use*'.

In aluminum extrusion practice, it is common for there to be little or no temperature difference between the billet and the surrounding tools^[64]. However, the generation of heat internally will establish a temperature differential. Therefore, in the calculation of temperature rise, the initial temperature difference between the billet and the tools could be ignored. The above equation then becomes,

$$\begin{aligned}\Delta T &= 0.9Pv_B t / C_1(t) & (2.9) \\ &= 0.9Pv_B t / (K_1 t^{1/2} + (K_2 + K_4)t^{2/3} + (K_3 + K_5)t^{1/3} + K_{11}t)\end{aligned}$$

All the constants are expressed as below,

$$K_1 = \frac{\pi(D_B^2 - D_E^2)}{\cos \phi} \left(\frac{k_s \rho_s C_{ps}}{12} \right)^{1/2} \quad (2.9a)$$

$$K_2 = \frac{\pi}{6} l_D (18k_s D_B (\rho_s C_{ps})^{1/2})^{2/3} \quad (2.9b)$$

$$K_3 = \frac{\pi}{6} l_D (18k_s D_B^4 (\rho_s C_{ps})^2)^{1/3} \quad (2.9c)$$

$$K_4 = \frac{\pi}{6} l_1 (18k_s D_B (\rho_s C_{ps})^{1/2})^{2/3} \quad (2.9d)$$

$$K_5 = \frac{\pi}{6} l_1 (18k_s D_B^4 (\rho_s C_{ps})^2)^{1/3} \quad (2.9e)$$

$$K_{11} = \rho_c C_{pc} Rv_B \pi D_E^2 / 4 \quad (2.9f)$$

where l_D is the deformation zone depth between the pressure pad and the dead metal zone, l_1 is the die land length, ϕ is the angle of dead metal zone, ρ , k , C_p are thermal properties of a material, and the subscripts s and c denote the steel for tools and the composite for the billet, respectively.

2.4 Finite Element Analysis of an Extrusion Process

2.4.1 Finite Element Analysis of an Extrusion Process

Modeling of an extrusion process for determination of punch pressure, stress/strain distributions, material flow pattern, etc., is of extreme importance to the manufacturing process designer for a number of reasons. It provides valuable information, not only for enhanced design of work tools and process parameters, but is also useful for improving existing extrusion methods or even inventing new routes.

Various kinds of extrusion processes have been analyzed for monolithic materials by the finite element method at a macroscopic level^[14-36], using both the *Solid Approach* and the *Flow Approach*. The *Solid Approach* treats the solid as an elastic-plastic material during forming. The significant shortcoming is its complex formulation and the computing cost^[25-29]. In contrast, the *Flow Approach* considers the materials to behave as a non-Newtonian viscous fluid. A typical shortcoming of this approach is that it cannot represent many of the subtleties of elastic-plastic constitutive laws; hence it does not provide information on residual stresses and also does not solve directly the displacements^[29-33].

For extrusion problems, depending on the type of model, the transient and steady-state components of the process can be analyzed. The transient portion is of interest if peak pressure and the deformation behavior at the beginning of the extrusion need to be examined. For the steady-state situation, the deformation behavior of the head end and the tail end of the billet cannot be analyzed; only the deformation behavior in the deformation zone can be investigated. The Eulerian description is suitable for this analysis with the *Flow Approach*. In the Eulerian description, the mesh is stationary while the material flows through the

deformation zone during deformation. However, for non steady-state (transient) problems, the total Lagrangian or updated Lagrangian description is preferable and is adopted by using the *Solid Approach* or *Flow Approach*. In a non steady-state process, such as at the initial stage of the extrusion process, the Lagrangian description suffers from major drawbacks when the workpiece endures large or localized deformation and also when the work tools, namely the punch and the die, have complex shapes or sharp edges. This may be attributed to the fact that, in the Lagrangian description, the finite element mesh remains embedded in the material and moves with it. Lack of control over the grid motion often results in excessively distorted elements, thus deteriorating the quality of the finite element solutions. Continuing the simulation beyond certain levels of deformation becomes impossible in many cases, on account of entangled or non-convex elements. Therefore, various remeshing schemes have been attempted to overcome these obstacles^[26,34-39].

Another approach is the application of an Arbitrary Lagrangian-Eulerian description (ALE) to industrial metal forming simulation^[16]. In Arbitrary Lagrangian-Eulerian description, the mesh moves at a different velocity from that of the material. The description is a hybrid between the Lagrangian and Eulerian descriptions, i.e., if the mesh moves at the same velocity as material, it is termed Lagrangian, and if the mesh velocity is zero, it is Eulerian. However, it is difficult to choose an appropriate mesh velocity; and it appears that remeshing is required during large deformation.

2.4.2 Development of an Extrusion Limit Diagram Using FEM

The above described semi-empirical equations in Section 2.3 for development of extrusion limit diagrams result in mean values for the variable. One recognized^[69] drawback of the semi-empirical approach is the problem of analyzing the close inter-relation of the

process variables- flow stress, strain rate and temperature. The intractability of the situation can lead to a large number of experiments being required.

A more attractive, and increasingly accessible approach is the use of finite element techniques^[70-74]. Grasmø *et al.*^[70] have used a finite element model to simulate the extrusion of an Al-Mg-Si alloy, AA6060. The model considers the material to behave like a fluid and does not include predictions during the billet upsetting phase. However, it is the most practical and complete model of extrusion developed to date using FEM techniques. Nevertheless, there is little literature using a finite element technique to develop extrusion limit diagrams.

For the extrusion of particulate reinforced composites, low speed cracking should be included in the limit diagram. However, no work has been found for the low speed cracking. Dixon^[9] proposed that the low speed cracking boundary is a function of extrusion ratio as schematically shown in Fig. 2.5. The low speed cracking boundary can be determined by a series of plant trials. Alternatively, a finite element model can also be employed to determine this boundary provided a suitable criterion is inserted into the model.

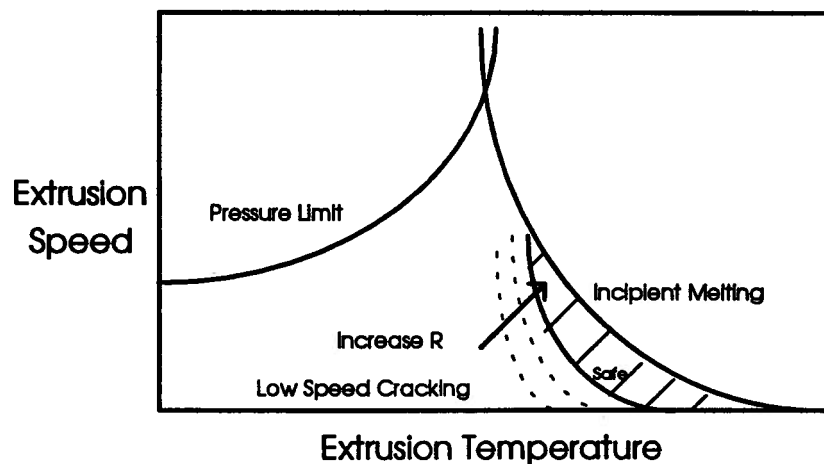


Figure 2.5 Schematic extrusion limit diagram with low speed cracking^[5]

2.4.3 Fracture Criteria for Monolithic Metals

Some fracture criteria for cold and hot working have been established to rationalize the data which are available for different test geometry, i.e., *Stress Criterion*; *Strain Criterion*, *Plastic-Work Criterion*^[49]. The *Stress Criterion* was based on the fact that cracking in metal-working was recognized to be associated with induced tensile stresses, even in processes such as forging in which the stresses are predominantly compressive. The importance of the tensile stresses was indirectly confirmed by the large increase in apparent ductility when materials are deformed under hydrostatic pressure. The tensile fracture of conventional alloys is considered in terms of the microvoid coalescence model (MVC) in which the fracture strain expected is the sum of the nucleation strain, the void growth strain until void coalescence occurs, and the final linkage strain, ϵ_L .

$$\epsilon_F = \epsilon_N + \epsilon_G + \epsilon_L \quad (2.10)$$

Usually ϵ_L is considered to be small relative to the other terms, therefore the fracture strain is expressed as:

$$\epsilon_F = \epsilon_N + \epsilon_G \quad (2.11)$$

However, in working operations, it is likely that both shear and tensile stresses play a part, since there is evidence that localized flow by shear is required to initiate cracks which are then propagated by tensile stresses. A *Strain Criterion* has also been suggested by some workers^[50] based on the total strain, but difficulties arise since the total strains vary markedly in different processes. Therefore, it is reasonable to assume that any criterion should be based on some combination of stress and strain rather than on either of these quantities separately. There are indications that the total plastic work to fracture may be an important factor (*Plastic-Work Criterion*). Cockcroft and Latham proposed that fracture occurs in a ductile

material when, for a given temperature and strain rate, the plastic work done by the highest tensile stress reaches a specified limit^[51].

$$\int_0^{\epsilon_p} \bar{\sigma}(\sigma_1 / \bar{\sigma}) d\bar{\epsilon} = C \quad (2.12)$$

Cockcroft and Latham successfully applied the criterion to cold working but did not test it for hot working. Sellars *et al.*^[49] tested the above equation and concluded that the equation could be a reasonable criterion for hot working as well as for cold working, but claimed that further data is required to test it more rigorously for hot working.

2.5 Finite Element Analysis of the PRMMCs

In modeling monolithic metal forming, some approximations are always made, such as constant volume of material, isotropy, coincidence of the axis of principle stress and strain, no influence of hydrostatic pressure and equivalent response to tensile and compressive loads. For the MMCs, these assumptions are not entirely valid. Therefore, a micro-material model needs to be developed to characterize the particle and the material behavior on a microscopic scale due to microstructural characteristics and their influences on properties. However, there is little published work on the microanalysis of mechanical working of the MMCs at elevated temperature. The micromechanical analysis of the particulate reinforced MMCs associated with thermal phenomena and simplified loading conditions are discussed to review the current methodology of the MMC deformation analysis.

A few studies have been attempted for the micromechanical analysis of materials, including fiber^[40-42] and particulate reinforced MMCs^[43-46], but most of them are based on a unit cell model with idealized boundary conditions. Aradhya *et al.*^[45] analyzed a simplified MMC structure under tensile loading, as shown in Fig. 2.6.

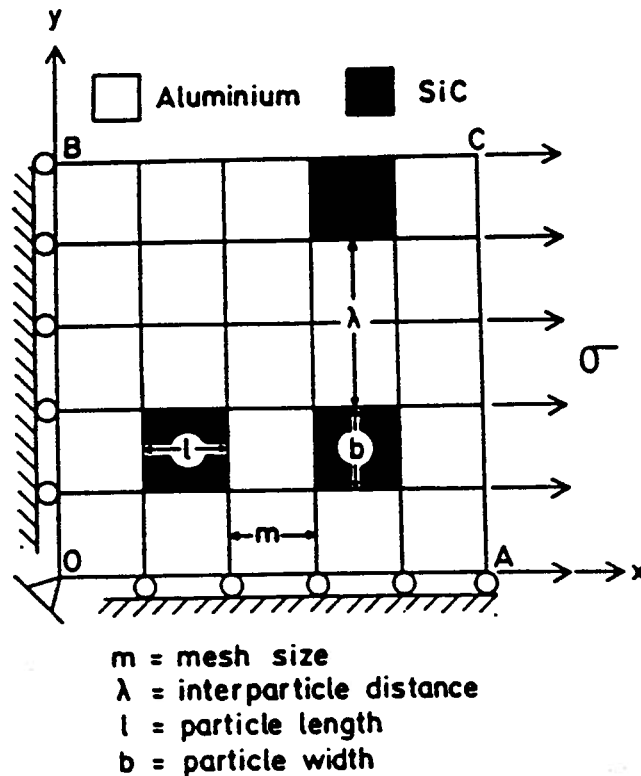


Figure 2.6 Finite element model used by Aradhya *et al*^[45]

Based on a two-dimensional finite element model, the mechanical properties of 6061 Al/SiCp composites and the effect of different volume fractions of SiCp on the tensile properties were investigated. In their analysis, the particle size was assumed to be $40\mu\text{m}$ and uniformly distributed, and the aspect ratio was taken to be unity. The model predicted that, below a certain critical volume fraction of SiCp (25%), the matrix material in the composite yielded at slightly lower stresses compared to the unreinforced material under the tensile loading conditions. This is obviously contrary to the experimental results which indicate that the 0.2% yield stress of composite is invariably higher than the unreinforced matrix alloy. The apparent discrepancy between the FEM and the experimental results was explained by the fact that the properties of the unreinforced matrix material were used in the model to describe the matrix material in the MMCs. The UTS values predicted by FEM were much lower than the

experimentally observed. The discrepancy between the elastic modulus prediction by FEM and experimentally measured values also existed, and the maximum difference was about 12% at volume fraction = 0.4. In spite of this, the unit cell model with idealized assumptions in a MMC micromechanical analysis, such as, uniform distribution of second phase particle with regular particle shape, idealized boundary conditions, etc. can give a preliminary insight of the microscopic behavior of the MMCs, although it is far from reality.

A more flexible discretization for different volume fractions of particulate reinforcements was developed by Ramakrishnan *et al.*^[46] using a master mesh, as shown in Fig. 2.7.

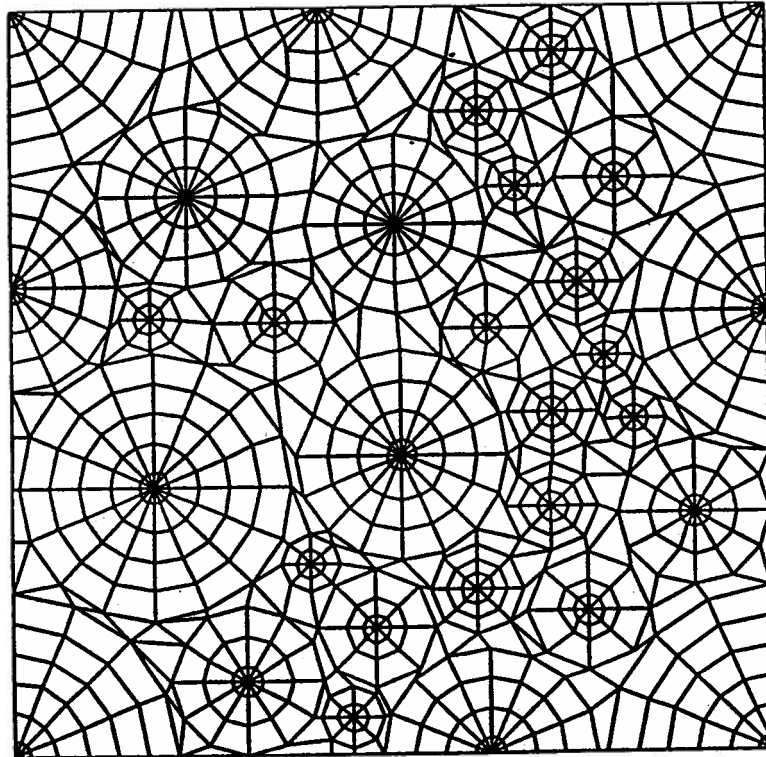


Figure 2.7 Master mesh for generating different microscopic morphologies^[46]

In their finite element analysis, some important aspects associated with the transformation induced plasticity in $\text{Al}_2\text{O}_3\text{-ZrO}_2$ were analyzed. These aspects included: (i) an estimation of the residual stress in the second phase, arising during post fabrication cooling, which affected the critical stress for transformation; (ii) the constitutive behavior of the material during the dilatational transformation of ZrO_2 and (iii) the crack deflection due to the transformation. The study was conducted for angular and spherical shapes of second phase particles and also for varying volume fractions of the second phase. The crack morphologies generated by the FEM study for different overall fractions of the angular ZrO_2 are shown in Fig. 2.8, based on the assumption that the particle/matrix was perfectly bonded. Because the master mesh model represents more closely the real situation of the MMCs (with randomly distributed second phase particle and its random shapes, angular or spherical) than regular arrangement of the reinforcements with idealized shapes, such as spherical, cylindrical, square, etc. assumed by other unit cell finite element models described above, the comparison of analytical solutions they derived assuming a spherical shape for the second phase particles with the results obtained through the simulation showed very good agreement. However, no experimental validation was provided due to the difficulties for a master mesh model to satisfy all the real boundary conditions. Moreover, in their study, since no large deformation was involved, the mesh size and its arrangement were not altered during the simulation. But for large deformation of the MMCs, the mesh which represents the matrix would distort, while the mesh representing the reinforcement would not distort due to its higher stiffness. Therefore, a remeshing technique has to be applied. It is evident that the master mesh model cannot be adopted on a microscopic scale in the extrusion process, because a large number of elements would be required and remeshing would be difficult. However, microscopic

mechanical analysis could be conducted based on an idea of multilevel finite element analysis during large deformation with some simplifications.

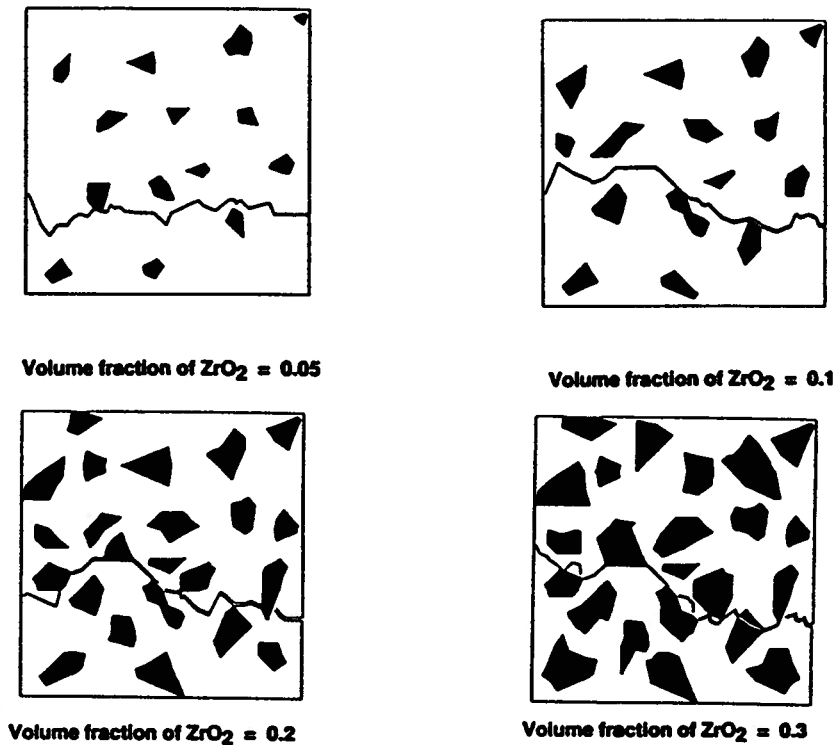


Figure 2.8 The crack morphologies generated by the FEM study for different overall fraction of the angular ZrO_2 with transformation^[46]

2.5.1 Multilevel Finite Element Method

Multilevel finite element analysis was first proposed by Kopp *et al.*^[47,48] in the simulation of metal forming processes to optimize the computation time. At Level 1 (Global Analysis) integral parameters such as the required force and required work are computed using a coarse FEM mesh; At Level 2 (Local Analysis), an optimized number of elements is used to determine continuum mechanics parameters like stress, strain and temperature; Microscopic phenomena are simulated at Level 3 (Microscopic Analysis), using special micro-material elements and thermodynamic models. The method has been applied to an upsetting

problem. The results from Level 1 are sufficient to provide reasonably accurate data for the estimation of the size of plant needed or the forming schedule of a process. When the formability of a workpiece is concerned, a more detailed analysis (Level 2) is required. Moreover, the results from Level 2 are useful in analysis at Level 3. At Level 3, either microstress or thermodynamic evolution, such as, recrystallization, etc., is of interest. Using a microscopic material element, the stress concentration around a second phase particle, such as a ceramic particle in the MMCs, can also be estimated by locally refining the finite element mesh as shown in Fig. 2.9(a).

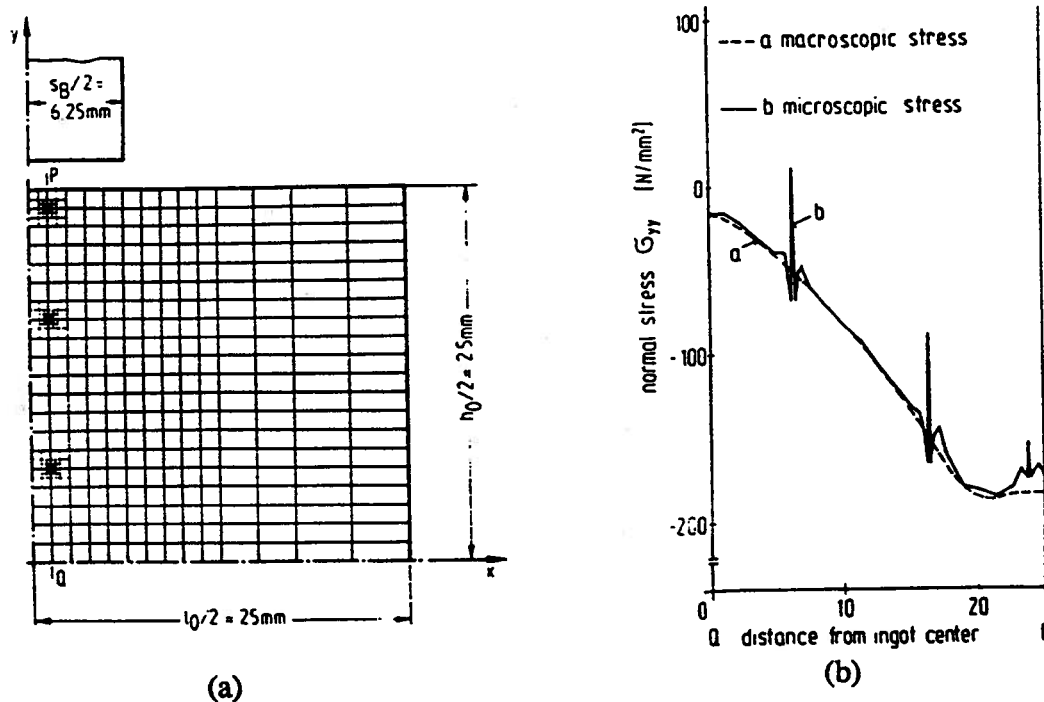


Figure 2.9 (a) FEM mesh with local refinement during a plane-strain upsetting;
 (b) Stress distribution along the line PQ ($\epsilon_n=1\%$ calculated with ABAQUS)^[47,48]

The results using a multilevel finite element system to calculate the stress concentration due to second phase particles are shown in Fig. 2.9(b), based on the distribution of second phase particles along the line PQ shown in Fig. 2.9(a). Figure 2.9(b) shows that the

continuum-mechanics based solution (Level 2: macroscopic stress) yields a normal stress (curve a), while substitution of the micro-elements (Level 3: microscopic stress) produces a stress curve (curve b) in the same figure with spikes at the positions of micro-elements. Obviously, the substitution of micro-element (or second phase particles in real materials) changes the local stress in the matrix. For metallurgical microanalysis, FEM results from Level 3 are needed to study microstructure evolution during hot deformation.

2.5.2 Particle Fracture Model during Deformation

Finite element analysis at level 2 can reveal the macroscopic deformation behavior of the MMCs during extrusion. However, criteria quantifying the microstructure (fracture) at level 3, based on the deformation behavior, are required. Brechet *et al.* [75-76] assumed that the probability of fracture of a particle, p_f , is a function of area-equivalent particle diameter, D , and strain, ϵ , at room temperature as below.

$$p_f = \beta D^3 \epsilon \quad (2.13)$$

where β is a constant and the probability is defined as the ratio of the number of cracked particles to total number of particles. Their experimental data had verified the linear relationship between the fracture (percentage of particles cracked) and the imposed level of strain by compressing a sample of Al(A356)-20%SiC. The model did not consider the shape of a particle (including aspect ratio). As observed in the microstructure in extrudates of alumina particulate-reinforced metal matrix composites, equiaxed particles crack less easily. To take aspect ratio into account, the probability of a particle cracking can be expressed as:

$$p_f = 1 - \exp(-\beta_1 D^3 \alpha \epsilon) \quad (2.14)$$

where α is the aspect ratio of a particle and β_1 is a constant ($= 1.6 \times 10^{-4} \mu\text{m}^{-3}$). It is noted that Eq. (2.14) is consistent with the experimental data from Brechet *et al.* [76]. Actually, if the

exponential term in Eq. (2.14) is less than 1, Eq. (2.14) could be approximately expressed as Eq. (2.13). Because the above equations are valid for room temperature, it is not clear whether or not the criteria apply to high temperature deformation such as the hot extrusion process. At high temperature, plastic relaxation around particles is easier due to possible dislocation climb, and work hardening is not dominant, while the strain rate is more sensitive to flow stress. Due to the compressive stress state in the hot extrusion process, particle cracking could be the dominant fracture mode. Humphreys and Kalu^[77] have investigated the low temperature transition of a second phase particle behavior in a model material of Al-Si alloy. At low temperature, there is an accumulation of dislocations at the particles, whereas at high temperatures climb is possible with the consequence that there is no stress build-up. Consequently there will be very little particle damage or interface decohesion. They proposed that at high temperature the critical strain rate below which stresses will not accumulate is given by:

$$\dot{\epsilon}_c = K_1 \exp(-Q_v / RT) / Td^2 + K_2 \exp(-Q_b / RT) / Td^3 \quad (2.15)$$

where K_1 and K_2 are material constants, Q_v and Q_b are the activation energies for bulk and surface diffusion, d is the diffusion distance, and T is the absolute temperature. They also pointed out that with appropriate adjustments to the constants, the above equation may be used with some confidence to predict the effect of second-phase particles on the mechanical behavior of alloys at elevated temperature.

Based on the above analysis, it would be feasible to neglect the strain effect because of less work hardening, but add the strain rate and temperature effect to account for the probability of a particle fracture at high temperature. Therefore, the strain rate compensated

variable, $Z = \dot{\epsilon} \exp(Q / RT)$, should be introduced to consider the probability of a particle fracture during deformation at high temperature. Moreover, 'healing' of fractured particles by intruding matrix materials into the gap of two halves has been observed in deformed materials with superimposed hydrostatic pressure. The pressure, p_h , required for the matrix material to intrude into the cracks is expressed as^[75]:

$$p_h(\epsilon) = \sigma_y \left[\frac{2}{3} + \frac{D}{3h_0} \left(\frac{\ln(D/h_0) - \epsilon}{\ln(D/h_0)} \right) \right] \quad (2.16)$$

where h_0 is the initial width of the gap of the crack and σ_y is the flow stress of the matrix. It is evident that easier 'healing' could occur at high temperature if this equation is applicable.

2.5.3 Microscopic Analysis of PRMMCs under Larger Deformation

It is known that a microscopic analysis of the PRMMC during industrial extrusion process is impractical. The multilevel system can be applied to the analysis of particulate reinforced MMC during large deformation in laboratory tests, although a specific micro-element material model is required on a microscopic scale to induce its anisotropy. At the macroscopic level, the MMCs are assumed to be isotropic and the continuum plasticity theory is used. The deformation behavior of the MMCs can be characterized and the formability of the MMCs can be analyzed by using a modified *Plastic-Work Criterion*. At a microscopic level, micromechanical analysis of the MMCs under large deformation can be conducted by a single particle model (micro-element material model) and a multiple particle model to be described in later section. In this study, the behavior of a particle during a cylindrical compression and a plane strain test will be analyzed at both the macroscopic and microscopic level, to help understand the microstructural evolution of the PRMMC during large deformation (including extrusion) at high temperature.

Chapter 3 SCOPE AND OBJECTIVES

Particulate reinforced MMCs are attractive for many applications in the automotive industry. However, the demand has been limited owing to the cost and insufficient knowledge of the behavior of the MMC materials. Many discontinuously reinforced MMC products require deformation processing via rolling, extrusion, or forging to achieve the final shape. Issues associated with these processing schedules include equipment capabilities, die wear due to the abrasive nature of the reinforcements and the influence of deformation conditions on microstructure and properties. To meet the goal of increased productivity with high quality and reduced costs, a better understanding is needed of how deformation processing influences microstructure and properties in these materials.

3.1 Scope and Objectives

From the literature review, it appears that the extrusion process is the widely used and one of the most economical secondary processing routes for particulate reinforced MMCs. It may also improve the mechanical properties of the material. The scope and objectives of this study are:

- 1) To conduct compression tests using a Gleeble[®] machine to develop constitutive equations for the PRMMCs. The constitutive law will be adopted in the finite element model;
- 2) To better understand the deformation behavior of the alumina particulate reinforced MMCs during extrusion with the aid of a finite element model, DEFORM[®] , at macroscopic level;

[®] Gleeble is a registered trade mark of Dynamic Systems, Inc., New York, USA.

3) To conduct extrusion plant trials to examine the microstructural evolution (e.g., particle fracture and size refinement) and the mechanical property change of the MMCs under different extrusion conditions; the plant trial data, such as extrusion force and temperature measurement will be used in validation of the finite element model predictions and the model predictions as well as plant trial data will be applied to the development of an extrusion limit diagram;

4) To establish a correlation between deformation parameters and the low speed surface cracking by microstructural examination and the finite element analyses at both macroscopic and microscopic levels.

3.2 Methodology

An integrated approach has been adopted for this study: Gleeble compression tests were conducted to develop the constitutive law of the alumina reinforced metal matrix composites. The constitutive law has been adopted in the finite element analysis of the extrusion process. Extrusion plant trials were conducted and the plant trial data were used in validation of the finite element model predictions. Microstructural evolution for the extrusion billet and extrudates was examined using an optical microscope and an image analyzer. A correlation between deformation variables (e.g., ram speed (strain rate), extrusion ratio and temperature), and composite failure (including surface cracking) was established based on an SEM surface crack examination and the FEM analyses. The effect of extrusion conditions on the mechanical property change was investigated by conducting tensile tests of the extrudates. Extrusion limit diagrams for the material were finally developed for the purpose of industrial production. The overall conception of the project is schematically shown in Figure 3.1.

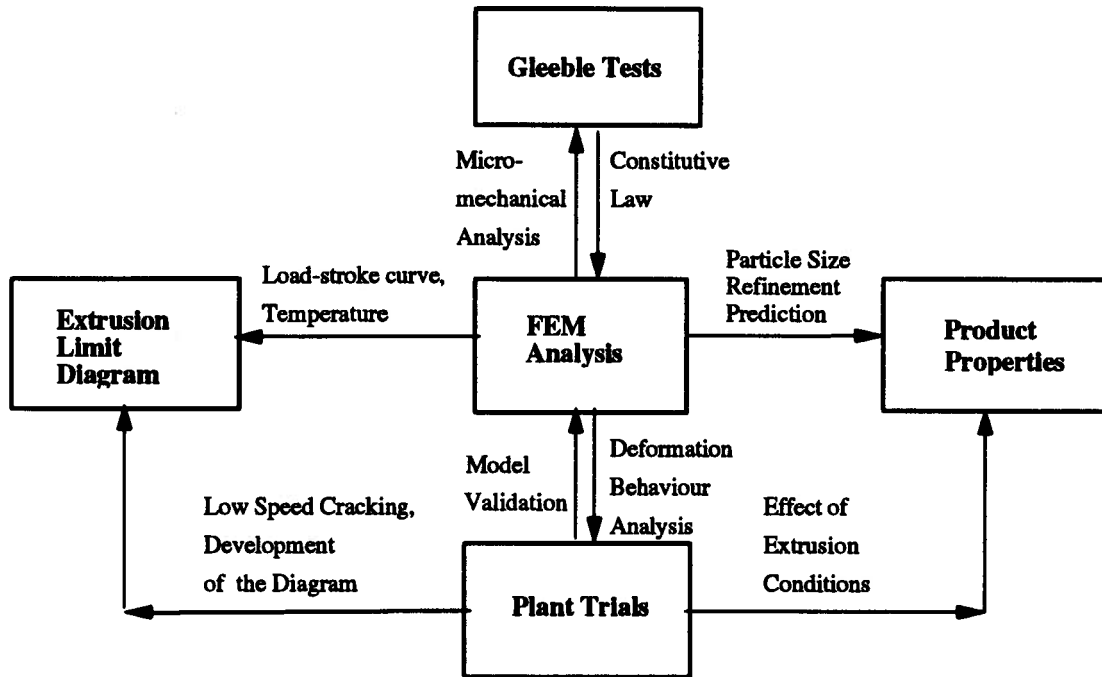


Figure 3.1 Methodology for the extrusion of alumina particulate reinforced MMCs

Chapter 4 EXPERIMENTAL

Laboratory tests and plant trials were conducted to better understand the behavior of the alumina particulate reinforced metal matrix composites during processing. Constitutive equations for three different volume fractions, 10%, 15% and 20%, of the MMCs were developed based on cylindrical compression tests using a Gleeble[®] machine. The constitutive equations will be used in extrusion process simulation with the aid of a finite element model. Two plant trials were conducted on a small press in the Kingston Research and Development Center (KRDC), and a large industry press at Universal Alloy Corporation (UAC), Anaheim, for two different volume fractions, 10% and 20%, of the composites. The extrusion data such as load-stroke and die temperature will be used for validation of a FEM model prediction and development of extrusion limit diagrams. Microstructure evolution of the composites during extrusion will be examined using microscopes and correlated with the tensile properties measured from the extrudates of the KRDC plant trials.

4.1 Gleeble Tests

Specimens of 6061/Al₂O₃ with three different volume fractions from 10% to 20% were machined from cast billet stocks into cylinders of 10mm diameter by 15mm long. The specimens were homogenized at 565°C for 2 hours to improve the as-cast structure, to reduce segregation and precipitates and large dispersoids. Compression testing was conducted using a 'Gleeble[®] 1500' thermomechanical simulator. The specimens were resistance-heated at 5°C/s to test temperatures in the range of 400°C to 525°C, held at that temperature for one minute, and then deformed to a true strain of 1.0 at a nominal strain rate of 0.05, 0.1, 1, or 10s⁻¹. Graphite shims were inserted between the specimen and ram to

prevent excessive barreling (Figure 4.1). The test conditions chosen were based on the extrusion conditions adopted in industry for the unreinforced aluminum alloys.

The hot working behavior of many conventional alloys has been characterized with an empirical equation derived from creep laws. The equation which is most applicable over the range of strain rates and temperature encountered of monolithic alloys during hot working is the hyperbolic sine constitutive equation (Equation 4.1)¹⁷⁸.

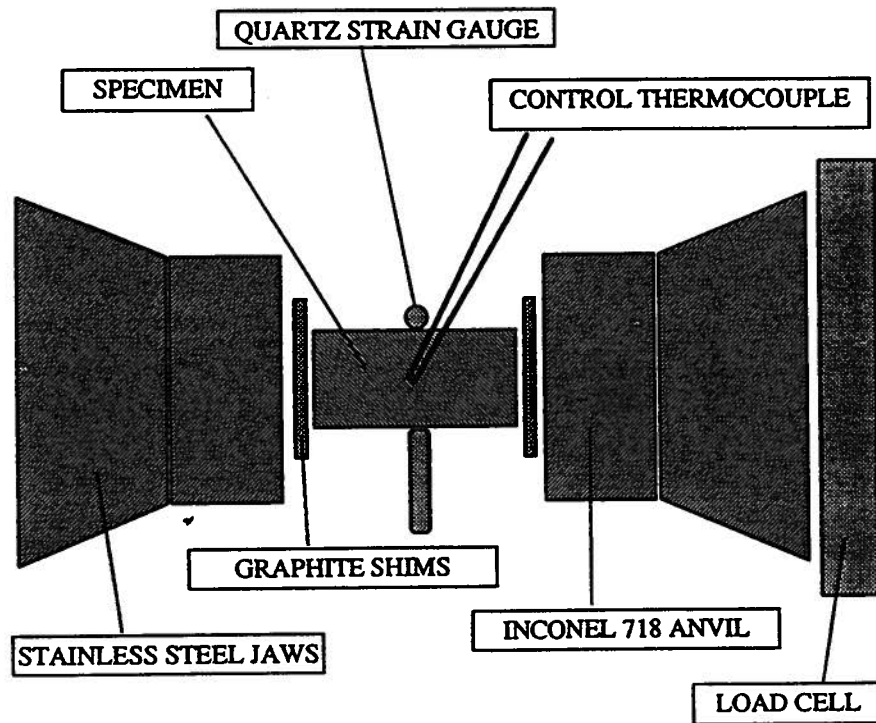


Figure 4.1 Schematic of the Gleeble test set-up

$$Z = \dot{\epsilon} \exp(Q / RT) = A \sinh(\alpha \sigma)^n \quad (4.1)$$

where Z is the Zener-Hollomon parameter (the temperature compensated strain rate), $\dot{\epsilon}$ is strain rate, Q is activation energy, R is the universal gas constant, T is the absolute temperature, σ is the flow stress and A , α , and n are constants. It is noted that the equation is strictly valid only over the steady state regime of deformation and as such, it may not be

applicable to the low strain range where transient behavior is observed. However, some workers have empirically applied the equation over the whole strain range of a test with a reasonable fit of the data^[79]. Typically during analysis for the equation constants, α is set to an arbitrary value and the other parameters are calculated using plots $\ln\{\sinh(\alpha \sigma)\}$ against $\ln \dot{\epsilon}$ to determine n , and $\ln\{\sinh(\alpha \sigma)\}$ against $1/T$ to determine Q . The method of unconstrained variables was used in this study to analyze the data for the four parameters in the constitutive equation. This method, based on a procedure first shown by Sheppard and Wright^[80], allows all four of the equation constants to vary during iteration to a solution, rather than fixing α , as is common in most other work. For the data analysis, true strain was calculated from transverse extensometer readings of the variation of specimen diameter during compression. The flow stress for the analysis was calculated at a strain of 0.5 in the steady state regime. The nominal strain rate was obtained from the recorded value over a strain range of 0.35 to 0.65, because it varied at the beginning and at the end of the deformation. The temperature used for the analysis was also the absolute value at a strain of 0.5. The values of the four parameters in the hyperbolic sine equation were determined through iteration by minimizing the absolute difference between the measured flow stress and the predicted flow stress. The values of each material constant for the composites are compared with those for the unreinforced parent alloy in Table 4.1. It is noted that the four constants were determined for the best fit of the experimental data^[81]. The correlation coefficient between the predicted and the experimental data for each volume fraction is also listed in Table 4.1 for reference. It is seen that a good correlation has been obtained between the predicted flow stresses and the experimental data.

Table 4.1 Material constants for the constitutive equation of the Composites^[81]

Material	Q(kJ/mol-K)	A(s ⁻¹)	α (MPa ⁻¹)	n	Correlation Coefficient
6061	197.5	1.97x10 ¹²	0.036	4.11	0.997
6061/Al ₂ O ₃ /10p	216	9.42x10 ¹⁴	0.023	5.24	0.988
6061/Al ₂ O ₃ /15p	210	9.77x10 ¹²	0.034	4.00	0.992
6061/Al ₂ O ₃ /20p	220	4.45x10 ¹⁴	0.024	4.41	0.987

4.2 Plant Trials at UAC, Anaheim

4.2.1 Extrusion Procedure

Two plant trials were held at Universal Alloy Corp., Anaheim, on the Duralcan composite and its unreinforced material. Two billets each of 6061, 6061/Al₂O₃/10p and 6061/Al₂O₃/20p were extruded in the first plant trial in September, 1992 (designated as 'S92', hereafter). Only the 6061 and one of the 6061/Al₂O₃/20p billets were homogenized. The remaining three billets were extruded in the as-cast state. The two 6061/Al₂O₃/10p billets were 508 mm (20") long and all the others were 304 mm (12") long. The diameter of all the billets were 178 mm (7") in the second plant trial in July, 1994 (designated as 'J94', hereafter). 22 billets, 14 of 6061/Al₂O₃/10p, and 8 of 6061/Al₂O₃/20p, were extruded using 4 different dies. They were all prehomogenized at about 570°C for four hours. The length of all 22 billets was 381mm (15"), and the diameter of all the billets was also 178 mm (7"). Details of the extrusion condition are listed in Table 4.2.

Table 4.2 Extrusion programs for the 7" press at UAC

Test No.	Material	Billet Dimension (L (mm) x D(mm))	Die Diameter (inch)	Pretreatment
S92-1	6061	305x178	1.25	Homogenized
S92-2	6061	305x178	1.25	Homogenized
S92-3	6061/Al ₂ O ₃ /20p	508x178	1.25	Homogenized
S92-4	6061/Al ₂ O ₃ /20p	508x178	1.25	as-cast
S92-5	6061/Al ₂ O ₃ /10p	305x178	1.25	as-cast
S92-6	6061/Al ₂ O ₃ /10p	305x178	1.25	as-cast
J94-1	6061/Al ₂ O ₃ /10p	381x178	2	Homogenized
J94-2	6061/Al ₂ O ₃ /10p	381x178	2	Homogenized
J94-3	6061/Al ₂ O ₃ /10p	381x178	2	Homogenized
J94-4	6061/Al ₂ O ₃ /10p	381x178	2	Homogenized
J94-5	6061/Al ₂ O ₃ /20p	381x178	2	Homogenized
J94-6	6061/Al ₂ O ₃ /20p	381x178	2	Homogenized
J94-7	6061/Al ₂ O ₃ /20p	381x178	2	Homogenized
J94-8	6061/Al ₂ O ₃ /10p	381x178	1.25	Homogenized
J94-9	6061/Al ₂ O ₃ /10p	381x178	1.25	Homogenized
J94-10	6061/Al ₂ O ₃ /10p	381x178	1.25	Homogenized
J94-11	6061/Al ₂ O ₃ /10p	381x178	1.25	Homogenized
J94-11b	6061/Al ₂ O ₃ /10p	381x178	1.25	Homogenized
J94-12	6061/Al ₂ O ₃ /20p	381x178	1.25	Homogenized
J94-13	6061/Al ₂ O ₃ /20p	381x178	1.25	Homogenized
J94-14	6061/Al ₂ O ₃ /20p	381x178	1.25	Homogenized
J94-15	6061/Al ₂ O ₃ /10p	381x178	1	Homogenized
J94-16	6061/Al ₂ O ₃ /10p	381x178	1	Homogenized
J94-17	6061/Al ₂ O ₃ /10p	381x178	1	Homogenized
J94-19	6061/Al ₂ O ₃ /20p	381x178	1	Homogenized
J94-20	6061/Al ₂ O ₃ /20p	381x178	1	Homogenized
J94-11a	6061/Al ₂ O ₃ /10p	381x178	1.5	Homogenized
J94-18	6061/Al ₂ O ₃ /10p	381x178	1.5	Homogenized

A schematic diagram of the press setup at UAC is shown in Fig. 4.2. Billets were preheated in a gas fired, three-zone, chain belt furnace. Initially the three zone temperatures were set to 121°C, 321-343°C and 466°C, but the preset temperature of the last zone was adjusted according to the required extrusion temperature, which is 420°C to 520°C. Billets resided in the furnace for typically 40 min., although, a billet only progressed when the preceding one was withdrawn. Contact thermocouples in each fire zone were employed to measure billet temperature for furnace control (Fig. 4.2). The final zone temperature was recorded in the data spreadsheet as the final billet temperature in the furnace. These temperature measurements have the potential to be inaccurate as they were taken directly after a flame had impinged on the billet surface. Further temperature measurements were taken from both the front and the back end of a billet using a hand-held K-type thermocouple immediately before the billet entered the transfer mechanism (Table 4.3).

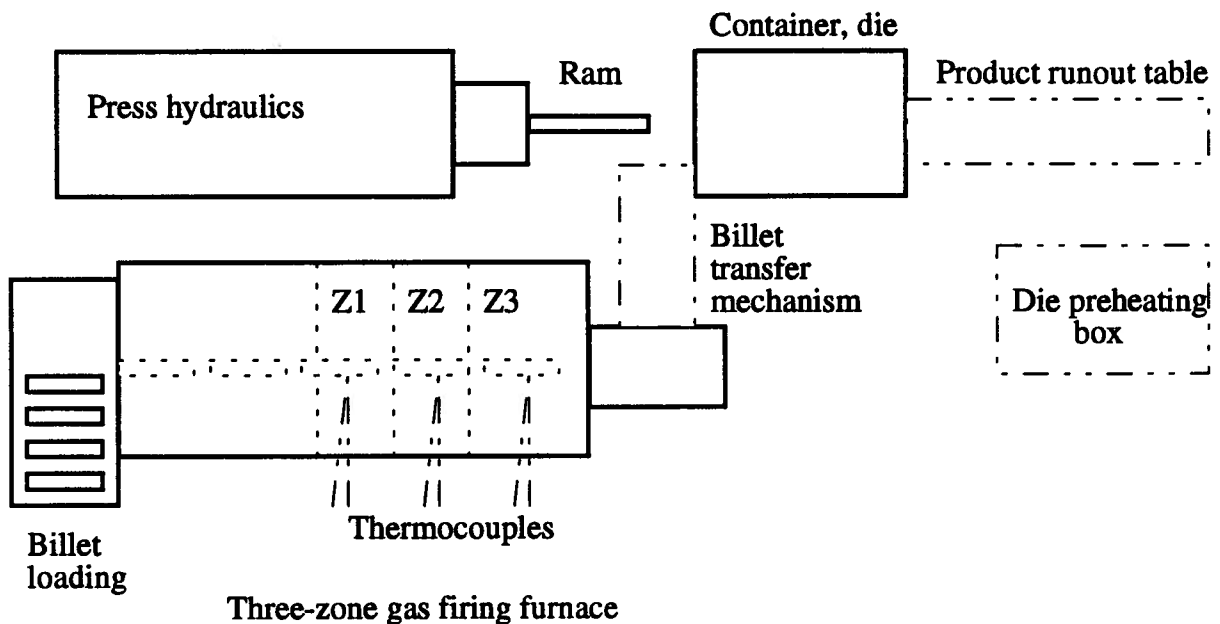


Figure 4.2 Schematic of extrusion setup for Duralcan trials

Table 4.3 Billet temperatures immediately prior to extrusion at UAC

Test No.	Material	Preset Temp. (°C)	Temp. @front (°C)	Temp. @back (°C)
S92-1	6061	427	452	454
S92-2	6061	427	424	438
S92-3	6061/Al ₂ O ₃ /20p	427	429	429
S92-4	6061/Al ₂ O ₃ /20p	427	391	391
S92-5	6061/Al ₂ O ₃ /10p	427	393	410
S92-6	6061/Al ₂ O ₃ /10p	427	431	443
J94-1	6061/Al ₂ O ₃ /10p	466	424	426
J94-2	6061/Al ₂ O ₃ /10p	493	399	399
J94-3	6061/Al ₂ O ₃ /10p	477	459	516
J94-4	6061/Al ₂ O ₃ /10p	493	516	519
J94-5	6061/Al ₂ O ₃ /20p	477	452	457
J94-6	6061/Al ₂ O ₃ /20p	477	444	460
J94-7	6061/Al ₂ O ₃ /20p	488	458	516
J94-8	6061/Al ₂ O ₃ /10p	488	463	521
J94-9	6061/Al ₂ O ₃ /10p	488	479	507
J94-10	6061/Al ₂ O ₃ /10p	488	482	496
J94-11	6061/Al ₂ O ₃ /10p	468	446	457
J94-11b	6061/Al ₂ O ₃ /10p	468	434	483
J94-12	6061/Al ₂ O ₃ /20p	468	423	460
J94-13	6061/Al ₂ O ₃ /20p	491	471	507
J94-14	6061/Al ₂ O ₃ /20p	491	461	514
J94-15	6061/Al ₂ O ₃ /10p	491	488	503
J94-16	6061/Al ₂ O ₃ /10p	491	498	465
J94-17	6061/Al ₂ O ₃ /10p	510	487	529
J94-19	6061/Al ₂ O ₃ /20p	510	484	503
J94-20	6061/Al ₂ O ₃ /20p	477	457	474
J94-11a	6061/Al ₂ O ₃ /10p	466	451	495
J94-18	6061/Al ₂ O ₃ /10p	466	451	457

It is seen from Table 4.3 that the temperature distribution is uneven for most of the billets at the end of heating. Ambient temperature was recorded at 28°C, rising to 38 to 49°C near the press. The total transfer time from furnace to the start of extrusion was 30 to 45 seconds. The pressure pad, or 'dummy block,' which was transferred along with the billet, was preheated to around 49 to 92°C (three measurements were made). The die was preheated to a setup temperature of about 427°C in a die box, whereas the bolster, upon which the die sits, was placed in the stack at ambient temperature. The die assembly would have lost heat because the thermocouple had to be inserted after removal of the assembly from the die box. However, this is of little importance as we have a continuous record of the die temperature. The container temperature was set to heat up to 427°C, but temperatures measured at the inlet part of the container with a hand-held device indicated a variation of 277 to 348°C.

The press is a 3000T horizontal press with no extrudate quenching capability. Extrusion speed was manually controlled by a pulley system, and varied significantly for the establishment of good extrudate surface conditions. A thermocouple was inserted in the die to a position approximately 1.6 mm away from the die bearing surface, and it seemed to give a good response to billet loading and extrusion. The container has an inside diameter of 184 mm. The pressure pad is 89 mm long with a flange at the contact end of 186 mm diameter by 12.7 mm, the rest being 178 mm diameter. All the tools were H13 steels, except for the 1.5-inch die used in the second plant trial of J94-11a and J94-18, which was ceramic material.

4.2.2 Extrusion Data

During extrusion, the load, ram speed and die and container temperatures were recorded. A typical load-stroke curve, with the variation of ram speed, is shown in Fig. 4.3 for the extrusion of Trial S92-3. The peak pressure is reached at the end of the filling-up

stage, when the billet is about to break through the die aperture. Then the extrusion force falls until the pad reaches the dead metal zone, due to the decrease in billet length and consequent reduction in friction force at the container interface. The reason for the variation in extrusion speed greater than about 1mm/s are due to operator actions: the process was surface quality driven with all other factors being subservient. One operator stood at the press exit and directed the actions of another operator who was manipulating the speed control. When surface cracking appeared at the front end of the extrudate, the ram speed was increased.

The increase in die temperature during extrusion is mainly because of heat conduction from the hotter billet (Fig. 4.4). The friction heat at the die interface also heats up the die temperature. After contacting each other, heat conduction occurs between the billet and the die, which causes the steep die temperature increase at the beginning. The die temperature tends to level off when the steady state is reached.

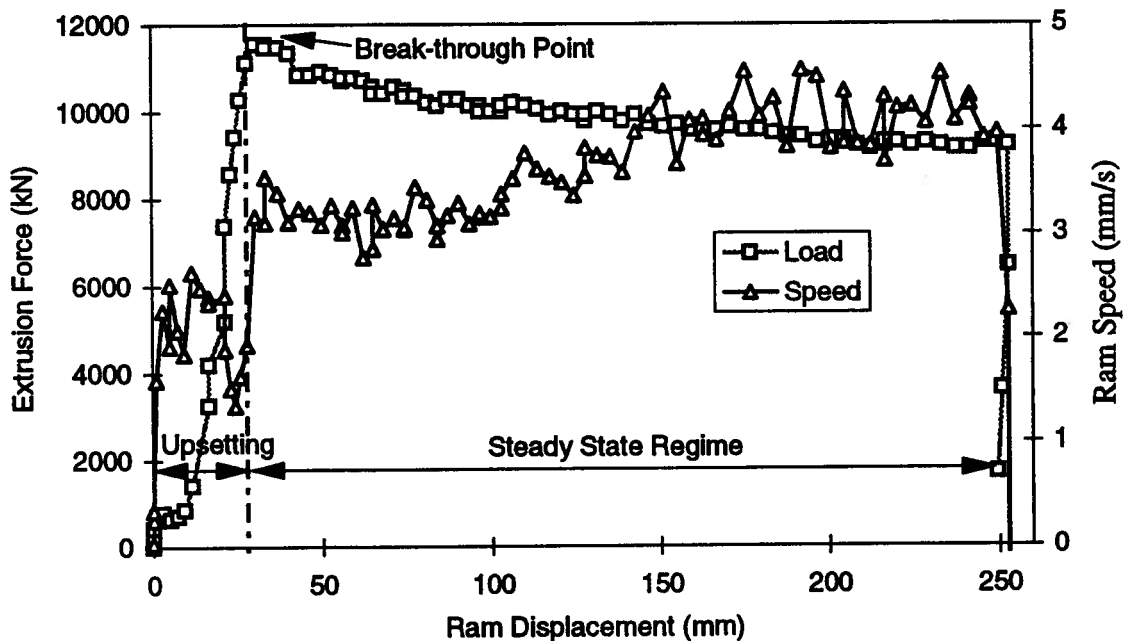


Figure 4.3 Typical load-stroke curve with variation of ram speed (S92-3)

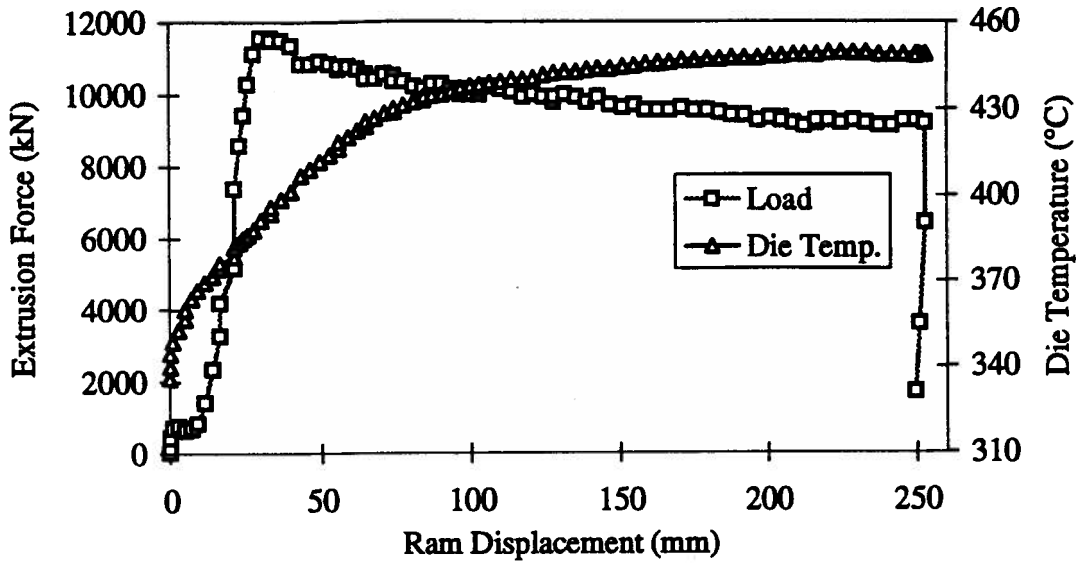


Figure 4.4 Die temperature increase during extrusion (S92-3)

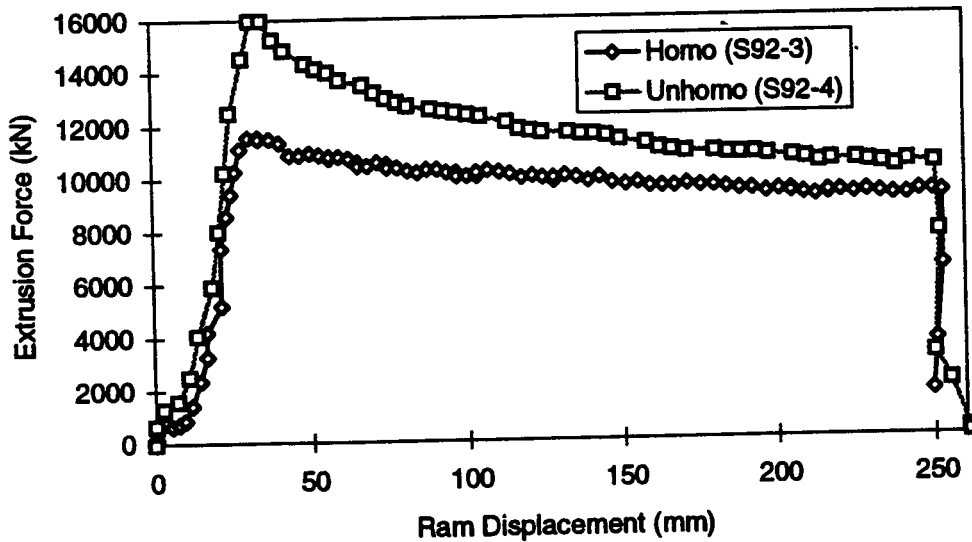


Figure 4.5 Effect of homogenization on extrusion force (S92-3 and S92-4)

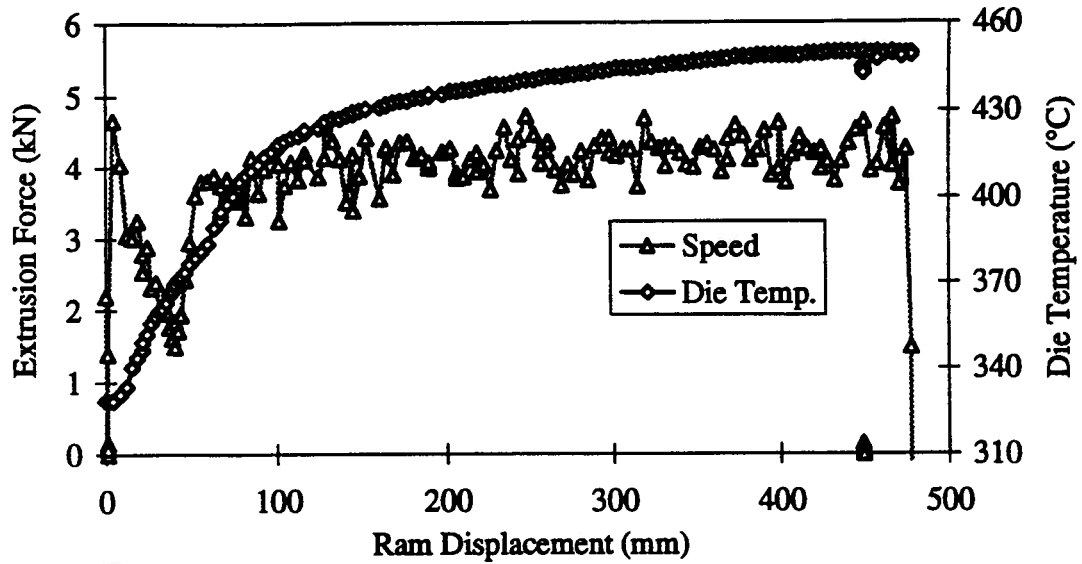


Figure 4.6 A weak correlation of increasing ram speed with increasing die temperature during extrusion (S92-5)

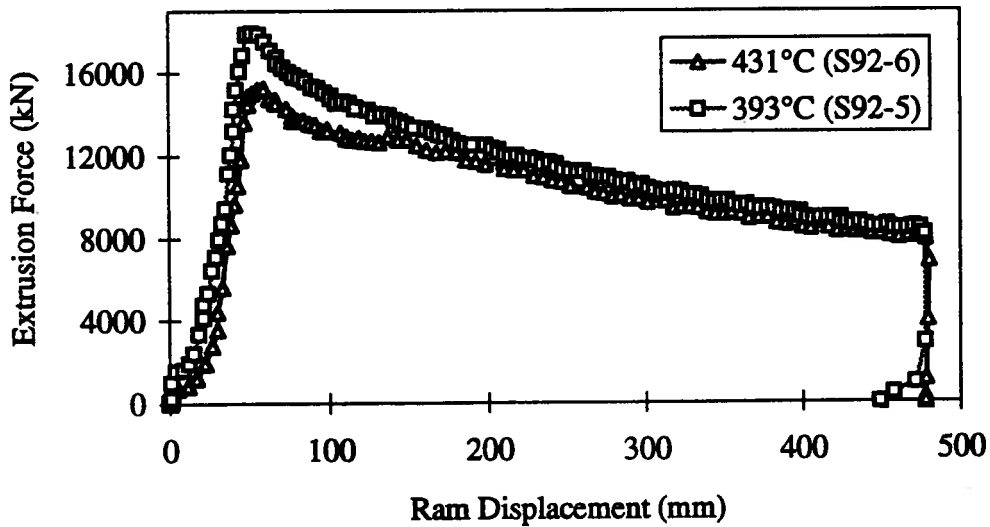


Figure 4.7 Effect of billet temperature on extrusion force (S92-5 and S92-6)

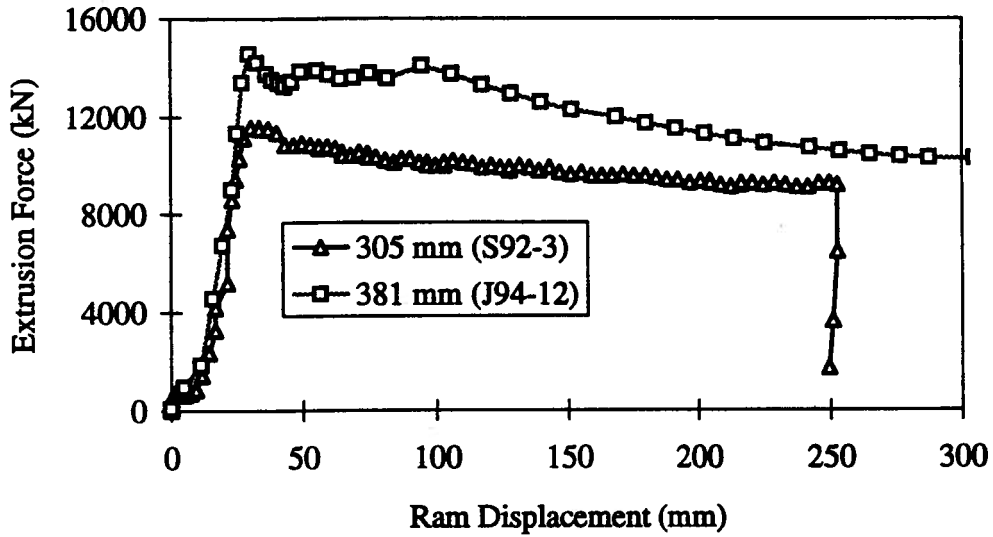


Figure 4.8 Effect of billet length on extrusion force during extrusion (S92-3 and J94-12)

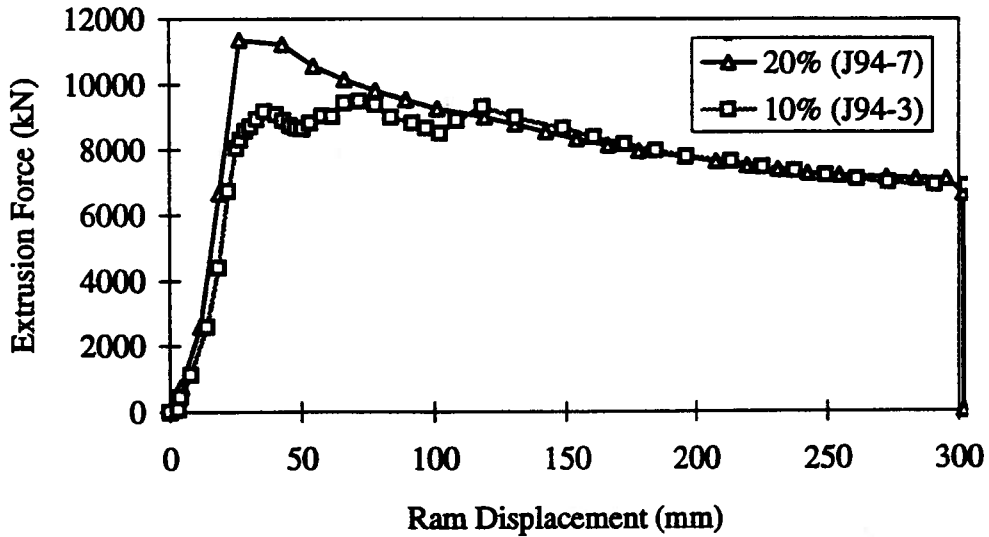


Figure 4.9 Effect of volume fraction on extrusion force during extrusion (6061/Al2O3/10p: J94-3, and 6061/Al2O3/20p: J94-7)

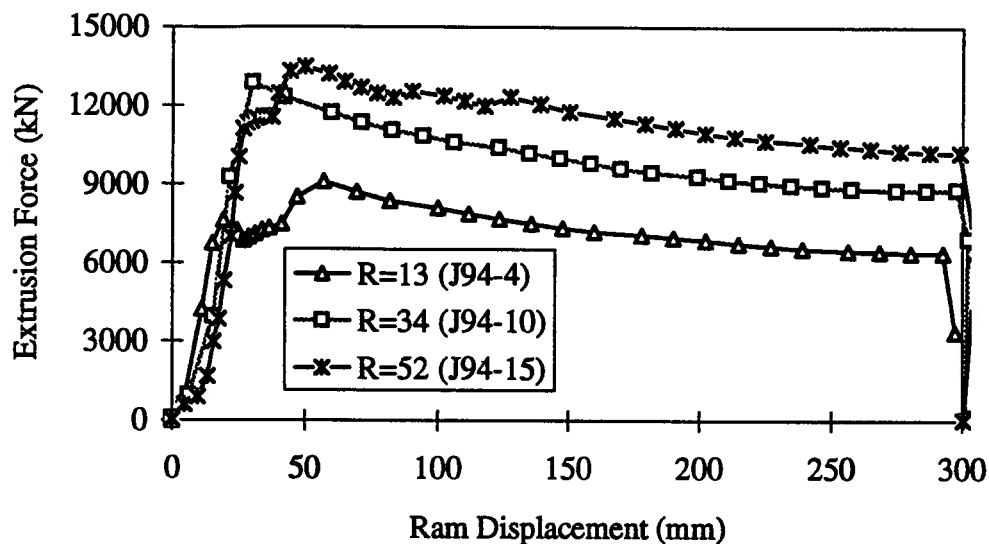


Figure 4.10 Effect of extrusion ratio on extrusion force (J94-4, J94-10, J94-15)

A higher load is required for extrusion of the non-homogenized billets (both 6061/Al₂O₃/10p billets of S92-5 and -6 and 6061/Al₂O₃/20p of S92-4, Fig. 4.5). This higher load is related to the microstructure of the non-homogenized materials, which contain segregated elements, precipitates and large dispersoids.

A weak correlation between increasing ram speed and a delayed increase in die temperature at the thermocouple position was observed, as shown in Fig. 4.6. This is because an increase in ram speed leads to a higher strain rate and a higher stress, which results in a higher rate of heat of deformation. Consequently, a higher billet temperature due to higher extrusion speed causes an increase in die temperature.

A higher load is also needed for extrusion of lower temperature billets, because of the higher flow stress at lower temperatures (Fig. 4.7). The extrusion pressure is dependent only on the flow stress when the extrusion ratio is constant. The increase in extrusion force

associated with an increase in billet length (Fig. 4.8) is due to friction at the container interface; the friction force at the container interface is proportional to the billet length. Figure 4.9 shows that the extrusion force increases with volume fraction of reinforcement because the composite with a higher volume fraction of the particle has a higher flow stress. However, the similar value of the extrusion force for both volume fractions at steady state is due to high initial temperatures of the billet at the back ends, (516°C, see Table 4.3), in addition to temperature rise due to heat of deformation, which results in a similar flow stress for both volume fractions. The effect of extrusion ratio on extrusion force, shown in Fig. 4.10, confirms that a higher extrusion ratio leads to a high extrusion pressure. The influence of extrusion ratio and billet length on extrusion force are also well explained by Eq. (2.2-5).

A higher initial billet temperature was also tested (e.g., J94-17, J94-19) to try to observe the incipient melting, but it failed because of low maximum ram speed of the press. The control device consists of a pulley rig which opens or closes a valve in the hydraulic system. This accounts for the fluctuations of less than about 1mm/s: the press does not have very good speed control, and the maximum speed which can be realized is less than 10mm/s.

4.3 Pilot Extrusion at KRDC, Kingston

4.3.1 Extrusion Procedure

A total of 14 extrusion tests were performed at Kingston Research and Development Center, Kingston, with two volume fractions (6061/Al₂O₃/10p and 6061/Al₂O₃/20p) under different extrusion conditions, as listed in Table 4.4. The microstructure of the extrudates were examined for different extrusion conditions. The extrusion data recorded were used

both in validation of a finite element model and in development of extrusion limit diagrams of the composites. The test number is designated hereafter as 'K-', as shown in Table 4.5.

Table 4.4: Plant trial conditions at KRDC

6061/Al ₂ O ₃ /10p	6061/Al ₂ O ₃ /20p
v ₁ = 0.8-0.9 mm/s	v ₁ = 0.8-0.9 mm/s
T ₁ = 400°C, T ₂ = 500°C	T ₁ = 400°C, T ₂ = 500°C
R ₁ = 10, R ₂ = 28, R ₃ = 64	R ₁ = 10, R ₂ = 28, R ₃ = 64

The billets were in the as-cast condition. The billet was typically 76 mm long and 53 mm diameter. All the billets were preheated in an electric furnace for about three hours to achieve a uniform temperature. The temperature of an instrumented billet of 6061 aluminum alloy in the furnace was monitored and controlled using a thermocouple. The die and the pressure pad were heated at the same time. However, the container was heated separately by three heaters around the outer surface of the container along its axial length (Fig. 4.11). The set-up temperature for the container was 500°C, but the air temperature measured in the container was ~410°C. The ambient temperature was recorded at 24°C. Before extrusion, the die was first inserted into the container from the bottom, then the billet was loaded from the top within 5-10 seconds; finally, the pressure pad was placed on the top of the billet before the stem began to press it. The press is a 100T vertical machine. A schematic drawing of the press set-up is shown in Fig. 4.11. During extrusion, load, ram speed, and ram position were recorded by a data acquisition system at a rate of 1 Hz. Unfortunately, no thermocouples were inserted into either the die or the container to record the temperature variation during extrusion. Only the billet temperature was measured before it was loaded into the container by a hand-held device.

Extrusion speed could not be controlled very well at high speeds (~4mm/s). Therefore, a ram speed of about 1 mm/s was adopted. Only one extra test was conducted at a ram speed of about 3.0mm/s with 6061/Al₂O₃/10_p. All the extrudates were air cooled. The surface finish of most of the extrudates was acceptable, except for K-10, which exhibited severe die land lines and K-11 which showed slight low speed cracks. More details on the low speed cracking will be described in Section 4.4.

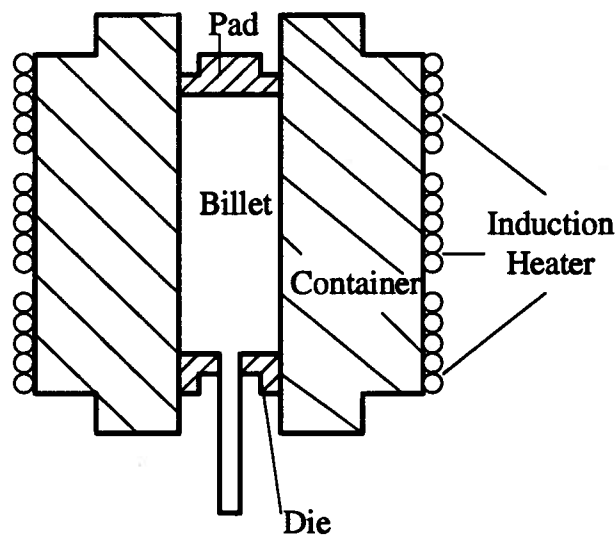


Figure 4.11 Schematic drawing of the extrusion press at KRDC

4.3.2 Extrusion Data

The dimensions of the billets and the extrudates after extrusion were measured (Table 4.5). The container had an inside and outside diameter of 57mm (2.25") and 111mm (4.375") respectively, and its length was 203mm (8"). The pressure pad was 19.05mm (3/4") long with a flange at the contact end of 57mm (2.25") diameter by 3.18mm (1/8"), the rest being 53mm (2.09"). The outside diameter of the die was the same as the inside diameter of the container. The die land lengths were 2.48mm, 1.73mm, and 4.15mm for the 1/4", 3/8", and 5/8" dies, respectively. All the other data are listed in Table 4.5.

Table 4.5 Billet dimensions of each test at KRDC

Trial No.	MMC (vol%)	Billet Dimension (mm)	Die Size (inch)	Extrudate Diameter (mm)	Discard Thickness (mm)
K-1	20%	50.80x87.0	5"/8	15.74	3.0
K-2	20%	50.80x87.0	5"/8	15.75	2.6
K-3	10%	50.80x87.0	5"/8	15.75	1.5
K-4	10%	50.80x87.0	5"/8	15.75	3.0
K-5	10%	/	/	/	/
K-6	10%	50.85x86.40	3"/8	9.72	4.0
K-7	20%	50.76x88.13	3"/8	9.72	11.3
K-8	20%	50.82x85.91	1"/4	6.42	6.0
K-9	10%	50.66x58.61	1"/4	6.40	1.8
K-10	10%	50.90x59.02	3"/8	9.72	2.0
K-11	20%	50.75x84.42	3"/8	9.46	5.0
K-12	20%	50.78x90.89	5"/8	15.875	6.0
K-13	10%	50.51x87.37	5"/8	15.75	4.0
K-14	10%	50.67x86.90	5"/8	15.75	5.5

Table 4.6 Measured test data of the plant trials at KRDC

Trial No.	Material (vol%)	T _B (Meas'd) (°C)	T _C (setup) (°C)	Ram Speed (mm/s)	Remark
K-1	20%	464	500	0.8-0.9	no crack
K-2	20%	464	500	0.8-0.9	no crack
K-3	10%	464	500	0.8-0.9	no crack
K-4	10%	464	500	0.8-0.9	no crack
K-5	10%	430	/	/	/
K-6	10%	496	500	0.8-0.9	no crack
K-7	20%	467	500	0.8-0.9	no crack
K-8	20%	482	500	0.8-0.9	no crack
K-9	10%	442	500	0.8-0.9	no crack
K-10	10%	418	475	0.8-0.9	die line
K-11	20%	400	475	0.8-0.9	surface crack
K-12	20%	435	475	0.8-0.9	no crack
K-13	10%	436	475	0.8-0.9	no crack
K-14	10%	436	475	2.70	no crack

where T_B and T_C are billet and container temperature respectively.

Figure 4.12 shows a typical force-displacement response and corresponding ram speed for test K-7. The extrusion data has the same characteristics as the data from UAC, Anaheim, and the salient features are provided below:

i) The typical load-displacement curve for direct extrusion is shown in Fig. 4.12. The first stage is upsetting of the billet to fill the container, followed by a characteristic "break-through pressure", which leads to a steady state region with decreasing force due to decreasing friction.

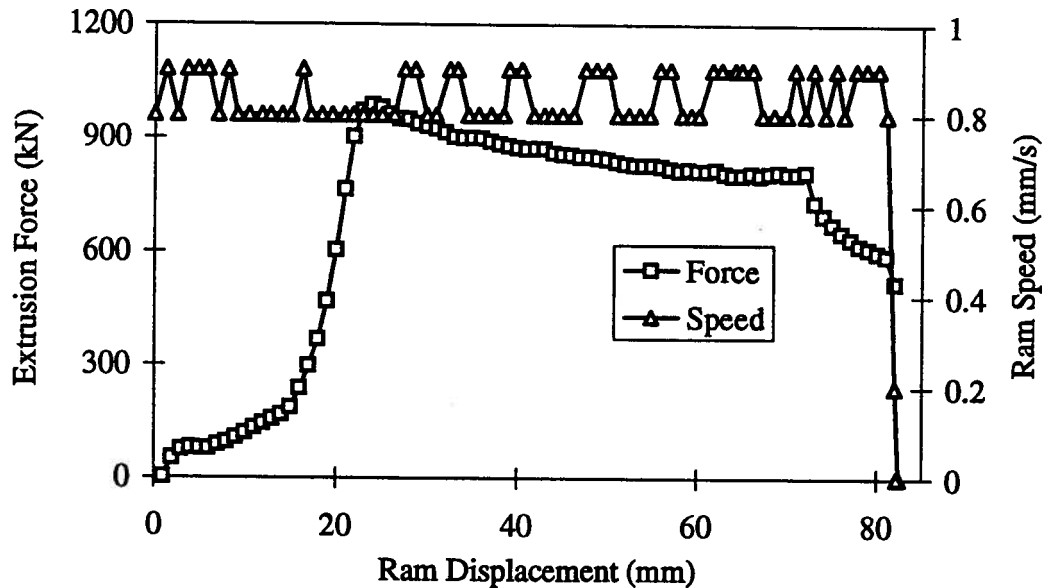


Figure 4.12 Typical load-stroke curve during extrusion at KRDC (K-7)

ii) the ram speed was controlled at approximately 1mm/s, except for those trials in which the extrusion force exceeded the press limit, such as trials K-8, K-10, K-11, K-12. When the extrusion force exceeded the press limit (100T), the ram slowed down automatically to keep pushing the billet through the die aperture, until the extrusion force required became less than the press limit, and then the ram speed increased again (Fig. 4.13).

iii) Other features, similar to those in the plant trials at UAC, were also observed, e.g., a higher extrusion force was obtained at either a lower extrusion temperature, a higher extrusion ratio or a larger volume fraction of the particle.

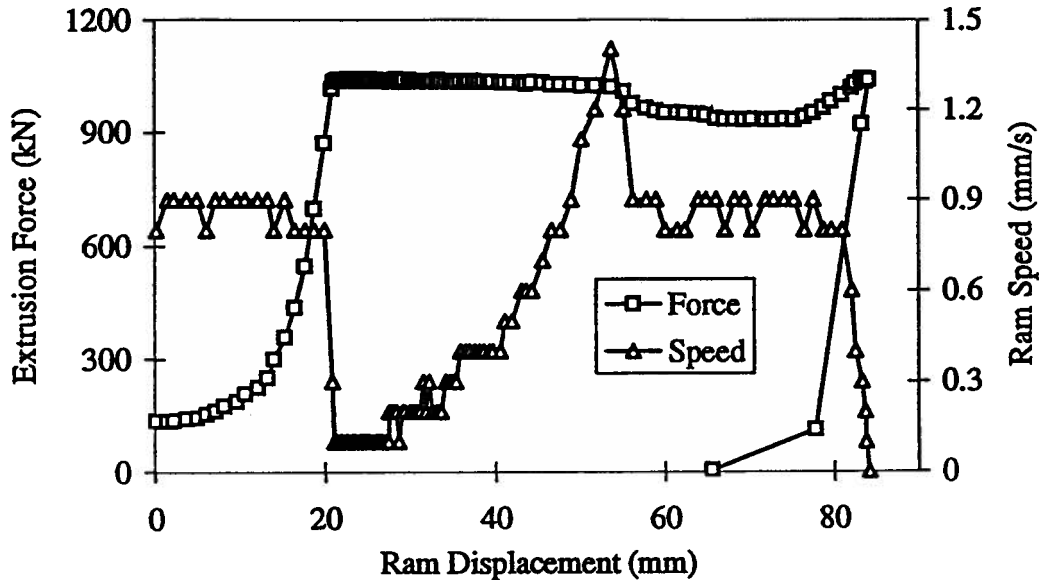


Figure 4.13 Variation of ram speed at the press pressure limit (K-11)

4.4 Extrusion Surface Defects

During the above two plant trials, the extrudates generally had a good surface finish. However, low speed cracks were observed at the front end of some extrudates from the plant trials at UAC when the ram speed was relatively low. This phenomenon disappeared if the ram speed was increased. It occurred more frequently in the extrudates of 6061/Al₂O₃/20p than in 6061/Al₂O₃/10p. The higher the extrusion ratio, the more severe the cracking. Figure 4.14 shows extrudates of 6061/Al₂O₃/20p with different extrusion ratios of 13, 34, 52 progressing from the ruler side; an extrudate of 6061/Al₂O₃/10p with the extrusion ratio of 34 is also shown at the right for comparison. It was interesting to note that low speed cracking happened much more frequently in the plant trials at UAC, Anaheim, than in the plant trials at

KRDC, Kingston. However, there was no low speed cracking in any extrudate when the ram speed was above 6mm/s at any extrusion ratio at UAC. The length of each extrudate covered with low-speed cracks for the plants trials at UAC was measured and is listed in Table 4.7. The mechanism of low speed cracking will be analyzed in Chapter 8 based on finite element analyses and microstructural examination.



Figure 4.14 Low speed cracking at the front end of two extrudates

Some minor defects were also noticed in the composite materials. These were due to agglomerates of alumina particles showing at the surface and were statistically likely, assuming that the agglomerations were uniformly distributed through the casting. Die lines were evident on all extrudates. These were present in all extrusions and cannot be countered with current technology. Some chatter crazing was observed on the last extrudates of each die. This defect was due to build-up of material on the die surface. Severe die wearing was evident, as shown by measurement of extrudate diameter from each die (Table 4.7). No high

speed cracking was observed, because the initial billet temperature and the ram speed for both plant trials were not high enough.

Table 4.7 Extrudate data from plant trials at UAC

Test No.	Material	Nominal Die Dia. (mm)	Extrudate Dia. (mm)	Coverage of low speed cracks at front end of extrudates	
				slight(mm)	severe(mm)
S92-1	6061	31.75	/	not available	not available
S92-2	6061	31.75	31.98	not available	not available
S92-3	6061/Al ₂ O ₃ /20p	31.75	32.00	not available	not available
S92-4	6061/Al ₂ O ₃ /20p	31.75	32.00	not available	not available
S92-5	6061/Al ₂ O ₃ /10p	31.75	32.03	not available	not available
S92-6	6061/Al ₂ O ₃ /10p	31.75	32.03	not available	not available
J94-1	6061/Al ₂ O ₃ /10p	50.80	50.95	0	0
J94-2	6061/Al ₂ O ₃ /10p	50.80	51.18	0	0
J94-3	6061/Al ₂ O ₃ /10p	50.80	50.93	0	0
J94-4	6061/Al ₂ O ₃ /10p	50.80	50.95	0	0
J94-5	6061/Al ₂ O ₃ /20p	50.80	51.10	102	0
J94-6	6061/Al ₂ O ₃ /20p	50.80	51.13	229	0
J94-7	6061/Al ₂ O ₃ /20p	50.80	51.03	38	0
J94-8	6061/Al ₂ O ₃ /10p	31.75	31.75	0	0
J94-9	6061/Al ₂ O ₃ /10p	31.75	31.75	76	0
J94-10	6061/Al ₂ O ₃ /10p	31.75	31.78	114	0
J94-11	6061/Al ₂ O ₃ /10p	31.75	31.85	3810	3048
J94-11b	6061/Al ₂ O ₃ /10p	31.75	31.95	406	0
J94-12	6061/Al ₂ O ₃ /20p	31.75	31.98	457	356
J94-13	6061/Al ₂ O ₃ /20p	31.75	32.00	127	102
J94-14	6061/Al ₂ O ₃ /20p	31.75	32.13	381	2286
J94-15	6061/Al ₂ O ₃ /10p	25.40	25.40	51	0
J94-16	6061/Al ₂ O ₃ /10p	25.40	25.43	203	0
J94-17	6061/Al ₂ O ₃ /10p	25.40	25.44	127	0
J94-19	6061/Al ₂ O ₃ /20p	25.40	25.53	127	0
J94-20	6061/Al ₂ O ₃ /20p	25.40	25.78	2286	4318
J94-11a	6061/Al ₂ O ₃ /10p	38.10	38.10	0	0
J94-18	6061/Al ₂ O ₃ /10p	38.10	38.10	0	0

4.5 Effect of Extrusion Conditions on Tensile Properties of Extrudates

Plant trials have been conducted at different extrusion conditions. It is known that mechanical properties of the PRMMCs are improved after extrusion compared to the as-cast state. However, the effect of extrusion conditions on the mechanical property change is not clear yet.

4.5.1 Tensile Tests

To investigate the tensile property change of the composites, four double-shoulder tensile specimens were machined from each extrudate of the plant trails at KRDC, Kingston, for tensile strength measurement and for elastic modulus evaluation for each condition. All the specimens were in T4 heat treatment condition before testing, i.e., 1 hour holding at 550°C, followed by quenching and aging at room temperature for 48 hours or more. A schematic of the tensile test specimen is shown in Fig. 4.15. The tests followed the ASTM standard procedure^[102].

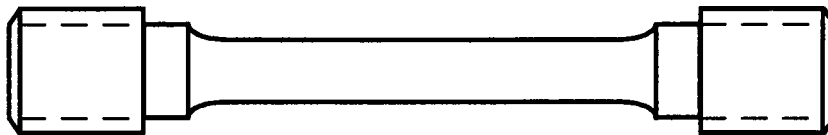


Figure 4.15 Schematic of a tensile test specimen

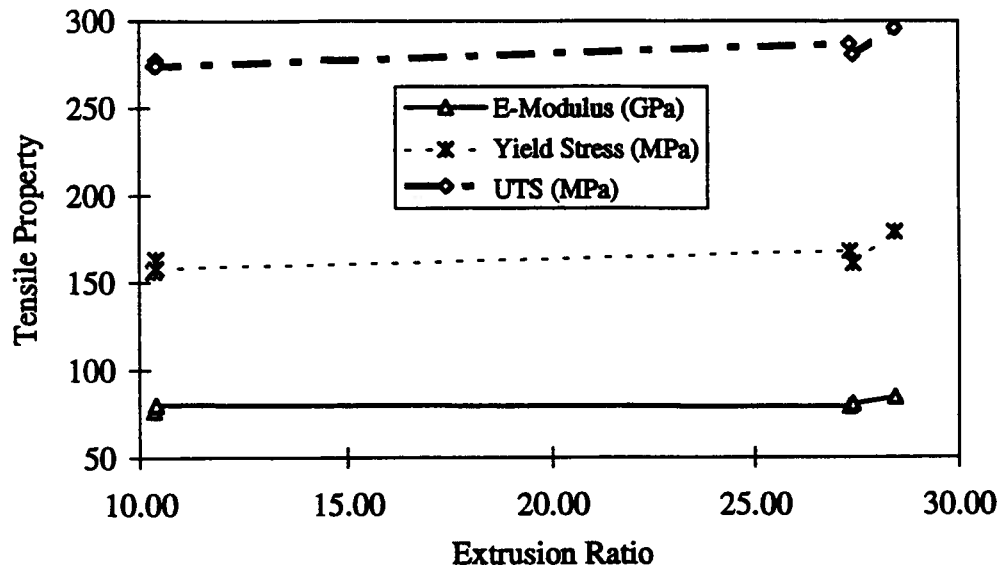
4.5.2 Tensile Properties under Different Extrusion Conditions

From the tensile tests, 0.2% offset yield strength, ultimate tensile strength (UTS), elastic modulus, and %-elongation, were all recorded for the extrudate obtained from the two different extrusion ratio tests performed at KRDC, Kingston. The mean value of the tensile

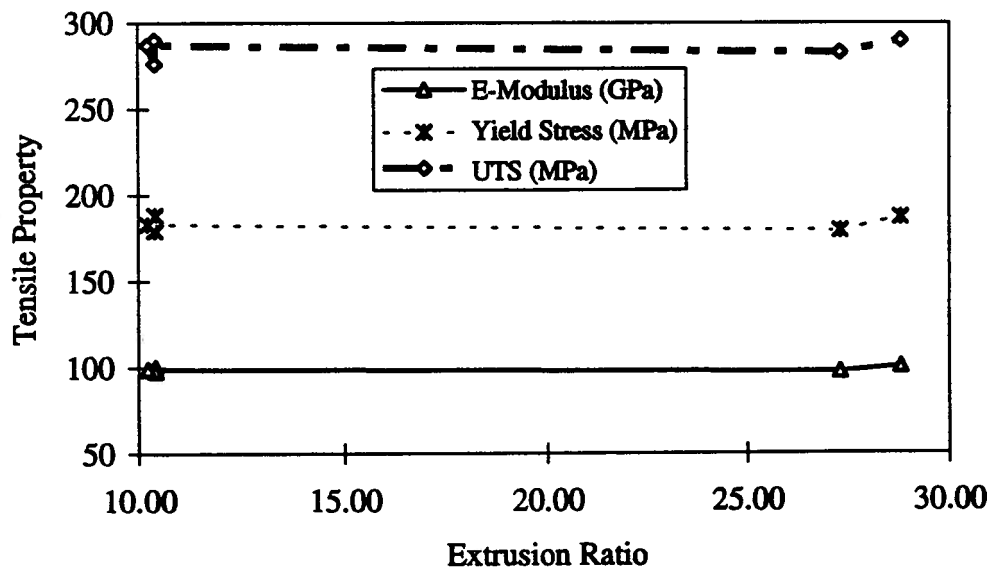
data from four samples tested for each condition is listed in Table 4.8. Unfortunately, only the standard deviation for tensile elongation is available. The exact extrusion ratio for each test was obtained based on the measurement of the extrudate diameter after extrusion. The variation of the values is mainly due to the change of die for each test. The tensile property change of the 6061/Al₂O₃/10p for different extrusion ratios is shown in Fig. 4.16(a). It is evident that the elastic modulus, yield stress, and ultimate tensile strength do not show a significant increase for extrusion ratios up to approximately 27. However, for ratios above 27, the properties increase slightly. The same is true of the extrudates of 6061/Al₂O₃/20p (Fig. 4.16(b)). A corresponding decreasing trend is evident in the elongation of the extrudates for both composites (Fig. 4.17). Although scattering of the data exists, the change in value of the elongation seems larger than the standard deviations (Table 4.8).

Table 4.8 Tensile test results of extrudates from the plant trials at KRDC

Trial #	True Vol. (%)	T _{Bmaxd} (°C)	Extrusion Ratio	E (GPa)	Yield (MPa)	UTS (MPa)	Elong./ Stand. Dev. (%)
6061/Al ₂ O ₃ /20p							
K-1	19.8	484	10.40	99.9	188.0	290.0	8.7/1.0
K-2	18.0	484	10.40	97.7	179.0	276.0	10.2/0.4
K-12	19.2	435	10.23	99.0	183.0	287.0	8.9/0.7
K-7	18.0	467	27.30	97.3	179.0	283.0	10.0/0.4
K-11	19.8	400	28.80	100.5	187.0	290.0	7.5/0.7
6061/Al ₂ O ₃ /10p							
K-13	9.0	436	10.28	81.5	160.0	276.0	15.7/1.0
K-14	7.0	436	10.35	76.6	156.0	274.0	20.0/1.3
K-3	7.4	484	10.40	79.8	163.0	277.0	17.0/0.3
K-4	7.4	484	10.40	80.1	158.0	274.0	16.0/0.6
K-6	8.8	496	27.34	79.0	168.0	287.0	15.0/1.0
K-10	7.0	418	27.42	80.4	161.0	281.0	17.0/1.2
K-5	7.0	430	28.44	84.3	179.0	296.0	12.0/1.7



(a) 6061/Al₂O₃/10p



(b) 6061/Al₂O₃/20p

Figure 4.16 Tensile property under different extrusion ratios

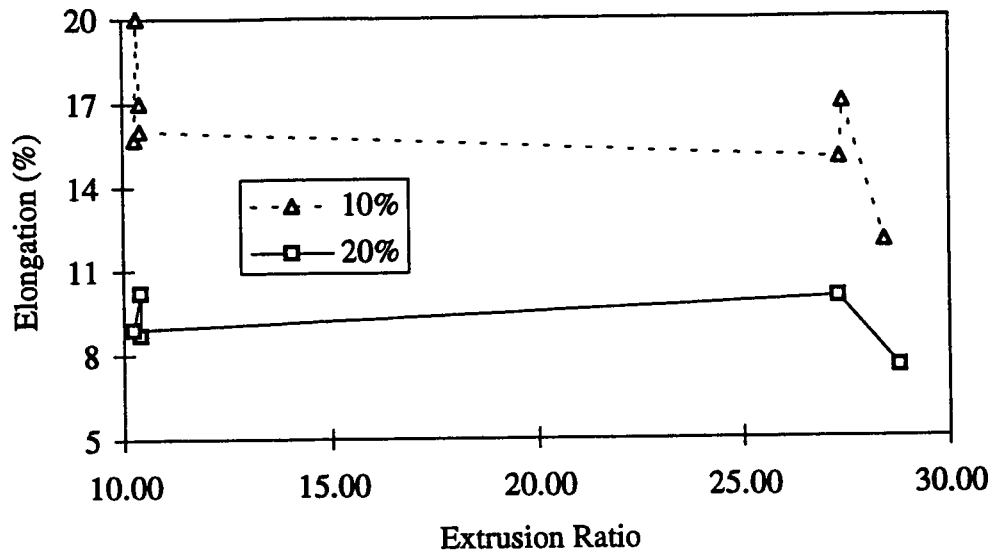


Figure 4.17 Elongation of the composites as a function of extrusion ratio

The tensile properties are dependent on the volume fraction of the particle, as seen by comparing the data of 6061/Al₂O₃/10p and 6061/Al₂O₃/20p. It is evident that a higher volume fraction results in a higher yield strength, UTS, and elastic modulus, but a lower elongation value. Therefore, the true volume fraction in each extrudate tested should be determined, because under the same nominal volume fraction of 10 and 20% the true volume fraction may vary from specimen to specimen. By dissolution of the matrix of the extrudates, more accurate volume fraction for each extrudate tested was obtained, as listed in Table 4.8 with the tensile properties. It is seen that for the extrudates of 6061/Al₂O₃/20p, the true volume fraction varies from 18% to 19.8%, while for the extrudates of 6061/Al₂O₃/10p, it changes from 7.0% to 9.0%. The evaluation of the property change at different extrusion ratios should be conducted at the same true volume fraction (rather than a nominal value, as plotted in Fig. 4.16 and Fig. 4.17). The results of the trials of K-1, K-12, and K-11 with a narrower range of volume fraction from 19.2% (K-12) to 19.8% (K-1, K-12) were re-plotted for

6061/Al₂O₃/20p in Fig. 4.18(a) and 4.19. For the 6061/Al₂O₃/10p, the trials of 7% volume fraction (K-14, K-10, K-5) to 7.4% (K-3, K-4) were adopted, as shown in Fig. 4.18(b) and Fig. 4.19. The effect of extrusion ratio on mechanical properties are shown in Fig. 4.18(a) and (b) for yield strength, UTS, and the elastic modulus, and Fig. 4.19 for the %-elongation. It is seen that for 6061/Al₂O₃/20p the elastic modulus, the yield strength and the UTS increase very little with increasing extrusion ratios from 10 to 28 (Fig. 4.18(a)). However, for 6061/Al₂O₃/10p, a slight increase in the elastic modulus, yield strength and UTS are shown in Fig. 4.18(b). The elongation of both composite materials decreases with an increase in extrusion ratio, while a more gradual decrease is seen for the 6061/Al₂O₃/20p than for the 6061/Al₂O₃/10p. However, it is worth pointing out that the small variation of the tensile strengths and the elastic modulus could be within the range of their standard deviation. Unfortunately, the values are not available at the moment.

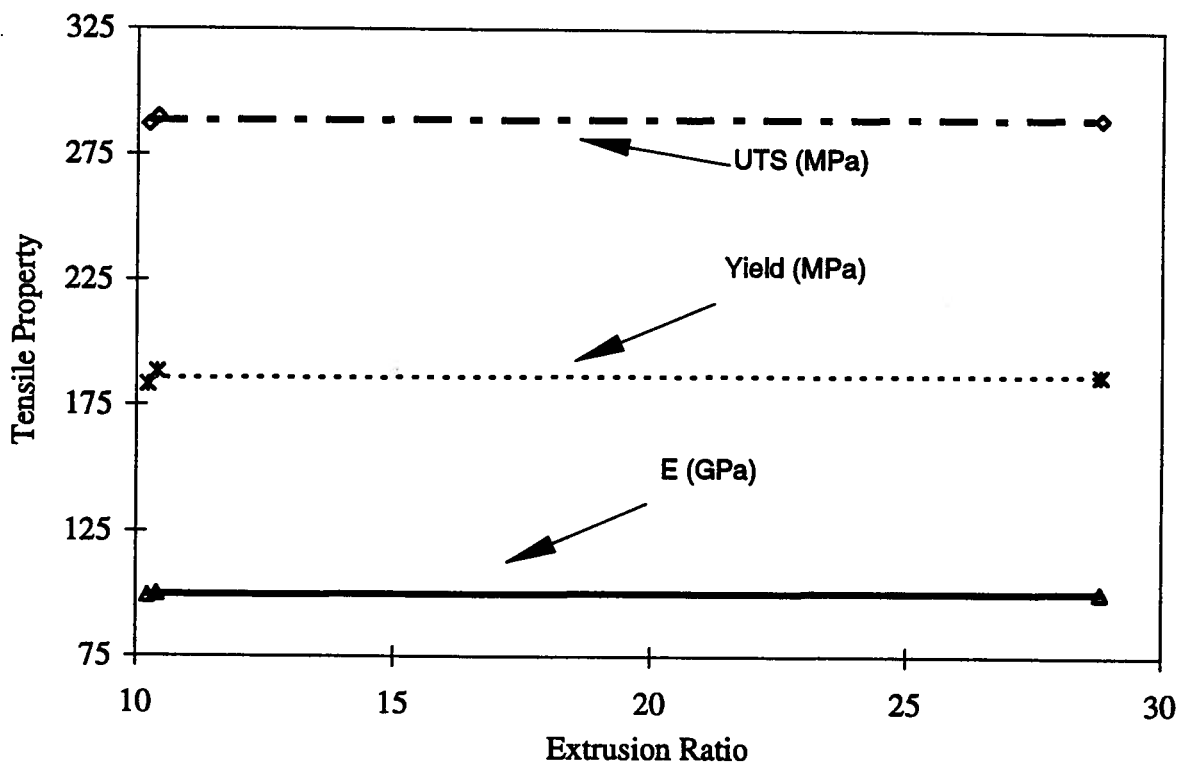


Figure 4.18(a) Tensile property change of 6061/Al₂O₃/20p for different extrusion ratios with a true volume fraction from 19.2% to 19.8%

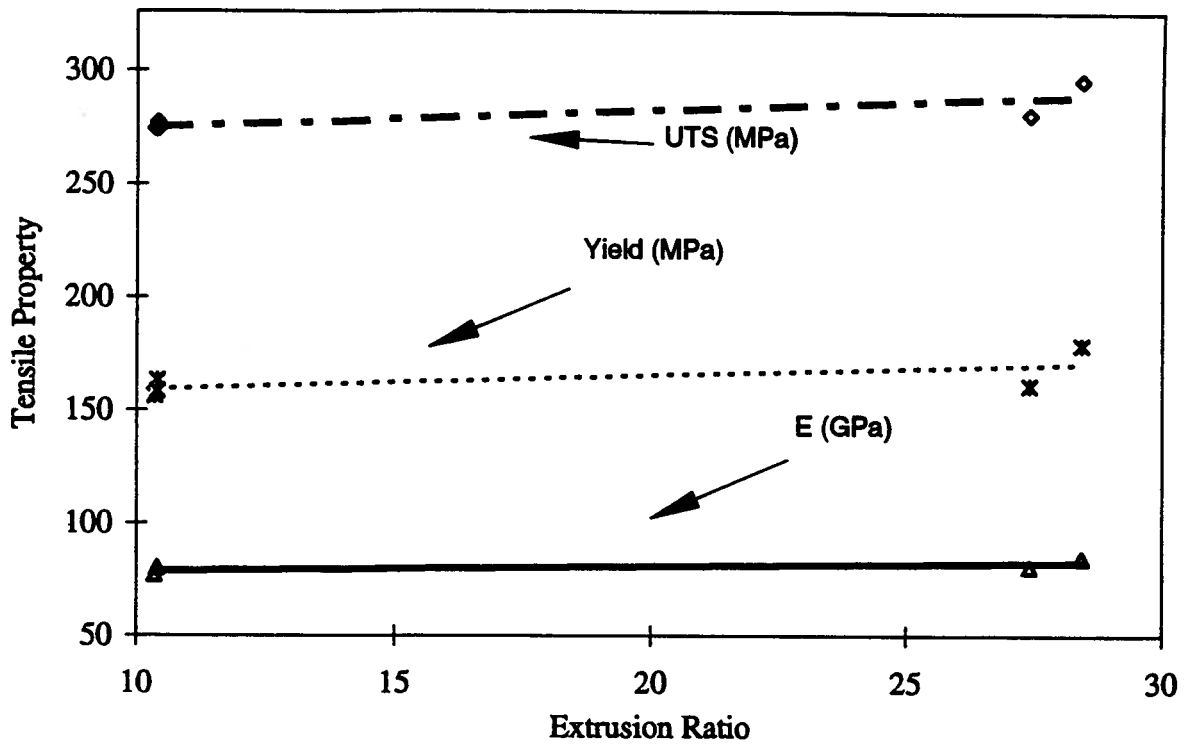


Figure 4.18(b) Tensile property change of 6061/Al₂O₃/10p for different extrusion ratios with a true volume fraction from 7.0% to 7.4%

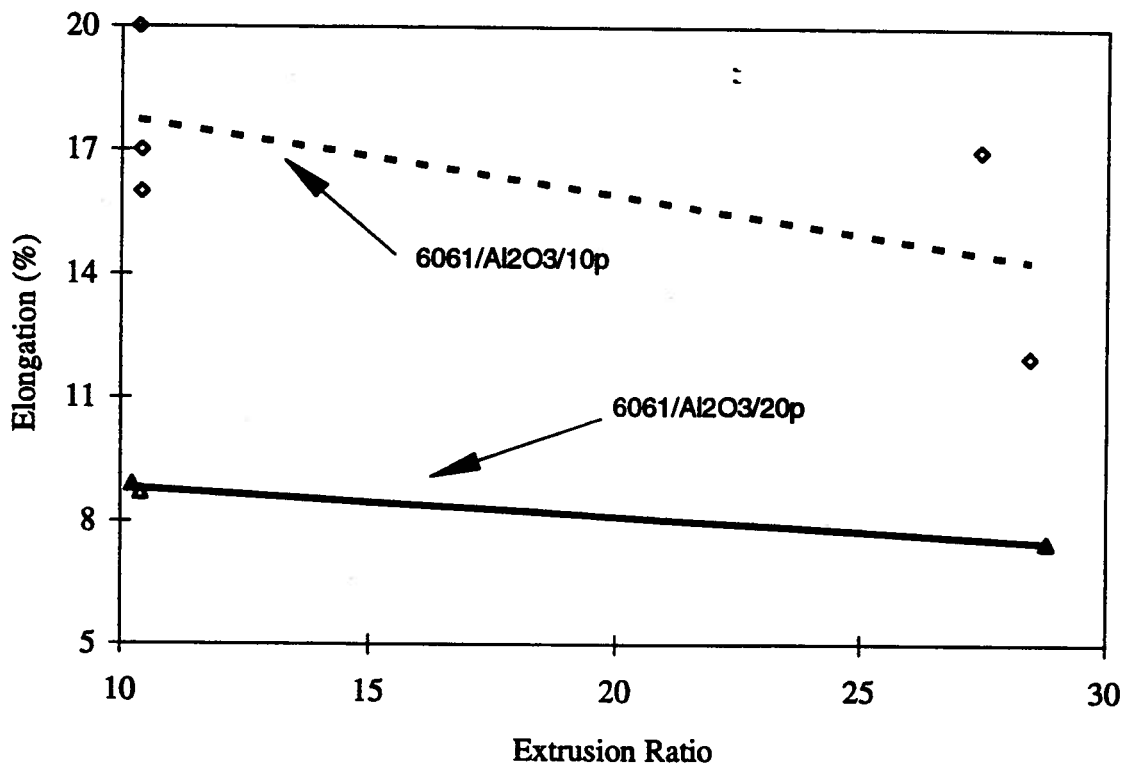


Figure 4.19 Corresponding elongation values at different extrusion ratios for both composites

Chapter 5 MODELING THE EXTRUSION OF THE PRMMCs

The literature review suggests that little work has been carried out on the analysis of a transient extrusion process at high temperature and none for the extrusion of the PRMMCs. To better understand the extrusion process, one test from each plant trial was simulated with the aid of a finite element package, DEFORM[®]^[82], by applying the alumina PRMMCs as a monolithic material. The plant trial data were then used to validate the model predictions. The results during hot extrusion will help to understand particle fracture and surface cracking.

5.1 Mathematical Model of Extrusion Process

5.1.1 Finite Element Model

5.1.1.1 Flow Formulation

DEFORM[®] is based on a *Flow Formulation* approach with a penalty function procedure using an updated Lagrangian procedure^[83]. The choice of the package was dictated by two factors: the requirement that it should be capable of modeling large scale hot deformation (strains of up to four and greater), and the need to predict loads over the whole range of deformation (i.e. under transient and steady-state conditions). It contains an automatic re-meshing feature, which facilitates the modeling of transient large deformation processes, such as are found for extrusion processes. In this study, the model consists of four objects to be simulated in the extrusion press: billet, pressure pad, container and die, as schematically shown in Fig. 5.1. The ram and stack were ignored, as was the elastic deformation of the extrusion presses, for the purposes of this work. Because of the large plastic deformation associated with the process, the billet material was assumed to behave as a

rigid-plastic material, whereas the other three objects were defined as being rigid in computation and only the billet was involved in deformation to which the flow formulation applies.

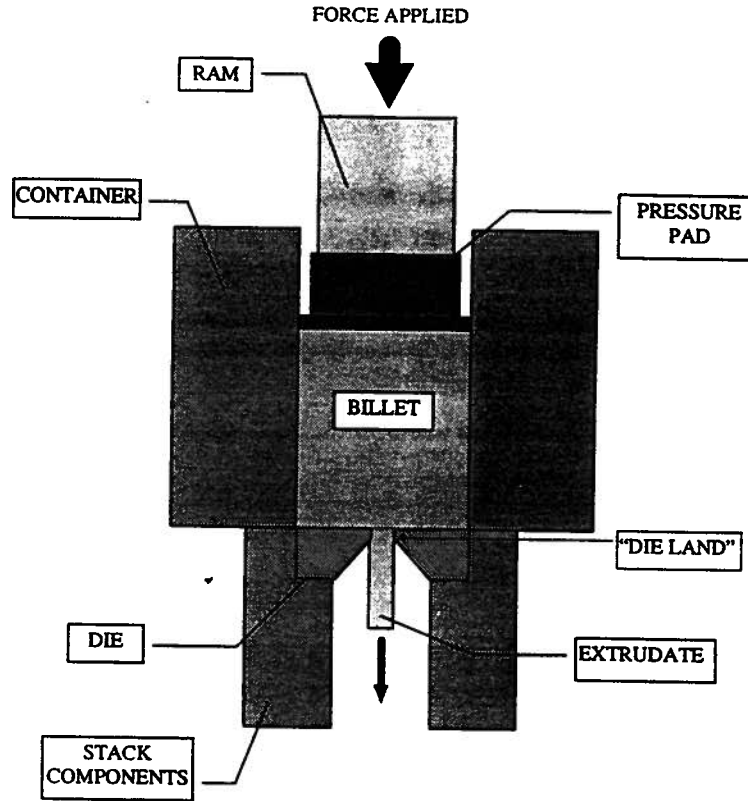


Figure 5.1 Schematic of an extrusion press

Based on the virtual work-rate principle, the following variational equation was obtained^[83].

$$\delta\Phi = \int_V \bar{\sigma} \delta \dot{\epsilon} dV + \int_V K \epsilon_v \delta \epsilon_v dV - \int_S F_i \delta v_i dS = 0 \quad (5.1)$$

where V is the flow domain of the billet, and F_i is the traction specified on the surface boundary S ; $\bar{\sigma}$ and $\dot{\epsilon}$ are effective stress and effective strain rate, respectively, which are defined as:

$$\bar{\sigma} = \left(\frac{3}{2} \sigma'_{ij} \sigma'_{ij} \right)^{1/2} \quad (5.2)$$

$$\bar{\dot{\epsilon}} = \left(\frac{2}{3} \dot{\epsilon}_{ij} \dot{\epsilon}_{ij} \right)^{1/2} \quad (5.3)$$

Due to incompressibility, the rate of volumetric straining should be zero, i.e.:

$$\dot{\epsilon}_v = \dot{\epsilon}_{ii} = 0 \quad (5.4)$$

To preserve the incompressibility condition valid in the deformation analysis, a term of $0.5K \dot{\epsilon}_v^2$, where K is a very large constant, $\sim 10^8$, or called penalty constant, was introduced into the virtual work principle functional to guarantee the volume constancy (second term in Eq. (5.1)). This is called the Penalty Function procedure, which is widely used in finite element deformation analysis^[83]. The mean stress, or the hydrostatic stress, which is defined as the mean of three normal stress components, σ_m , obeys the following equation based on the penalty function procedure^[83]:

$$\sigma_m = \frac{1}{2} K \dot{\epsilon}_v \quad (5.5)$$

The compatibility between the strain rate, $\dot{\epsilon}_{ij}$, and the velocity, v_i , is defined as:

$$\dot{\epsilon}_{ij} = \frac{1}{2} (v_{i,j} + v_{j,i}) \quad (5.6)$$

where the comma between the 'i' and 'j' denotes differentiation with respect to spatial coordinates.

The deviatoric stress, σ'_{ij} , is related to stress, σ_{ij} , and the mean stress, σ_m , as follows:

$$\sigma'_{ij} = \sigma_{ij} - \delta_{ij} \sigma_m \quad (5.7)$$

where δ_{ij} is the Kronecker delta. According to the Levy-Mises theory, the constitutive law can be expressed as follows:^[83]

$$\sigma'_{ij} = \left(\frac{3}{2} \bar{\sigma} / \bar{\dot{\epsilon}} \right) \dot{\epsilon}_{ij} \quad (5.8)$$

Equation (5.1) can be converted to a series of non-linear algebraic equations by a normal FEM discretization procedure, resulting in:

$$\frac{\partial \Phi}{\partial v_I} = \sum_j \left(\frac{\partial \Phi}{\partial v_I} \right)_j \quad (5.9)$$

Linearization of this equation was achieved by Taylor expansion near an assumed solution point $v = v_0$ (initial guess), resulting in,

$$\left[\frac{\partial \Phi}{\partial v_I} \right]_{v=v_0} + \left[\frac{\partial^2 \Phi}{\partial v_I \partial v_J} \right]_{v=v_0} \Delta v_J = 0 \quad (5.10)$$

where Δv_J is the first-order correction of the velocity v_0 . Equation. (5.10) can be written in matrix form,

$$[K_s] \{\Delta v\} = \{f\} \quad (5.11)$$

where $[K_s]$ is the stiffness matrix, $\{\Delta v\}$ is the velocity correction term, and $\{f\}$ is the residual of the nodal point force vector.

Since the PRMMCs are extruded at high temperature, heat transfer occurs throughout all the objects due to different initial temperatures and internal heat of deformation in the billet and friction heat at the interface. The governing equation for the heat transfer is:

$$kT_{,i,i} + \dot{q} - \rho c_p \dot{T} = 0 \quad (5.12)$$

where the first term of the equation is the heat transfer rate, with the comma denoting differentiation with respect to spatial coordinates and with the repeated subscript meaning summation; k denotes thermal conductivity. The second term is the rate of generation of heat arising from deformation, which is obtained from the following well known formula:

$$\dot{q} = \eta \bar{\sigma} \dot{\epsilon} \quad (5.13)$$

where η is the efficiency of conversion of deformation energy to heat, and is assumed to be in the range of 0.90 to 0.95, depending on the material being formed. Thus heat transfer and

deformation heating are coupled in the simulation. However, this heat generation rate term only applies to the billet, because all the surrounding tools are assumed to be rigid. The third term in Eq. (5.12) is the rate of accumulation of internal energy. Eq. (5.12) can be discretized following a traditional Galerkin finite element method and written in matrix form as^[84]:

$$[C]\{\dot{T}\} + [K_C]\{T\} = \{Q\} \quad (5.14)$$

where $[C]$ is the heat capacity matrix, $[K_C]$ the heat conduction matrix, $\{Q\}$ the heat flux vector, $\{T\}$ the vector of the nodal temperature and $\{\dot{T}\}$ the vector of the nodal temperature change with time.

5.1.1.2 Boundary Conditions

Four objects were discretized into a series of 4-node iso-parametric elements (Fig. 5.2). Due to axisymmetry, an axisymmetrical slice of the press setup was analyzed with a 2-D model. The basic variables: velocity and temperature, were linear within each element. The

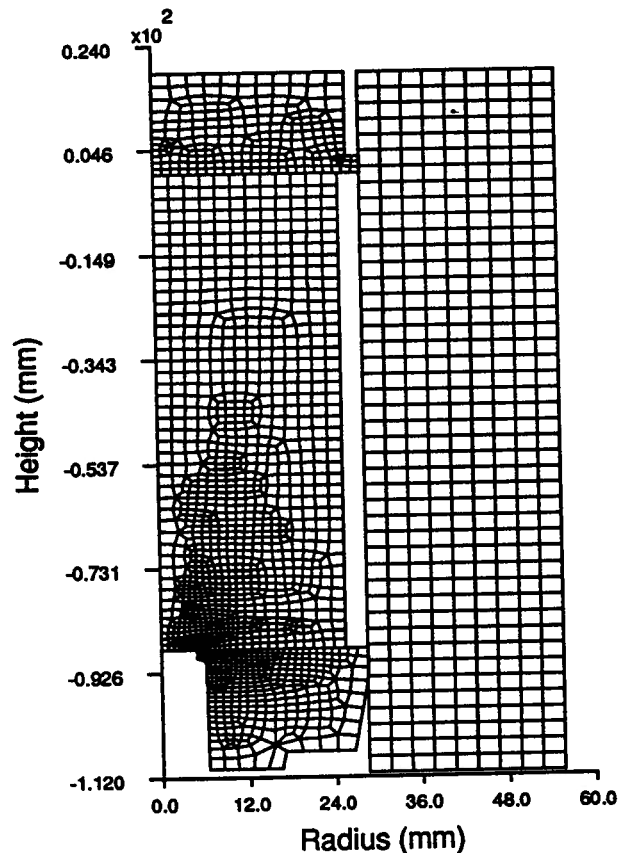


Figure 5.2 Initial finite element mesh for the billet and its surrounding tools

4-node iso-parametric element was used because it made remeshing easier^[37,82].

Due to limitation of the DEFORM[®] model, heat was only conducted between the billet and the surrounding tools. However, interface heat transfer between various tools, e.g., between pressure pad and container, between container and die, was ignored (Fig. 5.2). The thermal boundary condition between the billet and the tools is expressed as:

$$-kT_{B,i} = h(T_{Bs} - T_{Ts}) \quad \text{at interface boundary} \quad (5.15)$$

where k is the thermal conductivity of the billet, and T_{Bs} , and T_{Ts} are interface temperature of the billet and its contacted tool (pressure pad, container, and die), respectively; h is the heat transfer coefficient at the interface. For surfaces of all objects which are exposed to air, such as, a part of surface of the billet at the die aperture, the thermal boundary condition is expressed as:

$$-kT_{B,i} = h_{air}(T_{Bs} - T_{\infty}) \quad \text{at surface boundary exposed to air} \quad (5.16)$$

At the center line of the billet, due to axisymmetry, the heat transfer rate is zero.

$$kT_{B,i} = 0 \quad \text{at the center line of the billet} \quad (5.17)$$

At the outer surface of the container, because of the induction heater, the surface temperature was kept constant as measured, i.e.,

$$T_{Cs} = T_0 \quad \text{at outer surface boundary of the container} \quad (5.18)$$

For simplicity, the outer surfaces of the pressure pad and the die were assumed to be exposed to the air, as in Eq. (5.16), due to cold ram and die stack.

The mechanical boundary conditions of the deformed billet to be satisfied are as follows: at the center line of the billet, the velocity in the radial direction is zero;

$$v_r = 0 \quad \text{at the center line of the billet} \quad (5.19)$$

At the container and the die interfaces, the velocity normal to the boundary, v_n , is zero, while the velocity normal to the interface at the pressure pad is equal to the ram speed.

$$v_n = 0 \quad \text{at the container and die interface} \quad (5.20)$$

$$v_n = v_0(t) \quad \text{at the pressure pad interface} \quad (5.21)$$

In addition, a friction stress was applied to the interface between the billet and the surrounding tools as stress boundary conditions. The shear factor friction law, $\tau = mk$, was adopted in hot deformation, where τ is the friction stress, m the shear factor, and k the shear strength of the billet^[83]. The free surface at the bottom end of the billet and the free surface of the extrudate have no surface traction.

5.1.2 Input Data

In common with observations made by others^[64,85], sticking friction conditions were assumed to prevail at the interfaces between the billet and the container, and the billet and die, i.e., $m=1$, for the shear factor friction law, $\tau = mk$. For the interface between the pressure pad and billet, a shear factor of $m=0.7$ was assumed due to the cold pad^[83]. The heat transfer coefficient at these interfaces was assumed to be $200 \text{ kW/m}^2\text{K}$, based on the laboratory work on aluminum alloys by Hlady^[86]. A hyperbolic sine constitutive equation developed using the Gleeble[®] machine was employed in the model to calculate the effective stress in Eq. (5.8). The thermophysical properties of the billet (the PRMMCs) and the tools (H13) used in the heat transfer model were all temperature dependent, except for the density of the material, which was assumed to be constant^[118].

5.1.3 Solution Procedure

The convergence of the scheme requires consistency and stability. The consistency requirement ensures that as the size of the elements tends to zero, the approximation equation (5.14) will represent the exact differential equation (5.12) and its boundary conditions (Equations 5.15-5.16), and is satisfied by an approximation of the type,

$$T_{t+\Delta t} = T_t + \Delta t[(1 - \beta)\dot{T}_t + \beta\dot{T}_{t+\Delta t}] \quad (5.22)$$

The term β is a time integration factor used to average temperature over time, at time $t = t$, and $t = t + \Delta t$, and varies between 0 and 1. For unconditional stability, β should be greater than 0.5^[84], and in the current model a value of 0.75 was chosen. The total number of elements in the billet was 1000 at the upsetting stage, and increased to 1250 afterwards. For the surrounding tools (e.g., the pressure pad, the container, and the die), the number of elements in each rigid object was from 200 to 400, since only a heat transfer analysis was conducted. Because most of the deformation occurred in the die region after the upsetting stage, the elements of the mesh at the die exit zone were refined relative to the size of the elements under the pressure pad, to achieve a more accurate solution.

The solution of the velocity and temperature field was obtained alternatively by direct iteration followed by a modified Newton-Raphson method. The convergence criteria for velocity and extrusion force had to be satisfied for further temperature calculation in the same time step, viz.: for velocity $\frac{\|\Delta v\|}{\|v\|} \leq e_1 (=0.5 \times 10^{-3})$, where $\|v\|$ etc. is an error norm, defined as $(v^T v)^{1/2}$, and v is a vector, and for extrusion force $\frac{\|\Delta F\|}{\|F\|} \leq e_2 (=0.1 \times 10^{-2})$. After the temperature of all the objects was calculated, the geometry of the billet was updated based on nodal velocities. The velocity solution was iterated again at a new step. The simulation proceeded in this manner until a negative determinant of Jacobian matrix was encountered in one distorted element, which indicated that the mesh had been severely distorted. Therefore, remeshing was conducted over the whole billet. However, the distribution of the new mesh density was similar to that of the old one prior to remeshing; in this way remeshing errors

were minimized due to interpretation. The stroke step, Δs , ($= v_B \Delta t$, where v_B is the ram speed, and Δt is time step), adopted for the simulation was 0.25mm during the upsetting stage, and 0.05mm after that. The simulation was terminated when the extrusion reached the 'steady state' region.

5.2 Sensitivity Analysis of the Model

A sensitivity analysis in mathematical modeling should be conducted if values of some parameters are uncertain. In our study, the parameters, such as friction shear factor, m , heat transfer coefficient, h , at the interface, and heat generation efficiency, η , are reasonably well known as described in previous sections. However, the number of elements affects the accuracy of the results, therefore, a sensitivity analysis was conducted, with 500, 750, 1000, and 1250 elements in the billet. Because the surrounding tools were only involved with heat transfer, the number of elements in each tool (pressure pad, container and the die) were kept unchanged in the sensitivity analysis. The simulation and boundary conditions used in the model were the same as described in the above sections. The thermophysical properties for the surrounding tools (H13) and the billet of 6061/Al₂O₃/20p were obtained from Duralcan USA^[118] as mentioned in Section 5.1.2. The other input data are listed in Table 5.1.

Table 5.1 Some data for sensitivity analysis of the FEM model

Billet temperature, T_B	425°C
Container temperature, T_c	395°C
Die temperature, T_{Dc}	395°C
Pressure pad temperature, T_{Pd}	70°C
Extrusion ratio	34.0
Billet dimension	$\phi 178 \times 305 \text{mm}$

Because the peak extrusion force and the maximum temperature of the billet during extrusion is crucial to the development of extrusion limit diagrams, the effect of the number of elements in the billet on these two maximum values were studied. The maximum temperature was usually reached in the die land zone because of severe deformation at the die throat. This will be seen clearly in the section of model predictions (Section 5.3.2.2). The extrusion process of the large press at UAC, Anaheim, was simulated with four different number of elements. Each simulation was stopped when the steady state was reached at a ram displacement of 25 mm for the sake of CPU time. The load-stroke curves predicted for the four different numbers of elements are shown in Fig. 5.3. It is evident that the load is insensitive to the number of elements in this range. The effect of the number of elements on the maximum temperature is shown in Fig. 5.4. It is seen that when the number of elements increases, the curves of the temperature converge; although in the range of the number of elements from 500 to 1250, the differences between them are all quite small and within 5°C. This may result from the fact that although the total number of elements in the billet are different, the mesh size in the die exit zone for all the cases is fine enough to become insensitive to the peak load and the maximum temperature prediction. However, a small number of elements in the billet, e.g., 500, may cause other problems, such as an interference of billet mesh with the rigid die boundary at the die exit corner. This could affect the prediction of the effective strain rate and the stress at that corner. Hence, in industry process simulation, 1250 elements were used in the billet after the upsetting stage and the mesh was refined with a higher mesh density in the die exit zone to achieve a higher accuracy of the results (based on the fact that severe deformation occurred in the die exit zone) while only 1000 elements in the billet were adopted in the upsetting stage.

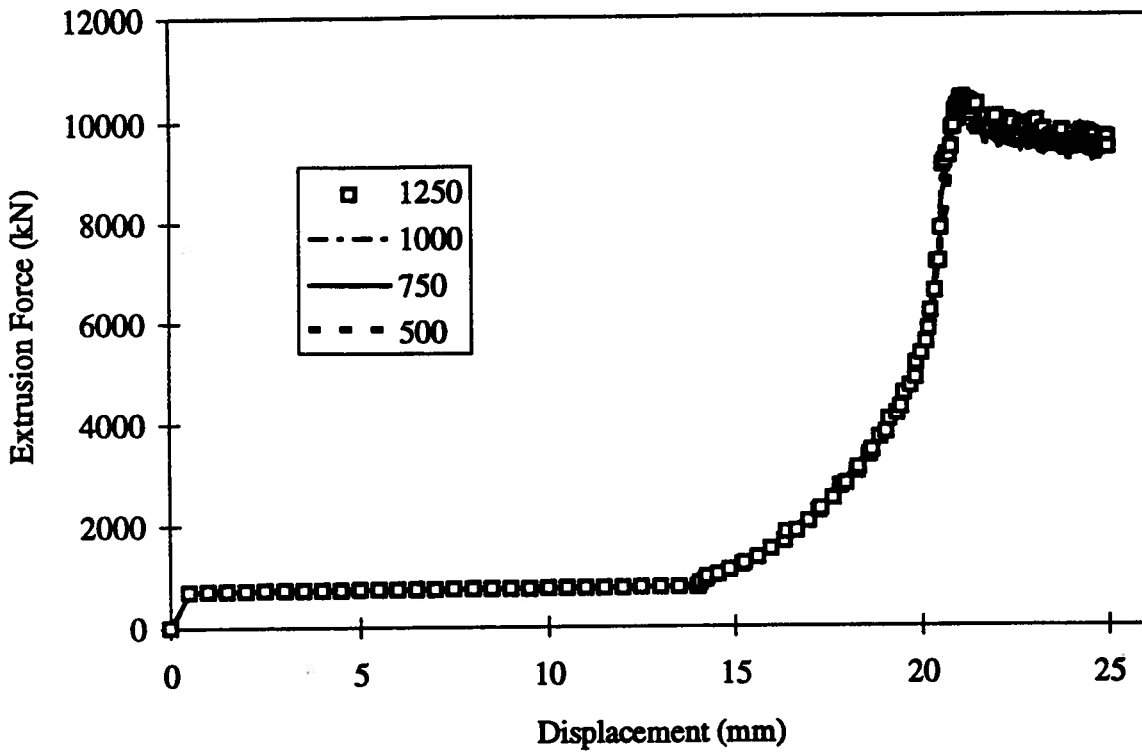


Figure 5.3 Sensitivity of load stroke curve to the number of elements in the billet

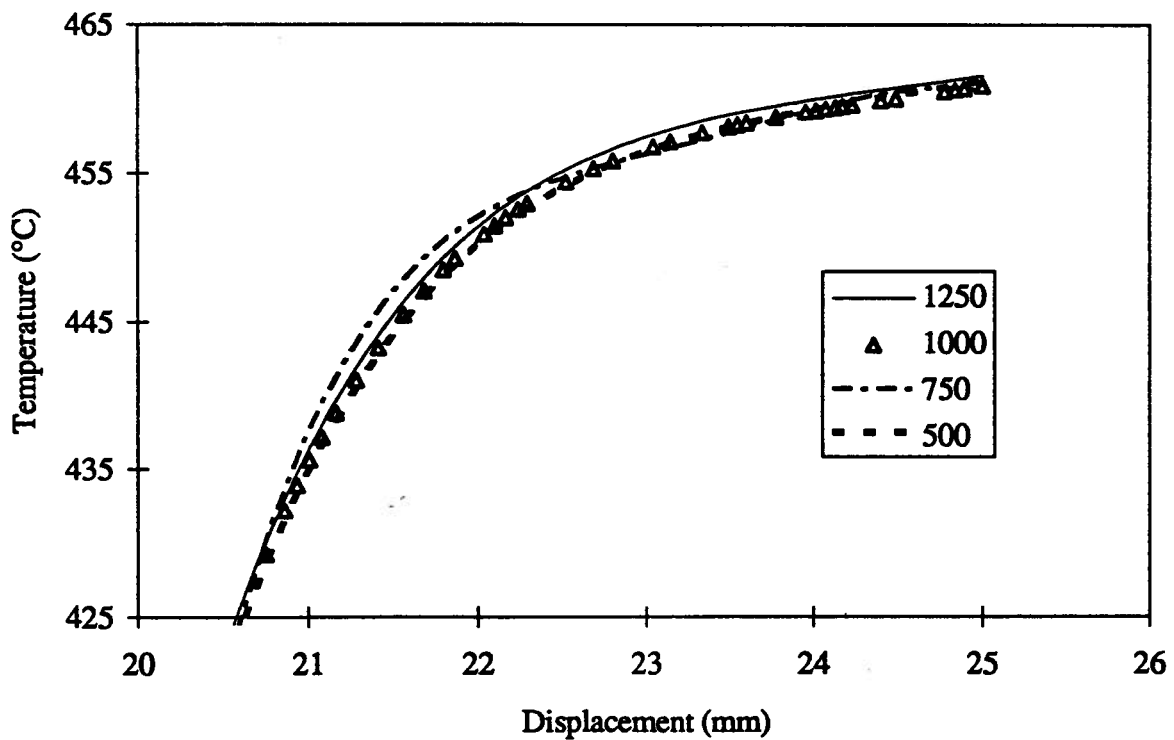


Figure 5.4 Sensitivity of the maximum temperature to the number of elements in the billet

This sensitivity analysis was conducted for the large press. However, the results should also be applicable to the small press because the extrusion ratios for both presses which are going to be simulated in the subsequent section are similar at approximately 30. Therefore the element size in the billet of the small press would be about 10 times smaller when the same number of elements was applied, because the deformation zone of the billet in the large press was about 10 times larger than that in the small press.

5.3 Extrusion Process Simulation

5.3.1 Processing conditions

The extrusion process simulation was conducted for one test from each plant trial: S92-3, for the large scale industrial machine, and K-7, for the laboratory press. In the first case, a homogenized billet of approximately 178mm diameter by 305mm was heated to 429°C in a continuous, gas fired furnace. The billet temperature at the furnace exit was recorded using a hand-held probe. The time to transfer the billet from the furnace to the press was around 40 seconds. The extrusion container was heated to a nominal temperature of 425°C, and the die to 336°C and the pressure pad to 70°C. The die was a flat faced die, with an aperture diameter of 32mm. A thermocouple was embedded in the die 1.6mm away from the die bearing, in order to record the temperature change during extrusion.

The billet for the second press was substantially smaller, around 51mm in diameter by 88mm in length, and was heated to 467°C in an electric muffle furnace. The delivery time of the billet from the furnace to the press was around 10 seconds. A flat-faced die with an aperture diameter of 10mm was employed. The die and pressure pad were heated in the same furnace as the billet; however, no continuous die temperature monitoring was conducted. The container was heated to 475°C by an induction heater placed around the

outside surface of the container. The details of the process conditions of the two plant trials simulated are summarized in Table 5.2 for clarity.

Table 5.2 Processing Conditions for Two Simulations

Parameter	S92-3, at UAC	K-7, at KRDC
T_b	429°C	467°C
T_c	425°C	475°C
T_{Die}	336°C	467°C
T_{Pad}	70°C	70°C
Ram Speed	~2.6mm/s	0.9mm/s
Transfer Time	40 sec	10 sec
Extrusion Ratio	34	28.0
Billet Dimension	$\phi 178 \times 305 \text{mm}$	$\phi 51 \times 88 \text{mm}$
No. of Elements in Billet	1250	1250

5.3.2 Model Predictions

Each of the extrusion trials was simulated from the start of extrusion until the steady state was reached after the peak pressure. The deformation behavior of the billet as well as the thermal history of each object, was predicted during extrusion. Material flow, stress state, strain and strain-rate distribution in the deformation zone, and also the temperature distribution in all the objects were characterized. The predicted extrusion load and die temperature were compared with the measured data.

5.3.2.1 Deformation Behavior

After the billet was loaded into the container, there was a gap between the billet and the inside surface of the container due to the smaller billet diameter than the inside diameter of the container (Fig. 5.2). When the pressure pad pressed the billet, it commenced upsetting, and the container was gradually filled up. Figure 5.5 shows the material flow near

the end of the upsetting stage. The arrowheads are the nodal velocities starting at node positions in the finite element mesh of the billet. The length of the arrow is proportional to the value of velocity. The apparent 'wavy' nature of the velocity arrows is due to the positioning of the nodes in the finite element mesh. It is seen that the gap between billet and the container had almost been filled, only the bottom-right part at the die-container corner remained to be filled up with the billet material flowing towards the corner. At the same stage, the part of the billet at the die aperture had been pushed into the die throat with a contact with the die bearing land, and apparently the material velocity in the die exit increased. The effective strain distribution at this stage was still relatively small with the large values concentrated at all the corners, such as die-container corner and die exit corner (Fig. 5.6).

As the extrusion proceeded, the die-container corner was filled up, and then all the material would flow towards the die aperture. A break-through pressure (the peak point in the load-stroke curve) was necessary for the billet to be pushed through the die land. After passing the peak pressure, the so-called 'steady-state' deformation began, although the extrusion force decreased due to the drop in friction force at the container interface. The velocity fields at the steady state are shown in Fig. 5.7 and Fig. 5.8 for both large and small presses. The velocities of the material at the die exit were significantly higher than those in the container because of the high extrusion ratio. The 'dead metal zone' at the corner between the die and the container was present in both instances (see also Figures 7.1 and 7.3). Although a tendency of material flow still appeared in the dead zone, the value of velocity at each node in the dead metal zone was close to zero (again, the apparent 'wavy' nature of the velocity arrows is due to the positioning of the nodes in the finite element mesh).

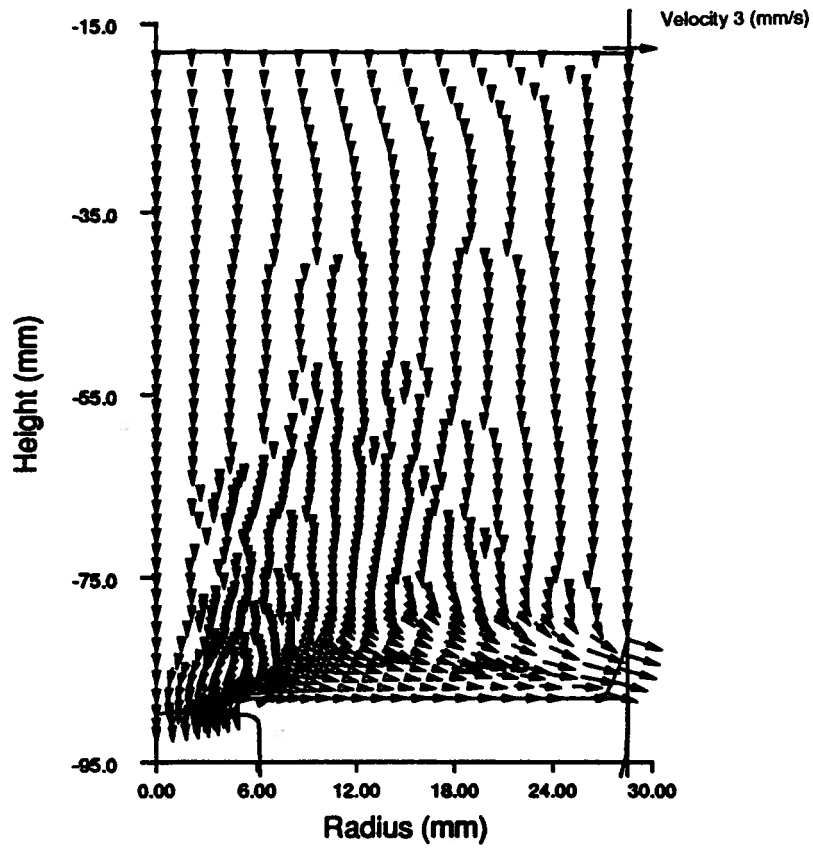


Figure 5.5 Material flow near the end of upsetting stage

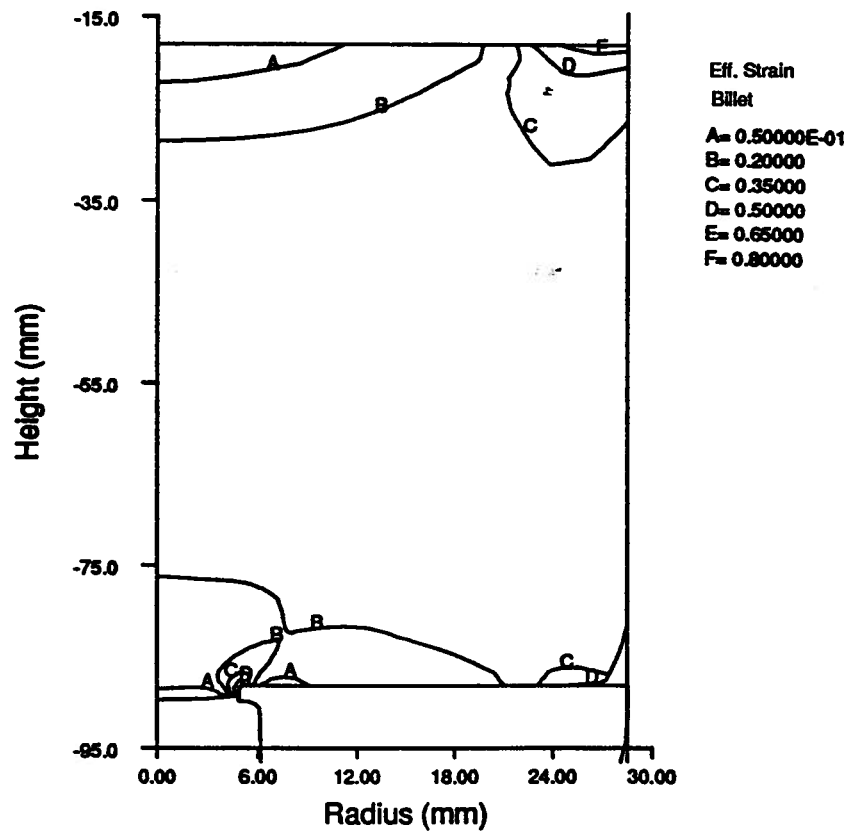


Figure 5.6 Effective strain distribution near the end of upsetting stage

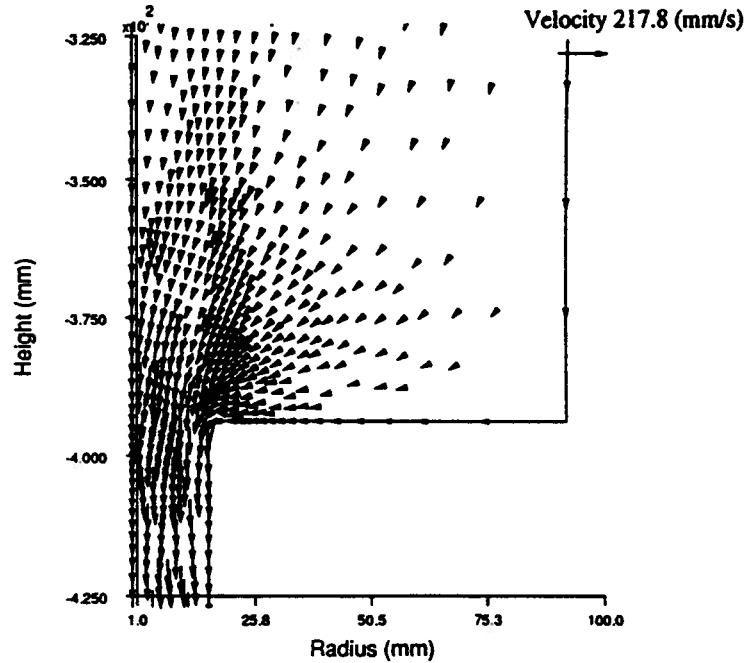


Figure 5.7 Velocity distribution in the billet after a ram displacement of 40.7 mm in the large extrusion press; length of arrow is proportional to velocity

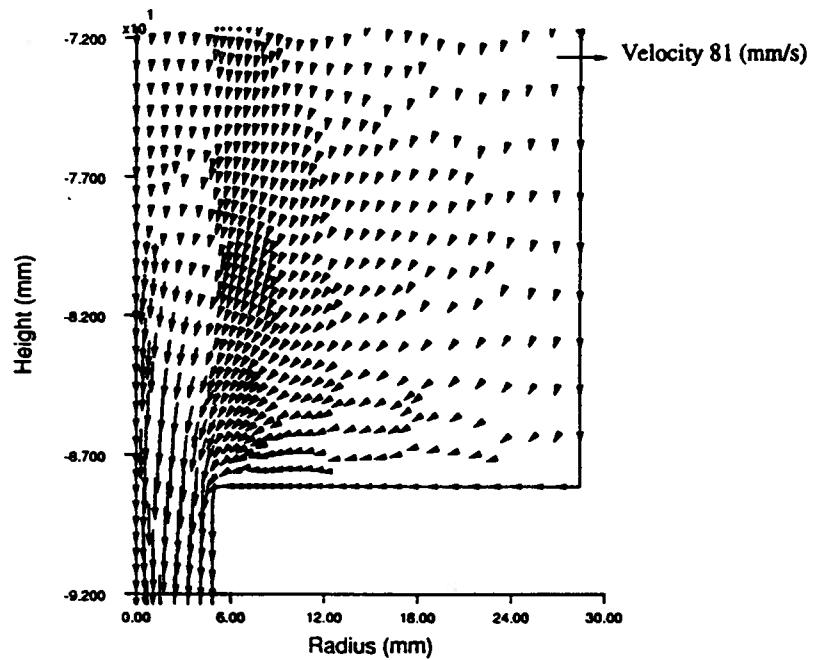


Figure 5.8 Velocity distribution in the billet after a ram displacement of 26.7 mm in a small extrusion press: length of arrow is proportional to velocity

It is worth pointing out that, in the finite element large deformation analysis, an absolute dead metal zone could not exist, because otherwise the nodal strain-rate in that zone would become zero, which could result in a numerical difficulty. For this, in our study, a limit strain-rate was defined which was 10^4 times less than the mean effective strain-rate over the deformation zone. If the calculated nodal strain-rate was less than the limit strain-rate, then the limit value replaced the corresponding nodal value, and the zone was taken as 'rigid'.

The mean stress is representative of the stress state because it is defined as the mean of all the normal stress components: if the mean stress is negative, a compressive stress state is dominant. However, if the mean stress is positive, there must exist at least one dominant tensile stress component. Fig. 5.9 and Fig. 5.10 show the mean stress distribution at steady-state during extrusion. It is evident that the stress state in the deformation zone is almost all in compressive except in the surface layer near the die land. The absolute value of the mean stress in the container decreases from the pressure end to the die exit, which implies that the billet tends to be in tension in the extrusion direction when approaching the die exit, due to elongation. The positive value in the surface layer apparently is due to two factors: firstly, the material flows faster in the center zone than in the surface layer, which has been confirmed by an experimental technique^[70]; and secondly, friction stress at the die land surface exists.

By comparing Figures 5.9 and 5.10, it is seen that the mean compressive stresses are significantly higher in the larger press, as would be expected due to the lower initial temperature of the billet and higher ram speed. However, a common feature for both presses is the negative value of the mean stress in the deformation zone and positive value in the surface layer at the die land area. The significance of the negative mean stress is that it may

help minimize the microstructural damages (e.g., potential void formation due to decohesion and particle fracture) during extrusion of the MMCs. However, the existence of a tensile stress component in the surface layer in the die land area might contribute to the source of low speed cracking, which is a specific feature of extrusion of the particulate reinforced MMCs.

This will be discussed in more detail in Chapter 8.

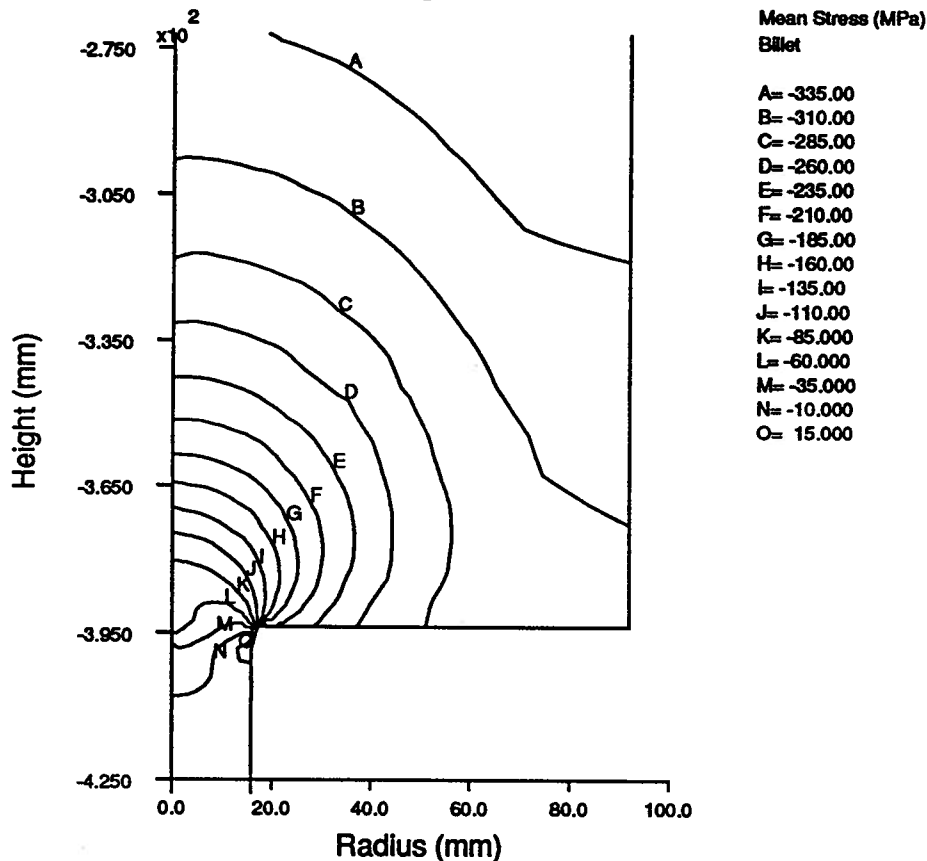


Figure 5.9 Mean stress distribution in the billet at a ram displacement of 40.7 mm in the large extrusion press (negative values denote compressive stresses)

Although the mean stresses are quite different, the effective strain near the die is in the range of about 4 - 5 for both presses, as expected because of their similar extrusion ratios. A typical effective strain distribution is shown in Figure 5.11 for the small press at a ram displacement of 26.7mm. The annular strain pattern in the extrudate is also as would be expected from a qualitative assessment of extrusions which shows a recrystallized ring after

extrusion^[119]. The corresponding effective strain rate distribution is shown in Fig. 5.12 for the small press. It is seen that the strain rate distribution is confined in the die throat zone, and its form is similar to predictions made by Chen, Oh and Kobayashi^[120] for extrusion through conical dies. The maximum strain rate is reached at the die exit corner where extrudate

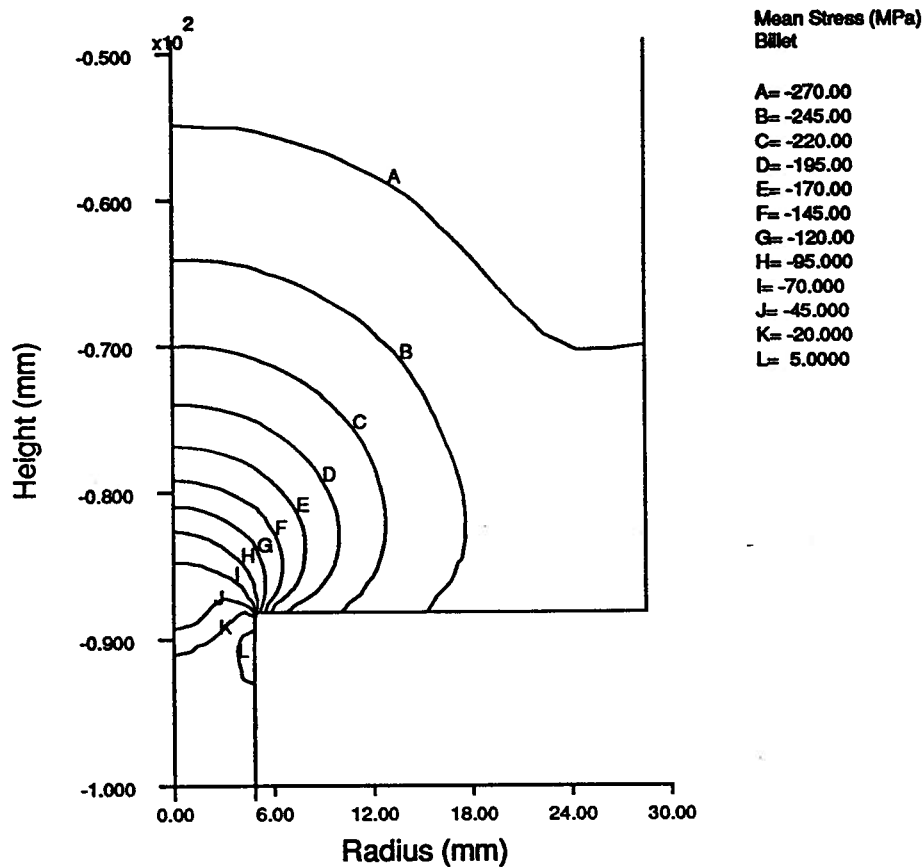


Figure 5.10 Mean stress distribution in the billet after a ram displacement of 26.7mm in the small extrusion press (negative values denote compressive stresses)

surface forms from both the shear zone and a small volume of dead zone at the bottom of the die interface^[117]. This feature is in accord with other observations, both experimental^[87] and FEM^[72,120]. The maximum strain rate is in the range of values typical of those found in extrusion^[63,65], and similar to the maximum strain rate of about 21.5 s^{-1} for the small press, estimated using another empirical equation (5.23)^[61]. However, the mean strain rate

calculated using an empirical equation (5.24)^[61] is only $2.4s^{-1}$. The low value estimated by the second empirical equation results from the assumption that the deformation is homogeneous throughout the billet. This restriction does not apply to the finite element analysis, which consequently predicts a higher mean effective strain rate of $13.7s^{-1}$, which probably more accurately reflects the deformation of the billet. Furthermore, the empirical equation (5.24) cannot take into account the large-scale variations in ram speed observed during the trials, whereas the finite-element analysis is ideal for this situation.

$$\dot{\epsilon}_{\max} = \frac{6v_B R}{D_E} \quad (5.23)$$

$$\dot{\epsilon}_m = \frac{4D_B^2 v_B \tan \phi}{(D_B D_E)^{3/2}} \quad (5.24)$$

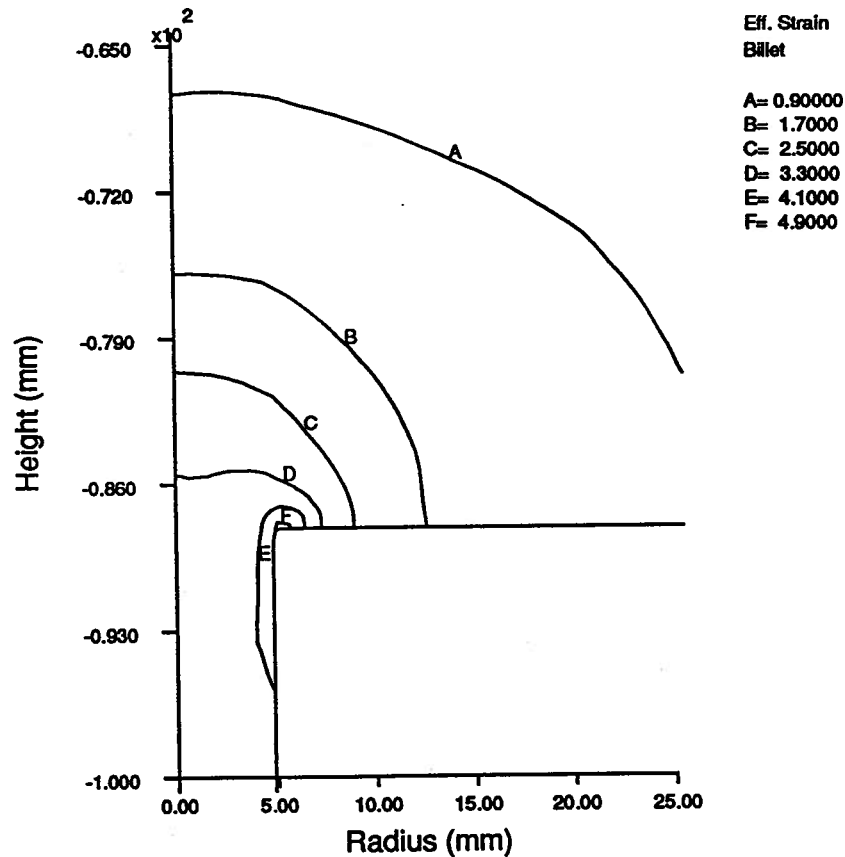


Figure 5.11 Effective strain distribution of the billet in the small press

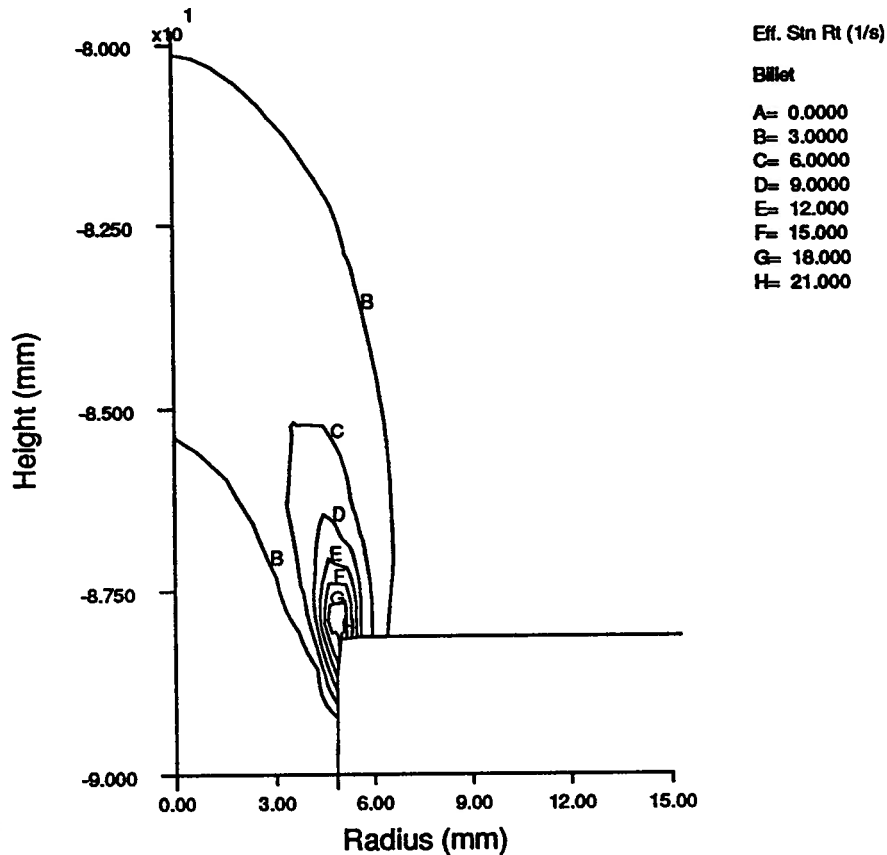


Figure 5.12 Effective strain rate distribution of the billet in the small press

5.3.2.2 Temperature Distribution

Because the flow stress of the composites is very sensitive to temperature, the temperature drop during transfer of the billet from the furnace to the container was also included in the simulation based on the measurement of the delivery time (Chapter 4). At the beginning of the extrusion, due to the cold pressure pad and lower initial die temperature of the large press, a 'chilling' effect exists at both ends of the billet, which consequently heats up the pressure pad and the die by heat conduction through the interface. After the upsetting stage, the billet temperature exhibits the effect of deformation heating toward the die entry, although in the larger billet, this is more pronounced because of its lower initial temperature (Figures 5.13 and 5.14).

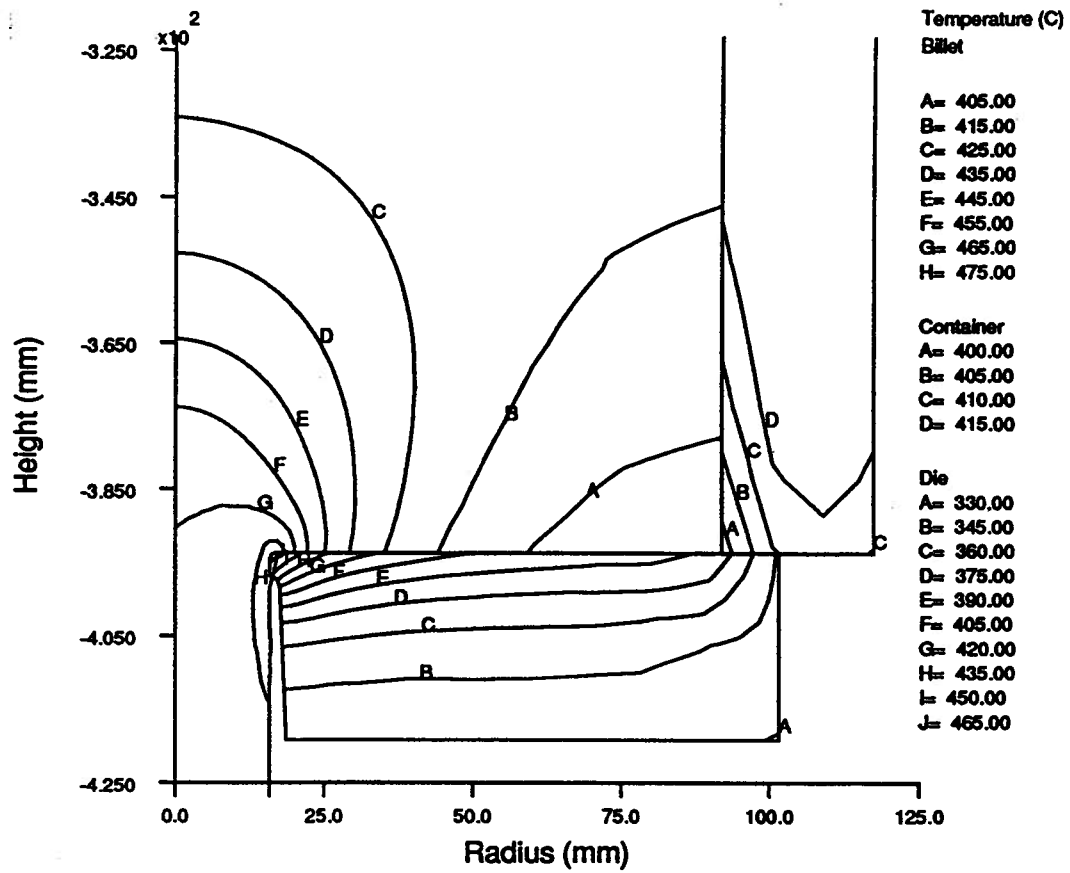


Figure 5.13 Temperature distribution in the large extrusion press

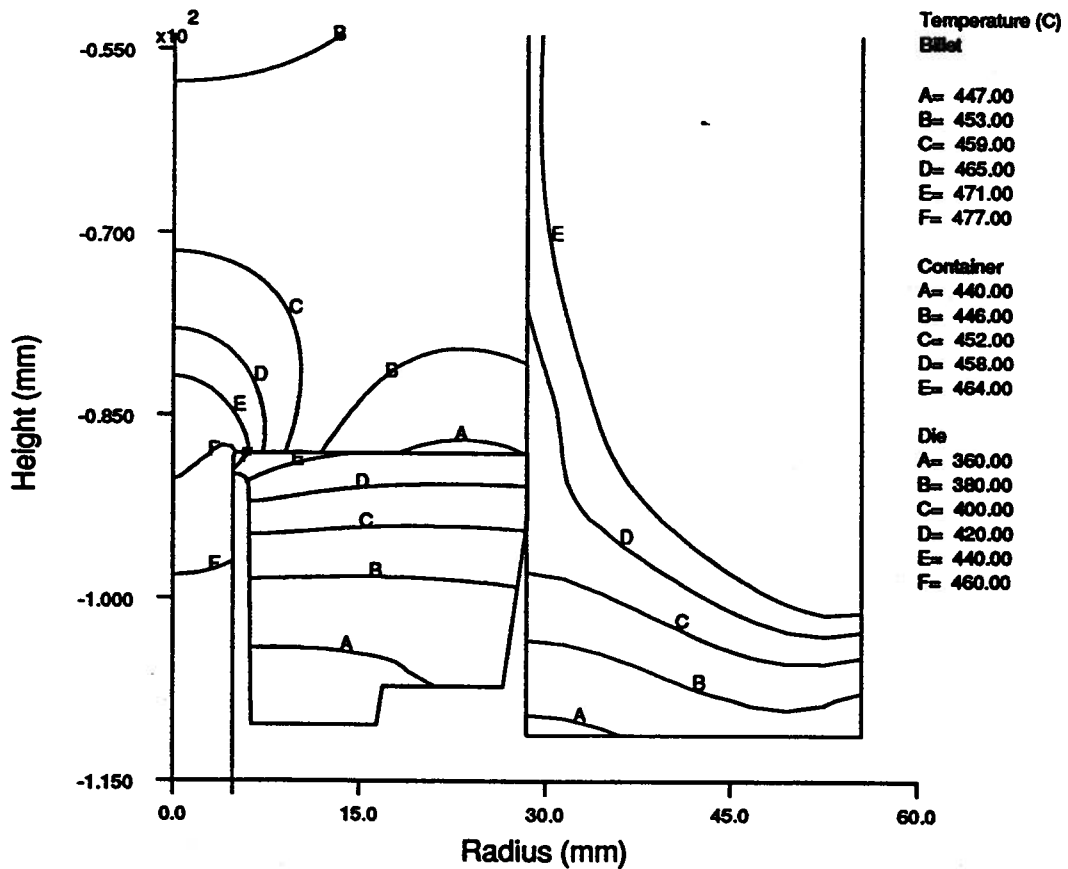


Figure 5.14 Temperature distribution in the small extrusion press

Temperature increases of approximately 70°C and 23°C were predicted for the large press and the small press, respectively, because of the heat of deformation. This is again due to the low initial temperature of the billet and higher ram speed of the large press, which increases the flow stress and the strain rate, resulting in a higher rate of heat generation. The maximum temperature of about 484°C and 479°C for the large and small presses, respectively, is reached at the surface of the extrudate in the die land zone. The maximum temperature of the die is about 10°C less than the maximum value in the billet due to the thermal resistance at the die interface. Because the thermal diffusivity of the die material (H13) is about 7 times less than that of the 6061/Al₂O₃/20p, a much larger thermal gradient exists in the die land than in the extrudate. The more pronounced thermal gradient in the die land for the large press is a result of the difference in initial die and billet temperatures while the large thermal gradient in the extrudate of the large press is due to the larger diameter of extrudate and the higher ram speed, which results in a more pronounced adiabatic heat effect.

5.3.2.3 Comparison of Predictions with Measured Data

Load / stroke predictions are compared with measured data for displacement beyond the peak load in Figures 5.15 and 5.16. The agreement is good during the upsetting stage, and within 10% at the higher loads in both instances. However, the load increase at the end of the upsetting stage is faster in the FEM prediction than in the measured data, especially for the small press, in which a larger shift in the peak load appears. This might be due to the assumption of rigid tools in the FEM model, while in reality there always exists deformation of the press. The large shift in the peak load might be partly due to the capacity of the small press (100T) which was almost fully loaded in the test, while the 3000T capacity of the large press meant it was only half used. Therefore the compliance of the press has to be estimated.

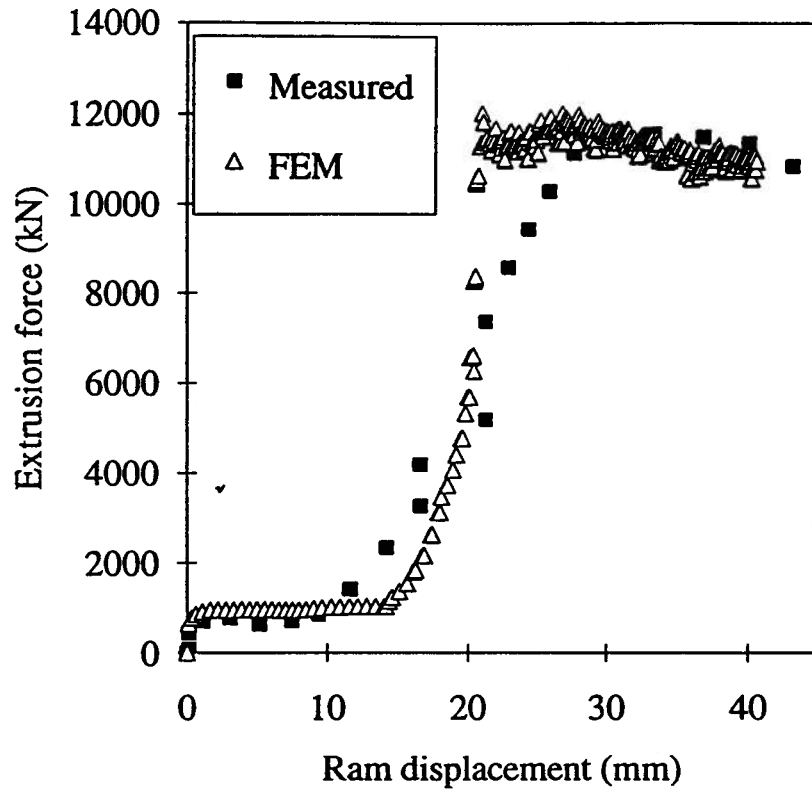


Figure 5.15 Comparison of predicted force with measured data (large press)

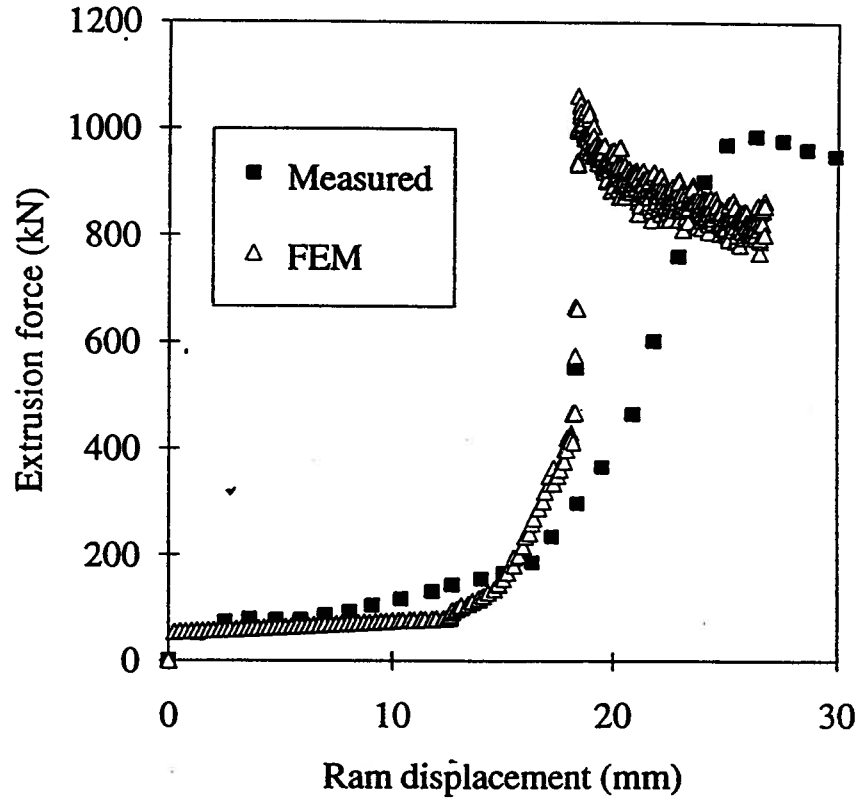


Figure 5.16 Comparison of predicted force with measured data (small press)

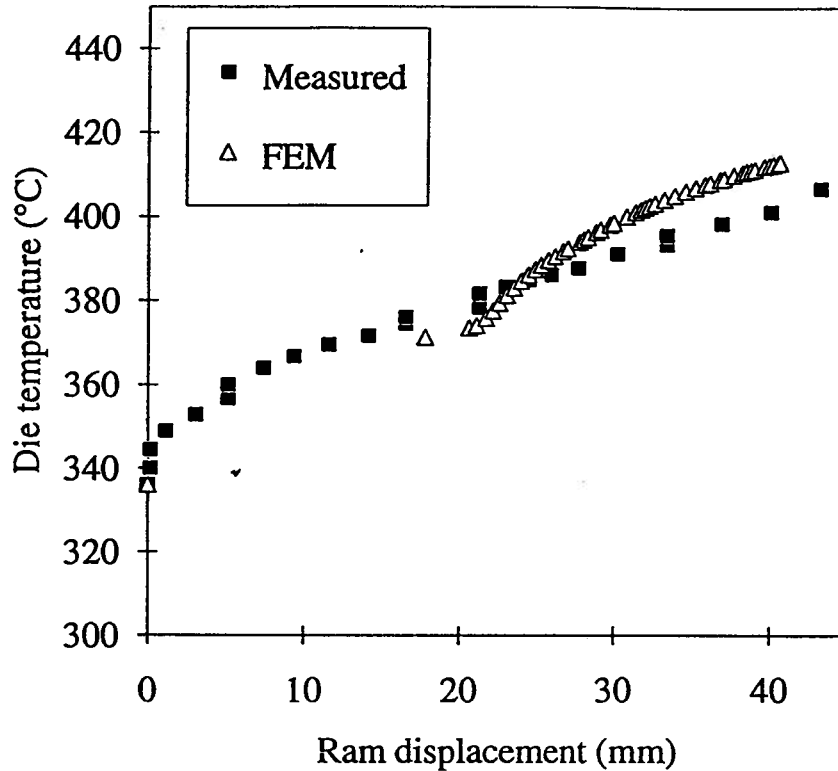


Figure 5.17 Comparison of predicted temperature with measured data (large press)

The predicted temperature at the thermocouple position of approximately 1.6 mm away from the die bearing in the die for the larger press (Figure 5.17) is within 10°C of the measured temperature over the range of the simulation, although it does not follow the variation closely. The model seems to have overpredicted the temperature after the peak load has been achieved, but the difference is still less than three percent. Actually, the discrepancy between the predicted and the measured temperature could also be due to the assumption of initial uniform die temperature and the error of the thermocouple position because the thermocouple was inserted into the hole in the die after the die was put into place before extrusion. It is worth pointing out that the reason for fewer predicted points in the upsetting stage in the FEM curve (Fig. 5.17) is that fewer time steps with predicted results

were saved to prevent a big size (could be up to 300MB) of the output database file during simulation. However, the load value was saved automatically for each step in the model.

5.4 Validation of Model Predictions

Model predictions must be evaluated in the light of the fact that the boundary conditions in some areas were not precisely defined, and this may affect the results. The friction between the billet and container or die surfaces was assumed to be sticking friction but was not measured. Furthermore, the temperature field in the billets extruded through the large-scale press was not accurately known, due to the constraints imposed by the conditions under which the trial was conducted. In addition, the temperature at the die in the smaller press was not recorded. The prediction of the forces required for extrusion is most susceptible to temperature variations. Finally, it must be recognized that the simulation is a two-dimensional simulation, and any results should be treated with caution, although for the axisymmetrical case considered here, errors are likely to be low.

Notwithstanding these limitations, the modeling has resulted in a reasonably accurate prediction of load and temperature rise. Furthermore, predictions in the upsetting stage are difficult with a fluid-flow type model^[70], but in this work the agreement between predictions and measured data was very good. The ability to predict forces in the upsetting stage has a concatenation effect in that it influences the subsequent predictions of, for example, temperature and strain.

Load predictions resulting from the finite-element analysis are close to the values measured from each press, although the prediction for the larger press is considerably closer to the measured value. The predicted sharp rise in load after upsetting of the billet does not accurately follow the measurements (the scale of the abscissa in Figs. 5.15 and 5.16 distorts

the difference however). This is not an anomaly of the model, as mentioned before, but rather is a consequence of defining the die, container, and pressure pad as rigid objects during the simulation. In reality, the components are not rigid, but this assumption was needed to complete the simulation in a reasonable CPU time. Thus, the model predicts only the response of the material, whereas the instruments on the press read the response of the whole system.

It is known that the difference between the length of a billet before extrusion and the length of the remained butt end after extrusion is the real displacement the billet experienced during extrusion. If the press (assuming the billet is rigid-plastic) were rigid, then the recorded ram stroke would be exactly the same as the real displacement. Therefore, the difference (a total elastic deformation of the press) between the real displacement and the recorded ram stroke was used as a simple examination of the contribution of machine compliance to the load-stroke curve. For the 100T press, the total elastic deformation, including the elastic deformation of the billet, was obtained to be 5.27mm for the given test.

The maximum ram stroke was reached when the final ram speed approached zero. Considering the measured extrusion force at the maximum ram stroke for that given test, $F_f = 808\text{kN}$, an overall elastic deformation constant for the press was calculated as:

$$E_o = F_f / (S_T - (L_o - L_R)) = 153\text{kN/mm} \quad (5.25)$$

Applying this constant to the measured stroke, the adjusted stroke excluding the elastic deformation, as simulated by DEFORM[®], can be obtained as:

$$S_a(t) = S_m(t) - F(t)/E_o \text{ (mm)} \quad (5.26)$$

where $S_a(t)$ and $S_m(t)$ are the adjusted and measured ram stroke, respectively; $F(t)$ is the extrusion force, and t denotes extrusion time.

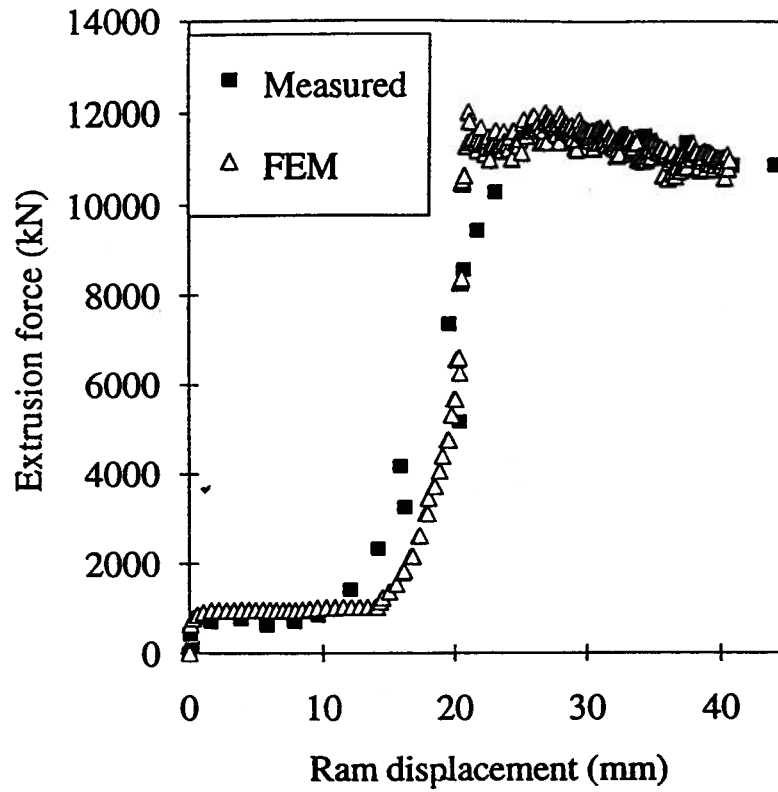


Figure 5.18 Comparison of FEM force with measured data corrected for extrusion press compliance according to Eq. (5.26); large press

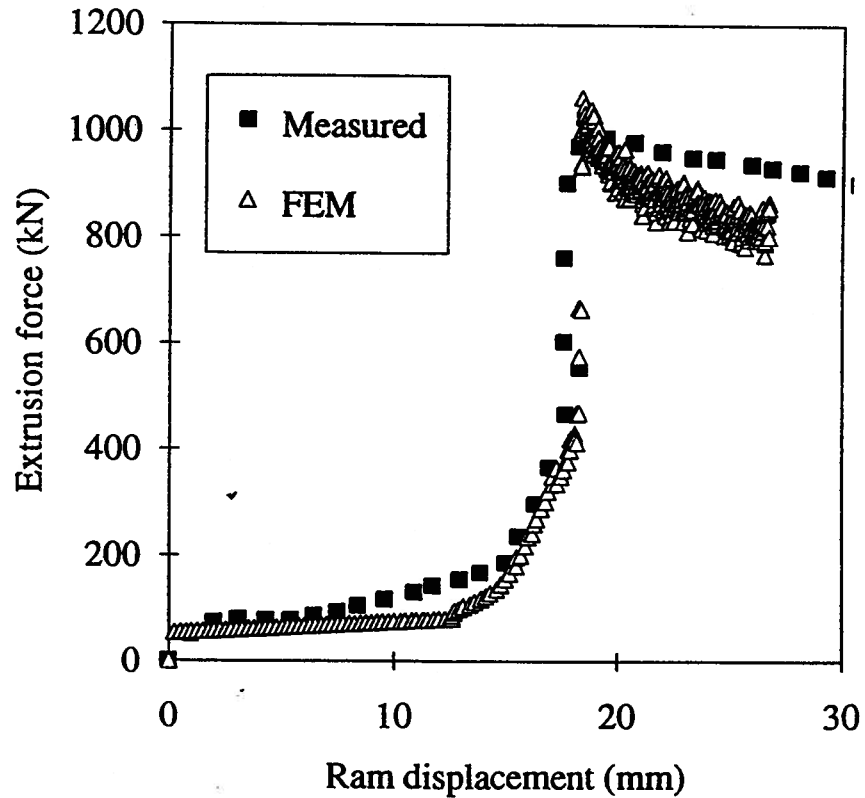


Figure 5.19 Comparison of FEM force with measured data corrected for extrusion press compliance according to Eq. (5.26); small press

Another way to calculate the E_0 is to measure the unloading slope of the extrusion force-stroke curve. The average E_0 for the larger press is measured as 2777kN/mm from four tests. Corrections to the measured data accounting for the machine compliance align the measurements with the simulation (Figures 5.18 and 5.19). In principle, the reverse is possible: the simulation could include an elastic component in order to better model the specific extrusion press under investigation, at the expense of simulation time.

The variation in the load prediction, after the peak load has been reached (Figures 5.15 and 5.16), is due to a node in the billet losing contact with the die and a consequent drop in the extrusion force. The software attempts to compensate for this node unpinning, causing the observed behavior. The prediction could be improved in a number of ways, although any benefit derived from eliminating the small variation (less than 10%) would itself be canceled out by the large increases in CPU time required to achieve the following solutions. Either the mesh at the die throat could be further refined by increasing the number of elements, or the Arbitrary Lagrangian-Eulerian (ALE) method could be used, though there is no guarantee that a re-meshing would not be required; furthermore, the mesh velocity would be difficult to determine. In addition, it is unlikely that in either case the proximity of the prediction to the measured data would be altered.

5.5 Summary

A model has been developed and verified to simulate the extrusion of PRMMCs. The model is a bulk forming model with the material assumed to be monolithic with the properties of the composites. Both the transient and steady state parts of extrusion were modeled. A description of the bulk extrusion of this MMC has been presented and shown to be valid for the prediction of extrusion loads, and consequently deformation in the billet during extrusion.

Load predictions resulting from this model agree to within ten percent of the measured value, and in the upsetting stage, to a higher accuracy. Temperature predictions agree to within less than three percent. Slight discrepancies between the model and measurements in the region of maximum rate of change in load have been accounted for by elastic deformation of the press components. The model is useful for macroscopic analysis, such as the development of extrusion limit diagrams, but cannot correctly predict deformation on the scale of the particles. However, the stress, temperature, and strain distributions can be related to the propensity for particle fracture and/or void formation.

Chapter 6 MICROMECHANICAL ANALYSIS OF THE PRMMC DURING LARGE DEFORMATION

6.1 Obstacles and Challenges of Micromechanical Analysis of the PRMMCs

In recent years, micromechanical analysis of particulate reinforced MMCs has been conducted^[105-108] to better understand the MMC's response during either thermal or mechanical changes. However, almost all of the finite element analysis on particle behavior of the MMCs were based on the unit cell model with simplified boundary conditions, as described in the literature review (Chapter 2). The characterization of behavior of the particulate reinforced MMCs under large deformation conditions has received little attention, probably because of the obstacles stated below.

6.1.1 Particle Phenomena

It is the presence of particles that results in the improvement of properties of the MMCs in many aspects. However, the particles have some specific features in real MMCs: (a) the shapes of particles in the MMCs are not regular rectangles or circles as assumed by some investigators in two-dimensional unit cell models; (b) the size of the particles varies widely from a few microns to 50 μm or even more for the Duralcan[®] composites; (c) it is known that large particles tend to fracture more easily than small particles; (d) more importantly, the distribution of the particles in as-cast MMCs fabricated by the molten route is not uniform but contains clusters and voids due to solidification; and micro-fracture initiates more easily within clusters during deformation. Therefore, to account for particle behavior under large deformation with the aid of a finite element model, the shape and size of the

particles and clusters should be taken into account. However, because the average dimensions of a particle (up to 50 μm) in the MMCs are significantly ($\sim 10^4$ times) smaller than those of the workpiece (e.g. 10 mm), if the deformation of the particles in the MMCs were studied, at least 10^8 elements would be necessary for a two dimensional analysis with the element size close to a particle dimension. Obviously, this is impractical from a computational stand point. Then the question is, how can a micromechanical analysis of the MMCs be conducted with a traditional finite element model?

6.1.2 Matrix Phenomena

The MMCs are not simply a mixture of the particles and the matrix. In fact, the interactions of a second phase particle with the matrix during deformation is very complex. It is known that additional phenomena will occur, such as (a) precipitation of fine particles formed by chemical reaction between the particles and matrix alloy; (b) interface bonding and its strength; (c) residual stress due to mismatch of the thermal expansion coefficient between the particle and the matrix; (d) strain induced dynamic recovery and particulate stimulated nucleation for recrystallization; (e) fracture of particle and decohesion of the interface, rotation and migration of the particle during deformation, etc., The question is, how could a finite element model take those factors into consideration?

6.1.3 Modeling Constraints

To investigate the micromechanical behavior of the MMCs, a physical constitutive equation (not like the phenomenological one as developed in Chapter 4) needs to be developed by combining microscopic variables and macroscopic process parameters. Although a few simplified physical constitutive equations have been developed, they are incomplete. Hence, how can a physical constitutive equation be developed which includes all

the factors or at least the most dominant (if known) ones influencing the dynamic behavior of the MMCs by combining both the macroscopic and microscopic process parameters? If it were developed, could it be applied to a multiaxial stress state during processing by validating only through uniaxial compression and/or tensile testing? It seems impractical to overcome all these obstacles by the available plasticity theory and computation technology.

6.2 Micromechanical Analysis during Plane Strain Compression

Under the above mentioned circumstances, it is therefore impractical to conduct micromechanical analysis of the MMCs during industrial extrusion. Nevertheless, a laboratory plane strain test was simulated to analyze the behavior of particles during hot deformation. To simplify the analysis, a twin-particle model and a multiple-particle model were adopted with each particle size of $40 \times 40 \mu\text{m}^2$ in the planar cross section. In the twin-particle model, two particles were arranged such that the particle movement in the lateral direction perpendicular to the loading direction could be analyzed. In the model, the matrix around the particle behaves as a monolithic material with the deformation properties of the composite, and the particle has its own properties and flows along with the matrix during deformation. The DEFORM[®], as described in Chapter 5, was adopted for the micromechanical analysis.

The initial setup of the plane strain test simulation with finite element meshes for each object is shown in Fig. 6.1. Because the particle size is only $40 \mu\text{m}^2$, the element size around the particles is tremendously refined. The detailed finite element mesh around the two particles is shown in Fig. 6.2 for the twin-particle model. For a plane strain test simulation, only a half of the set was analyzed due to its symmetry. The friction shear factor, m , and the heat transfer coefficient, h , at the interface between the specimen and the anvil were assumed

to be 0.7 and 200 kW/m²K^[86], respectively. The test simulation conditions are listed in Table 6.1. The nominal strain rate is 0.05/s. The total reduction was about 50%.

Table 6.1 Simulation conditions for plane strain deformation

Object Name (No.)	Material	Size (mm)	Temperature (°C)	Number of Elements
Upper Anvil (#1)	718 (rigid)	8.64x3.0	445	100
Specimen (#2)	6061/Al ₂ O ₃ /20p (rigid-plastic)	25.4x10	450	2500
Bottom Anvil(#3)	718(rigid)	8.64x3.0	445	100
Particle (#4)	Al ₂ O ₃ (elastic)	40x40 μm ²	450	18-36

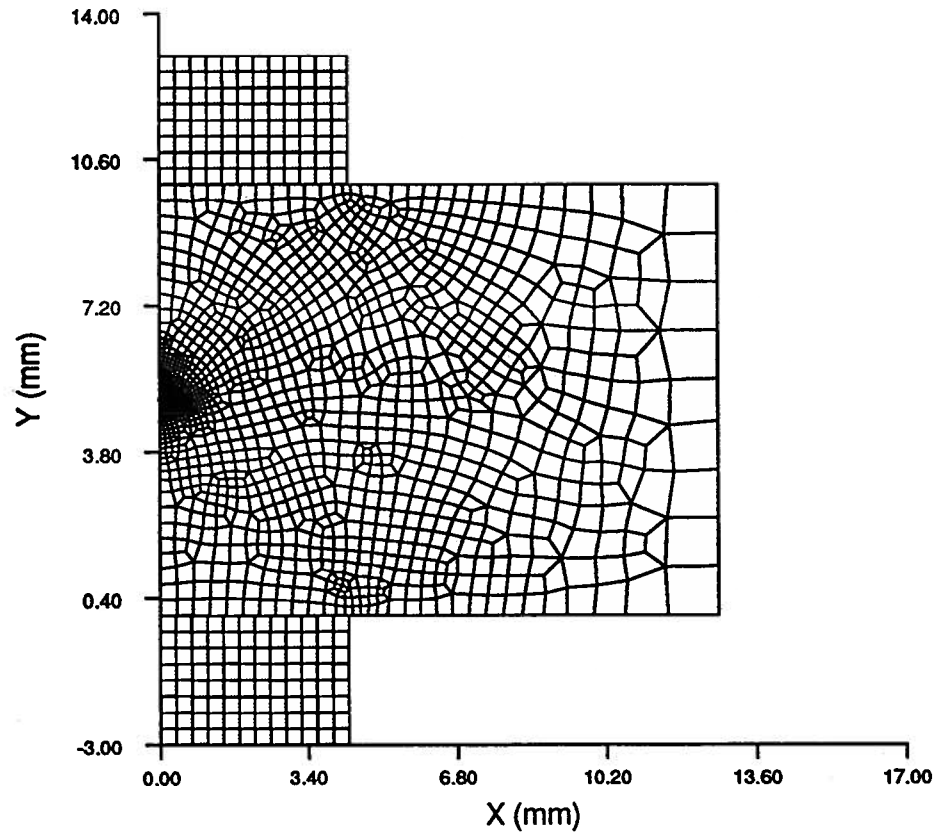


Figure 6.1 Initial finite element meshes for each object of plane strain deformation

6.2.1 Twin Particle Model

For the twin-particle model, one particle was located at the center line of the specimen, therefore only half of the particle was considered due to symmetry. The other particle was initially located $40\mu\text{m}$ apart in the lateral direction(see Fig. 6.2). The interface between the particle and the matrix was assumed to be perfectly bonded. The elastic modulus of the particle was 450 GPa; the Poisson ratio was 0.25, and the coefficient of thermal expansion was $7.7 \times 10^{-6}/^\circ\text{C}$ with the reference temperature of 450°C , based on data in the literature for the same kind of MMC^[94].

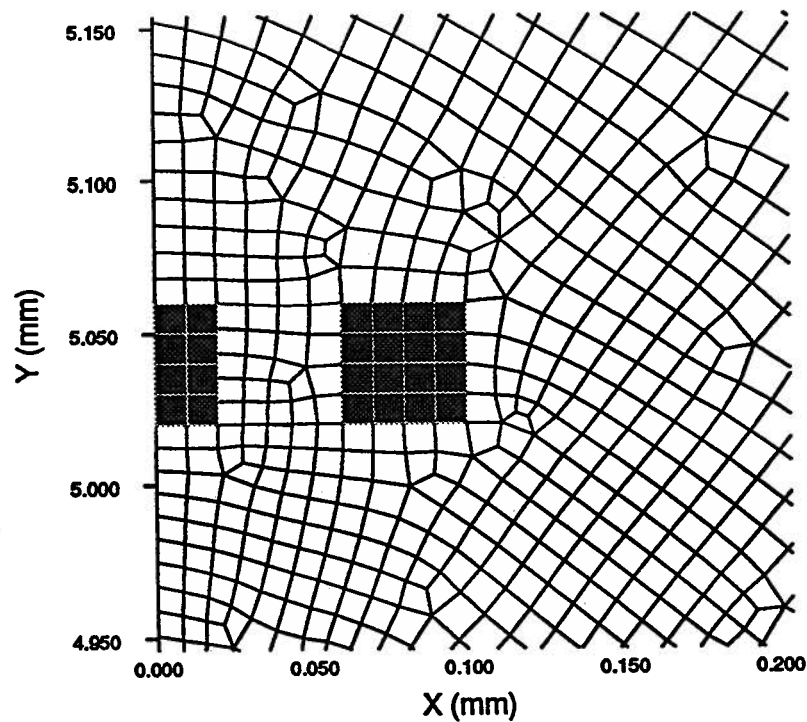
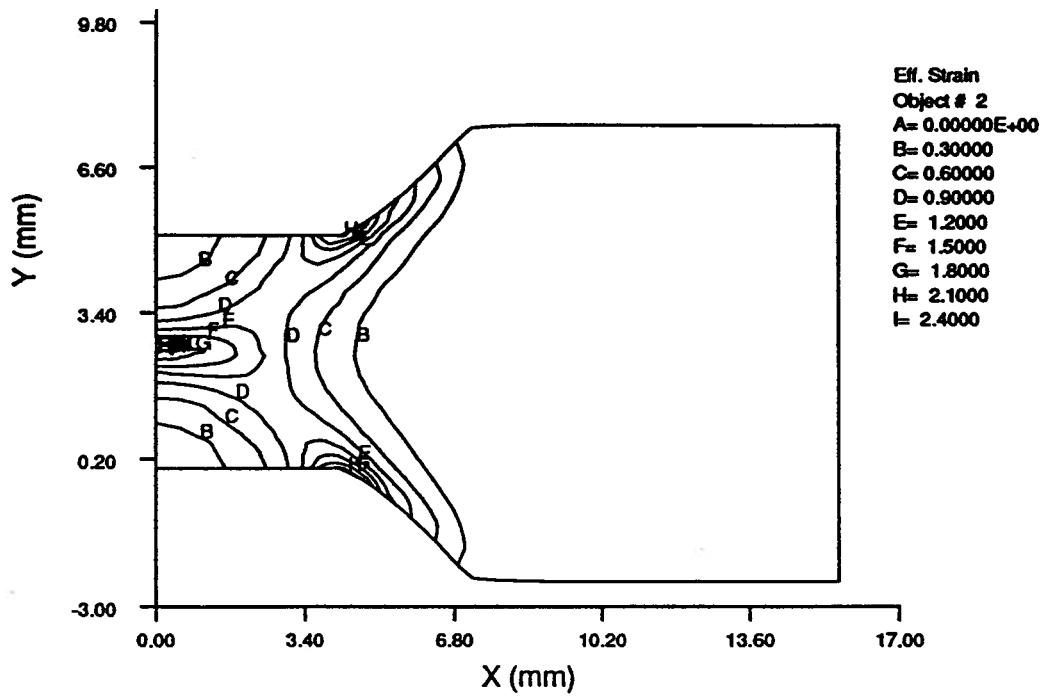


Figure 6.2 Initial finite element mesh around two particles

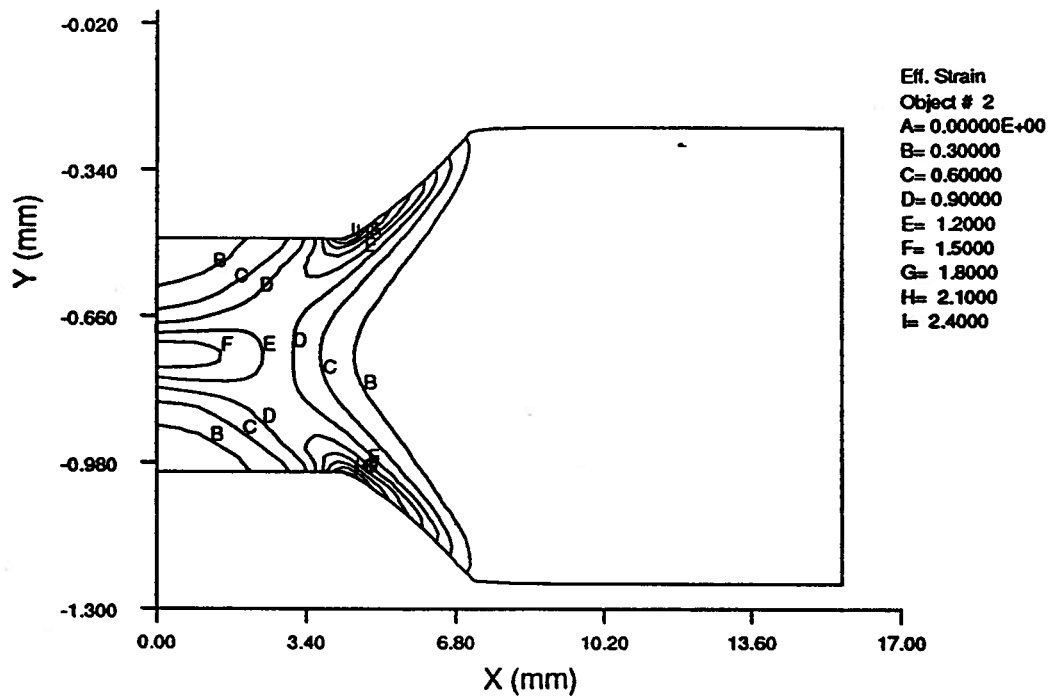
The effective strain distribution in the specimen at a reduction of about 49% is shown in Fig. 6.3(a) and (b) with and without particles, respectively. From the figure, it is seen that the overall effective strain distributions for both cases are quite similar, but deformation

localization occurs around the particles. This is because only two particles are considered in the micromechanical analysis. The localized effective strain is shown more clearly in Fig. 6.4 as a function of reduction. Fig. 6.4 (a) shows the effective strain distribution around two particles at a reduction of 10%. It is seen that the highest strain is concentrated in the middle of the two particles (Contour line 'C'), and the strain around the two particles is at about the same level (contour line 'B'). As the reduction increases, the particle located outside the center line is pushed away by matrix material along the flow direction. The distance between the two particles becomes about $130\mu\text{m}$ (Fig. 6.4(b)). As a result, the effect of clustering is decreasing, although the highest strain is still concentrated between the two particles (Contour line 'F'). At a reduction of about 49%, two closely distributed particles are pushed apart from an initial spacing of $40\mu\text{m}$ to more than $300\mu\text{m}$ (Fig. 6.4(c)). It is seen that a low strain zone (contour line 'F') appears close to the particle. The highest strain is obtained outside the low strain zone both parallel and perpendicular to the loading direction (Contour line 'H'). This indicates that as the reduction increases, the interaction between two particles becomes weak, and each particle plays its own part in the material during deformation. Obviously, the migration of particles in real composites helps break the clusters formed in casting and improves the homogeneity of particle distribution after secondary processing. Especially, in extrusion processing, due to large deformation, fractured particles can be separated by shear deformation and healed by compressive hydrostatic pressure.

The effective stress in the particles at two different reductions of 10% and 49% is shown in Fig. 6.5. It is seen that the stress level is much higher than that of the effective stress in the matrix, which is about 60MPa. This is partly due to the assumption of plane strain deformation, in which the strain in the third direction is constrained to be zero. Therefore,

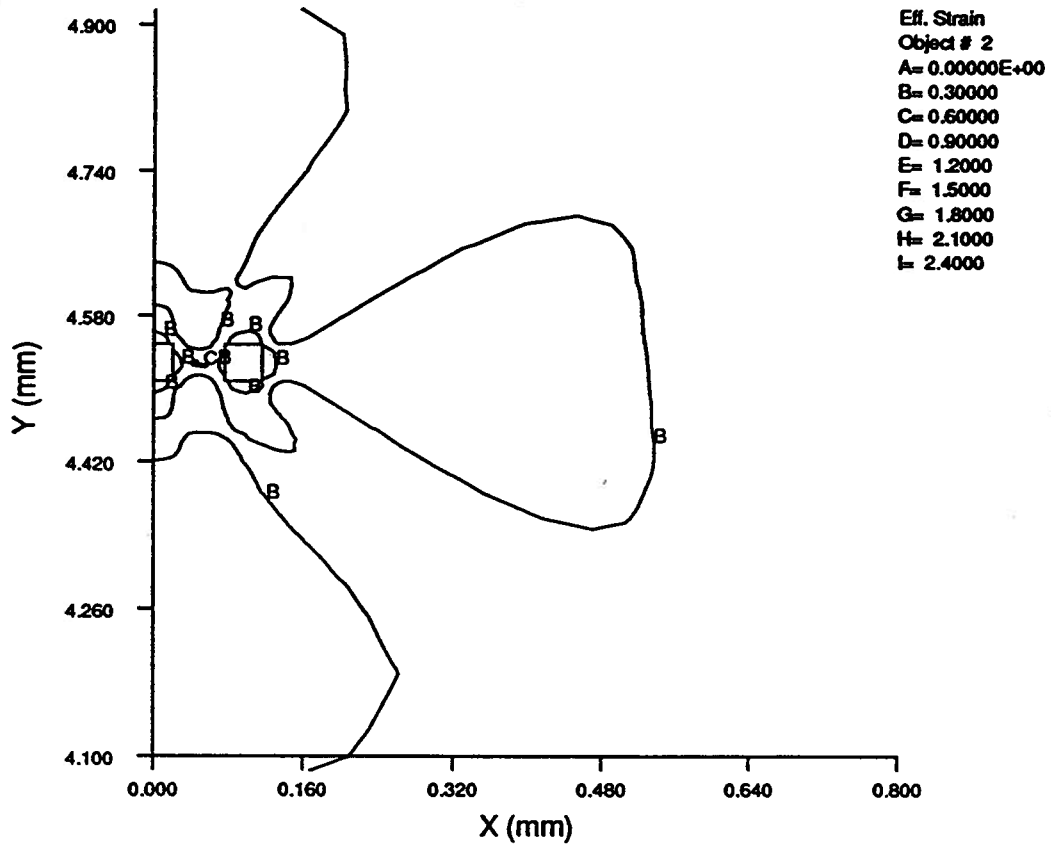


(a) Twin particle model

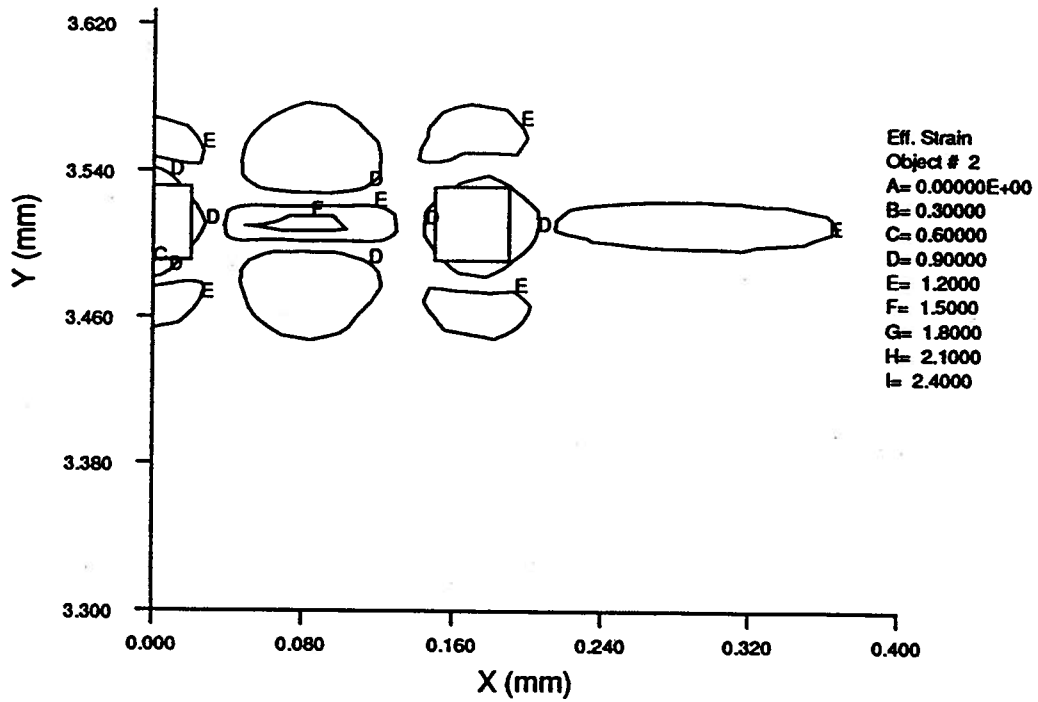


(b) homogeneous MMCs

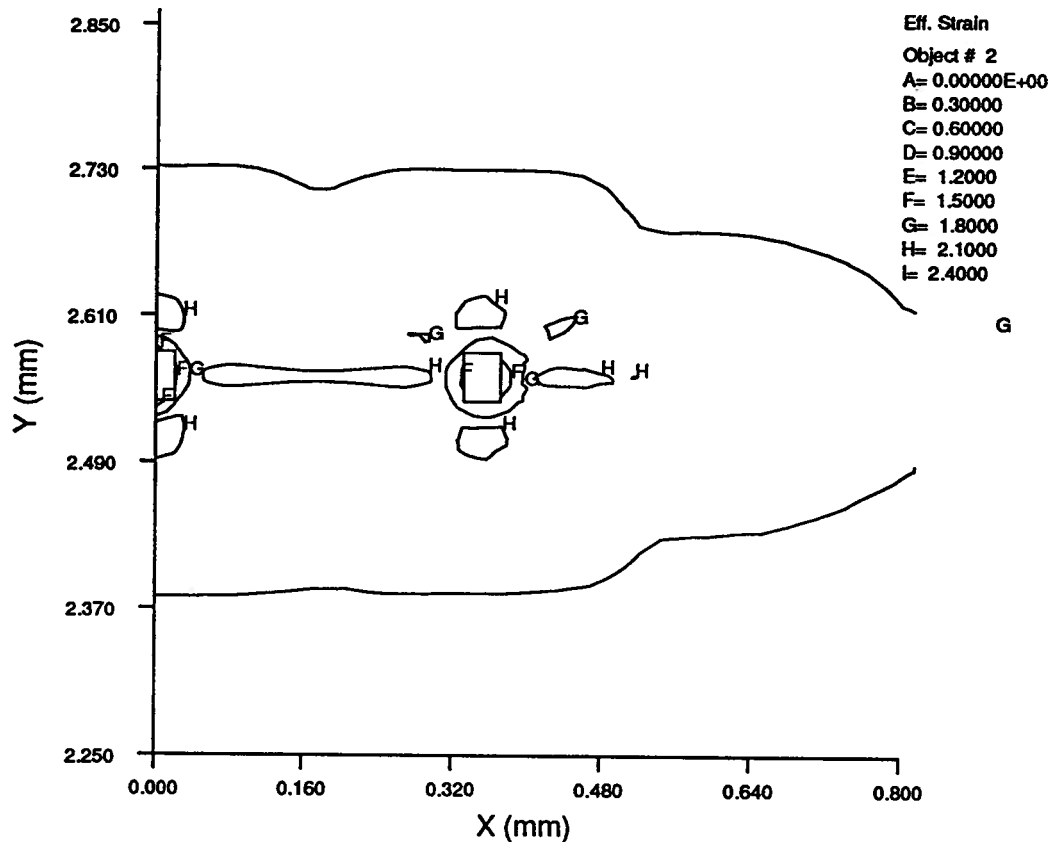
Figure 6.3 Effective strain distribution at a reduction of 49%



(a) at a reduction of 10%



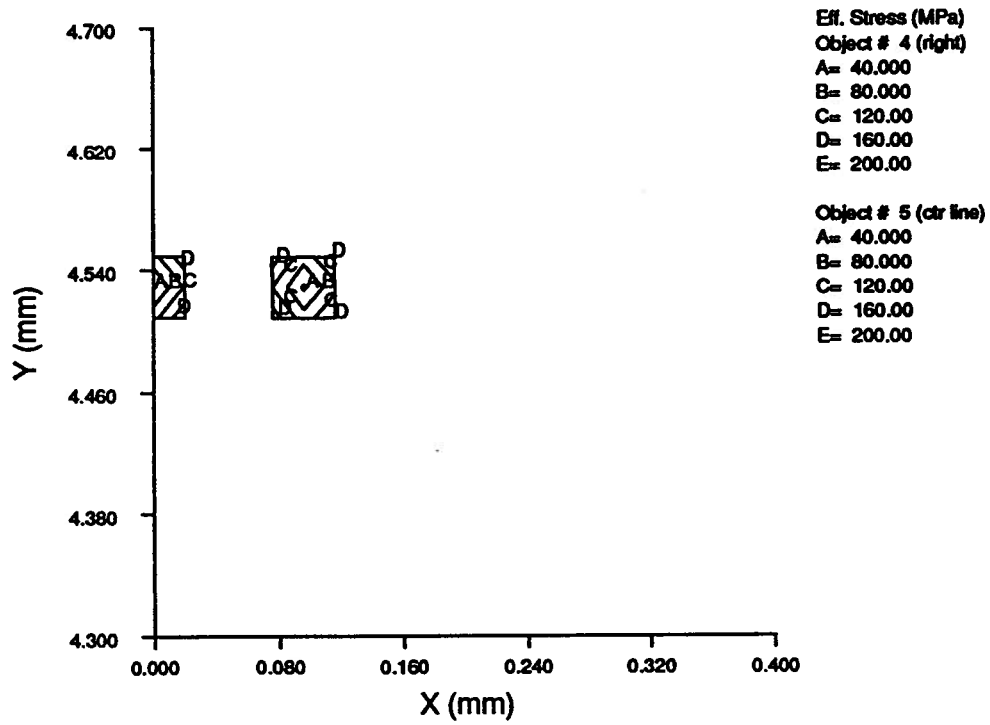
(b) at a reduction of 30%



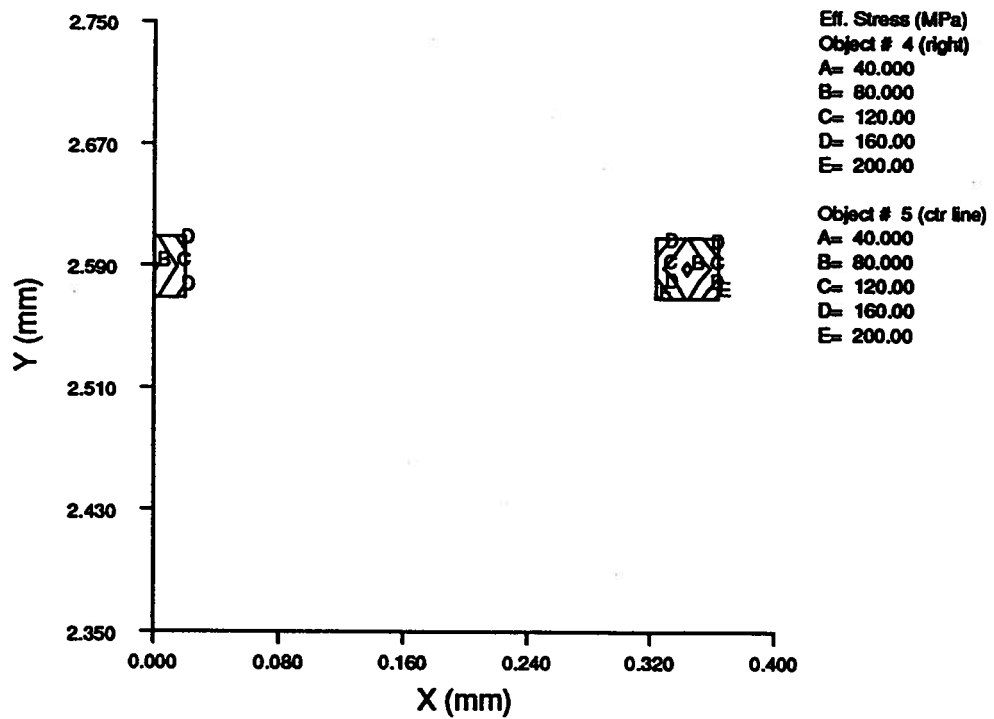
(c) at a reduction of 49%

Figure 6.4 Localized effective strain distribution around two particles
at different reductions

even a very small strain in the third direction could lead to a large stress because of high elastic modulus of the particle. It is also interesting to see that the value of the effective stress in the particles increases as the reduction increases. Besides the effect of matrix deformation, this could be also due to the build-up of thermal stress in the third direction when temperature in the particle changes during deformation. The larger value of the effective stress in the particles at a small reduction during large deformation confirms that particles could fracture at an early stage of deformation, if the fracture stress of the particle is reached^[92].



(a) at a reduction of 10%



(b) at a reduction of 49%

Figure 6.5 Effective stress in the particles at different reductions

6.2.2 Multiple-Particle Model

To consider the effect of clustering of particles in a composite, a four-particle model was developed with two more particles added to the twin-particle model, as shown in Fig. 6.6. Due to the presence of more hard-to-deform elastic particles in this model, remeshing for the matrix around four particles becomes very difficult. Therefore, a total reduction of only 1% was considered. The effective strain distribution in the cluster zone in Fig. 6.6 shows that a higher strain zone (Contour line 'B') appears in the middle of two particles in both the loading and the lateral directions in the planar cross section; however, a lower strain zone (Contour line 'A') exists in the center of four-particle cluster. This is because at the early stage of deformation, four particles act as a cluster; therefore, the center of the cluster is hardly deformed. The effective stress distribution in both particles and the matrix is shown in Fig. 6.7. Considering the stress distribution in the matrix, it is seen that a low stress zone (Contour lines 'D') exists in the center of the four-particle cluster. Again, the effective stress in the particles are more than 4 times higher than that in the matrix, which is similar to the twin particle model as described above. The mean stress distribution in the matrix shows a tensile stress state in the zone between the two particles in the lateral direction (Fig. 6.8), whilst the stress state between the two particles in the loading direction is compressive. The stress state in each particle is quite similar: a tensile stress component exists at the top and the bottom surface of each particle (the locations of contour line 'E' in each particle) due to the positive value of the mean stress, which could be a potential site for cracking.

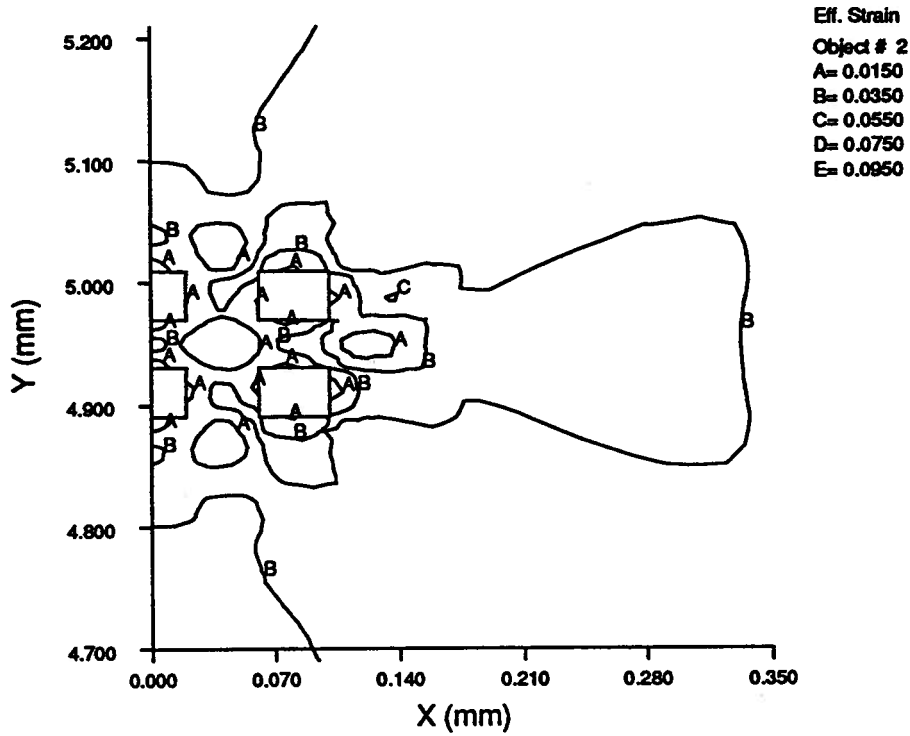


Figure 6.6 Localized effective strain distribution at a reduction of 1%

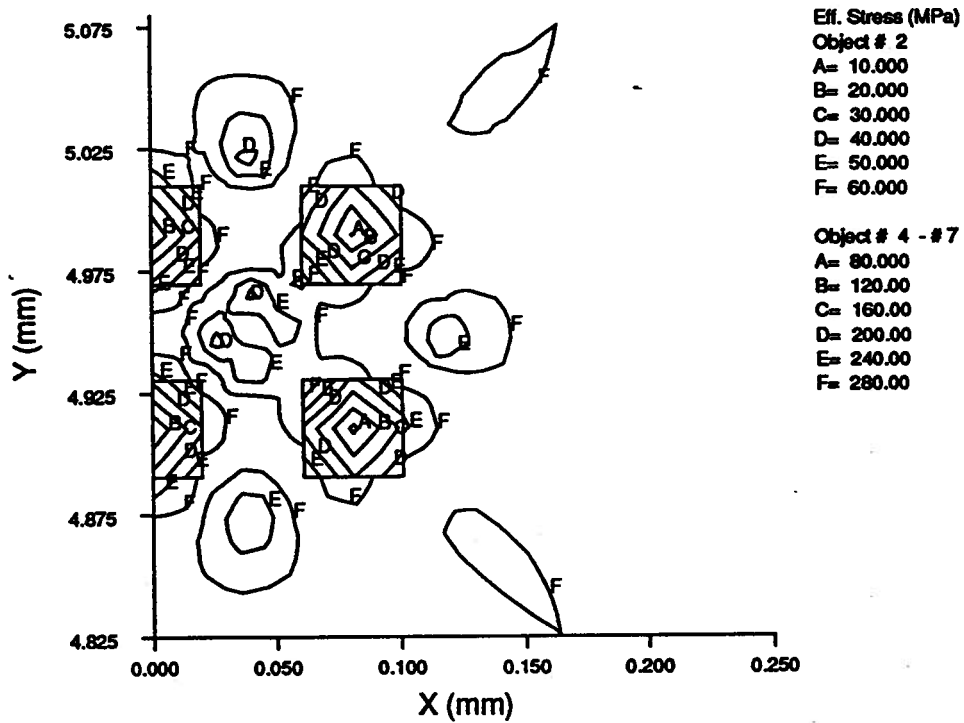


Figure 6.7 Localized effective stress distribution at a reduction of 1%

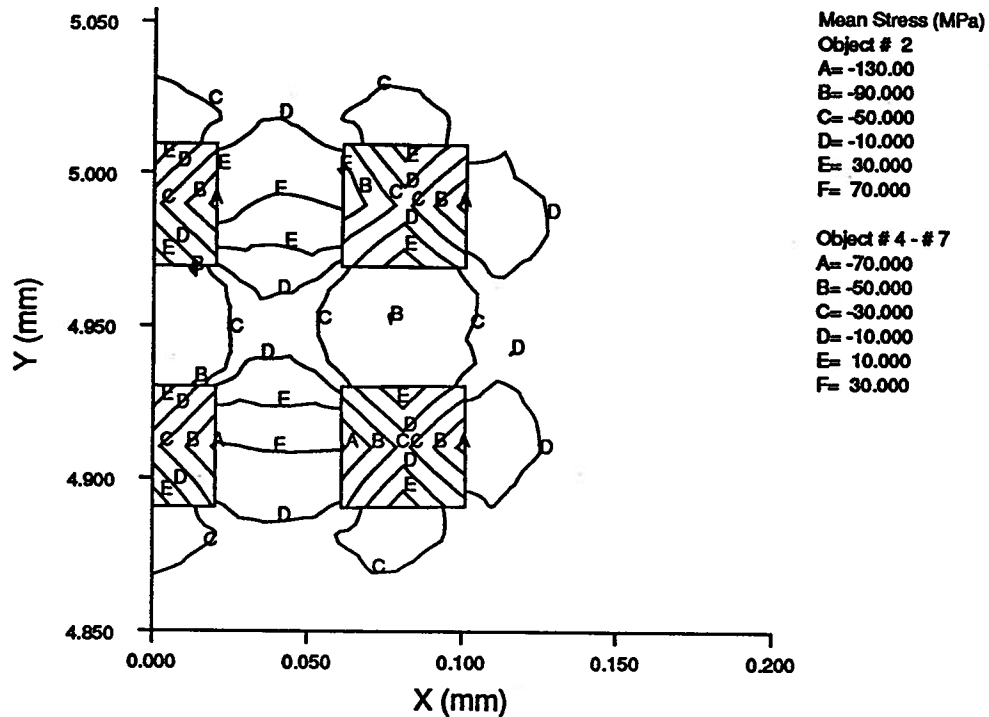


Figure 6.8 Localized mean stress distribution at a reduction of 1%

6.3 Micromechanical Analysis during Cylindrical Compression

Although a unit cell model in plane strain condition has been widely adopted by researchers for particle analysis at a microscopic level, obviously the particle model is not representative of a real three dimensional particulate, but instead of an infinite bar in the third direction (perpendicular to the plane). Therefore, it would be ideal to develop a three-dimensional model. However, the large number of elements needed for 3-D analysis, as mentioned in Section 6.1, would be impractical from the perspective of computation costs. Hence a laboratory axisymmetric cylindrical compression test was simulated by inserting particles at the center line of the specimen. As a result, the shape of a particle is either

cylindrical or spherical in 3-D due to axisymmetry. The simulation conditions are listed in Table 6.2.

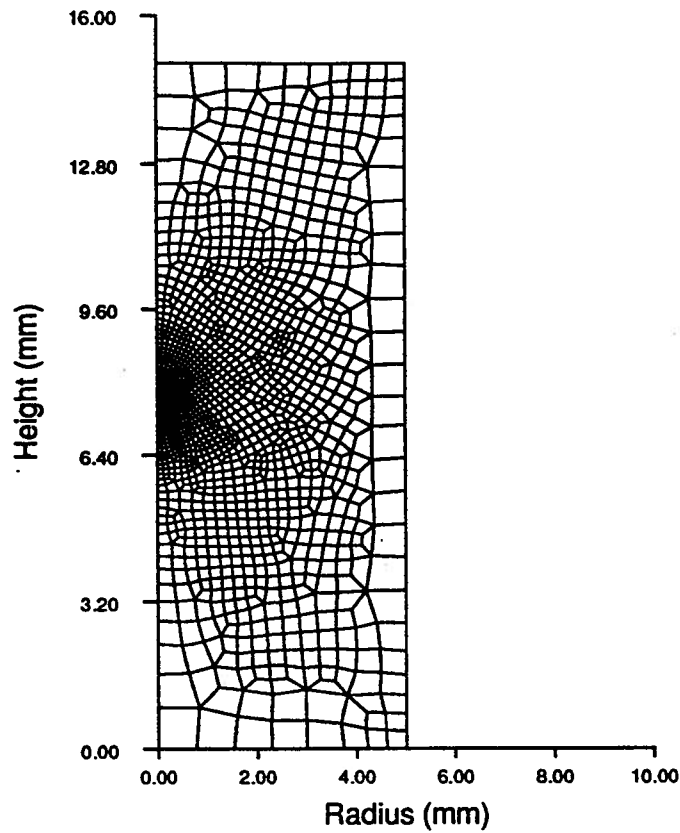
Table 6.2 Simulation conditions for cylindrical compression test

Object Name (No.)	Material	Size	Temperature(°C)	No. of Elements
Upper Anvil (#1)	718 (rigid)	Φ20x20mm	449	150
Specimen (#2)	6061/Al ₂ O ₃ /20p (rigid-plastic)	Φ10x15mm	450	2500
Bottom Anvil (#3)	718 (rigid)	Φ20x20mm	449	150
Particle (#4)	Al ₂ O ₃ (elastic)	Φ20-Φ40μm	450	18-36

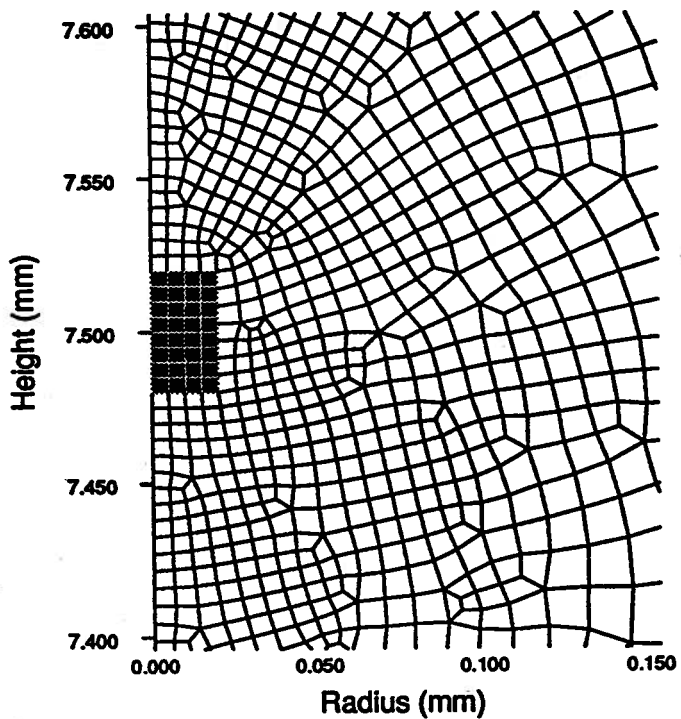
The initial finite element mesh of a specimen including particles is shown in Fig. 6.9(a). Again, the element size around the particle was tremendously refined, as shown in Fig. 6.9(b) for a single particle and Fig. 6.9(c) for a twin-particle model. The nominal strain rate for the test is 0.05/s, and the nominal strain is 1.0. The other boundary conditions are the same as in the plane strain simulation.

6.3.1 Single Particle Model

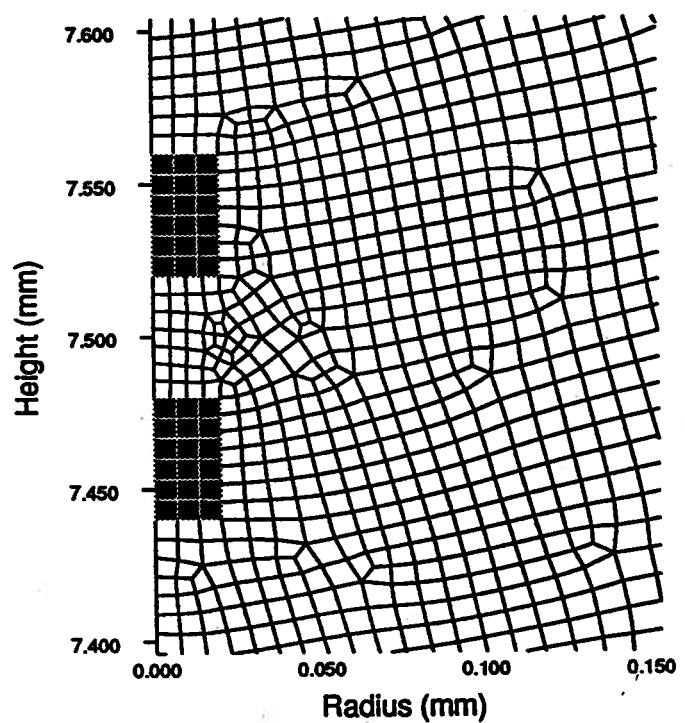
A single-particle model refers to a cylindrical specimen under large hot deformation containing only one particle at the center line. For the cylindrical compression test, only an axisymmetrical plane was analyzed due to its axisymmetry. The particle had to be in the center line because otherwise it would become a ring. Two extreme shapes of a particle were considered, i.e., a cylinder and a sphere in three dimensions. Four different particle cases were studied. The particle size for each single-particle model adopted is listed in Table 6.3.



(a) initial finite element mesh in a specimen



(b) mesh around a particle



(c) mesh around the twin particles

Figure 6.9 Initial mesh and location of a particle in a cylindrical specimen

Table 6.3 Particle sizes studied

Case	Comp-1	Comp-2	Comp-3	Comp-4
Shape	Cylinder	Cylinder	Sphere	Cylinder
Size($\mu\text{m} \times \mu\text{m}$)	$\Phi 40 \times 40$	$\Phi 20 \times 20$	$\Phi 20^3$	$\Phi 20 \times 80$
Aspect Ratio	1.0	1.0	1.0	4.0

6.3.1.1 Material Flow of a Cylindrical Specimen Containing a Particle

The effective strain distribution in a cylindrical specimen with and without a particle is shown in Fig. 6.10(a) and (b) for a reduction of 65%. It is evident that the overall strain distributions for two specimens are very similar, but a larger strain is reached near the particle due to strain localization. Details of the local strain distribution around the particle are shown in Fig. 6.11 for the $\Phi 40 \times 40 \mu\text{m}$ particle. In the loading direction, it is seen that a low-strain zone appears at both the top and the bottom of the particle; however, a high strain zone shows up adjacent to the low strain zone. This is because during compression, matrix material near the center line flows towards the particle which is located at the center of the specimen; and material changes its flow direction when it approaches the particle due to the high elastic modulus of the particle. A dead metal zone thus forms around the cylindrical surface. Effective strain variations along the center line in the loading direction for different reductions are shown in Fig. 6.12. It is seen that, as the reduction increases, the non-uniformity of strain distribution becomes more severe. The effective stress distribution for both cases, with and without particles, is shown in Fig. 6.13(a), and (b). Again, the overall distributions of the effective stress are quite similar to each other; but stress localization occurs around the particle (Fig. 6.14). A maximum effective stress of around 260 MPa in the particle is reached, which is almost 4 to 5 times larger than that of the matrix. The corner of the particle is a

region of high stress concentration, which implies that the corners are the potential crack initiation sites. This prediction is consistent with the phenomenon of corner fracture of a sharp particle observed in microstructure during extrusion (see Fig. 7.5). Mean stress distributions in the deformation zone of the matrix for both cases show that compressive stresses prevail during compression, except in the bulge zone, where a tensile hoop stress exists which might lead to surface cracks at the bulge surface under some conditions (Fig. 6.15(a) and (b)). The mean stress distributions in both the matrix around the particle and in the particle are shown in Fig. 6.16, in which a tensile stress component (positive value) appears in the upper and the bottom zone in the particle.

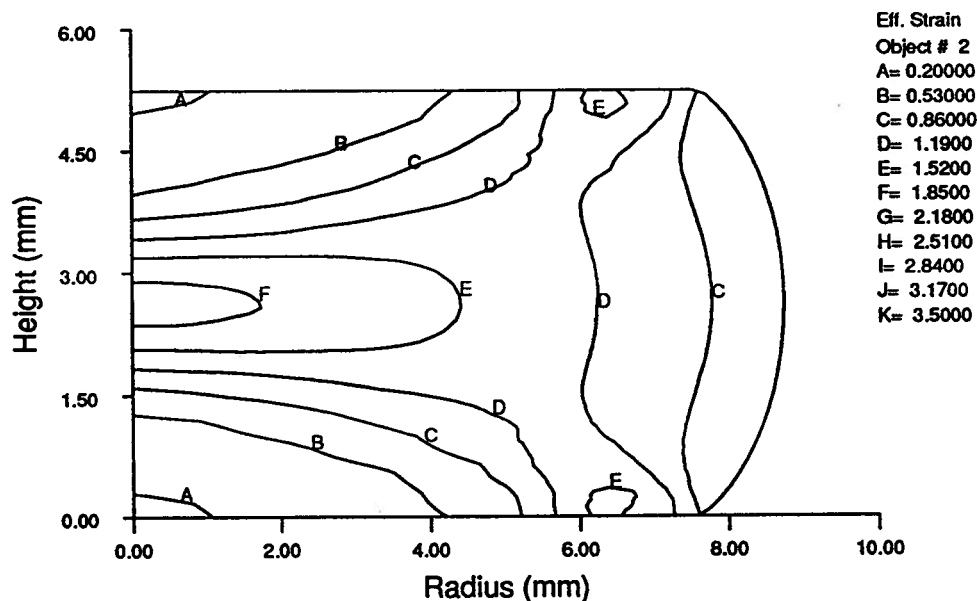


Figure 6.10 Effective strain distribution in the cylindrical specimen
at a reduction of 65%: (a) monolithic

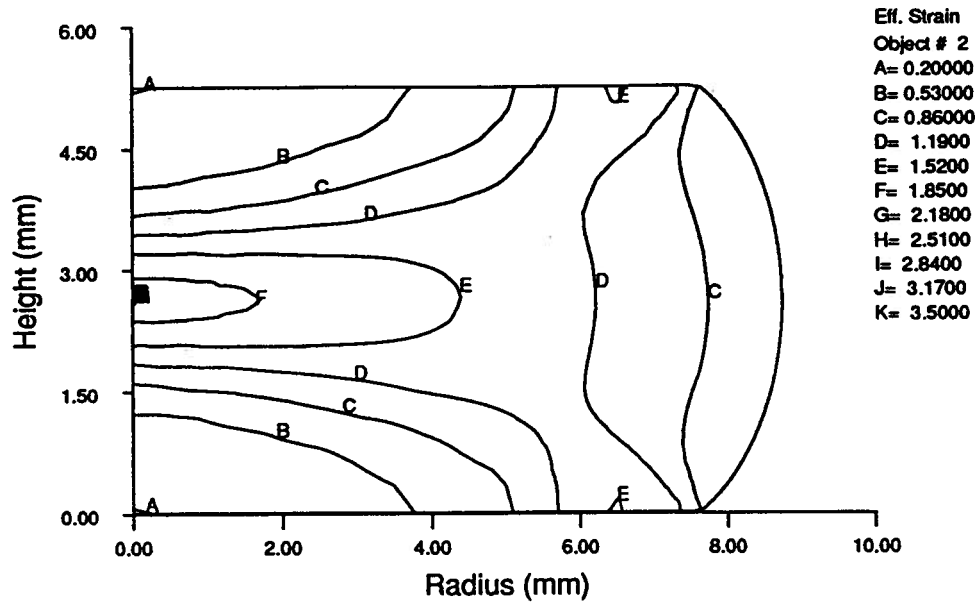


Figure 6.10 Effective strain distribution in the cylindrical specimen at a reduction of 65%: (b) with a particle

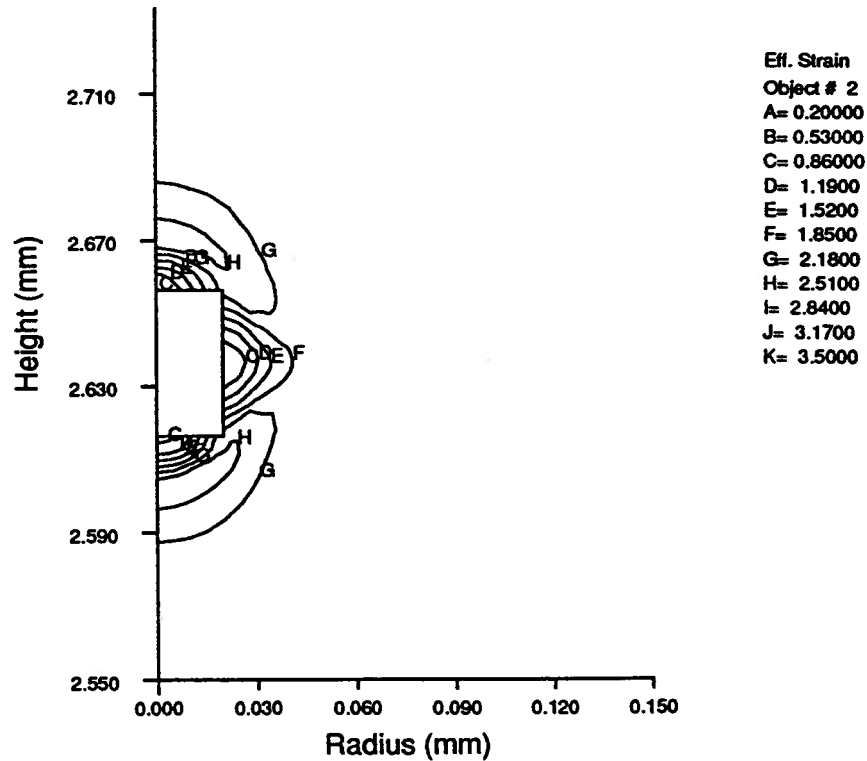


Figure 6.11 Effective strain distribution around the particle at a reduction of 65%

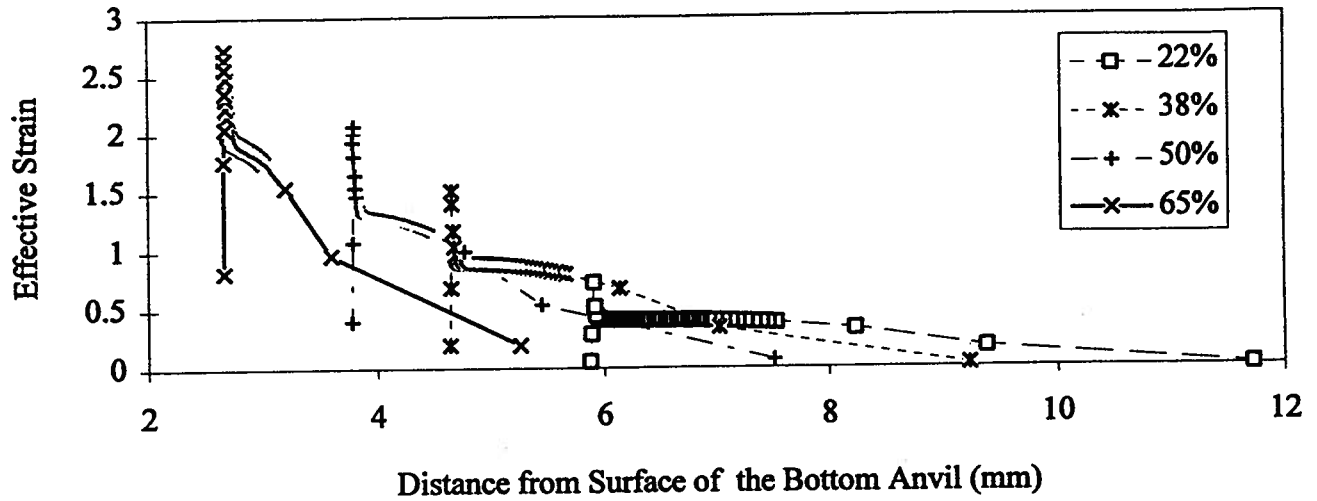


Figure 6.12 Effective strain distribution along the center line of the specimen under different reductions

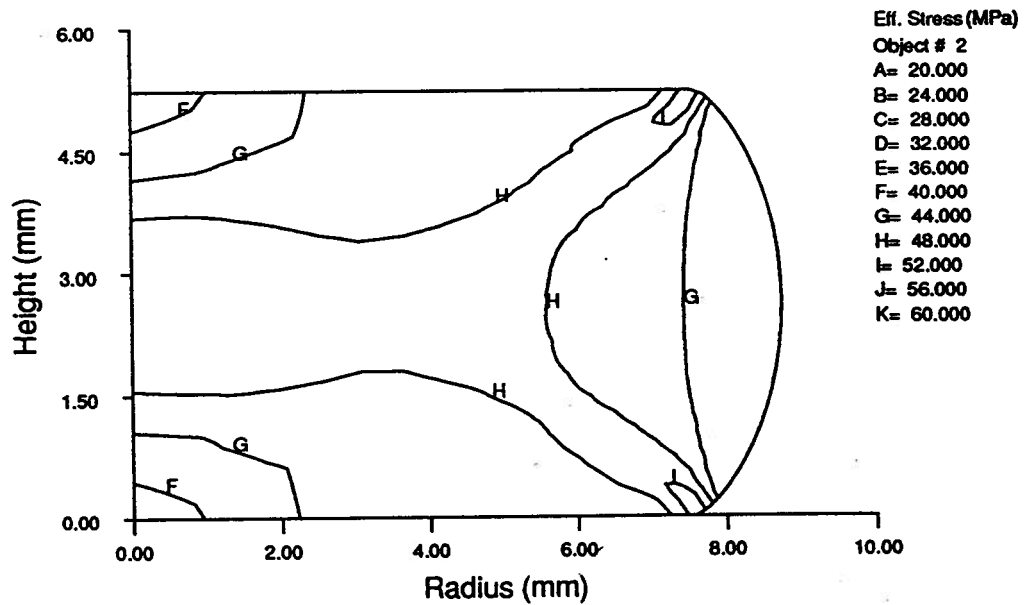


Figure 6.13 Effective stress distribution in the cylindrical specimen at a reduction of 65%: (a) monolithic without a particle

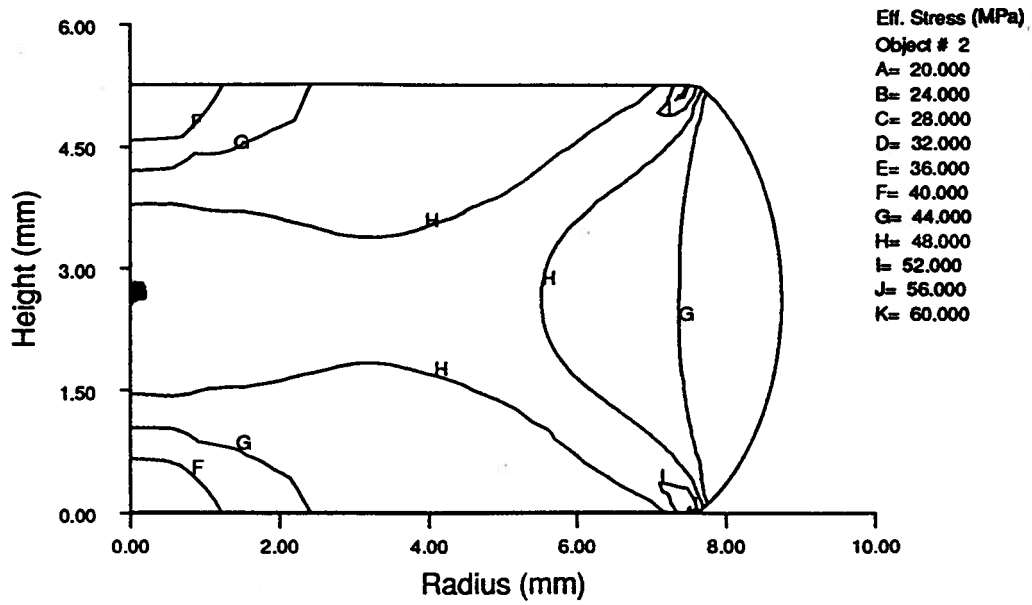


Figure 6.13 Effective stress distribution in the cylindrical specimen at a reduction of 65%: (b) with a particle

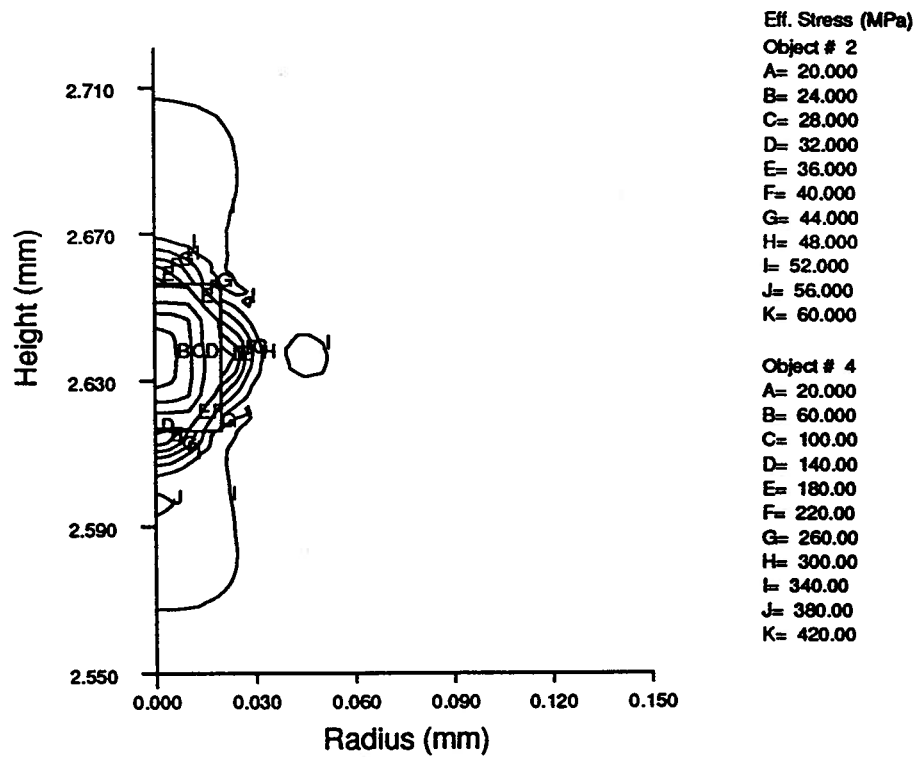
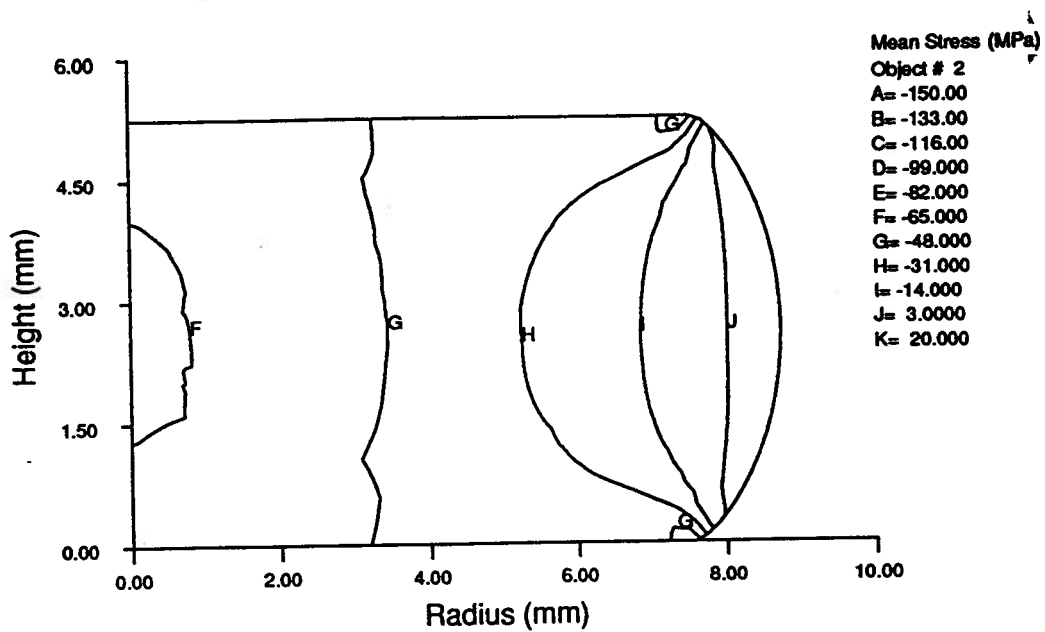
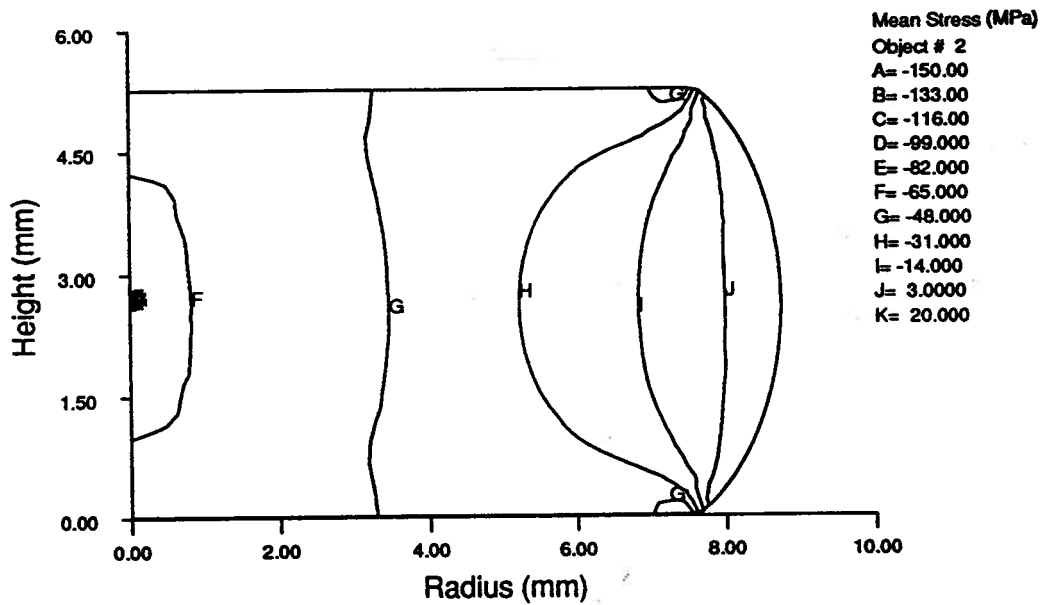


Figure 6.14 Effective stress both in the matrix and in the particle at a reduction of 65%



(a) monolithic without a particle



(b) with a particle

Figure 6.15 Mean stress distribution in the cylindrical specimen with and without a particle at a reduction of 65%

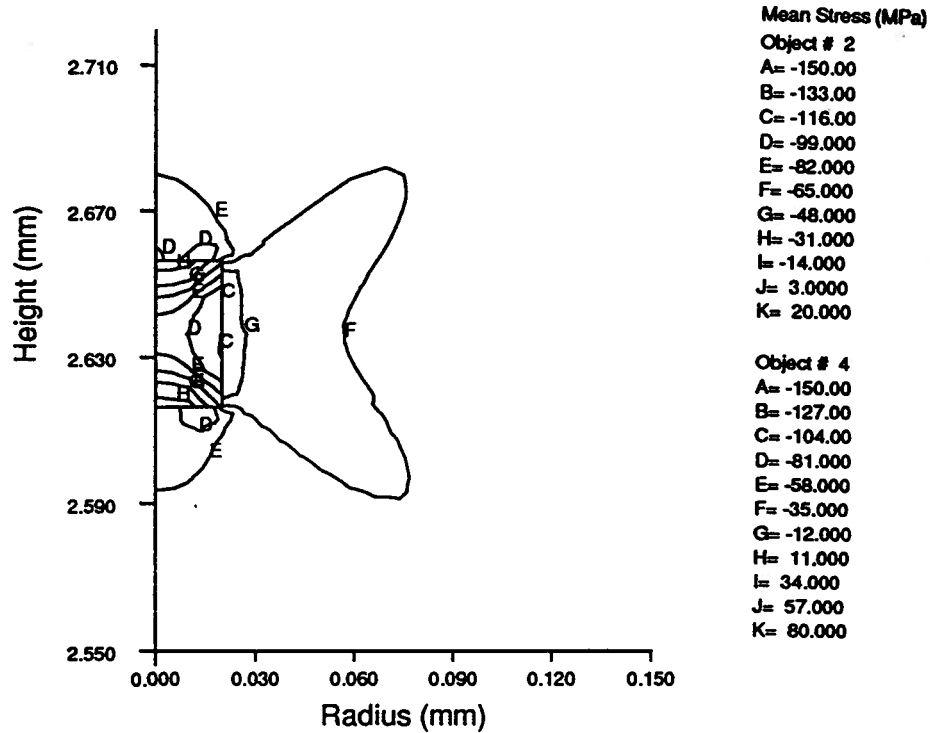


Figure 6.16 Mean stress distribution both in the matrix and in the particle at a reduction of 65%

6.3.1.2 Effect of Particle Shape

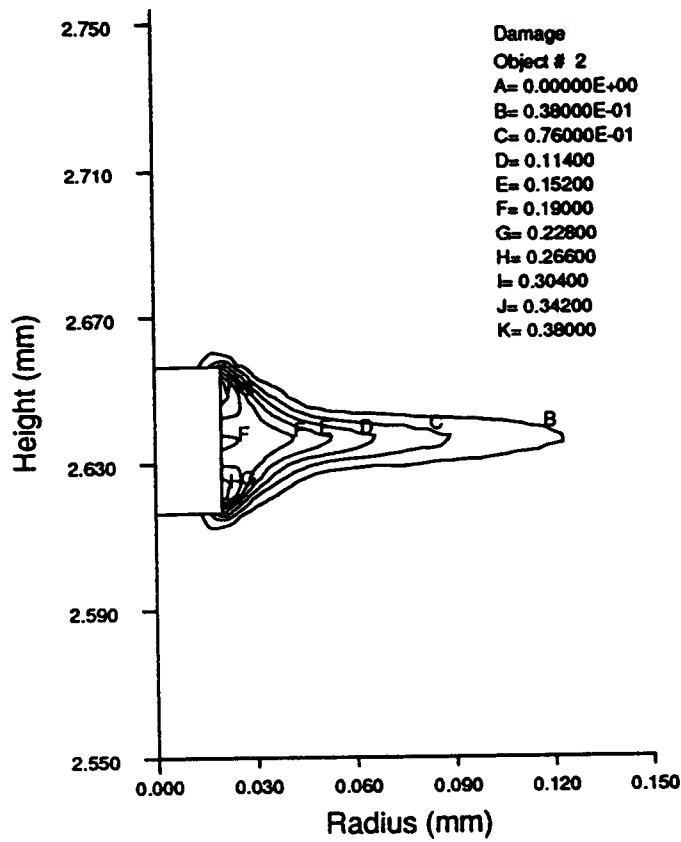
Different particle shapes were analyzed during the compression test, as listed in Table 6.3. A damage factor was modified based on the *plastic work fracture criterion* proposed by Latham and Cockcroft^[51], and was used to compare the effect of particle shape on the stress and strain state at a reduction of 65% during compression (Fig. 6.17)(a)-(d)).

$$D_f = \int \left(\frac{\sigma_1}{\bar{\sigma}} \right) d\bar{\epsilon} \quad (6.1)$$

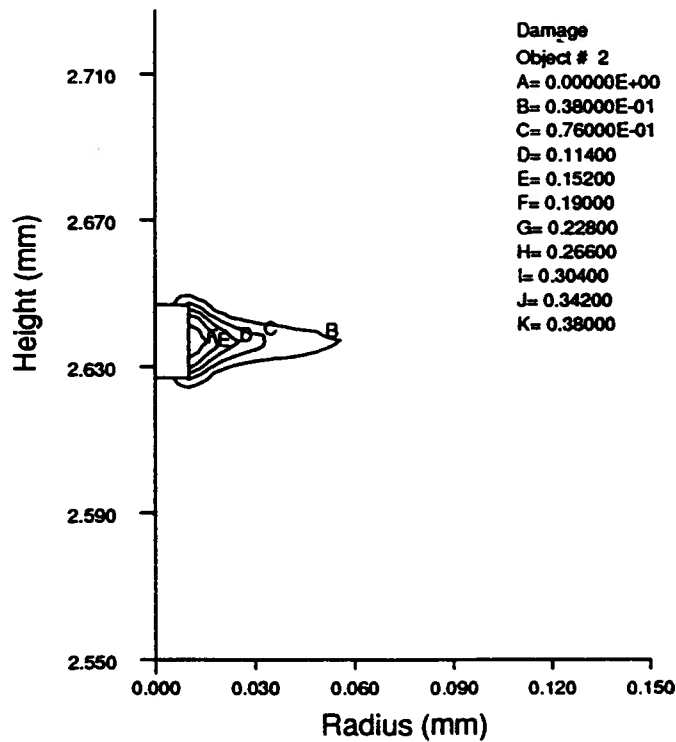
where σ_1 is the maximum principal tensile stress, $\bar{\sigma}$ is the effective stress, and $d\bar{\epsilon}$ is the effective strain increment. As described in the literature review, in cold forming operations, it was found that failure of a monolithic material at some point occurs when the damage factor reaches a critical value. This criterion, together with finite element modeling, has been used

extensively to predict the occurrence of damage during cold forming^[49,109]. Sellars *et al.*^[49] tested the above equation and concluded that the equation could be a reasonable criterion for hot working as well as for cold working, but further data is required to test it more rigorously for hot working. By comparing the above fracture criterion to both the *Stress Criterion* and the *Strain Criterion* described in the literature review, Syu and Ghosh^[112] confirmed that the proposed fracture criterion is the best for the development of forging limit diagrams for particulate reinforced MMCs in laboratory upsetting tests. Figure 6.17 shows that the maximum value of the damage factor near the particle with the an aspect ratio of 4 is about twice as large as that near the spherical particle; a greater value of the damage factor is predicted for the larger cylindrical particle than for the smaller particle. These results indicate that a spherical particle gives rise to the least damage potential in the surrounding matrix material, and non-regular particles, such as the particle with an aspect ratio of 4, have the largest effect. For the equiaxed particles, larger particles have a more severe effect on the matrix damage than the small ones, especially at the corners (Fig. 6.17).

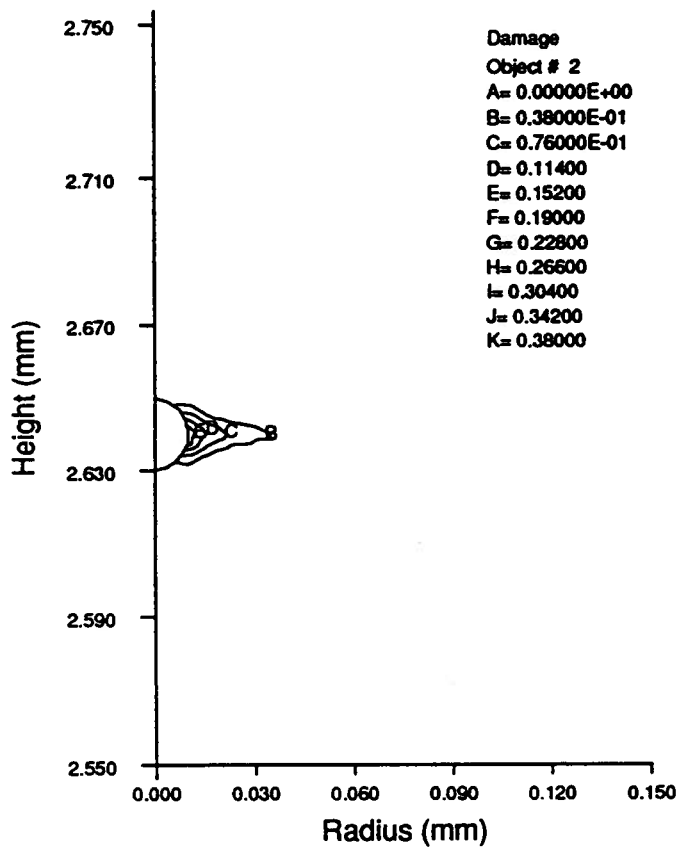
Figure 6.18(a) shows the effect of particle shape on the effective strain variation along the center line near the particle at a reduction of 65%. It is shown again that severe localized strain occurs around all the particles, with the particle of the largest aspect ratio having the highest strain and the spherical particle, the smallest. The effective strain along the horizontal mid-plane is shown in Fig. 6.18(b). It is evident that the strain near the spherical particle is quite uniform compared to the case with no-particle. However, a significant strain drop was predicted in the radial direction near the interface of particles of $\Phi 20 \times 80 \mu\text{m}$ and $\Phi 40 \times 40 \mu\text{m}$.



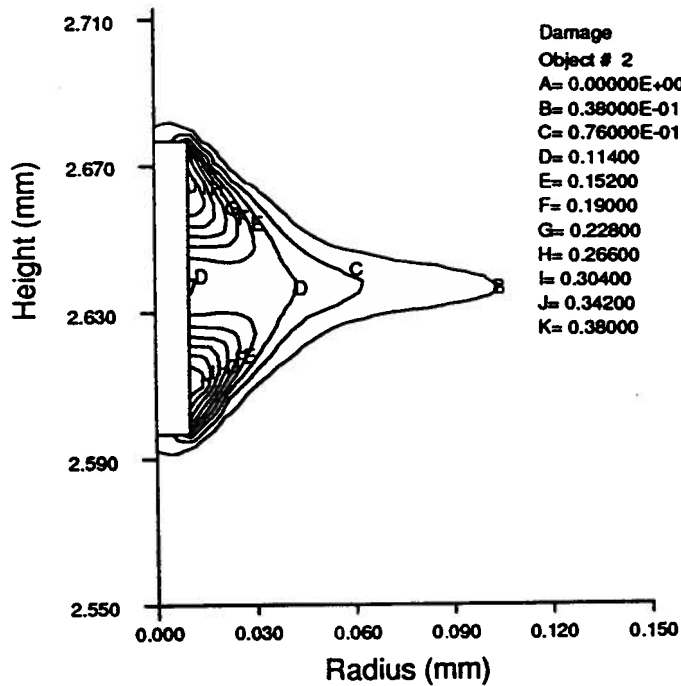
(a) $\Phi 40 \times 40$ (cylinder)



(b) $\Phi 20 \times 20$ (cylinder)

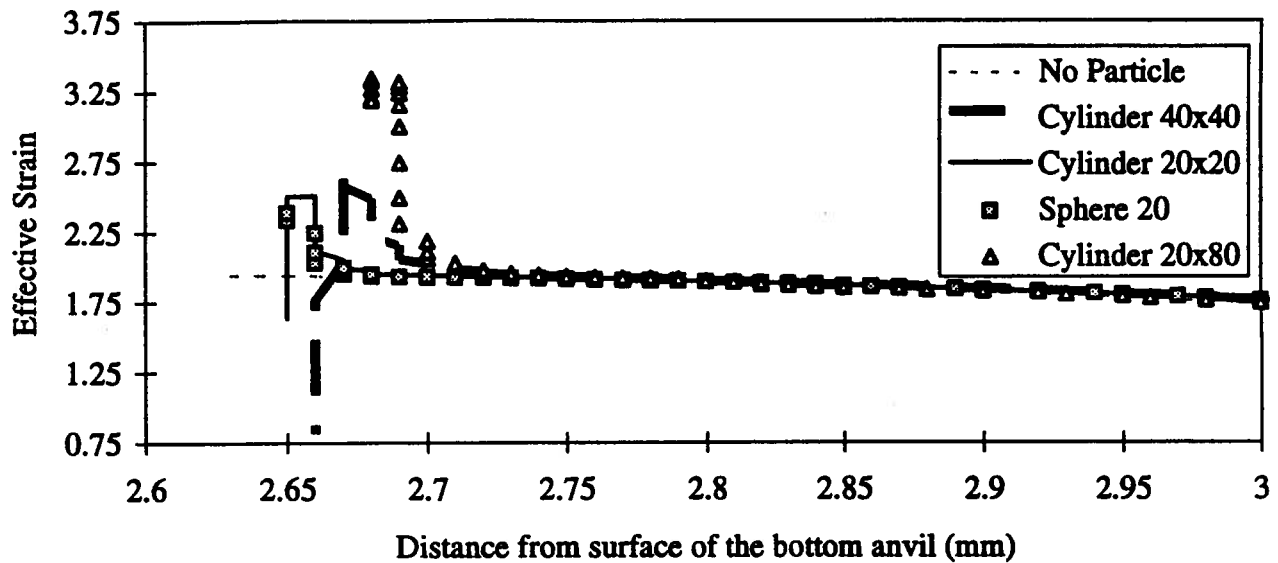


(c) $\Phi 20$ (sphere)

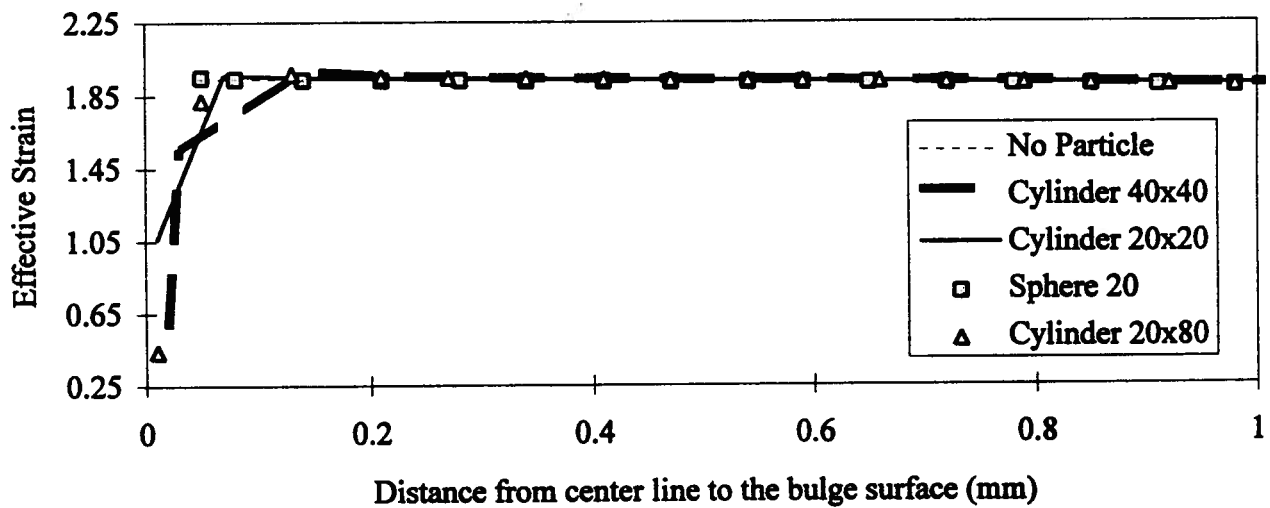


(d) $\Phi 20 \times 80$ (cylinder)

Figure 6.17 Effect of particle shape on damage factor at a reduction of 65%



(a) along the center line of the specimen (40x40 etc are the particle size in microns)



(b) along the mid-plane in radial direction (40x40 etc are the particle size in microns)

Figure 6.18 Effect of particle shape on strain distribution at a reduction of 65%

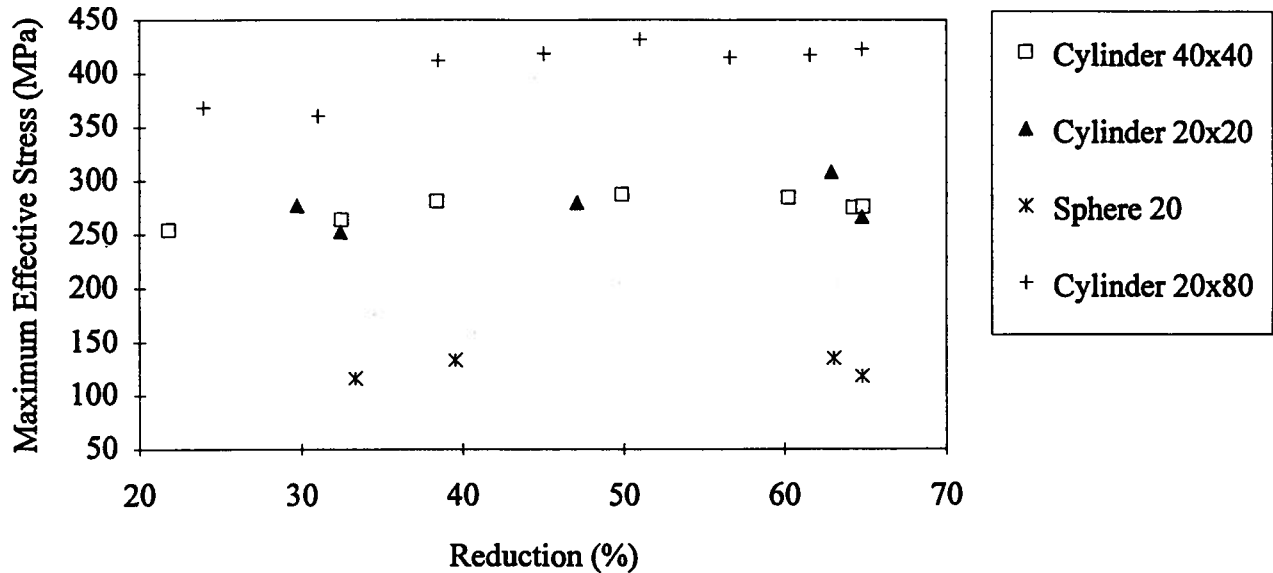


Figure 6.19 Effect of particle shape on effective stress variation during compression (40x40, 20x20, 20, and 20x80 are all the particle sizes analyzed in microns)

The effective stress in the particle is not so sensitive to the reduction for all the four particle shapes, as shown in Fig. 6.19; however, the particle shape itself affects the stress value quite significantly, from about 125MPa for the spherical particle ('Sphere 20 μ m'), to 425MPa for the highest aspect ratio particle ('Cylinder 20x80 μ m' in Fig. 6.19). The values for the cylindrical particles with an aspect ratio of unity are quite close. Therefore, it is concluded that the particle fracture is sensitive to the shape of particles, especially for those with a larger aspect ratio, while the size of equiaxed particles is less important.

6.3.2 Multiple Particle Model

The characterization of single particle behavior during cylindrical compression might only apply to the situation in which particles are separated by a large distance relative to their

size. However, for the particulate reinforced MMCs fabricated by a cast route, particle aggregations, or clusters, are always present. Therefore, a multiple particle model is needed, in which twin cylindrical particles with a particle size of $\Phi 40 \times 40$ located at the center line of the compression specimen were studied.

6.3.2.1 Effect of Reduction

Particle spacing changes during compression, as predicted in plane strain compression in Section 6.2. For a starting particle spacing of 120 μm in the center line, the effective strain distribution is relatively uniform at a reduction of 33%, and its characteristics are quite similar to that of a single particle model (Fig. 6.20(a)). However, at a reduction of 65%, deformation around the particle becomes more severe. A localized strain zone extends in the radial direction as a result of material flow (Fig. 6.20(b)). The maximum value around the particle is larger for the twin-particle case than that for the single particle, which indicates that more severe deformation occurs for the multi-particle situation. The mean stress distribution in each particle at a reduction of 33% (Fig. 6.21(a)), also shows similarity to the single particle model (Fig. 6.11) due to the large spacing, although the values of stress are different. The mean stress distribution around the particle under this reduction is relatively uniform at a level of -12 MPa to -44 MPa. At a reduction of 65% (Fig. 6.21(b)), the value of the mean stress changes from -44 MPa to -300 MPa; also a large mean stress gradient appears in the gap between the two particles, which implies a complex tri-axial stress state.

6.3.2.2 Effect of Particle Spacing

Three different initial particle spacings of 20, 40, and 120 μm were studied. The effect of particle spacing on strain values along the center line of the specimen are shown in Fig. 6.22(a). It is seen that the strain reaches a maximum at a point about half a particle size above

the particle, and the maximum values for each spacing are not much different, with the smallest spacing being the largest. The minimum strain value is located at the right top of the particle, with the smallest value for the largest spacing (120 μm). In the zone between two particles, obviously, the larger the spacing, the larger the strain. This is because for large spacing the matrix deformation is increased. Figure 6.22(b) shows the strain distribution along the radial direction in the mid-plane between the two particles. It is seen that a smaller particle spacing (20 μm) leads to less deformation in the gap.

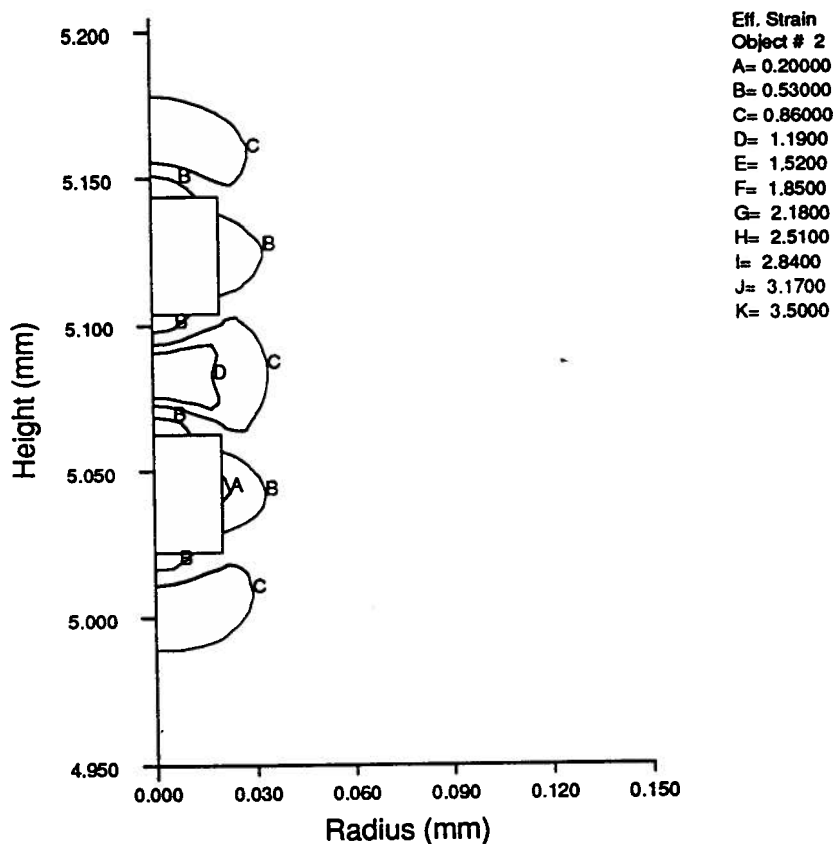


Figure 6.20 Effective strain distribution at different reductions with a starting particle spacing of 120 μm : (a) 33%

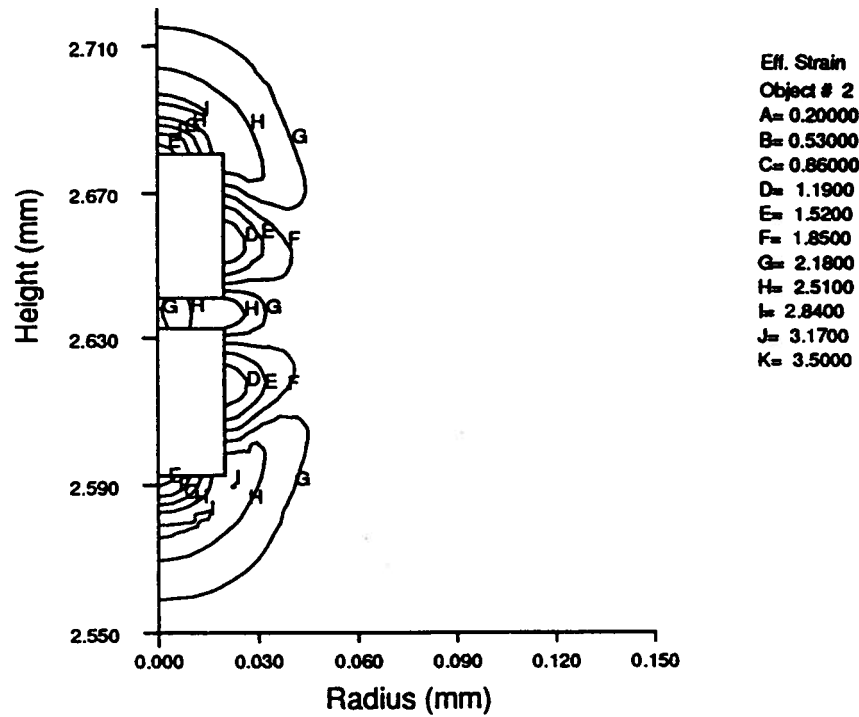


Figure 6.20 Effective strain distribution at different reductions with a starting particle spacing of 120 μm : (b) 65%

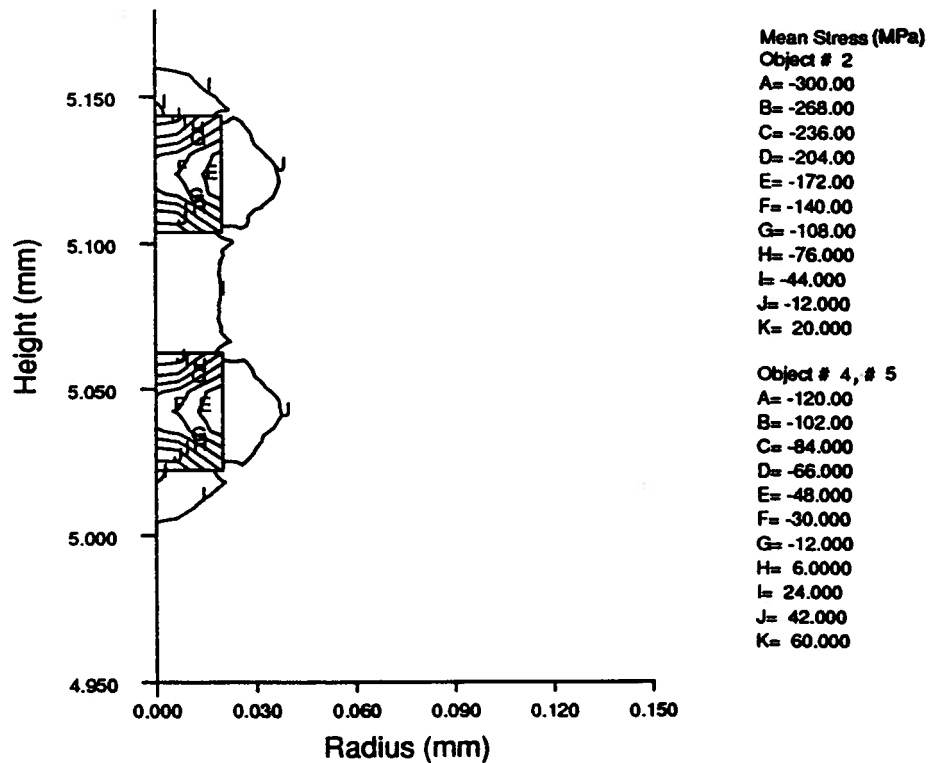


Figure 6.21 Mean stress distribution in the matrix and in the two particles under different reductions with the initial particle spacing of 120 μm : (a) 33%

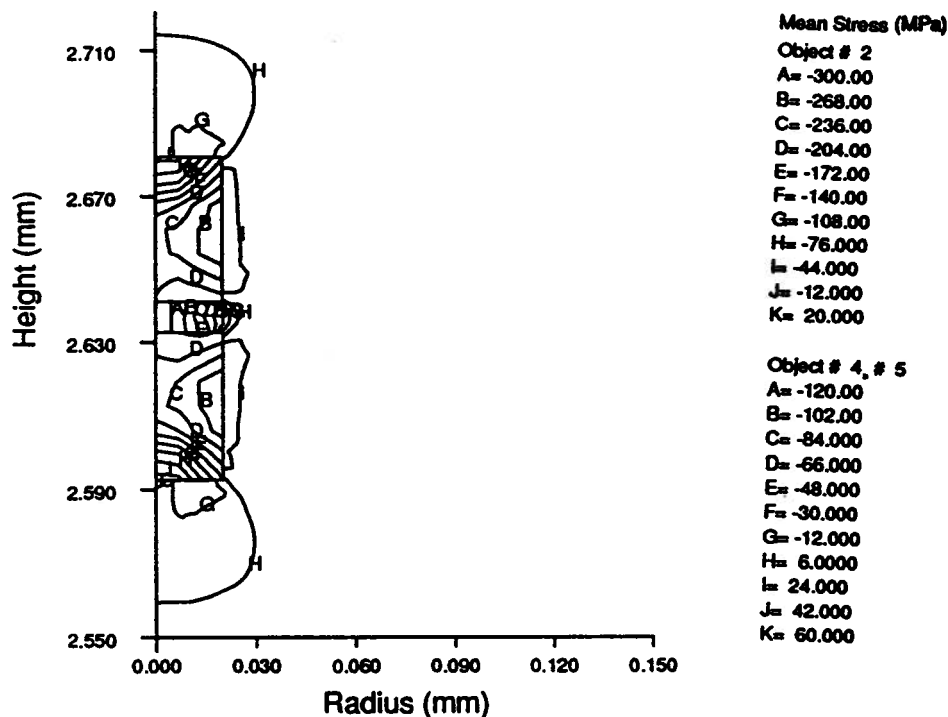
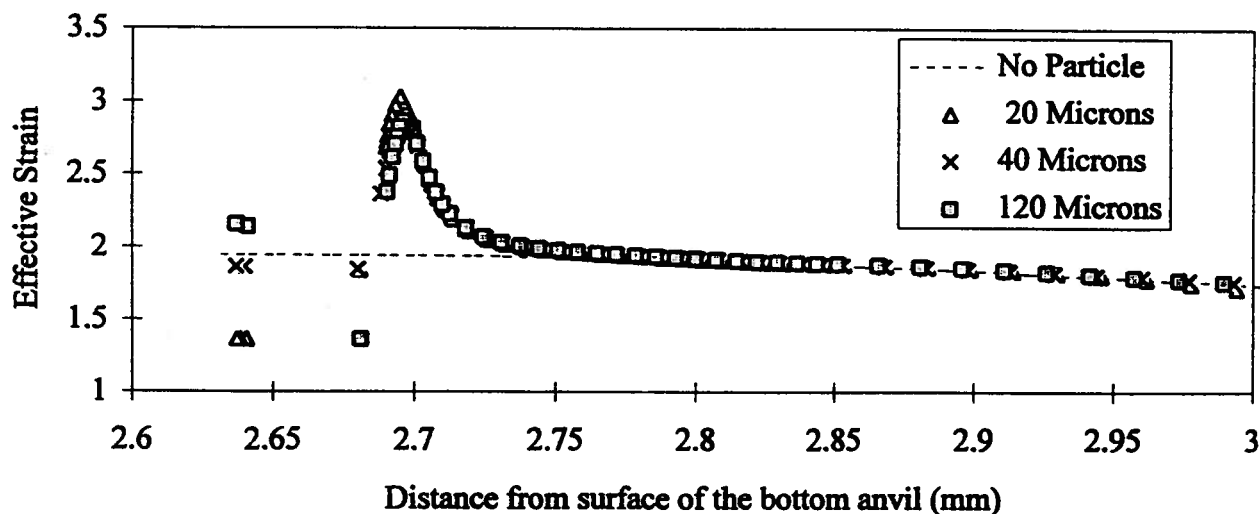
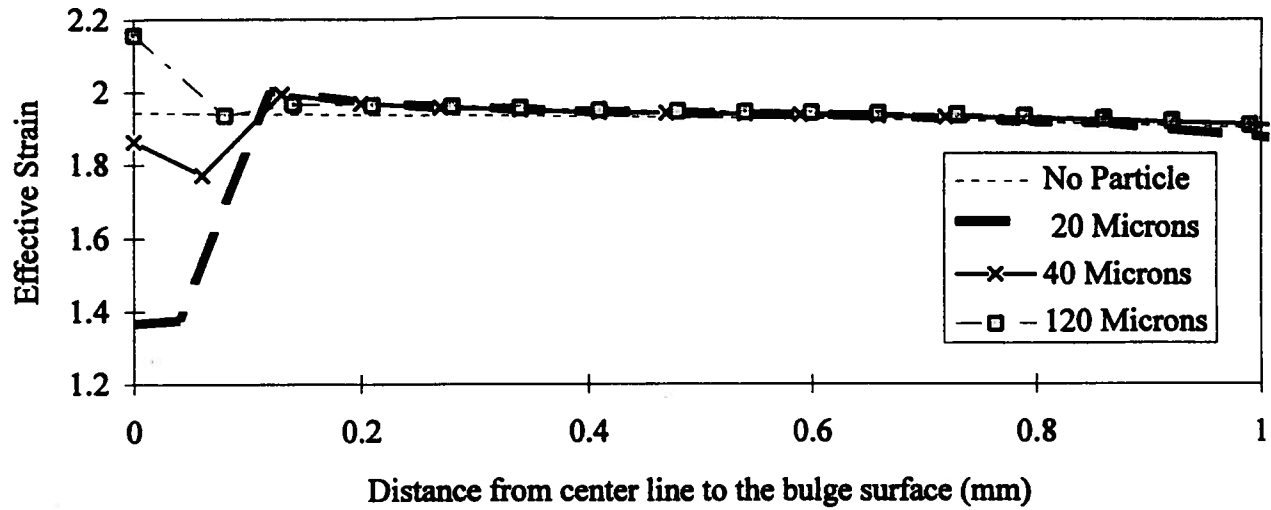


Figure 6.21 Mean stress distribution in the matrix and in the two particles under different reductions with the initial particle spacing of 120 μm : (b) 65%



(a) along the center line of the specimen



(b) along the mid-plane between two particles in radial direction

Figure 6.22 Effect of particle spacing on strain distribution at a reduction of 65%

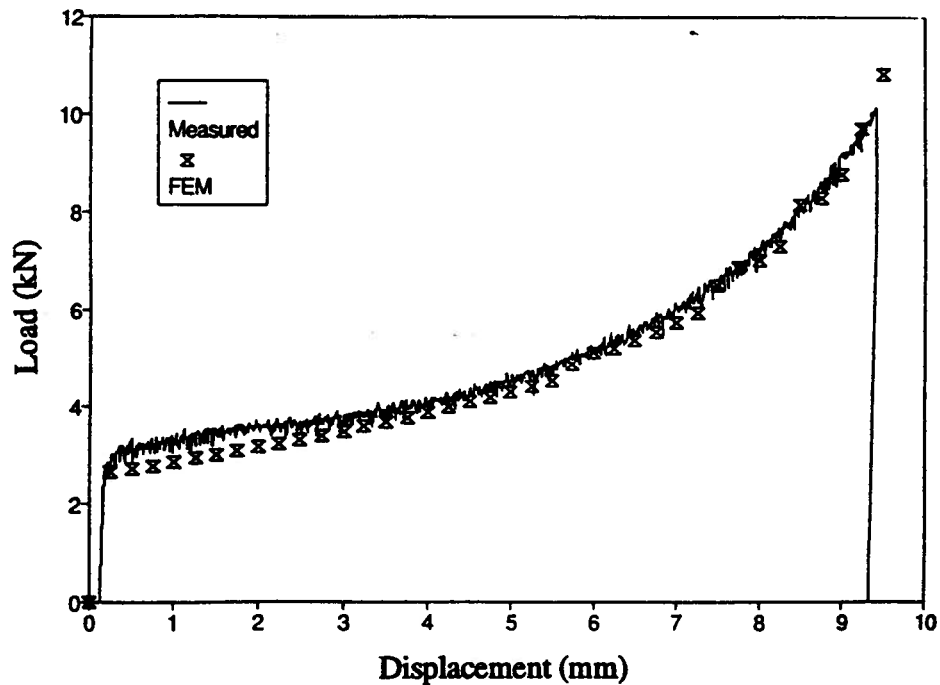


Figure 6.23 Comparison of predicted value with measured data

6.4 Model Validation

For validation of the model predictions, the final geometry of the simulated cylindrical test specimen was measured. Table 6.4 shows the final maximum diameter measured and predicted during compression, which suggests barreling.

Table 6.4 Comparison of model predictions with measured data

Cases	Homogeneous	Single-particle	Twin-particle	Measured
Bulge Dia.(mm)	17.49	17.48	17.48	17.48±0.05

It is seen that the predictions are in very good agreement with the measured data. This can be further validated by comparison of the load-displacement curve for the monolithic model with the measured data (Fig. 6.23).

6.5 Conclusions

Based on the above micromechanical analysis, some conclusions can be drawn on particle behavior in MMCs during large hot deformation.

1) Large deformation leads to more severe localized deformation around the particle, and also to particle rotation and migration. The particle migration during large deformation helps break clusters and heal the fractured particles;

2) The stress value in a particle is not very sensitive to strain during hot deformation. Therefore, particle fracture may occur at a very small strain, if the stress in a particle is large enough;

3) The shape of a particle has a large effect on fracture of both the particle and its surrounding matrix under large deformation, and particles with sharp corners and large aspect ratios have the greatest propensity to fracture;

4) Particle fracture is not very sensitive to the size of equiaxed particles; however, it is known that the probability of particle fracture is a function of the probability of finding a flaw in the particle and the probability of activating a flaw. Apparently, larger particles may have a high frequency of flaws. Because this effect has not been considered in this work, it is still true that large particles may have higher probability to fracture during large deformation.

5) Small particle spacing results in a complex stress state in the cluster zone. However, as the particle spacing increases, the interaction between particles decreases. The tensile stress generated in the interparticle zone in the flow direction may cause void formation during deformation or promote void growth if the voids are present while the hydrostatic pressure may help stop void formation and growth.

6) Localized particle deformation does not affect the macroscopic performance of the material. Therefore, a phenomenological constitutive law of the MMCs characterizes the macroscopic behavior of the material.

Chapter 7 PARTICLE FRACTURE OF THE PRMMC DURING EXTRUSION

Commercial exploitation of MMCs is dependent on the reproducibility of properties and achieving high productivity at minimum cost. Thus, controlling the fracture of particles during extrusion of the PRMMCs is of interest. Particle fracture is a potential defect if associated with void formation: notably the modulus of the resultant extrudate could be deleteriously affected. However, if void formation is suppressed, then benefits in terms of mechanical properties may result from the increased homogeneity of particle distribution, and from a decrease in particle size.

The fracture of particles during cold deformation has been extensively investigated over the past few years^[77-78,89-95] but the systematic examination of fracture during hot deformation has received little attention. Furthermore, deformation to high strain at low temperature has been limited by the low failure strain of the MMCs. Therefore, there are features of low temperature deformation which are expected to relate to deformation under conditions characteristic of extrusion. Particle fracture occurs owing to the inability of the material to accommodate local stresses. Fracture at low temperature is related to strain, particle size, particle aspect ratio^[75,76] (see also Section 8.2 for the micromechanical analysis) and volume fraction^[93]. The superimposed hydrostatic pressure during deformation extends the ductility, and effectively inhibits void formation^[11,90-91]. Under such circumstances matrix material may also flow into the voids between fractured particles under large deformation.

To elucidate the nature of particle fracture during the hot extrusion process, the microstructure of the composite in the deformation zone and of the extrudates of

6061/Al₂O₃/10p and 6061/Al₂O₃/20p was examined, i.e., particle distribution, size refinement, and orientation and migration of particles were characterized.

7.1 Specimen Preparation for the PRMMCs

A specimen of area about 10x10 mm² was cut using either a hack saw, or a TiV cutting wheel blade. The specimen was mounted and polished in an automatic polishing machine. The detailed polishing procedure adopted at KRDC, Kingston, is listed in Table 7.1.

Table 7.1 Polishing procedure for Duralcan materials at KRDC

Step	Paper/Cloth	Grit Size (μm)	Time (min.)	Lubricant	Load (N)	Remark
1	SiC paper	Grit 120	until flat	water	100	flat
2	Petrodisk Diamond plate	15	10	Struer's blue lubricant	80- 100	flat with less scratches
3	Perforated cloth	15	10-15	Struer's blue lubricant	100	more shinny
4	Perforated cloth	3	10	Struer's blue lubricant	100	less scratches
5	Pan W polishing cloth	3	5	Struer's red lubricant	100	very few scratches
6	OP Chem. final polishing cloth	0.05	1-2	Colloidal SiO ₂ suspension	100	clean boundary around particles

Another polishing procedure modified from Newell^[100] was adopted for the automatic polishing machine at UBC, as listed at Table 7.2. A very clean background resulted following polishing for both procedures, which was necessary for microstructural analysis, especially

image analysis. The last step was quite effective to clean the boundaries between the matrix and the particles.

Table 7.2 Polishing procedure used at UBC for Duralcan materials

Step	Paper/Cloth	Grit Size (μm)	Time (min.)	Lubricant	Pressure (psi)	Remark
1	SiC Paper	180	3	Water	30	overall flat
2	SiC Paper	320	3	Water	30	flat
3	SiC Paper	500	3	Water	30	flat with less scratches
4	SiC Paper	1000	3	Water	30	less scratches
5	Texture Paper	6 μm	10	Diamond suspension	30	few scratches
6	Texture Paper	3 μm	5	DP-suspension	30	very few scratches
7	OP Chem. final polishing cloth	0.05 μm	1-2	Colloidal SiO ₂ suspension	30	clean boundary around particles

7.2 Macroscopic Examination of Metal Flow in the Deformation Zone

Macro-examination of metal products can reveal the grain size and shape as well as fabricating or casting defects. An end-of-extrusion billet of 6061/Al₂O₃/20p from the trial of S92-3, 184 mm in diameter, was sectioned by a hacksaw along the extrusion direction. The extrusion conditions are listed in Table 7.3 for convenience.

Mixed-acid etchants are excellent for revealing grain size, shape, and contrast. The etchant used for the composite was a mixed solution of 10ml HCl (concentrated), 30ml HNO₃ (concentrated), 20ml H₂O, and 5g FeCl₃^[96]. The solution was mixed just before use. The

longitudinal section of the billet was first ground on SiC paper (Grit 60 - 600), and then was immersed at room temperature into the solution for a few seconds, rinsed in cold water, and repeated until the desired effect was obtained, as shown in Fig. 7.1.

Table 7.3 Extrusion conditions of the Trial S92-3 of 6061/Al₂O₃/20p

Billet Temperature (°C)	429
Billet Diameter (mm)	178
Extrudate Diameter (mm)	32
Extrusion Ratio	33.6

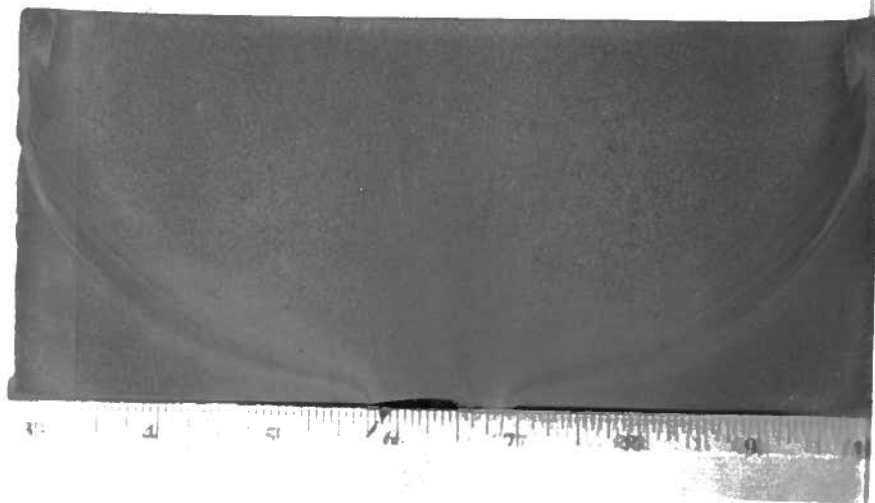


Figure 7.1 Metal flow of a billet in a container

A dead metal zone existed at the corner between the die and the container, and a shear zone showed up between the dead metal zone and the deformation zone. The accumulation of the metal at the corner of the pressure pad and the container was probably due to the sticking friction at the container interface. Some porosity was also observed at the etched surface.

More detailed metal flow of the billet was examined by an optical microscope with a magnification of 50X. The zones examined in the billet are schematically shown in Fig. 7.2.

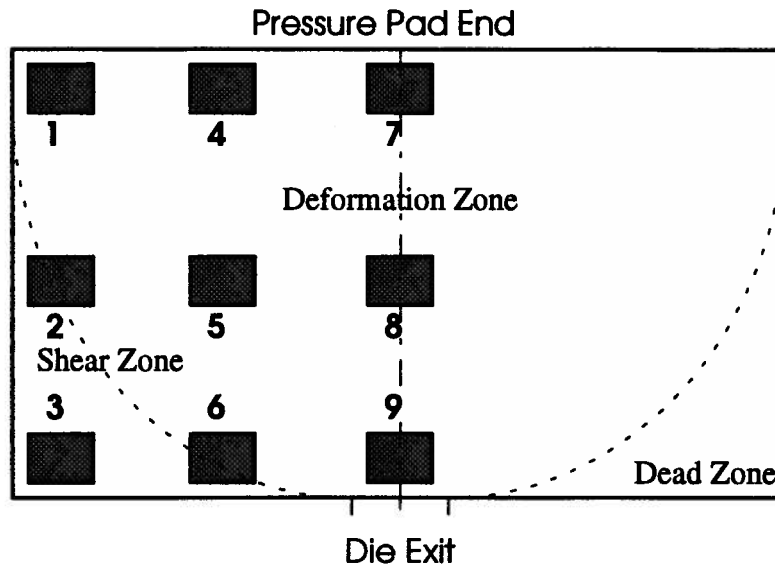


Figure 7.2 Schematic positions for the pictures taken with low magnification

The metal flow at each location is shown in Fig. 7.3. At Location 1, the matrix material has accumulated due to sticking friction at the interface between the billet and the container. A localized material flow pattern near the gap between the pressure pad and the container is revealed in Fig. 7.3 (Location 1).

At Location 2, in the shear zone, the metal flow along the shear boundary is clearly shown. However, in the dead metal zone there is little metal flow (Location 3). At Location 4, only a small tendency of metal flow in the downward direction can be seen. Metal flow lines are clearer in Location 5, in the deformation zone; here the flow lines approach the horizontal direction near the die interface (Location 6). At the center line of the deformation zone, due to axisymmetry, metal flows close to the extrusion direction, and the tendency increases from under the pressure pad (Location 7) to the die entry (Location 9). At Locations 4 and 7, under the pressure pad, a hard-to-deform zone exists.

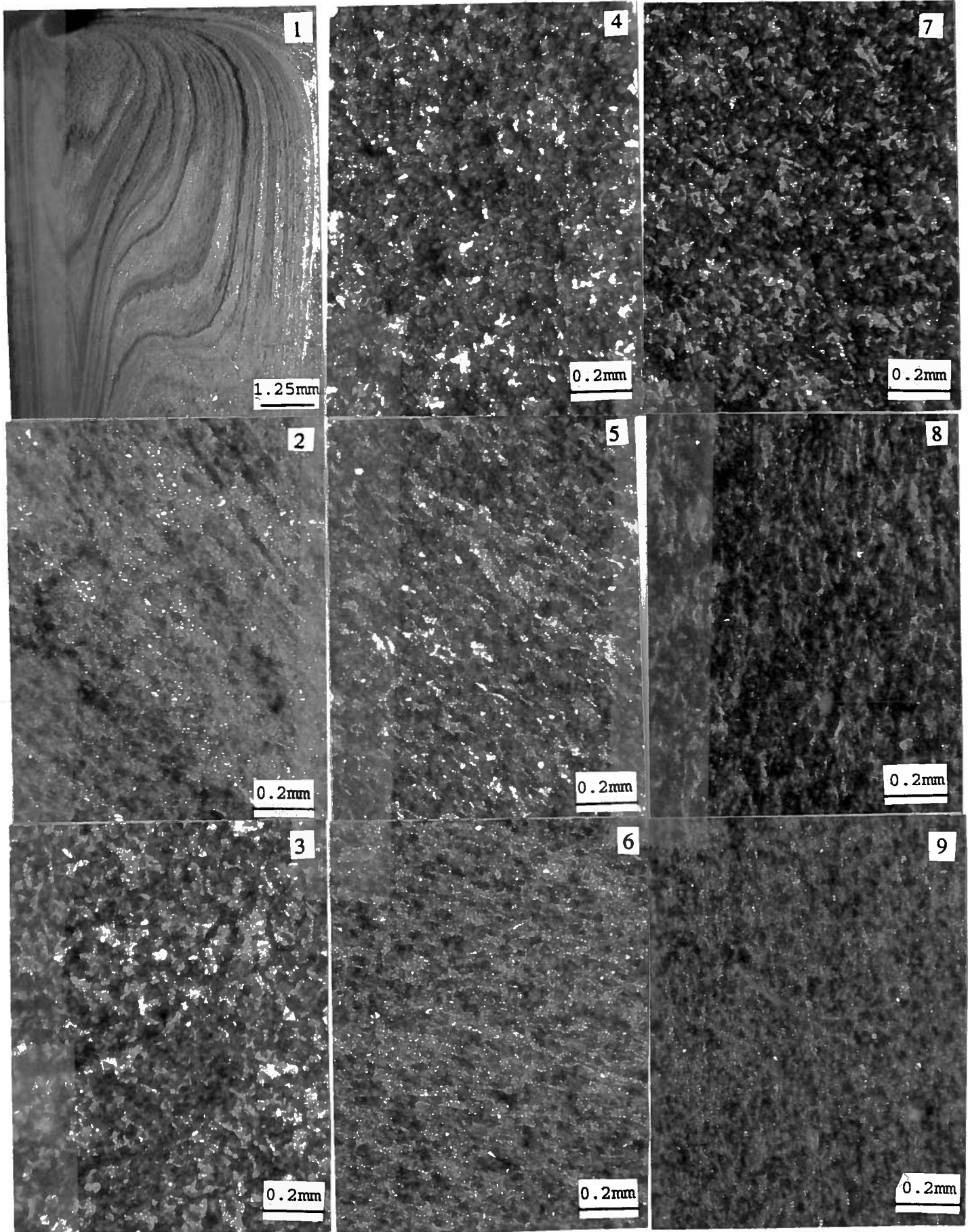


Figure 7.3 Metal flow in the deformation zone during extrusion

The metal flow pattern shown here is consistent with experimental observation by other researchers^[121], and also, qualitatively, with the velocity vector distribution of the FEM model prediction in Chapter 5.

7.3 Particle Fracture during Extrusion

A microscopic study of particle fracture and particle distribution was conducted both qualitatively, using an optical microscope, and quantitatively using an image analyzer. The dynamic behavior, such as recovery and recrystallization, which occurs in the hot extrusion process, is beyond the scope of this project.

7.3.1 Qualitative Microstructure Analysis

7.3.1.1 Particle Deformation Behavior in the Deformation Zone

The other half of the butt-end was divided into several small sections on a cutting machine with a Ti-V wheel blade, and 9 samples from the longitudinal section, with an area of about $10 \times 10 \text{ mm}^2$, were polished at UBC for micro-examination. The location of the 9 samples in the billets inside the container are schematically shown in Fig. 7.4.

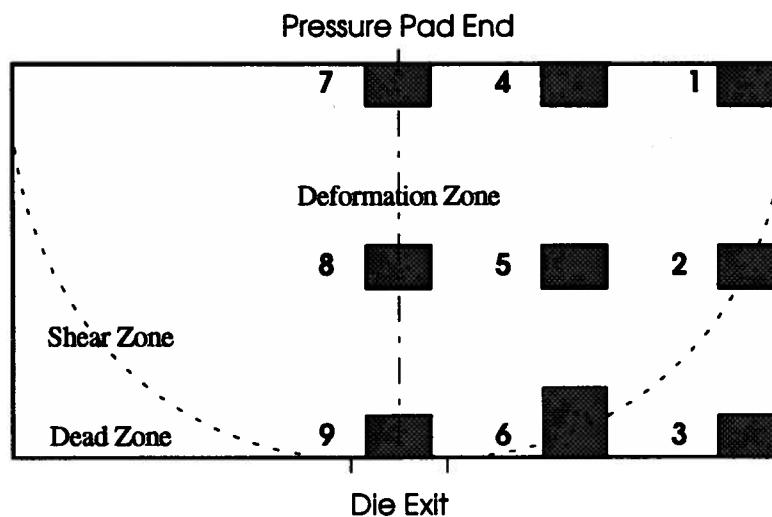


Figure 7.4 Schematic positions for the pictures taken for micro examination

The particle distribution and particle fracture behavior for each sample, located in different zones, was investigated under an optical microscope. At Location 1, the upper right corner of the billet where there is contact with the pressure pad and the container, a "particle-free" zone (with a small number of particles) was formed (see Figs. 7.1 and 7.3). This is the result of accumulation of the matrix material near the gap between the pressure pad and the container: during extrusion, as the pressure pad pushes the billet forward, the matrix material adheres to the container, while the particles in the subcutaneous layer of the billet were pushed forward. As a result, matrix material accumulated at the corner. Very few particles were trapped in this 'particle-free' zone. Beside this large 'particle-free' zone, more particles were found but still with lower local volume fraction compared to other locations, as shown in Location 1, Fig. 7.5(a).

Roughly a 1-mm thick particle-free layer at the billet surface was observed at Location 2 ($r = R_0$). The formation of this layer was again a result of adhesion with the container. At the intersection of the shear boundary and the container interface (See Fig. 7.1), part of this layer began to flow into the shear zone along the shear boundary to form a particle-free band during extrusion. It is this particle-free band that outlined the dead metal zone in the macroetched butt-end (Fig. 7.1). In the adjacent zone, severe particle fracture was evident due to large shear deformation (Location 2, Fig. 7.5 (a)). Most of the particles were orientated along the shear direction. All the large particles that did not crack were found to have a regular shape with an aspect ratio close to unity, which implies that equiaxed particles are harder to fracture even with a larger diameter(Location 2, Fig. 7.5 (a)). This result confirms the predictions of the effect of particle shape on particle fracture in the micromechanical analysis in Chapter 6. With a ~1 mm thick particle-free layer being also

present at the billet surface in the dead metal zone (Location 3), a conclusion can be drawn that during hot extrusion of particle reinforced MMCs, a particle-free layer is formed at the interface of the billet and container because of adhesion, and part of the matrix material in this layer flows into the shear zone to form a particle-free band in the shear direction. In the dead metal zone, all the particles were distributed with no preferred orientation and had a similar spatial distribution to those in the as-cast composites. Fractured particles were occasionally observed but not separated as in the shear deformation zone, i.e., the particles were just cracked (Location 3, Fig. 7.5(a)).

Mid-way between the container interface and the center line of the billet ($r \approx R_0/2$) under the pressure pad (Location 4), it was observed that fewer particles were fractured due to formation of the 'hard-to-deform' zone, and particle clusters also remained (Location 4, Fig. 7.5(b)). Fewer clusters, but more fractured particles, were observed in the region below the 'hard-to-deform' region, as deformation increased. Particles were orientated towards the direction of metal flow (No. 5, Fig. 7.5(b)). At Location 6, which included both a part of the deformation zone and a part of the dead metal zone, a 'particle-free' band was also observed in the shear zone with more particles present than in the up stream band. Due to the low local volume fraction of the particles in this band, no extensive particle fracture was observed. However, in the adjacent zone, more fractured particles were found due to the large shear deformation, as seen in Location 6, Fig. 7.5 (b). Moreover, particles in the shear zone tended to align in the shear direction.

At the top surface zone around the center line ($r \approx 0$) of the billet (Location 7), some particle clusters remained, as observed at Location 4, with similar particle distribution to the as-cast products. However, fractured particles in clusters were observed occasionally because

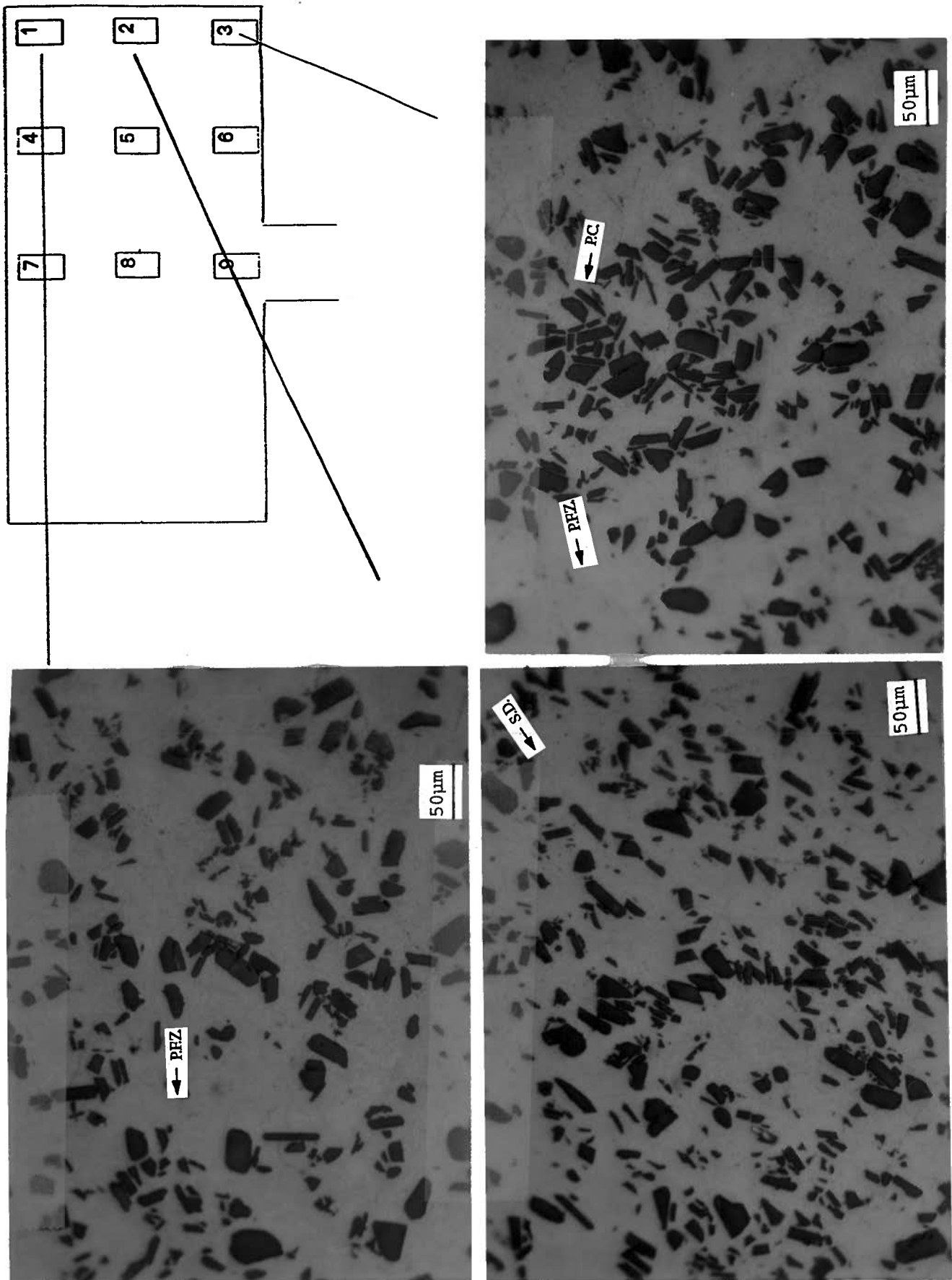


Figure 7.5 (a) Typical particle distribution in the Locations 1, 2 and 3

(‘P.C.’= particle cluster; ‘P.F.Z.’=particle-free zone; ‘P.F.B.’=particle-free band; ‘S.D.’=shear direction)

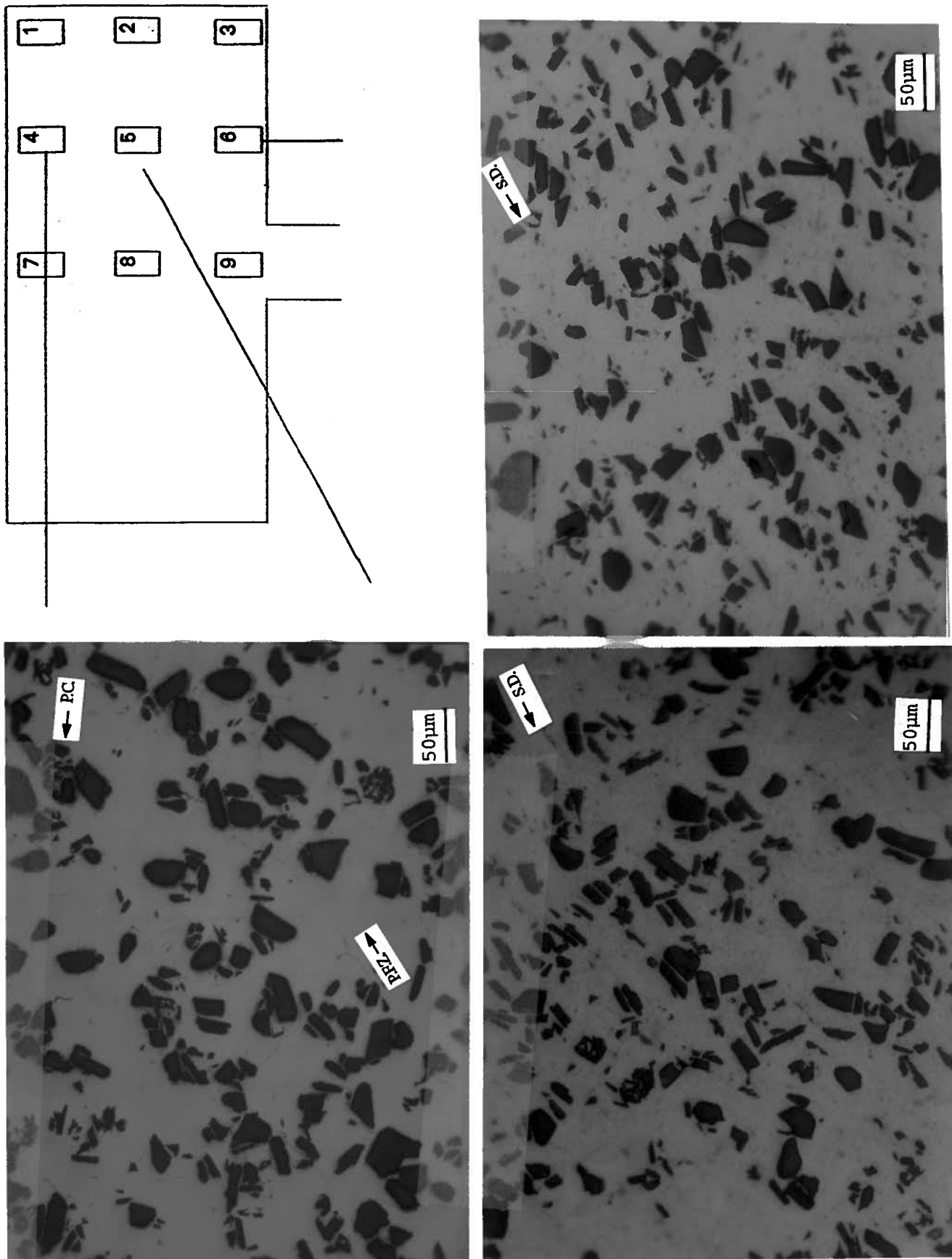


Figure 7.5 (b) Typical particle distribution at the Locations 4, 5 and 6

(‘P.C.’= particle cluster; ‘P.F.Z.’=particle-free zone; ‘P.F.B.’=particle-free band; ‘S.D.’=shear direction)

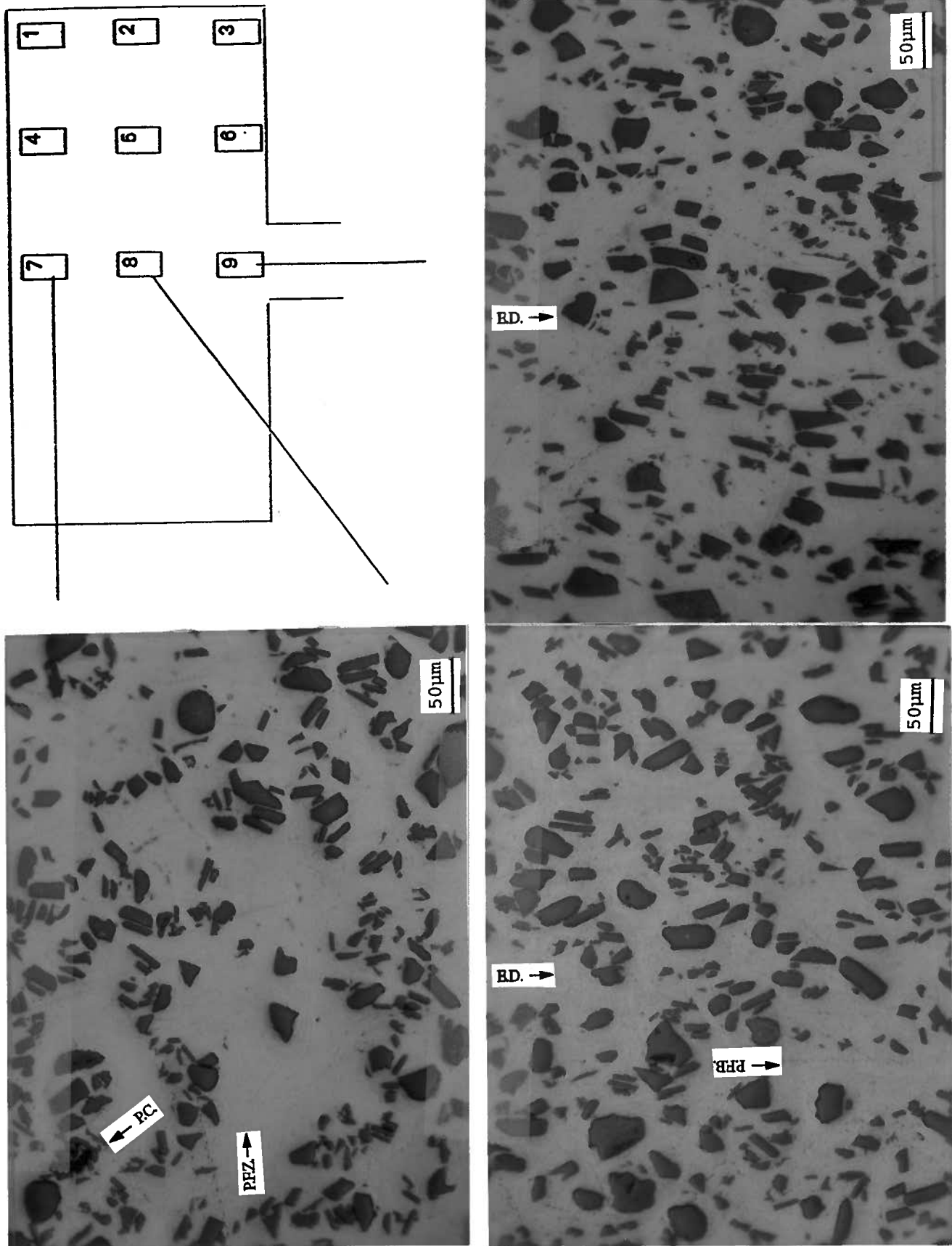


Figure 7.5 (c) Typical particle distribution at the Locations 7, 8 and 9

(‘P.C.’= particle cluster; ‘P.F.Z.’=particle-free zone; ‘P.F.B.’=particle-free band; ‘E.D.’= extrusion direction)

of local tri-axial stresses (Location 7, Fig. 7.5 (c)). The most obvious characteristics at Location 8 were the alignment of the particles and the formation of particle-free bands along the extrusion direction. This is due to axisymmetric material flow which forces particles to align in the extrusion direction and also elongates the particle-free zones in the cast material to form the 'particle-free' bands (Location 8, Fig. 7.6(c)). It was interesting to note that although some cracks in the deformation zone align along the flow direction due to shear stress, other cracks perpendicular to the flow direction were observed, especially for those particles with a large aspect ratio. This is a result of load transfer from the matrix to the particle along the flow direction, which generates tensile stresses in the particle (See Chapter 8). If the tensile stress exceeds the fracture stress of the particle, it cracks perpendicular to the flow direction. Near the center line at the die entry, alignment of particles and particle-free bands along the extrusion direction were even more obvious. However, at positions off the center line, particles were aligned not in the extrusion direction, but in the flow direction. Near the die throat, more small particles were found which implies severe particle fracture due to shear deformation (Location 9, Fig. 7.5(c)).

It is worth pointing out that all the features described above in the deformation zone are a summary of an overall examination of the sample at each location. However, they all could not be shown in one typical picture for each location, as in Fig. 7.5.

7.3.1.2 Microstructure Analysis of the Extrudates

Two samples of each extrudate were cut from both the front end (named "*F*") and the back end (named "*B*"). Caution was taken when each piece was sectioned along the extrusion direction using a Ti-V wheel blade, as shown in Fig. 7.6. All the specimens were polished at UBC following the procedure listed in Table 7.2. The particle distribution in both the

transverse section (perpendicular to the extrusion direction) and the longitudinal section (parallel to the extrusion direction) was examined by an optical microscope. The samples examined are listed in Table 7.4.

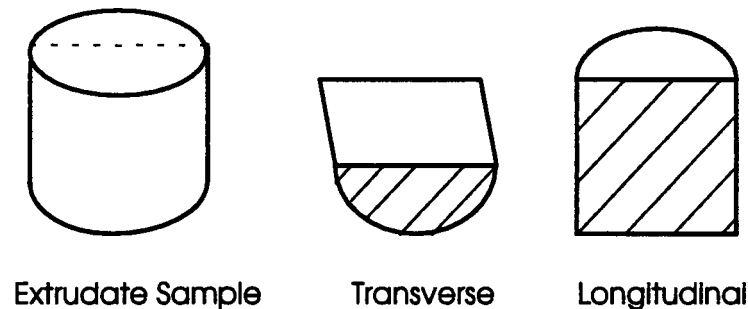


Figure 7.6 Schematic of examined extrudate specimen

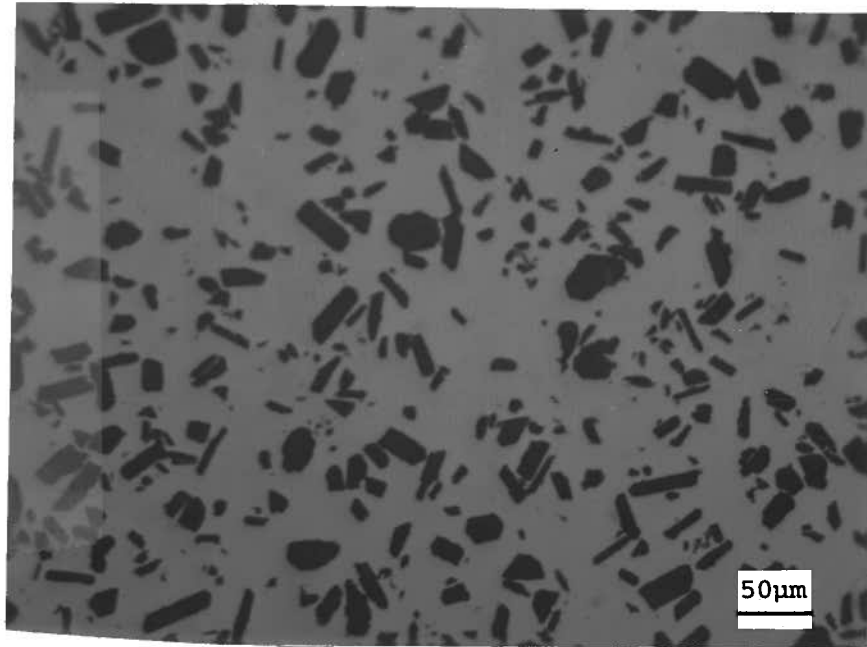
Table 7.4 List of examined extrudates with two different cross-sections

Sample Name	Cross Section	6061 Alloy	6061/Al ₂ O ₃ /20p (W6A20)	6061/Al ₂ O ₃ /10p (W6A10)
Trial No.		S92-2	S92-3	S92-6
Front End	Transversal	F2-T	F3-T	F6-T
Front End	Longitudinal	F2-L	F3-L	F6-L
Back End	Transversal	B2-T	B3-T	B6-T
Back End	Longitudinal	B2-L	B3-L	B6-L

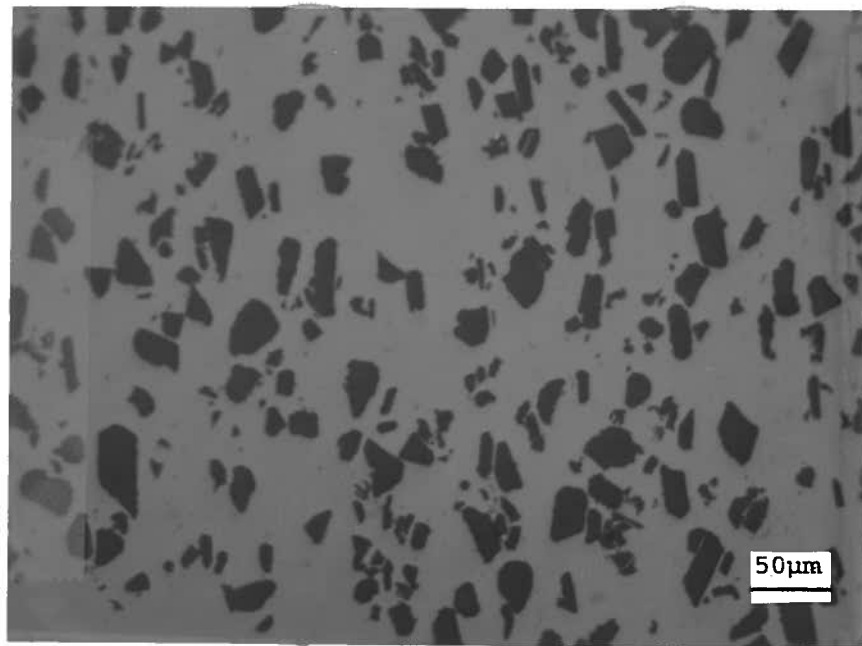
A. Comparison of Microstructure in Longitudinal and Transverse Sections

Based on the optical microscopic examination of transverse and longitudinal sections of the extrudates of 6061/Al₂O₃/20p, some typical characteristics of the particle distribution in the transverse section of the specimen are summarized:

- (i) particles were randomly oriented, i.e., with no preferred orientation;
- (ii) particle size was non uniform;



(a) Transverse



(b) Longitudinal

Figure 7.7 Typical characteristics of particles after extrusion of 6061/Al₂O₃/20p at an extrusion ratio of 34

- (iii) many small particles were observed;
- (iv) particles were quite uniformly distributed. The particle distribution in the transverse section with some of the above features is shown in Fig. 7.7(a).

In the longitudinal section, some salient features are summarized as:

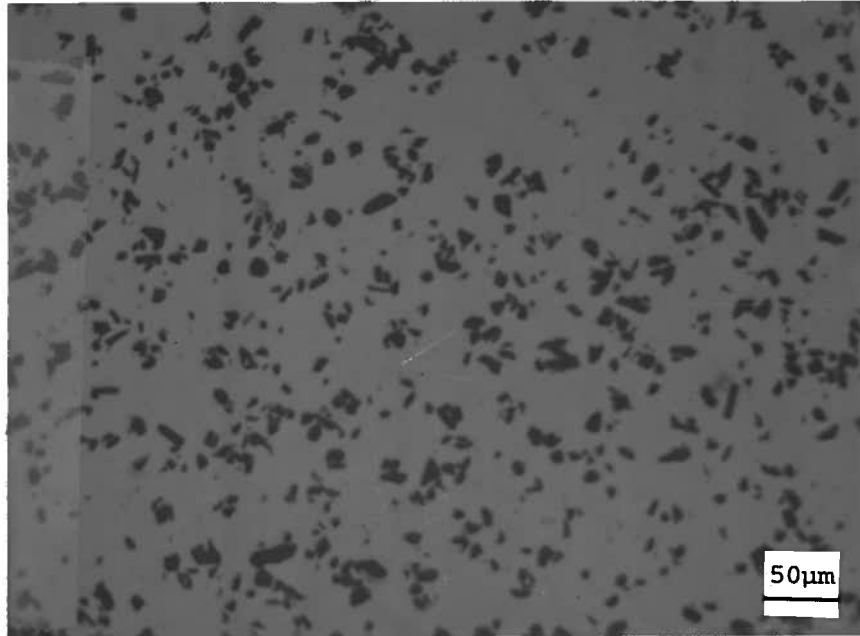
- (i) most of the particles with a large aspect ratio were aligned in the extrusion direction;
- (ii) fractured particles were found in clusters;
- (iii) equiaxed particles (i.e., aspect ratio of the particle is close to unity) were harder to crack;
- (iv) for the situations where a single particle positioned between two large particles, the middle particle had a high tendency to fracture;
- (v) more extensive particle fracture was observed in the longitudinal section; however fractured particles seemed to have healed with intrusion of the matrix material into the resulting gap under high hydrostatic pressure, or because fractured pieces were shifted by local metal flow during shear deformation;
- (vi) most of the cracks (the gap between two fractured parts) were in the extrusion direction.

This was due to the fact that particles were fractured in the shear deformation zone and finally rotated into the extrusion direction, if these cracked parts had not been shifted sufficiently far apart. A typical particle distribution with some of the above features is shown in Fig. 7.7(b).

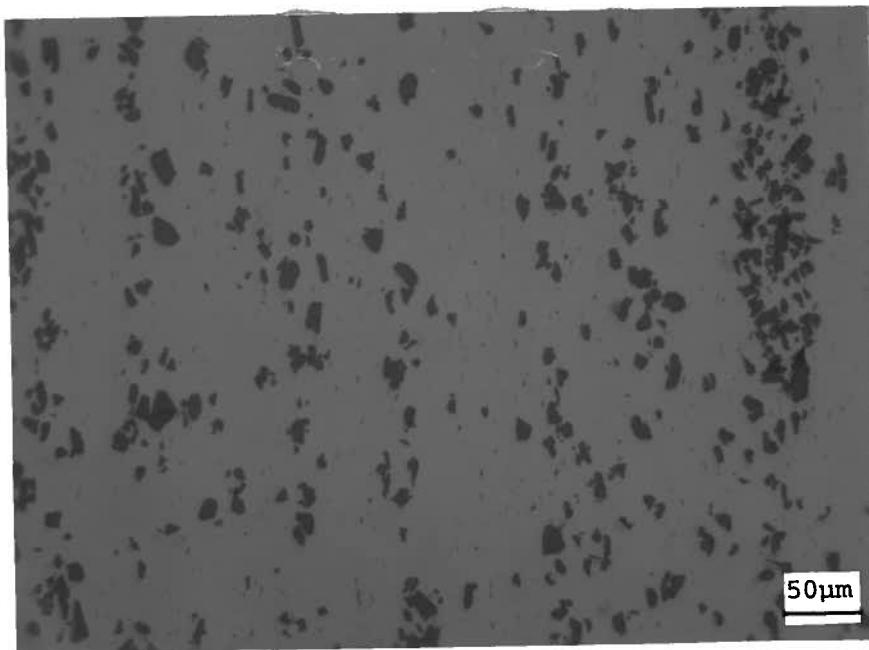
B. Comparison of Microstructure for 6061/Al₂O₃/20p and 6061/Al₂O₃/10p

For the extrudates of 6061/Al₂O₃/10p, similar characteristics of particle fracture to the 6061/Al₂O₃/20p were also recognized (Fig. 7.8), such as:

- (i) particles were also randomly oriented in transverse section, but aligned in the extrusion direction in the longitudinal section;



(a) Transverse



(b) Longitudinal

Figure 7.8 Typical characteristics of particles after extrusion of 6061/Al₂O₃/10p at an extrusion ratio of 34

(ii) multiple fracture was observed from large particles with a high aspect ratio and those in clusters.

The salient features of the microstructure of the extrudates of 6061/Al₂O₃/10p compared to 6061/Al₂O₃/10p are:

- (i) particle size was much smaller than that in the 6061/Al₂O₃/20p, and the size distribution was more uniform;
- (ii) large particle-free zones in the transverse section and particle-free bands were more frequently observed in the longitudinal section due to the small volume fraction and non-uniform distribution of particles in the cast billet. The ratio of the length to the width of the bands in the longitudinal section was measured under the microscope and found to lie in the range of 20 to 27, which is comparable to the extrusion ratio of 34. This implies that the formation of the particle-free bands are most probably due to elongation of the particle-free zone in the as-cast billet;
- (iii) more clusters remained after extrusion;
- (iv) although the aspect ratio change is not as obvious, most of the small particles have an aspect ratio close to one.

For the extrudates of the aluminum alloy, 6061, many precipitates were present, most of which were Mg₂Si. It was found that the size of the precipitates was around one micron and they were quite uniformly distributed throughout each section. In the longitudinal section, the precipitates were aligned in the extrusion direction. These precipitates were also present in the composite extrudates, though not visible at the magnification shown in Fig. 7.7 and 7.8.

7.3.2 Image Analysis of Particle Distribution in Extrudates

An image analyzer was used to quantify the particle size and orientation. The particle size was measured in terms of particle area and maximum and minimum diameter. The particle area was defined as the cross sectional area of a particle on the polished surface, while the maximum and minimum diameter were defined as the longest and the shortest dimension of a particle on the polished surface, respectively. In addition, particle aspect ratio and orientation were also measured. The particle aspect ratio was defined as the ratio of the maximum diameter to the minimum diameter, and the orientation of a particle was determined by the angle from the direction of its longest axis with respect to a specified direction, e.g., the extrusion direction in the longitudinal section. Thus, if the angle was zero degree, the particle was considered as aligned in the extrusion direction. A total of more than 2000 particles were measured for a relative error in the measurements of less than $\pm 5\%$ with 95% confidence^[97].

7.3.2.1 Homogeneity of Particle Distribution

The homogeneity of particle distribution is difficult to characterize quantitatively. However, the variation of local volume fraction in the composites could be a measure of the uniformity of particle distribution. A particle-free zone results in a zero local volume fraction, while a field full of clusters might approach 100% local volume fraction in extreme conditions. Apparently, a uniform distribution of particles would lead to a small range of variation in the local volume fraction.

The local volume fraction from position to position was measured using a Letiz Image Analyzer. A total of 500 fields were examined. The local volume fraction varied from 5% to 29% for the extrudates of 6061/Al₂O₃/10p. The frequency of local volume fractions in the range of 1% to 30% is shown in the histogram in Fig. 7.9 for the extrudate of

6061/Al₂O₃/10p for both the transverse and the longitudinal sections. The mean volume fraction for the transverse section and longitudinal section were calculated to be 12.48% and 14.52%, respectively. The corresponding standard deviations were 2.34% and 3.52%, and the relative coefficients were 0.1875 and 0.2424, respectively, which is defined as the ratio of the standard deviation to the mean value. Obviously, the distribution of the particles in the 6061/Al₂O₃/10p composite is non-uniform, and the non-uniformity in the longitudinal section is even more than in the transverse section based on the standard deviation and relative coefficient values. This is due to the band formation in the longitudinal section.

The histogram of the volume fraction for the extrudate of 6061/Al₂O₃/20p in Fig. 7.10 shows that the variation of local volume fraction varied from 13% to about 35%. The mean values of the volume fraction in the transverse and longitudinal sections are 24.52% and 24.45%, respectively, while the corresponding standard deviations are 3.74% and 4.05%, with the relative coefficients being 0.1525 and 0.1656, respectively. The values of relative coefficients indicate that, firstly, the particle distribution for the 6061/Al₂O₃/20p is more uniform than in the 6061/Al₂O₃/10p (Table 7.5); secondly, the particle distribution in the transverse section is more uniform than in the longitudinal section for both volume fractions. However, all the measured values of the volume fractions were larger than the nominal values, as the designation indicates.

Table 7.5 Statistical results for volume fraction distribution of the two composites

Section	6061/Al ₂ O ₃ /10p			6061/Al ₂ O ₃ /20p		
	Mean Value (%)	Standard Deviation (%)	Relative Coeff.	Mean Value (%)	Standard Deviation (%)	Relative Coeff.
Transverse	12.48	2.34	0.188	24.52	3.74	0.152
Longitudinal	14.52	3.52	0.242	24.45	4.05	0.166

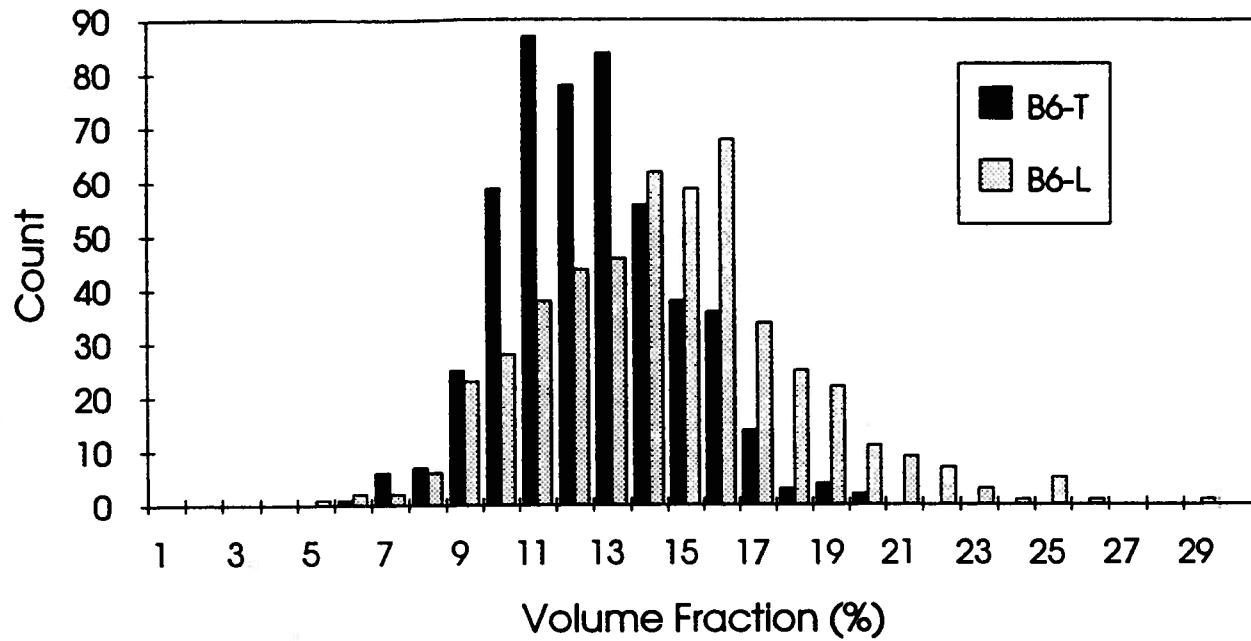


Figure 7.9 Histogram of volume fraction for 6061/Al₂O₃/10p

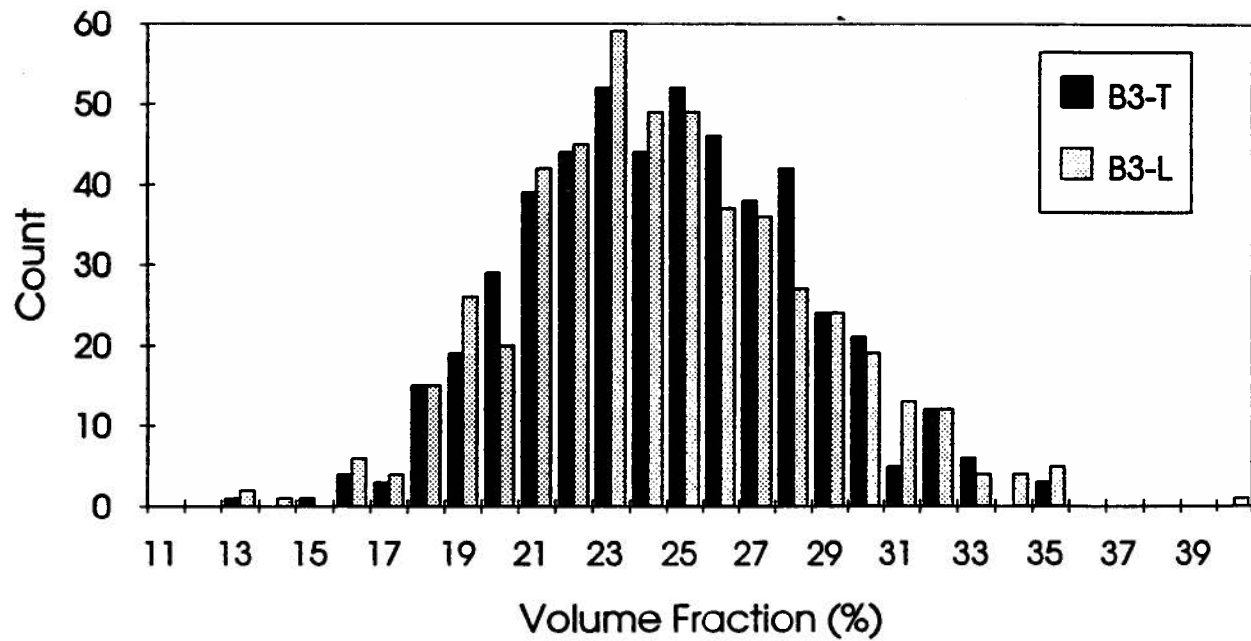


Figure 7.10 Histogram of volume fraction for 6061/Al₂O₃/20p

7.3.2.2 Particle Size

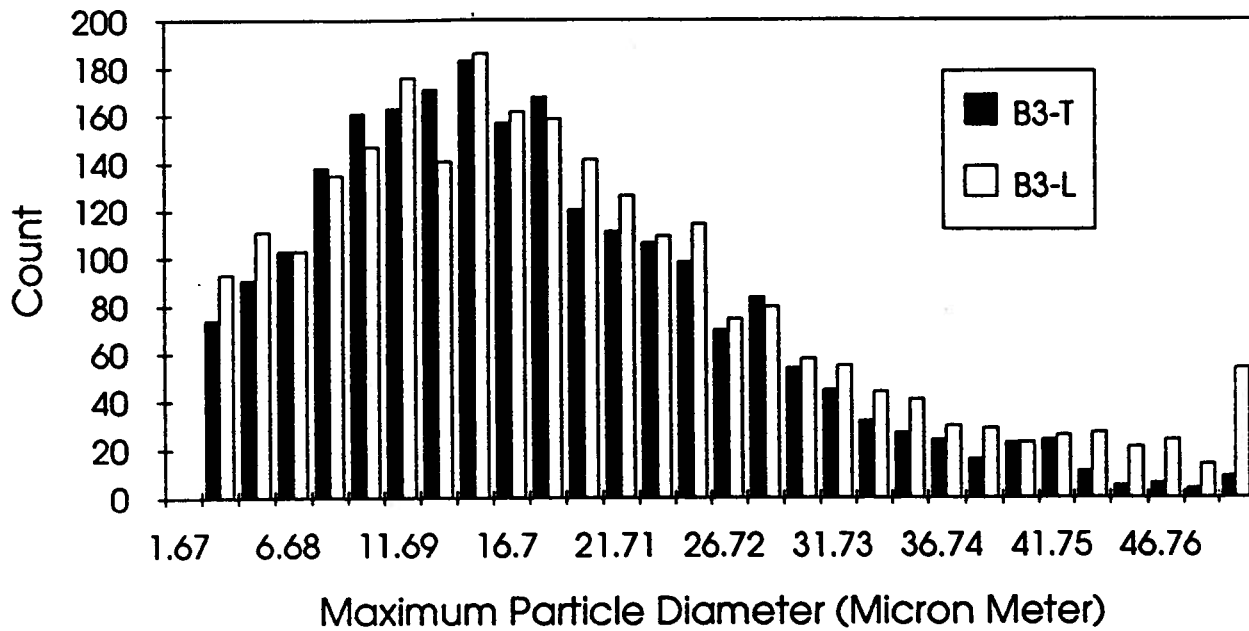
To evaluate the particle size variation in the composites after extrusion, the dimensions of a particle in terms of its area, maximum and minimum diameter (dimension) were measured. The details of the measurements with statistical analysis are listed in Table 7.6.

A. Particle Diameter

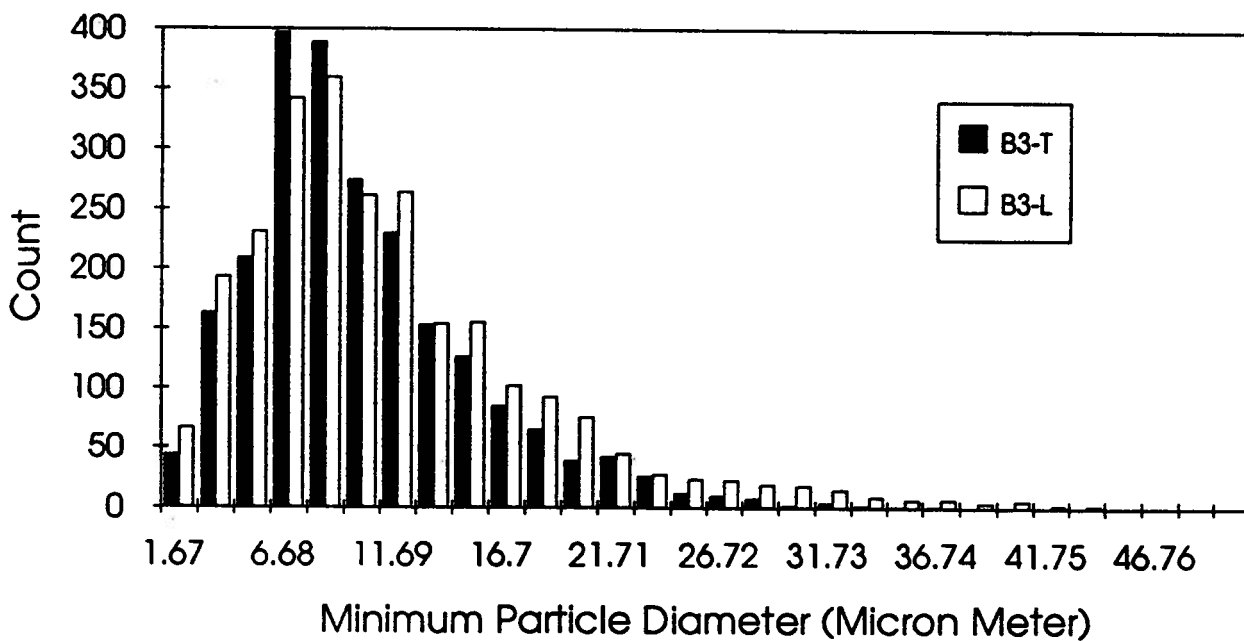
The histograms of the maximum diameter and minimum diameter for B3 (Back end of the extrudate S92-3: 6061/Al₂O₃/20p) and B6 (Back end of the extrudate S92-6: 6061/Al₂O₃/10p) are shown in Figs. 7.11 and 7.12. From Fig. 7.11, it is seen that the variation of the maximum diameter in a total count of about 2000 particles in B3 is from 50.0 μm to 3.3 μm, while the minimum diameter varies from 1.67 μm to 44 μm. However, the mean values of both the maximum and minimum diameter are larger in the longitudinal section than in the transverse section, as seen in Table 7.6. For 6061/Al₂O₃/10p (B6), in Fig. 7.12, it is seen that the range of the variation of the maximum diameter is from about 3 μm to 28 μm and the minimum diameter from 1.3 μm to 15 μm, which is almost half of the values of the particles in 6061/Al₂O₃/20p (B3 and F3). Similar to the 20% composite, the mean values of both the maximum and minimum diameter of the particles are larger in the longitudinal section than in the transverse section for the 10% composite, as seen in Table 7.6.

B. Particle Area

The variation of particle area may reflect the particle size distribution in the composites more directly. Figure 7.13 shows the particle area distribution for the same count of particles in the extrudate of 6061/Al₂O₃/20p at the back end. It is seen that there is a large variations in the particle area, from ~16 μm² to 480 μm². Again, the mean value of the particle area in the longitudinal section are larger than those in the transverse section, which is

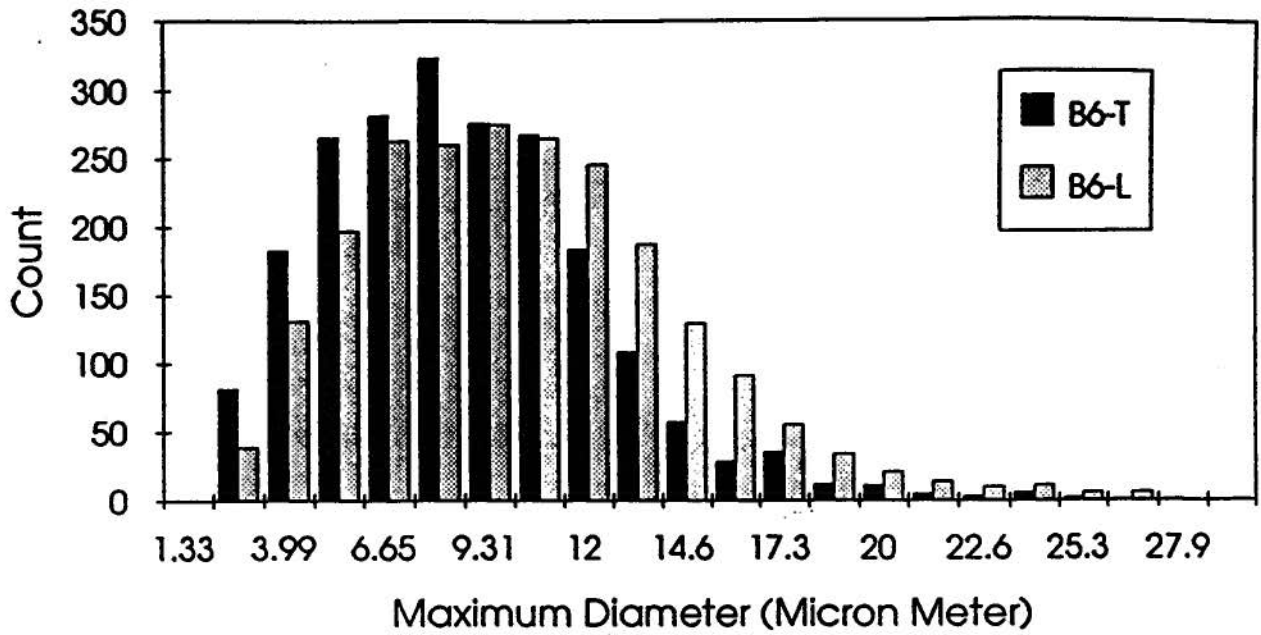


(a) Max. Diameter

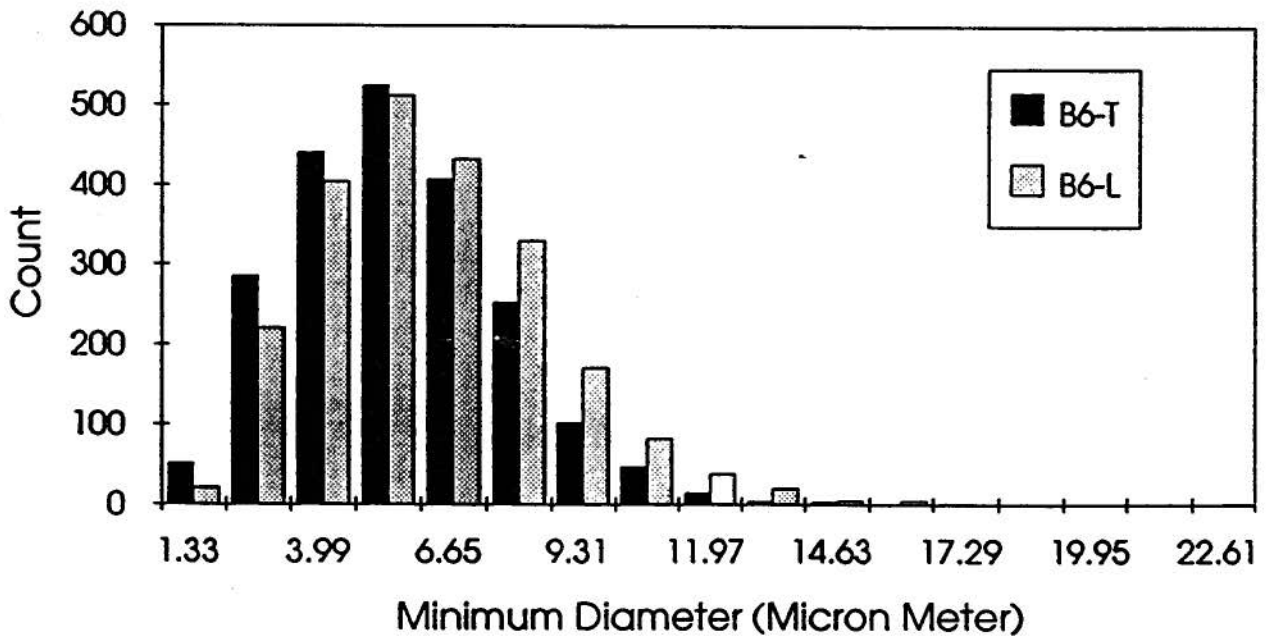


(b) Min. Diameter

Figure 7.11 Histogram of the particle diameter for Sample B3 of 6061/Al₂O₃/20p



(a) Max. Diameter



(b) Min. Diameter

Figure 7.12 Histogram of the particle diameter for Sample B6 of 6061/Al₂O₃/10p

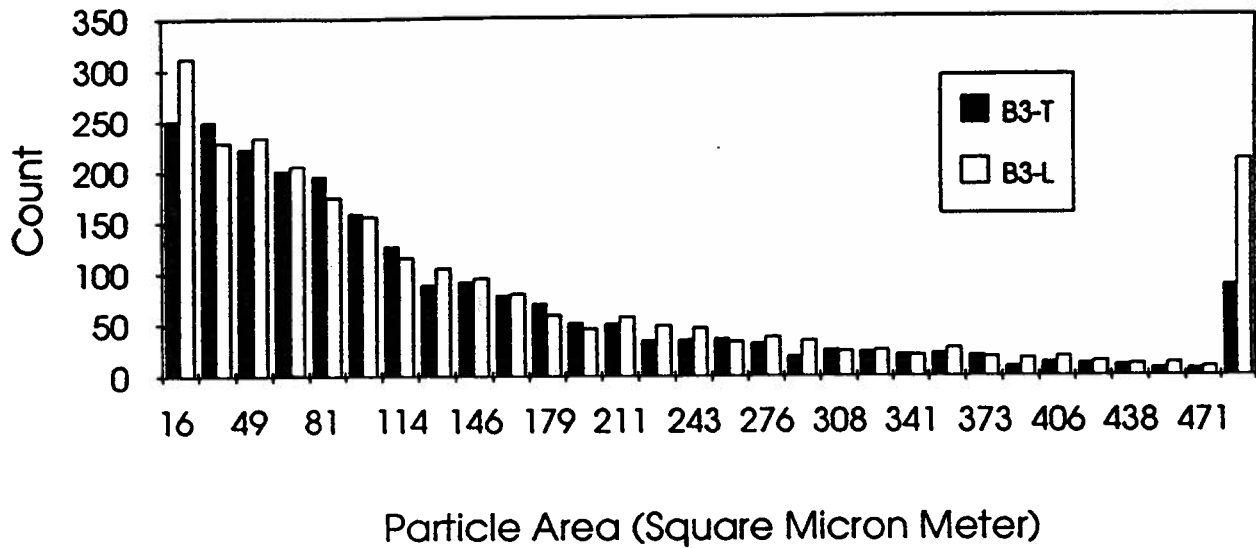


Figure 7.13 Histogram of the particle area for Sample B3 of 6061/Al₂O₃/20p

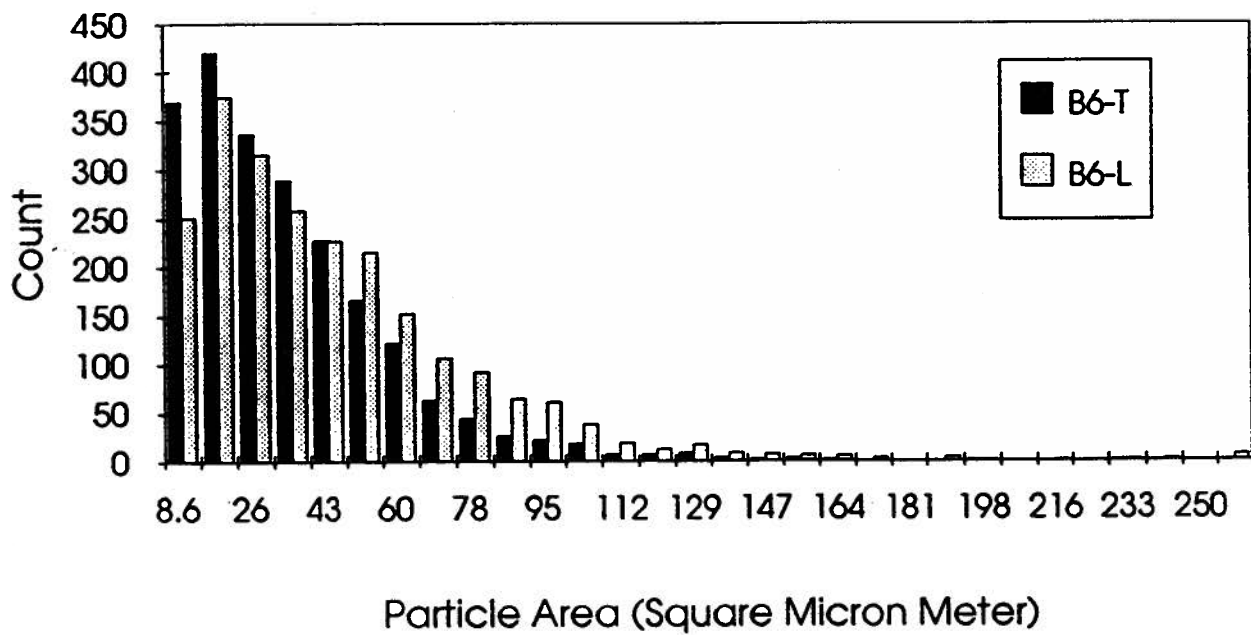


Figure 7.14 Histogram of the particle area for Sample B6 of 6061/Al₂O₃/10p

Table 7.6 Statistical results for the quantitative metallography

MMC	No. of Particles	Particle Area (μm^2)		Max.Diameter (μm)		Min.Diameter (μm)		Aspect Ratio	
		Mean Value	Std. Dev. / Rel. Coeff	Mean Value	Std. Dev. / Rel. Coeff	Mean Value	Std. Dev. / Rel. Coeff	Mean Value	Std. Dev./ Rel. Coeff
Location 4 in Fig. 7.4 (S92-3)	2259	179.79	140.21 / 0.780	21.61	9.94 / 0.460	12.12	5.99 / 0.494	2.01	0.59 / 0.294
Location 7 in Fig. 7.4 (S92-3)	2256	161.63	132.43 / 0.819	20.83	9.73 / 0.467	11.23	5.73 / 0.510	2.12	0.66 / 0.311
B3-T	2282	134.09	122.52 / 0.914	17.97	9.47 / 0.527	10.07	5.24 / 0.520	2.00	0.56 / 0.280
B3-L	2508	174.07	143.27 / 0.823	19.57	11.23 / 0.574	11.43	6.73 / 0.589	1.99	0.55 / 0.276
F3-T	3269	136.90	124.37 / 0.908	18.62	9.60 / 0.516	10.14	5.20 / 0.513	2.07	0.62 / 0.300
F3-L	2020	161.59	140.19 / 0.868	20.17	10.65 / 0.528	11.50	6.44 / 0.560	1.99	0.57 / 0.286
B6-T	2137	34.37	24.67 / 0.718	8.75	3.72 / 0.425	5.55	2.19 / 0.395	1.77	0.47 / 0.266
B6-L	2245	44.16	33.34 / 0.755	10.17	4.27 / 0.420	6.16	2.45 / 0.398	1.87	0.54 / 0.289
F6-T	1965	31.20	22.04 / 0.706	8.64	3.66 / 0.424	5.13	2.06 / 0.401	1.92	0.57 / 0.297
F6-L	3004	38.54	35.54 / 0.922	8.99	4.56 / 0.507	5.71	2.72 / 0.476	1.75	0.47 / 0.269

Note: 'Rel. Coeff.' in the table is a relative coefficient which is defined as the ratio of standard error to the mean value.

due to the re-orientation of particles along the extrusion direction. The variation of the particle area for the 6061/Al₂O₃/10p is from 8.6μm² to around 200μm² (Fig. 7.14). The mean value of the particle area is about 4 times less than that of the 6061/Al₂O₃/20p (Table 7.6). This is principally due to different initial range of particle sizes adopted in the fabrication of the composites.

7.3.2.3 Aspect Ratio of Particles

The aspect ratio of a particle is defined as the ratio of its maximum dimension to its minimum dimension. The distributions of aspect ratio in the two samples with different volume fractions are shown in Figs. 7.15 and 7.16. It is seen that the variation of the aspect ratio is from 1.2 to 4.5 for both materials. The mean aspect ratio in extrudates for the 6061/Al₂O₃/20p is around 1.99 to 2.07, while the aspect ratio for the 6061/Al₂O₃/10p is around 1.75 to 1.92 (Table 7.6), which confirms the observation that more particles have an aspect ratio close to unity in 6061/Al₂O₃/10p. The relative coefficients (Table 7.6) of the particle size (e.g., area, diameters) are generally smaller for 6061/Al₂O₃/10p than for 6061/Al₂O₃/20p, which also confirms that the particle size is more uniform in extrudates of 6061/Al₂O₃/10p than in 6061/Al₂O₃/20p, because the particle size is smaller.

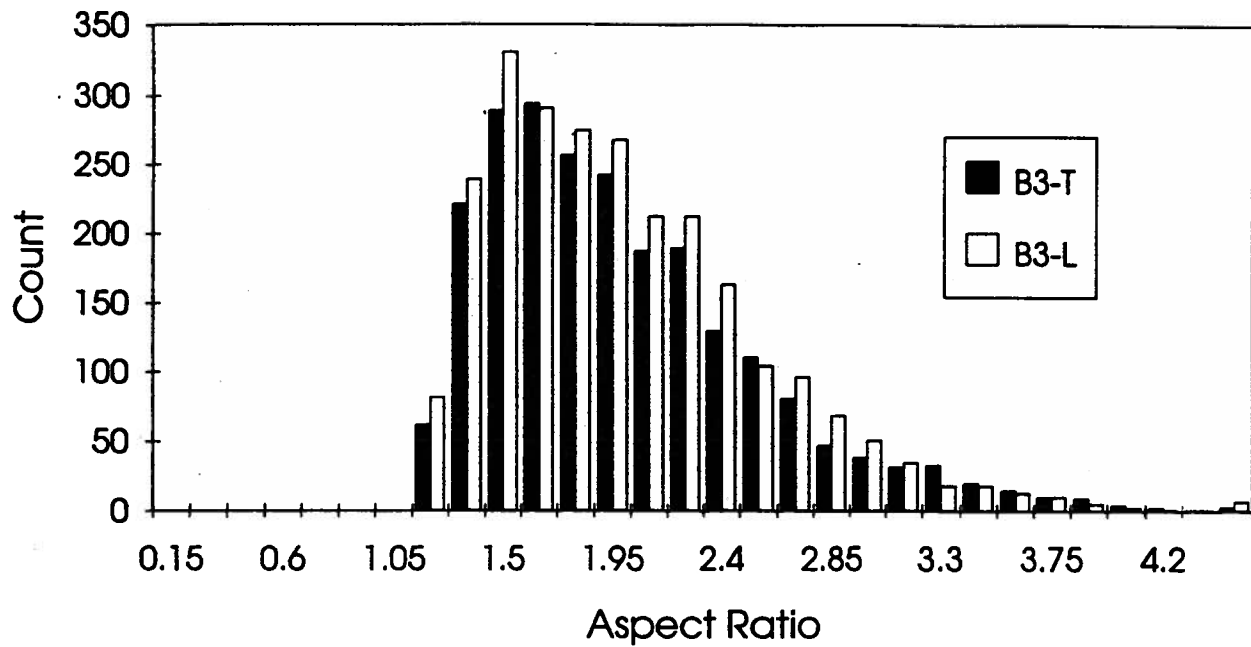


Figure 7.15 Histogram of the aspect ratio for Sample B3 of 6061/Al₂O₃/20p

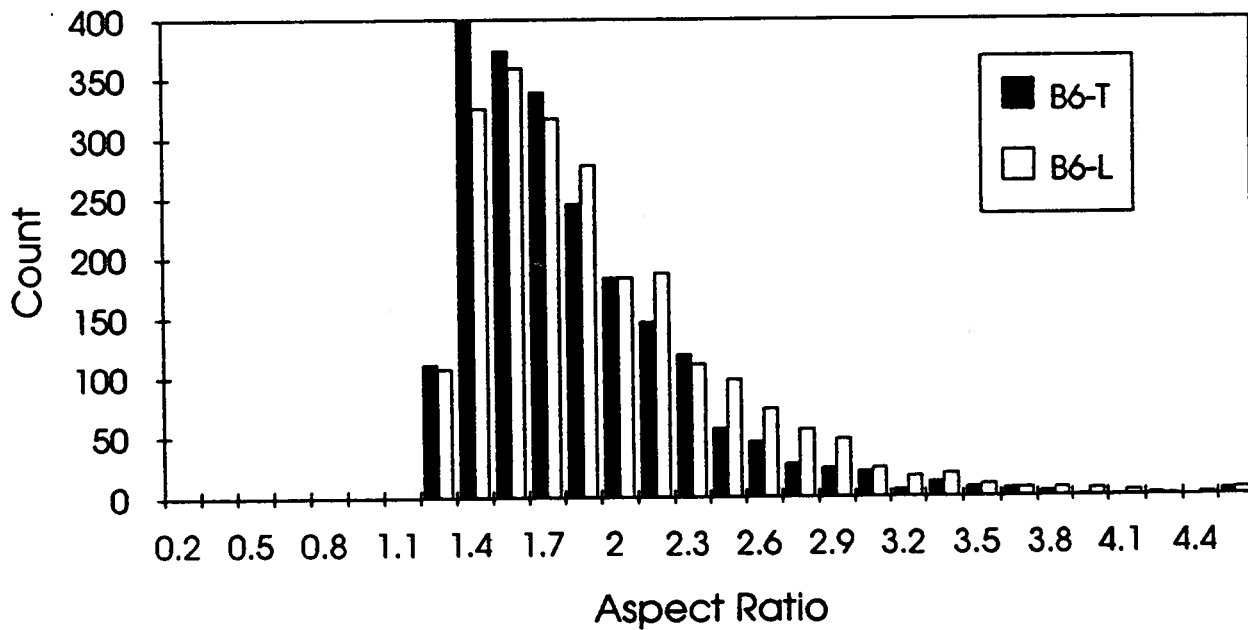


Figure 7.16 Histogram of the aspect ratio for Specimen B6 of 6061/Al₂O₃/10p

7.3.2.4 Particle Orientation

Orientation of the particles with respect to extrusion direction was also analyzed with the Leitz Image Analyzer. The extrusion direction was set to be 0° or 180° . The entire range from 0° to 180° was divided into 12 groups, with the group width being 15° . The frequency of the particle orientation with respect to its maximum dimension in the different groups for the extrudates is shown in Figs. 7.17 and 7.18. It is obvious that particles in the transverse section have no preferred orientation, because the frequencies (counts) of the orientation for each class are similar. However, higher frequencies of the particle orientation in 0 to 30° and 165 to 180° were measured in the longitudinal section, which means the particles in the longitudinal section are aligned in the extrusion direction. These measurements are consistent with the microscope observations (Figs. 7.7 and 7.8).

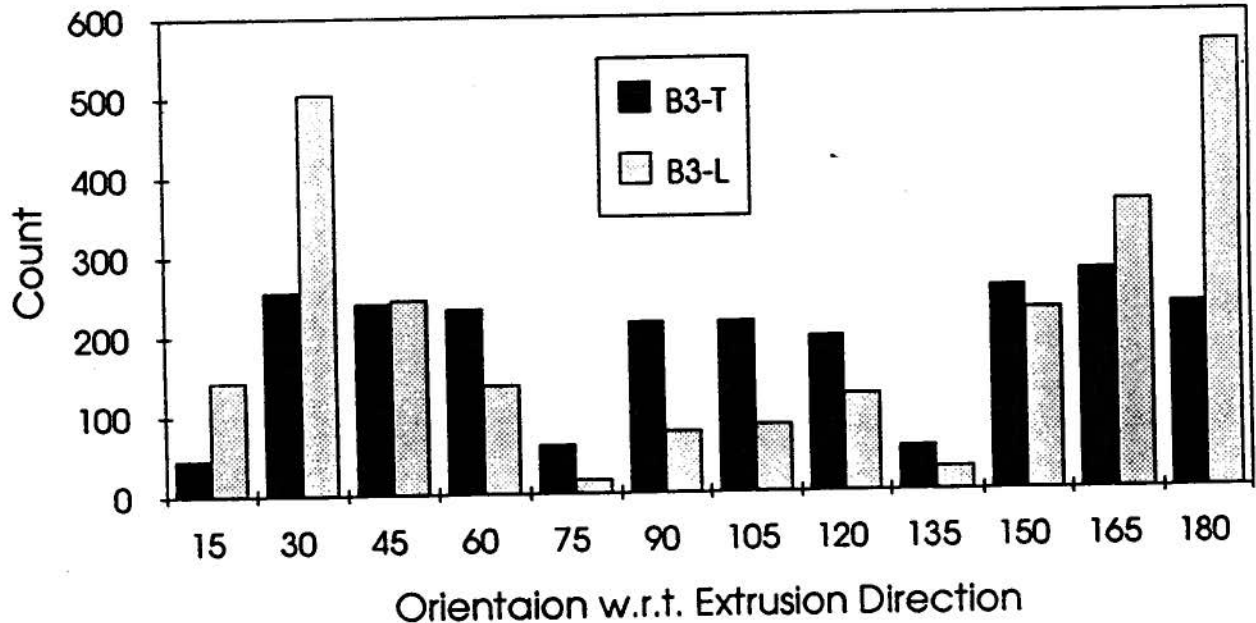


Figure 7.17 Histogram of orientation of the particles with respect to extrusion direction

for the Sample B3 of $6061/Al_2O_3/20p$

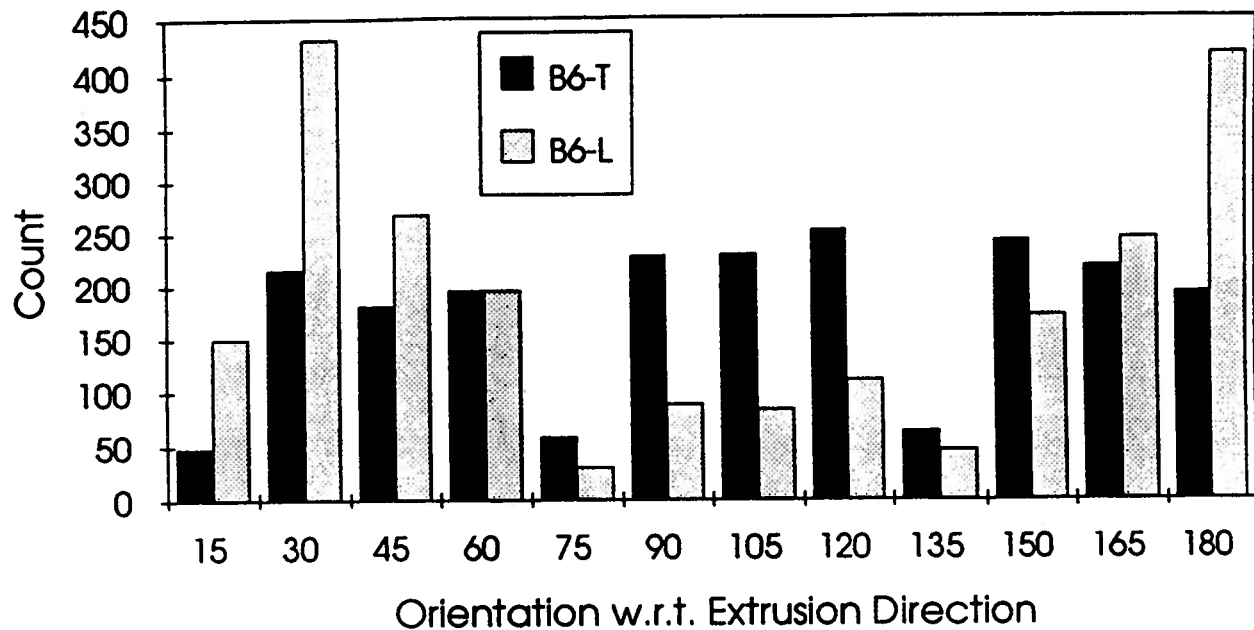


Figure 7.18 Histogram of orientation of the particles with respect to extrusion direction

for the Sample B6 of 6061/Al₂O₃/10p

7.4 Particle Fracture Model during Extrusion

7.4.1 Particle Fracture Probability at High Temperature

Particle fracture has been observed during the extrusion process; and this results in particle size refinement. There are two factors which are known to determine particle fracture and its influence on material properties in service: local stress (related to imposed strain at low temperature), and hydrostatic pressure, which is obviously of importance during extrusion. At low temperature the probability of fracture is correlated to strain^[75,76], (see also Eq. 7.1), whereas, at high temperature it is expedient to correlate fracture to the Zener-Holloman parameter and its time effect, as it is the Zener-Holloman parameter that determines the flow stress of the matrix material during hot extrusion.

$$p_f = 1 - \exp(-\beta D^3 \alpha \epsilon) \quad (7.1)$$

If the particle fracture process is stochastic, then the fracture probability can be derived to predict the particle size refinement during hot extrusion.

$$p_f = 1 - \exp\left(\int_0^t (-\beta_1 D^3 \alpha Z) dt\right) \quad (7.2)$$

where β_1 is a constant with the unit being $[1/\mu\text{m}^3]$, and determined by quantitative microstructure analysis; D is the volume equivalent particle diameter, $[\mu\text{m}]$; α is the mean particle aspect ratio; and $Z = \dot{\epsilon} \exp(Q/RT)$, $[1/\text{s}]$. It is noted that dt considers the accumulation effect of particle fracture in the extrusion process. The term $-\beta_1 D^3 \alpha Z$ reflects the flow stress level, which controls the particle fracture process, and also represents the fracture rate during extrusion^[103]. In the subsequent section, this fracture probability will be applied to the hot extrusion process to calculate the particle size refinement.

7.4.2 Particle Fracture Model during Extrusion

It was observed that particles undergo multiple fracture. Hence, the assumption that a particle fractures into two approximately equal halves^[75,76], may require re-evaluation for a model of particle fracture under extrusion conditions. In the case under evaluation, it would seem that this assumption denies the evidence of a large increase in small particles. To estimate the average number of parts formed from a single particle fracture event, a total number of around 50 counts of a single particle fracture event was made for both transverse and longitudinal section of an extrudate. The number of parts fractured from a single particle event (including a fracture event in a cluster) was recorded. Therefore, the average number of parts, n , formed from a single particle fracture event, is simply;

$$n = \frac{\sum_{i=1}^N N_i}{N} \quad (7.3)$$

where N is the number of counts, 50 in this case as mentioned above and N_i is the number of parts counted from each fracture event. It was found that a large single particle often fractures into two parts with one part twice the area of the other one. However, a particle in a cluster often is crushed into 3 or more parts with equivalent size. With respect to different extrusion ratios, more fractured particles were observed at a high extrusion ratio. The average number of parts from a single fracture event for different sections of an extrudate at different extrusion ratios is listed in Table 7.7. It is seen that more parts are formed from a single particle fracture event in an extrudate at a higher extrusion ratio than at a lower extrusion ratio. This also implies that the higher the extrusion ratio, the larger the particle size reduction.

Table 7.7 Average number of parts fractured from a single particle in 6061/Al₂O₃/20p

Extrusion ratio of an Extrudate	Longitudinal (‘L’)	Transverse (‘T’)	Both in ‘L’ and ‘T’
64.00 (K-8)	2.78	2.44	2.63
28.80 (K-11)	2.52	2.18	2.37
10.23 (K-12)	2.42	2.22	2.24

The particle fracture probability, p_f , is a function of temperature and strain rate, and is also associated with the deformation time. To determine the final fracture probability of particles at the die exit during extrusion, an integration over the deformation zone is necessary, i.e.,

$$p = \int_0^t (-\beta_1 D^3 \alpha Z) dt = \int_0^t \sigma_f(r, z) dt \quad (7.4)$$

where σ_f provides the fracture rate, which varies both in the radial direction, r , and in the extrusion direction, z , over the deformation zone of the billet. To simplify the numerical calculation, an average fracture rate over a cross section of the billet in the deformation zone during extrusion was determined first, i.e., the fracture rate was integrated over a cross sectional area at a certain depth, z , in the deformation zone, and was divided by the cross sectional area to obtain an average as described below.

$$\bar{p} = \int_0^{R_1} 2\sigma_f(r, z) r dr / R_1^2 \quad (7.5)$$

where R_1 is the radius of the deformation, which is outlined by the shear zone boundary. It varies from the initial radius of the billet (R_0) at the back end of the deformation zone, to the radius of the extrudate (R_E) at the die exit. If one assumes that a particle with a volume equivalent diameter, D , is fractured into n equally sized particles during extrusion, the volume equivalent diameter of each fractured piece is $D/\sqrt[n]{n}$. Because the number of broken particles, N_f^b , is equal to $p_f * N_f^t$, where N_f^t is the total number of particles in the deformation zone, the mean refined particle diameter can be derived as:

$$\bar{D}_1 = \left(\frac{(D/\sqrt[n]{n})^3 * n * N_f^b + (N_f^t - N_f^b) * D^3}{N_f^t + (n-1) * N_f^b} \right)^{1/3} = \frac{1}{(1+(n-1)p_f)^{1/3}} D \quad (7.6)$$

Then, the particle size reduction at that stage is defined as:

$$\frac{\Delta D}{D} \% = \frac{D - \bar{D}_1}{D} \times 100\% \quad (7.7)$$

7.4.3 Application of the Model

From an image analysis of the extrudate from Trial S92-3 at UAC, Anaheim, the mean particle diameter, $D_{1\text{mean}}$, in the extrudate was found to be 12.41 μm ; while the mean size of the particle, $D_{0\text{mean}}$, at the back-end of the billet was 13.07 μm . The mean value of the maximum

diameter of the particles, was $18.77\mu\text{m}$ and $21.22\mu\text{m}$ for the extrudate, $D_{1\text{max}}$, and the billet, $D_{0\text{max}}$, respectively. Using Eq. (7.6), the overall fracture probability was estimated as 12.20%, and consequently the constant β_1 in the fracture model (Eq. 7.2) is $3.07 \times 10^{-21} [1/\mu\text{m}^3]$. Both the mean particle size (diameter) and the mean value of the maximum diameter are predicted using the DEFORM results for temperature and strain rate in the deformation zone (Table 7.8). It is evident that there is good agreement between the mean particle diameter and the mean value of the maximum particle dimension.

The probability variation at each time step through the deformation zone was estimated using Eq. (7.2). Figure 7.19 shows that a maximum fracture probability is reached near the exit of the die aperture. This indicates that the most severe particle fracture occurs near the die throat by severe shear deformation due to choke of metal flow into the die aperture, which is consistent with the microstructural examination in the deformation zone. The corresponding mean particle size reduction is shown in Fig. 7.20.

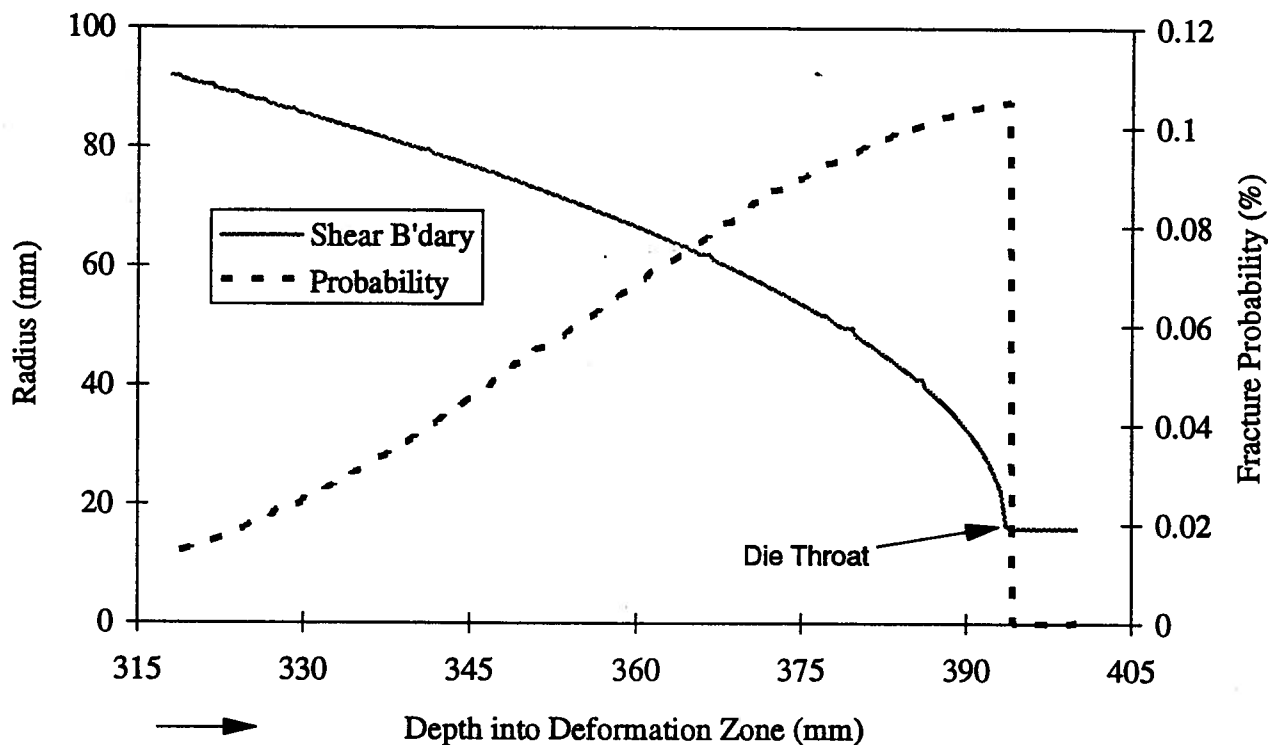


Figure 7.19 Fracture probability variation in the deformation zone

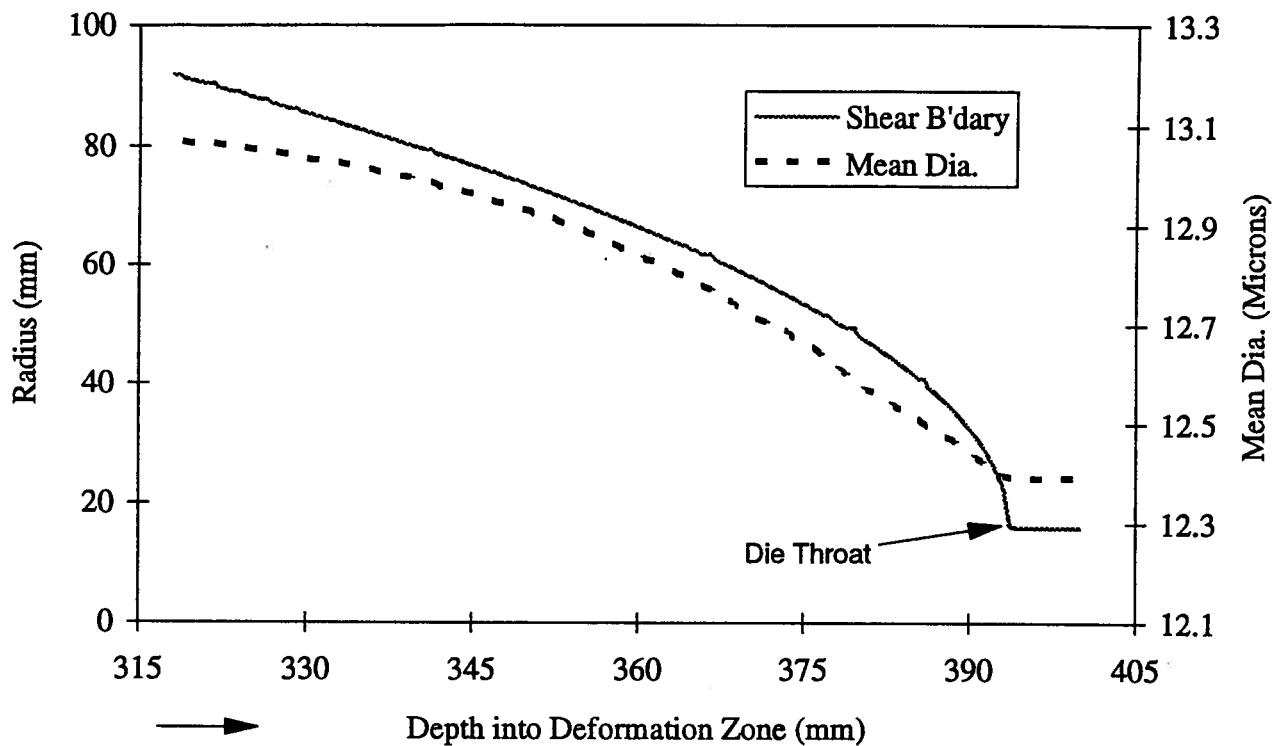


Figure 7.20 Particle size reduction during extrusion

Table 7.8 Comparison of model predictions with measured data

Mean Particle Diameter Reduction				
	$D_{0\text{mean}}(\mu\text{m})$	$D_{1\text{mean}}(\mu\text{m})$	Red (%)	p_f
Measured	13.07	12.41	5.02	12.20
Model	13.07	12.39	5.19	11.02
Average Maximum Particle Dimension Reduction				
	$D_{0\text{max}}(\mu\text{m})$	$D_{1\text{max}}(\mu\text{m})$	Red (%)	p_f
Measured	21.22	18.77	11.55	32.48
Model	21.22	17.64	16.87	33.36

7.5 Discussion

The particle distribution has been examined during the extrusion process. However, some questions remain. What is the influence of the extrusion process on particle

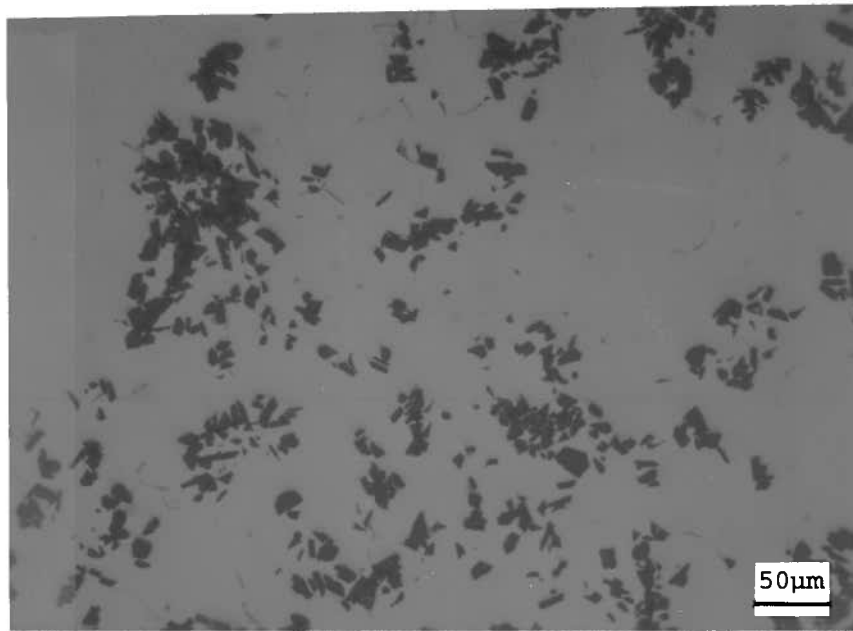
distribution? How is a particle fractured during deformation, and what is the correlation between extrusion deformation behavior and the particle fracture?

7.5.1 Microstructure Comparison before and after Extrusion

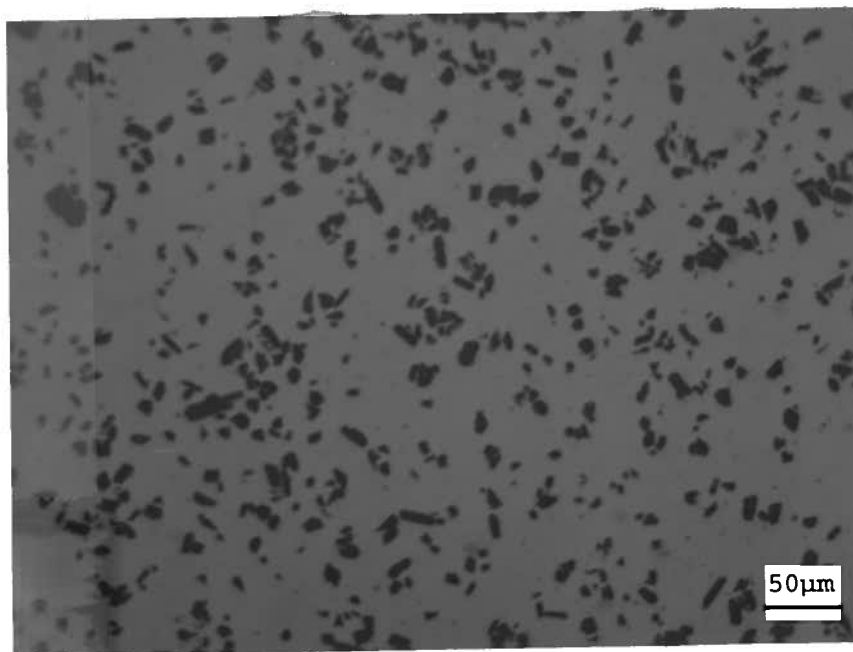
7.5.1.1 Comparison of Particle Distribution before and after Extrusion

Porosity and voids have been considered to be the most detrimental defects in cast products^[6]. In cast PRMMC products, other defects, such as surface defects (cracks), agglomeration and clustering may also be present. In the microstructure study conducted by Kalu and McNelley^[54], it was found that Al_2O_3 particles were clustered in the as-cast 10vol% material provided by Duralcan. Similar features were found in 6061/ Al_2O_3 /10p, shown in Fig. 7.21(a). The distribution of the particles was more uniform in a higher volume fraction, e.g., 6061/ Al_2O_3 /20p composite, as shown in Fig. 7.22(a). The non-uniformity is a result of entrapment of the particles in the interdendritic regions during solidification. These are potential sites for crack formation in service because a complex tri-axial stress state is easily established in clusters (see Fig. 6.8 in Chapter 6).

The microstructures of a transverse section of the 10vol% and 20vol% composites after extrusion at a ratio of 34 at UAC, are shown in Fig. 7.21(b) and Fig. 22(b), respectively. It is quite obvious that the homogeneity of particle distribution is improved after extrusion, especially for 6061/ Al_2O_3 /10p, although some clusters still remain in the transverse section, while extrusion bands are evident in the longitudinal section. The number of small particles increases as a result of particle fracture during extrusion. This is more obvious with quantitative particle size analysis using the image analyzer. Evidently, heavier extrusion ratios improve the homogeneity of particle distribution. However, a larger extrusion ratio at a relatively low temperature may introduce voids in the surface layer of extrudates due to tensile

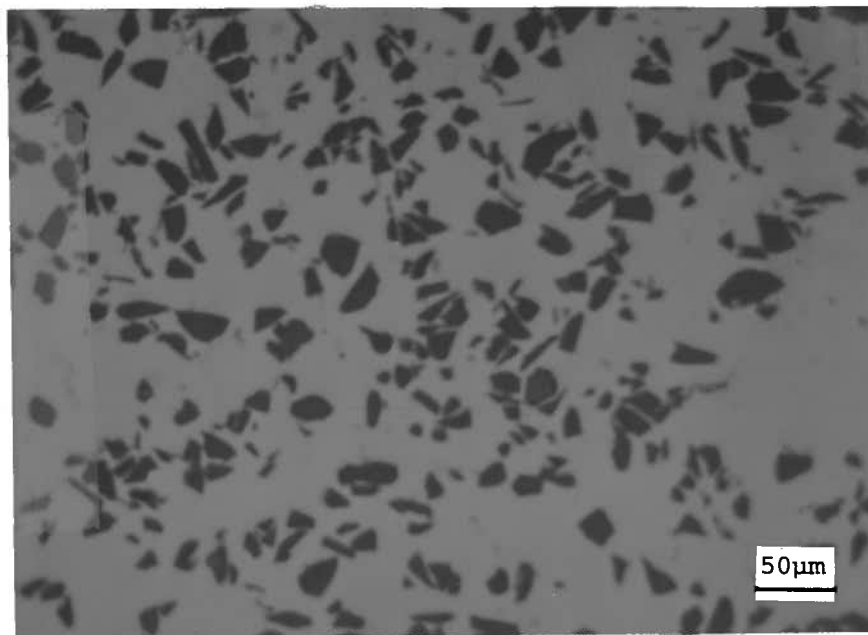


(a) Before extrusion

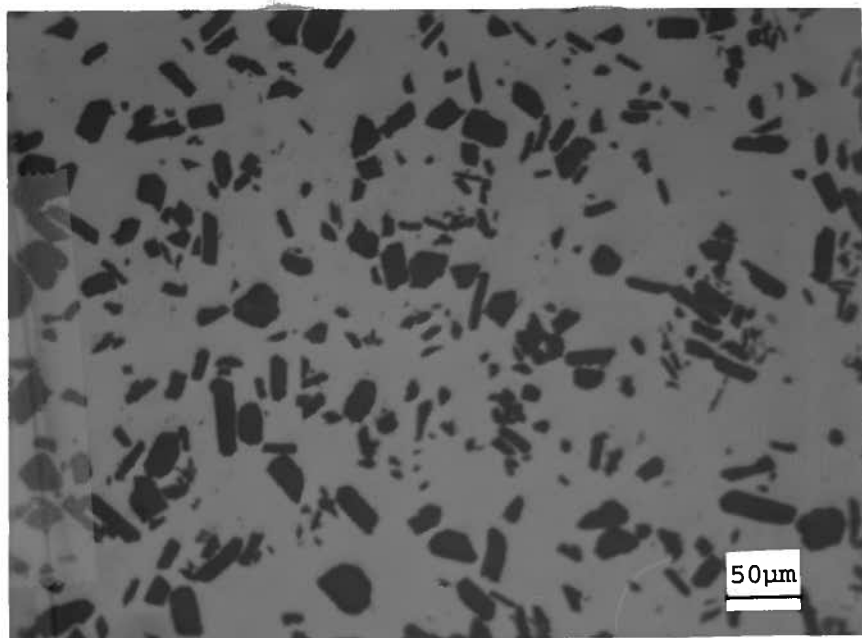


(b) After extrusion

Figure 7.21 Microstructure of 6061/Al₂O₃/10p before and after extrusion

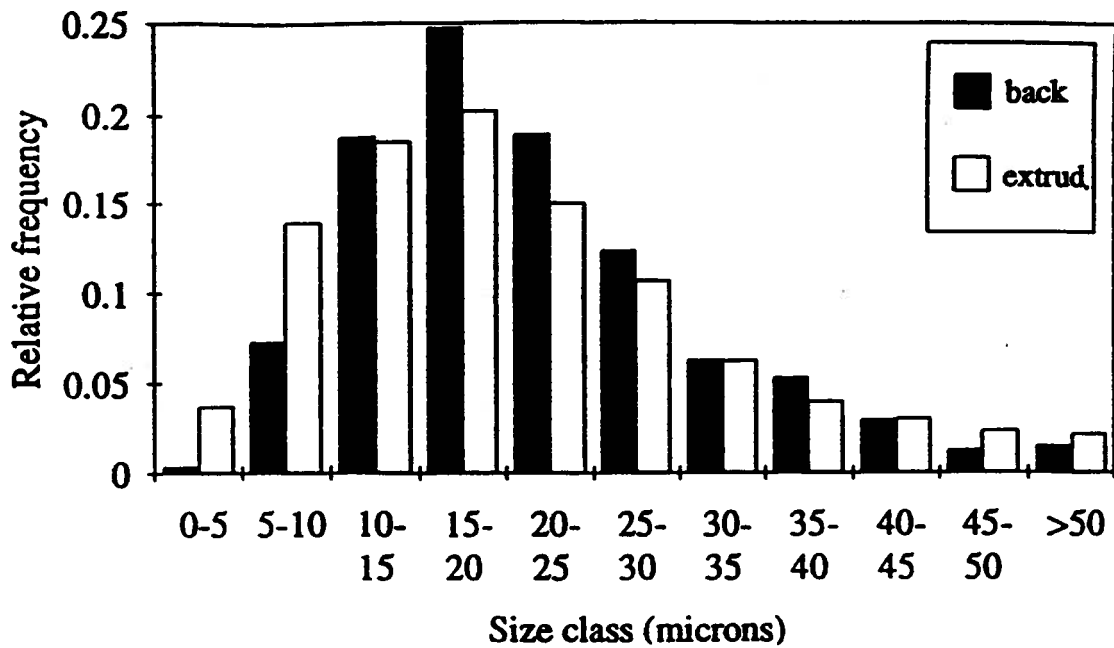


(a) Before extrusion



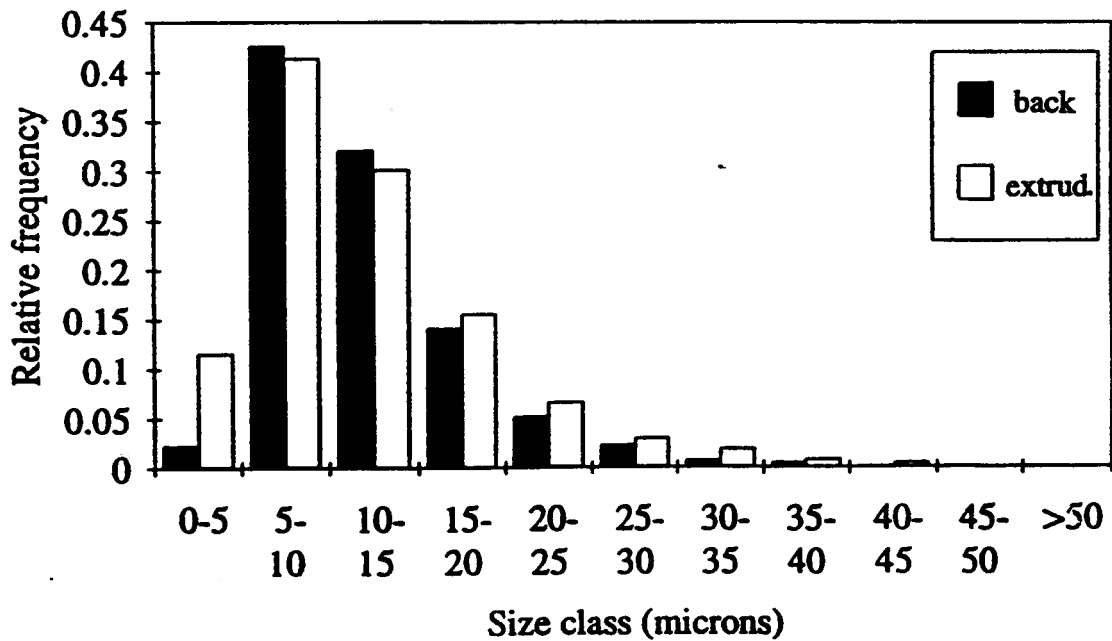
(b) After extrusion

Figure 7.22 Microstructure of 6061/Al₂O₃/20p before and after extrusion



(a) Maximum alumina particle dimension of 6061/Al₂O₃/20p

in back end of a billet and in extrudate



(b) Minimum alumina particle dimension in 6061/Al₂O₃/20p

in back end of a billet and in extrudate

Figure 7.23 Variation of maximum and minimum alumina particle dimension

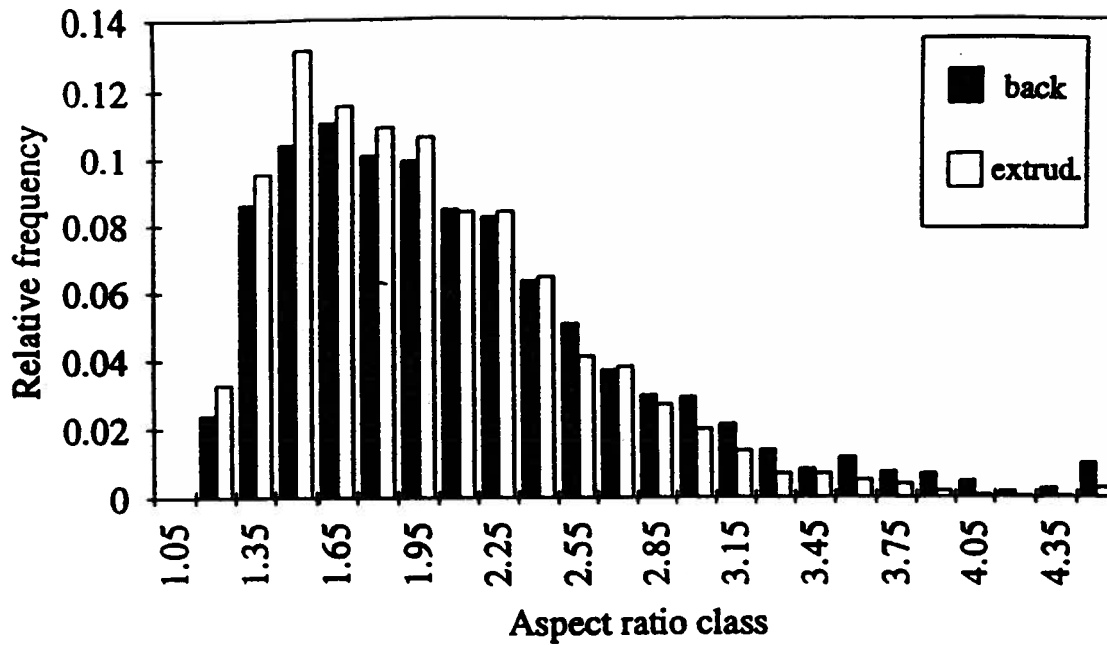


Figure 7.24 Aspect ratio of alumina particles of 6061/Al₂O₃/20p in back end of a billet and in extrudate

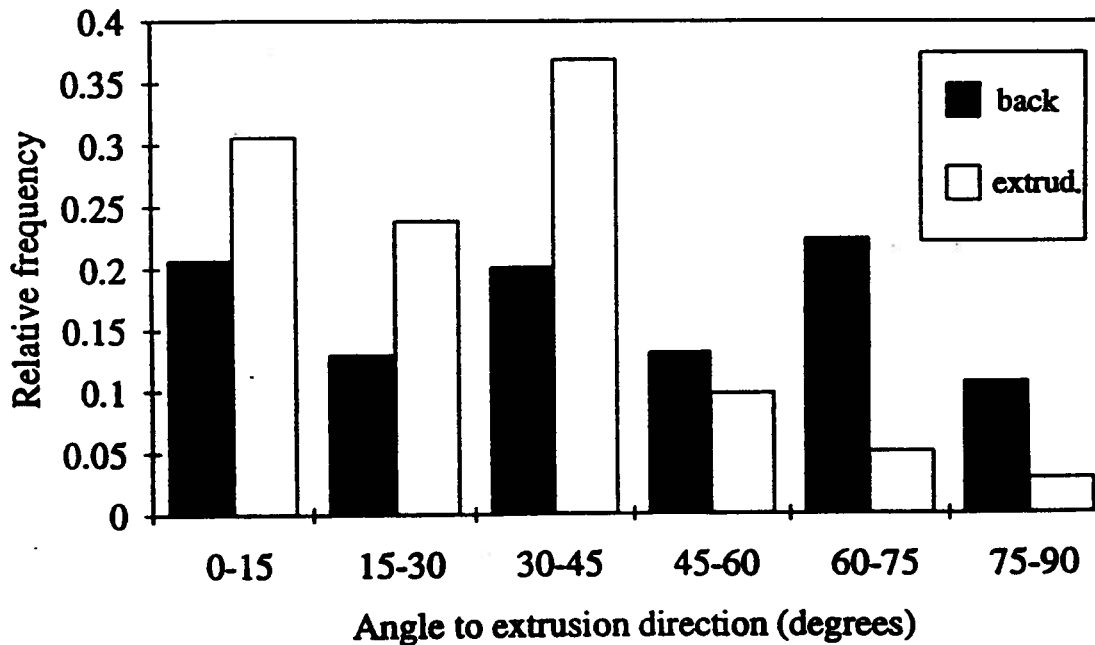


Figure 7.25 Orientation of alumina particles of 6061/Al₂O₃/20p in back end of a billet and in extrudate

stress, which may cause deterioration of the mechanical properties of the MMCs, based on the studies on the materials at low temperature^[92-95, 122].

7.5.1.2 Particle Size Refinement after Extrusion

To quantify the change in particle size during processing, the particle size distribution at two locations was analyzed, at the back end of the billet (Locations 4 and 7 in Fig. 7.4), and from the longitudinal section of the extrudate. The statistical results shown in Table 7.6 reveal that the variables characterizing particle size, such as particle area, maximum and minimum dimension, and even aspect ratio, are greater at Locations 4 and 7. The smaller relative coefficients of particle size at Locations 4 and 7 indicate that the particle size distribution is more uniform in the material before extrusion; in other words, some particles fracture into smaller pieces during extrusion. This can also be seen through the distribution of the maximum and minimum particle dimensions (Figure 7.23(a)-(b)). The increase in number of small particles is quantified. The decrease in mean aspect ratio of particles is accompanied by a rise in the class of particles with an aspect ratio close to one, as shown in Figure 7.24. The orientation distribution of particles is distinct in Figure 7.25.

7.5.2 Particle Fracture Modes during Extrusion

The tendency for the particle size distribution to skew towards lower size classes is in accord with observations of material deformed at low temperature under hydrostatic pressure^[76] (Fig. 7.23(a) and (b)). Such observations are indicative of the comminution of particles^[98] (Comminution mode in Fig. 7.26(a)). It is also noted that in the transverse section of the extrudate there appear to be substantially more small particles than in the longitudinal section: this is, in part, an effect of particle re-orientation. It was observed that fractured pieces healed due to the low flow stress of the matrix material and high hydrostatic pressure

encountered during extrusion, which results in matrix material being forced into cracks^[75,90]. This feature is the major difference between low strain/low temperature and large strain/high temperature behavior. However, at high temperature, under tensile stress, the PRMMCs tend to form voids behind the particles^[101]. This will be discussed in more detail in subsequent chapters.

Particle re-orientation during extrusion may also have an effect on the propensity of particles to fracture. It was interesting to note that most of the cracks in the particles (fracture gap) were parallel to the flow direction, and particles seem to be most affected when they lie parallel to the extrusion direction in the longitudinal section of the extrudate. This may be caused by the shear stress acting on the particles under high hydrostatic pressure (Shear mode in Fig. 7.26(b))^[99].

The skewing of the aspect ratio data (Fig. 7.24) suggests that particles with a large aspect ratio are more likely to fracture during extrusion. From the microstructure examination, some cracks were observed perpendicular to the flow direction for those particles with a large initial aspect ratio. The fracture may result from tensile load transfer between the matrix and the particle due to its large initial aspect ratio. A tensile mode of particle fracture was therefore proposed during extrusion (Fig. 7.26(c)). This is also a fracture at low temperature in the loading direction^[76], and is retained at high temperatures.

Based on the above analysis, three basic modes are proposed for particle fracture during extrusion, i.e., the comminution mode, the shear mode and the tensile mode (Fig. 7.26). Particle fracture during extrusion is a very complex phenomenon. Not only does a single mode function, but particle fracture may be affected by a combination of two or even three modes at the same time, especially for particles in a cluster. However, from

microstructural examination, the shear mode may be more applicable in the shear deformation zone, where most of the deformation occurs; the tensile mode may be more effective at the position where elongation is very severe, such as near the die exit zone; and the comminution mode may occur anywhere in the deformation zone for a single particle, but most probably in clusters where large compressive tri-axial stresses are present.

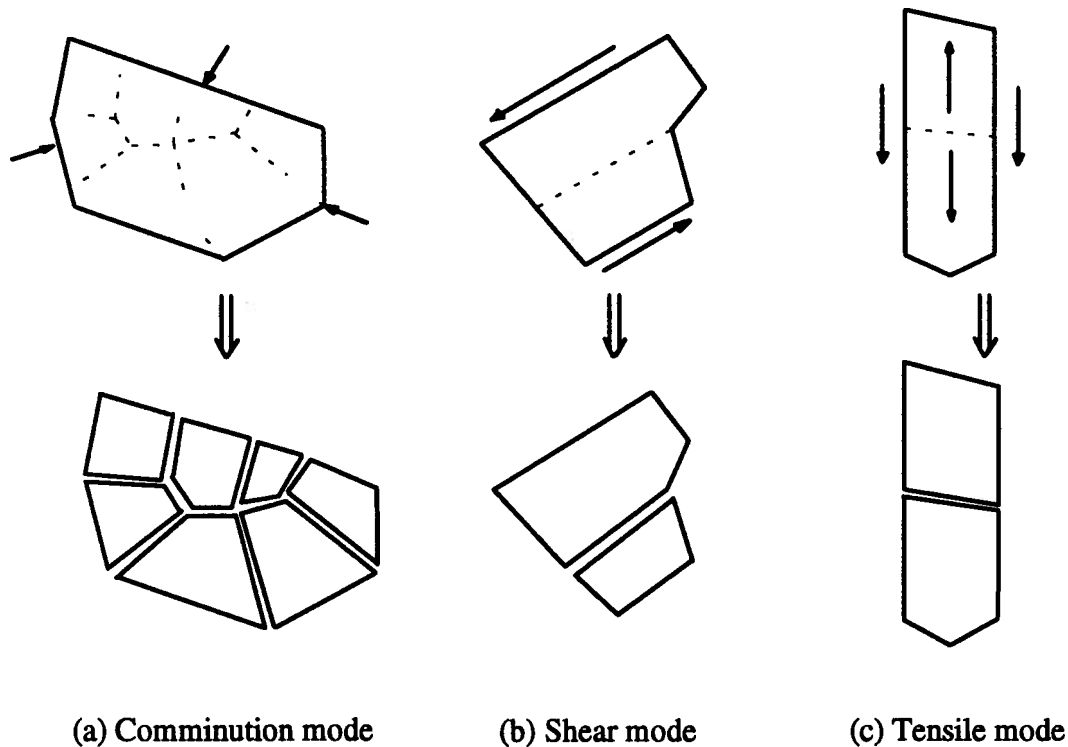


Figure 7.26 A schematic diagram for three particle-fracture modes during extrusion

7.5.3 Correlation between Particle Fracture and Bulk Deformation Behavior

To understand the particle fracture during extrusion, the deformation behavior of the composite billet was analyzed with the aid of DEFORM[®] as described in Chapter 5. A typical effective strain rate distribution near the die exit area at a steady state is shown in Fig. 7.27.

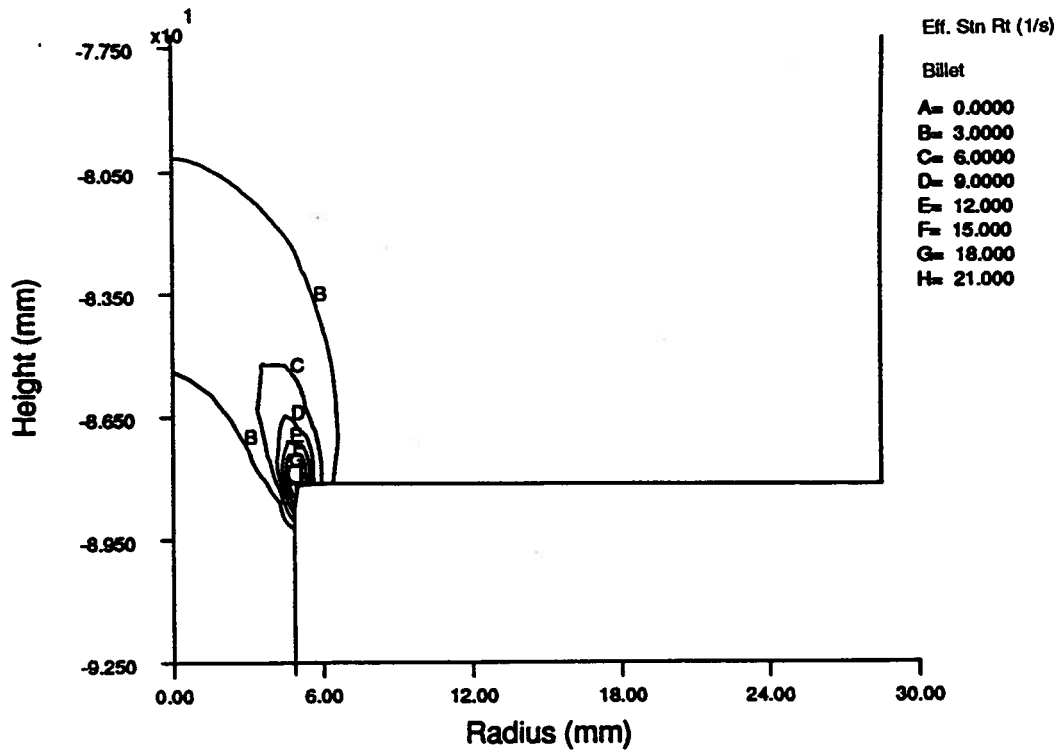


Figure 7.27 Effective strain rate distribution in the deformation zone

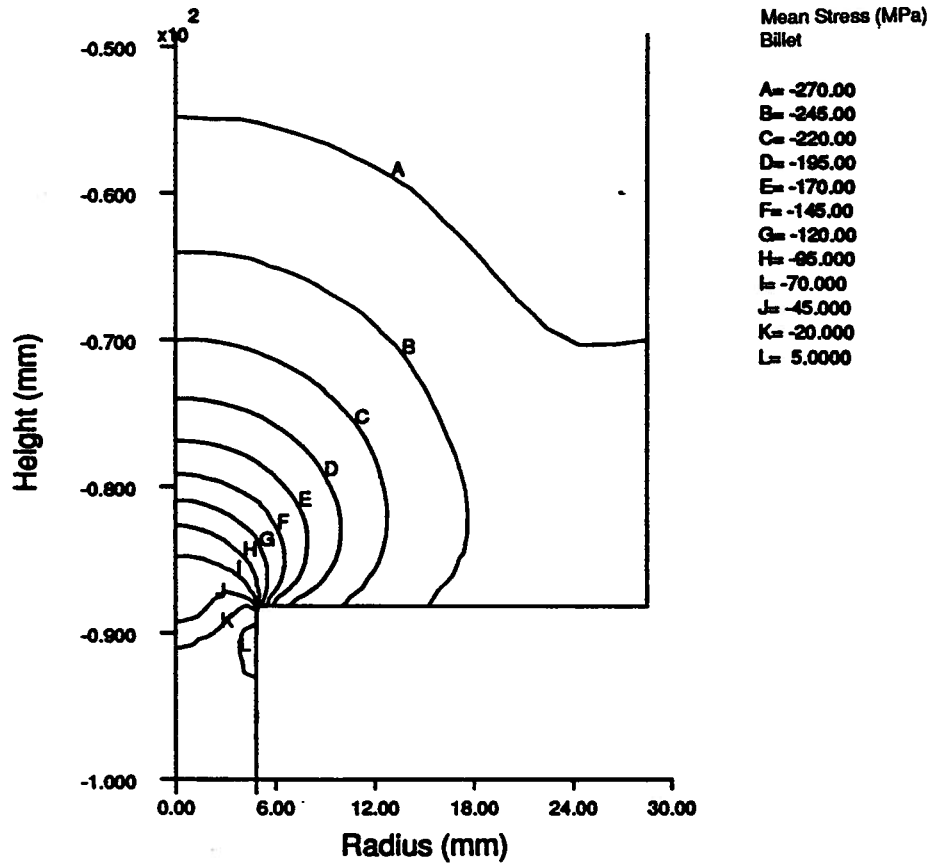


Figure 7.28 Mean stress distribution in the deformation zone

It is seen that the highest strain rate is reached at the die throat, where metal flow was choked. Therefore, most severe particle fracture could occur in this choked zone. This is also consistent with the particle fracture probability prediction in Section 7.4.3. The mean stress (hydrostatic stress) corresponding to the strain rate state is shown in Fig. 7.28. It is evident that over most of the billet, the stress state is in compression (negative value), and a very high hydrostatic pressure exists in the deformation zone. Comminution of a particle or particles in a cluster could result under such a large hydrostatic pressure which may also heal the fractured particle under the large deformation during extrusion (Comminution mode). However, near the die exit zone, tensile stresses appear, especially at the die-bearing interface, which is due to high elongation of the billet and the friction stress at the die interface. These tensile stresses could lead to particle fracture (Tensile mode), or voids behind particles. FEM model predictions confirm the existence of a large shear zone during extrusion, as shown in Fig. 7.29. In this shear zone, velocity gradients appear from the dead metal zone to the deformation zone. As a particle flows along the shear direction, the shear deformation forces the particle to rotate into the flow direction (which finally leads to an alignment of the particles along the extrusion direction). However, if the stress in the particle from both the shear and the hydrostatic pressure is large enough, the particle could fracture (Shear mode); healing could consequently occur if the matrix material intrudes into the gap of the crack under high hydrostatic pressure or the fractured pieces were shifted apart because of the velocity gradient under large deformation^[11]. Evidence of particle fracture and healing are presented in this chapter.

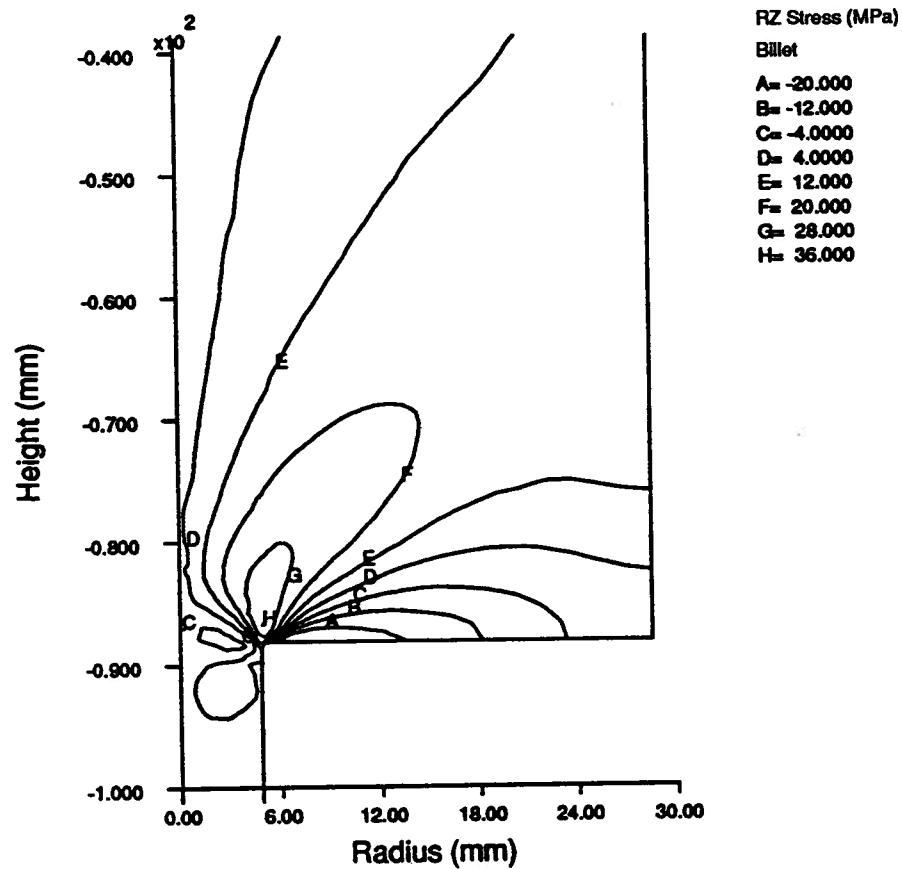


Figure 7.29 Shear stress distribution during extrusion

7.6 Summary

Macro- and micro-examination of a billet during extrusion sheds light on the metal flow pattern and particle fracture. It was found that the particles fractured in the severe shear deformation zone at the die throat, but most fractured parts healed in the extrudates due to the high temperature and large hydrostatic pressure, which has also been confirmed by Duralcan USA^[105]. Some major findings are summarized below.

(i) Due to adhesion friction between the billet and the container in hot extrusion, a particle-free layer was formed at the interface, and the particle-free matrix material flows into the shear deformation zone to form a particle-free band in the extrudates in the extrusion direction. In this zone, very few particles reside, and therefore there was less fracture of the particles;

(ii) More obvious particle alignment along the flow direction was observed in the severe deformation zone than in the dead metal or hard-to-deform zone under the pressure pad. The formation of the particle-free bands along the extrusion direction was obviously due to the elongation of the particle-free zone in the as-cast material during extrusion. The frequency of particle fracture depended on deformation conditions. In the deformation zone, more fractured particles were observed than in the dead metal zone, but most severe particle fracture occurred in the shear deformation zone at the die throat. The fractured parts were healed due to the low flow stress of the matrix material at high temperature and the large hydrostatic pressure. However, clusters in the hard-to-deform zone under the pressure pad, or even in the dead metal zone, showed evidence of particle fracture due to the comminution effects. In the dead metal zone, some particles were cracked, but not separated, due to small deformation;

(iii) Most of the single particles that fractured had a large aspect ratio or sharp corners. Equiaxed particles were much harder to fracture; all the large particles which remained unfractured in different zones had an aspect ratio close to unity;

(iv) Many cracks in particles were in the flow direction due to shear deformation, but some cracks perpendicular to the flow direction were also observed, especially in particles

with a large aspect ratio. This was probably due to the tensile stress in the particle in the flow direction.

The size and distribution of the particles in the extrudates have also been examined using both an optical microscope and an image analyzer. Comparing the transverse section with the longitudinal section, some important features are:

(i) Orientation of the cracks in the transverse section was randomly distributed. However, many of the cracks in the particles in the longitudinal section were either parallel or perpendicular to the extrusion direction. Most of the particles with an aspect ratio greater than one were aligned in the extrusion direction;

(ii) Particles with a different aspect ratio were observed in both the transverse and the longitudinal sections. Larger particles especially with sharp corners or large aspect ratios, and those in clusters, fractured more easily. More small particles were found in the transverse sections than in the longitudinal section, partly because of re-orientation of particles during extrusion;

While comparing the extrudate of 6061/Al₂O₃/10p to that of 6061/Al₂O₃/20p, it was found that:

(i) Particles were much smaller in 6061/Al₂O₃/10p than in 6061/Al₂O₃/20p. However, the particle distribution was less homogeneous in 6061/Al₂O₃/10p than in 6061/Al₂O₃/20p, i.e., more clusters and more particle-free bands remained in the extrudates of 6061/Al₂O₃/10p;

(ii) The mean aspect ratio of particles in 6061/Al₂O₃/10p was less than that in 6061/Al₂O₃/20p.

Quantitative metallography and statistical analysis were conducted using an image analyzer. The particle dimensions, such as minimum and maximum dimension, area, aspect ratio, and particle orientation were quantified at different positions in the deformation zone.

The most salient points are:

(i) Particle alignment along the extrusion direction was confirmed. Particle fracture during extrusion leads to more smaller particles. The average aspect ratio of the particles after extrusion is around 1.74 to 2.07 with more uniform size distribution in 6061/Al₂O₃/10p than in 6061/Al₂O₃/20p. The mean size of the particles in the longitudinal section is larger than in the transverse section due partly to re-orientation of particles during extrusion. However, the particle distribution is more uniform in the transverse section than in the longitudinal section;

(ii) The four-fold difference in size of particle area in the extrudates between 6061/Al₂O₃/10p and 6061/Al₂O₃/20p is mainly due to a difference in initial particle size of the composites. The change in particle size, size distribution, homogeneity, and orientation, and healing of the 'damage' which accompanies a fracture event, may all have benefits for the in-service mechanical properties of extruded components. However, the influence of particle fracture on mechanical properties, the correlation between the particle size and the deformation parameters, and the mechanism of the low speed cracking, need to be clarified.

Chapter 8 ORIGIN OF LOW SPEED CRACKING DURING EXTRUSION OF THE PRMMCs

The particle fracture analysis presented in the previous chapter revealed the improvement in homogeneity of particle distribution and particle size refinement after extrusion. This could be beneficial with respect to mechanical properties of the composites. However, low speed cracking was observed in the plant trials at UAC, which is specific to the composite material. It is essential to explore the mechanism of the low speed cracking during extrusion.

8.1 Microstructure Examination of Low-speed Cracks

As observed in the plant trial at UAC, low speed cracking occurred at the front end of extrudates in most of the trials. Although some explanation for the low speed cracking was proposed by researchers, as described in Chapter 2, it was incomplete because the interaction between the particles and the matrix were not considered. To study the mechanism of low speed cracking, extrudates with severe low speed cracks were cut and polished to examine both longitudinal and transverse sections. The samples were cut from the front end of the extrudates of J94-14 and J94-20 of 6061/Al₂O₃/20p with very severe low speed cracking, and J94-11B of 6061/Al₂O₃/10p with slight cracking. The polishing procedure of Table 7.2 was followed by using an automatic polishing machine at UBC. The samples were examined under an SEM, because it is harder to investigate void formation by using an optical microscope, due to its low depth of field. Before examination, a very thin film of Au-Pd was sputter-coated on the surface of the polished specimens for about 4 minutes for 6061/Al₂O₃/20p, and

about 3 minutes for 6061/Al₂O₃/10p samples. As a result, good contrast between the particles and the matrix was obtained with little electronic charging of the Al₂O₃ particles. Under the SEM, it was found that the low speed cracks penetrated into the surface layer, and that extensive voids existed around the low speed crack tips in all three samples, as shown in Fig. 8.1 for J94-14. It is seen that most of the voids were associated with particles and located at the two ends of particles in the extrusion direction (orientation of particles with large aspect ratio in the picture). The same phenomenon was also observed around the crack tips of J94-11B for 6061/Al₂O₃/10p, as shown in Fig. 8.2. This is due to the tensile stress state in the matrix between particles in the flow direction, as predicted by the micromechanical analysis in Chapter 6.

It is interesting to note that more severe low speed cracking was observed in J94-14 of 6061/Al₂O₃/20p than in J94-11B of 6061/Al₂O₃/10p, although the initial billet temperature of J94-14 was higher at 461 °C than 434°C used for J94-11B, as listed in Table 4.3. This is due to the fact that the lower volume fraction results in higher ductility of the composite, while the fracture behavior is controlled by exhaustion of matrix ductility due to the constraints on matrix plastic flow by the elastic reinforcing particles^[122]. A high volume fraction of second phase particles results in more severe constraints of the matrix flow around the particles during extrusion, although the 6061/Al₂O₃/10p composite has a less uniform distribution than the 6061/Al₂O₃/20p composite, as described in Chapter 7. Crushed particles were also observed at the surface which form the minor defects observed in the extrudate surface. Cracked particles in clusters remained without evidence of healing, although interface decohesion seems to be dominant in the surface layer.

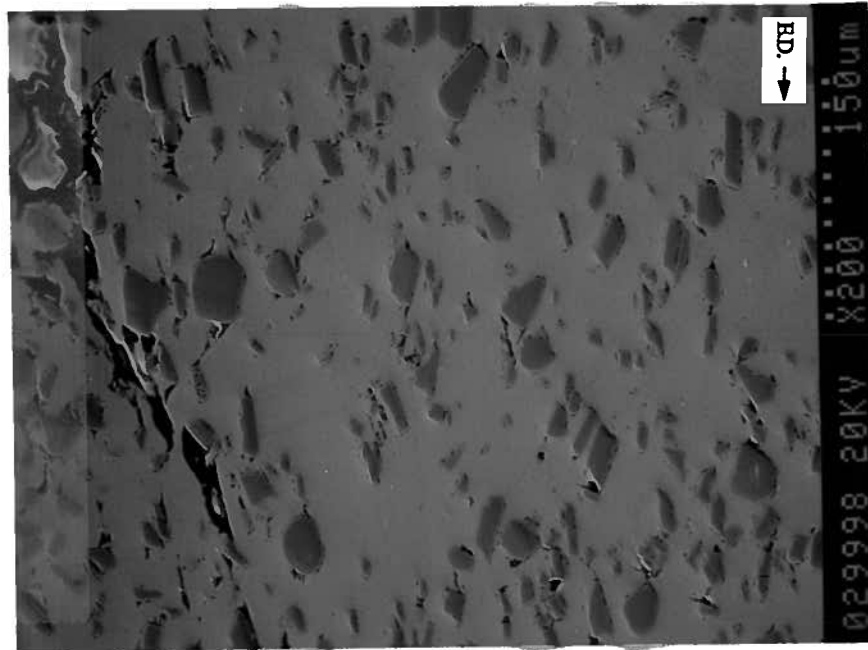


Figure 8.1 Void formation near a low speed crack tip of J94-14 of 6061/Al₂O₃/20p in longitudinal section

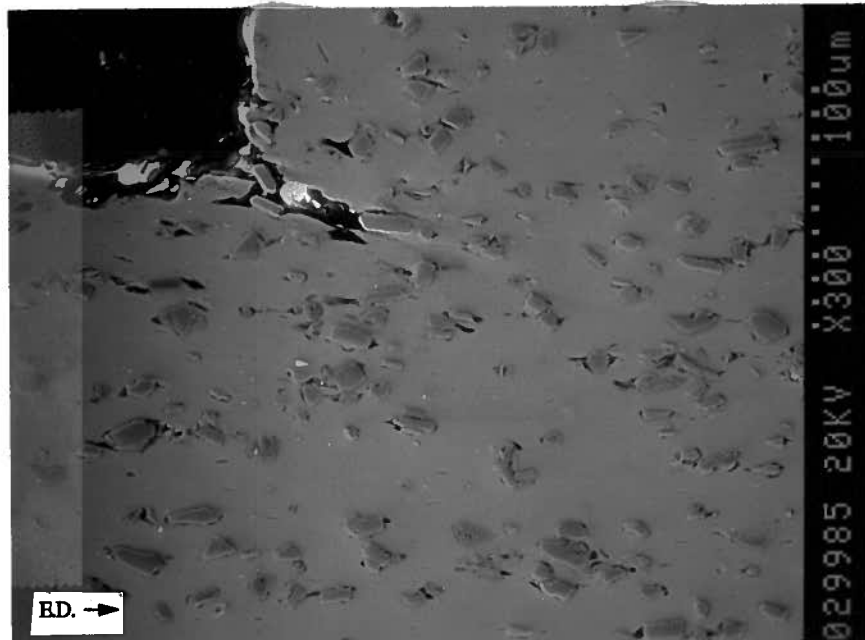


Figure 8.2 Void formation near a low speed crack tip of J94-11B of 6061/Al₂O₃/10p in longitudinal section

8.2 Particle Behavior and Microscopic Damage

The above microstructure indicates that the low speed cracking is associated with particle behavior and its consequent microscopic damage, such as particle fracture and void formation. Therefore, particle behavior and its constraints to the plastic flow of the matrix material becomes important.

Micromechanical analysis of particle behavior under both the plane strain and the cylindrical compression has been conducted in Chapter 6. All the particle models (Single-, Twin- and Multiple-particle Model) predict a localized deformation behavior around the particle, although the overall deformation behavior of a specimen with and without a particle are quite similar to each other. It is the localized deformation that intrinsically leads to dynamic microstructural evolution (such as particle fracture, void formation, etc.) during extrusion.

8.2.1 Particle Fracture

At a microscopic level, the predicted localized matrix flow in the vicinity of large alumina particles, especially at both the sharp ends of angular particles and in the vicinity of particle clusters, was confirmed for alumina particulate reinforced metal matrix composites by Ferry and Munroe in the form of shear bands in the matrix around the particles, based on their microstructural study in Al/Al₂O₃ composites^[111]. They also found that large particles and those with a high aspect ratio had the greatest propensity to fracture during deformation. Some particles fractured into very fine (1-2 μm) pieces and redistributed along the shear band during deformation. These observations are also consistent with the single-particle model prediction of different shapes of a particle during cylindrical compression and with the prediction of particle migration in the plane strain simulation. The interaction between the

particles and the matrix is mutual: the particles in a cluster and those with an irregular morphology force the matrix to deform in a highly constrained manner (localized deformation), and the highly deformed matrix material inversely affects the particle behavior, e.g., the rotation and migration of the particle, and consequently the stress state in the particle. Therefore, matrix flow and particle behavior are very much temperature dependent. If the temperature is low, the matrix work-hardens more easily and the stress in the particle will be higher, which in turn leads to particle fracture. Because the flow stress of the matrix at low temperature is high, the cracked parts are harder to heal by intrusion of matrix material into the gap. In contrast, at high temperature, due to the low flow stress, there is little work hardening and the matrix flows more easily around the particle. Consequently, the stress in the particle is low and the particle is harder to fracture. Even if a particle fractures, the cracked parts heal easily by matrix intrusion into the crack under hydrostatic pressure, or the two cracked parts are separated away by shear deformation, as observed in extrusion processing. A tensile stress was predicted in a particle with an aspect ratio of 2 under plane strain conditions at a reduction of 10%, as shown in Fig. 8.3. This is consistent with the proposal of the 'Tensile mode' of particle fracture during extrusion, i.e., if a particle moves in the matrix flow direction, a tensile stress is generated in the particle. The larger the aspect ratio, the higher the tensile stress, and consequently, the higher the propensity to fracture. This is also predicted by study of particles with different aspect ratios under a plane strain condition, which have some similar deformation characteristics to the extrusion process (Table 8.1). The table shows that generally a particle with a large aspect ratio has a higher internal tensile stress in the flow (x) direction. However, as the reduction increases, the tensile stress

decreases. This is because the interparticle spacing increases, and subsequently, the interaction between the two particles becomes weaker.

Table 8.1 Tensile stress in particles and matrix at different reductions

Aspect Ratio	Object No. (Material)	Reduction: 10%		Reduction: 30%		Reduction: ~50%	
		Min. (MPa)	Max. (MPa)	Min. (MPa)	Max. (MPa)	Min. (MPa)	Max. (MPa)
A.R.=1	#2(Matrix)	-50	42	-51	30	-64	38
	#4(Particle off C.L.)	-8	83	-28	89	-45	72
	#5(Particle @ C.L.)	-4	89	-18	69	-34	50
A.R.=2	#2(Matrix)	-131	125	-60	54	-57	34
	#4(Particle off C.L.)	9	158	-12	84	-26	55
	#5(Particle @ C.L.)	56	170	8	92	-24	54

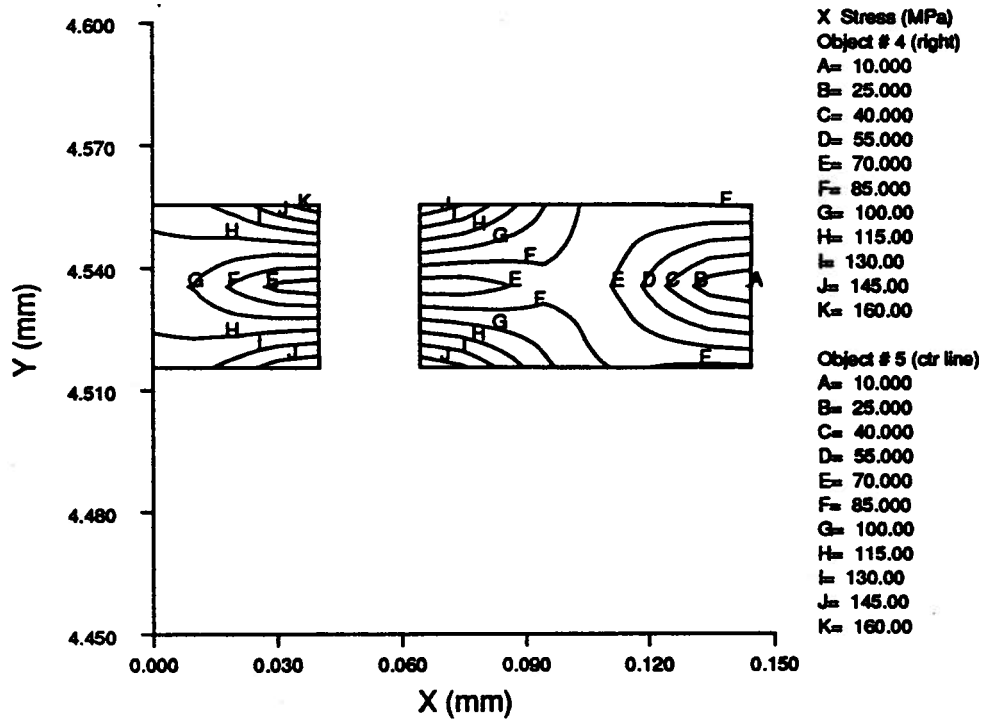
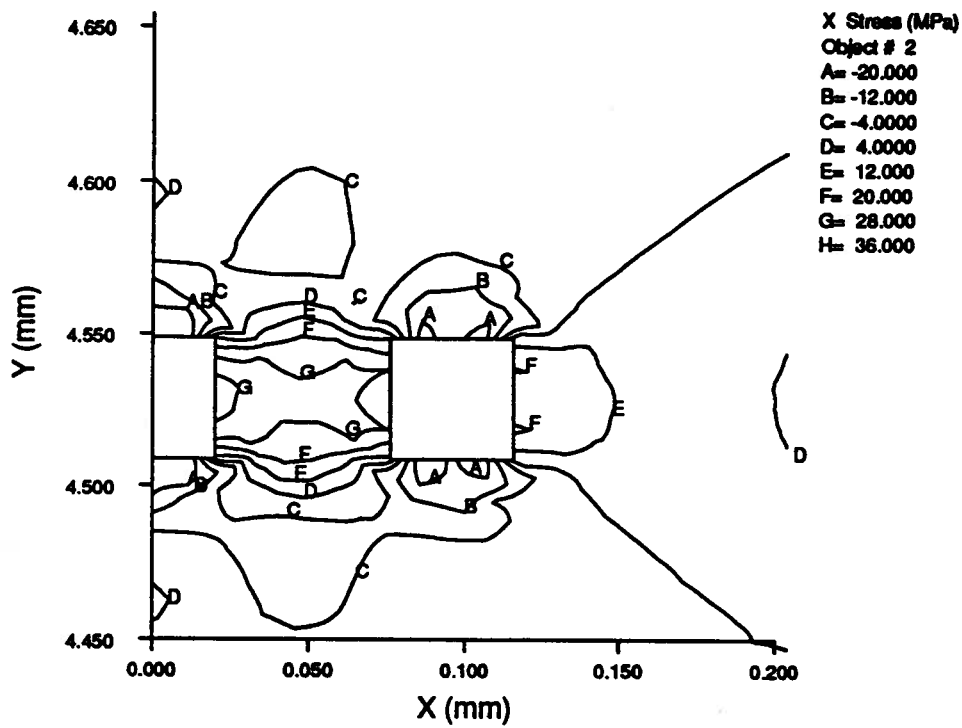


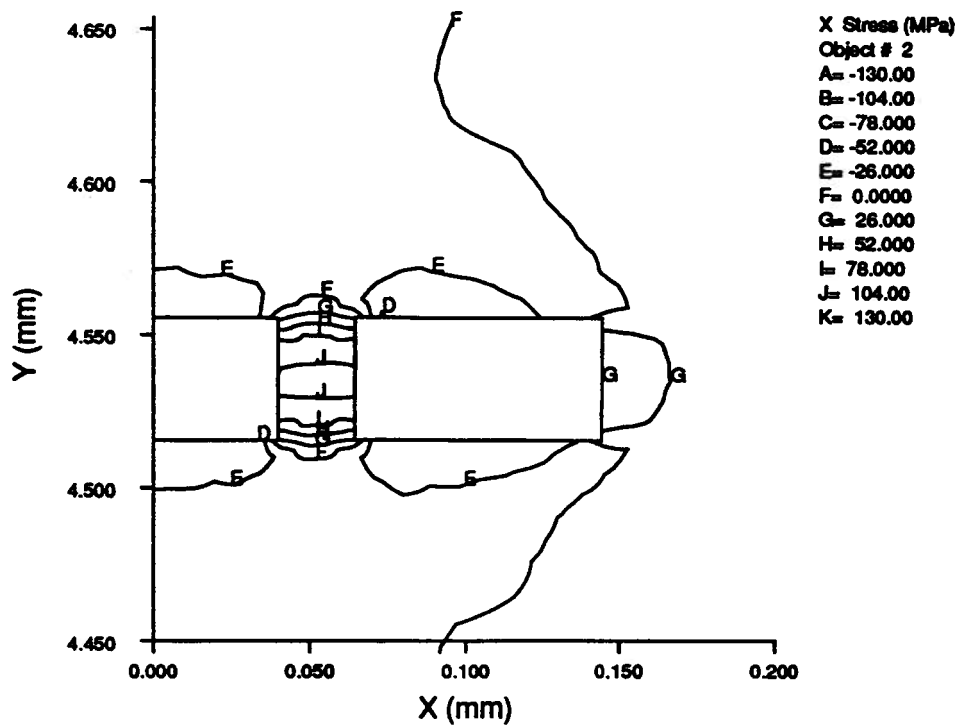
Figure 8.3 Tensile stress in a particle under plane strain condition at a reduction of 10%

8.2.2 Void Formation

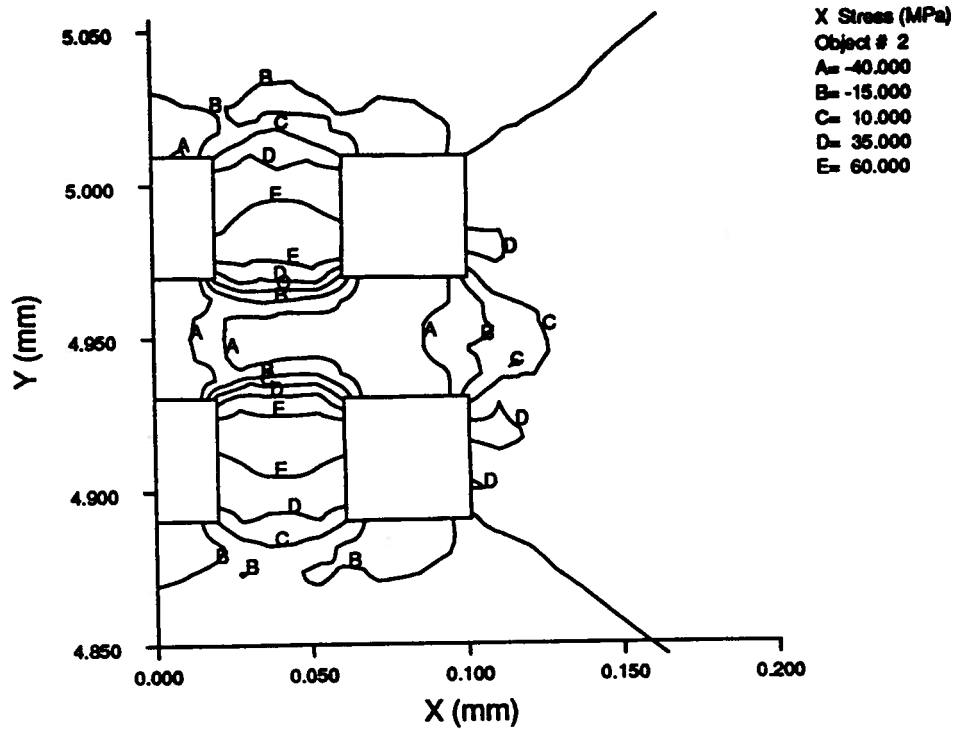
Voids have been observed with an SEM in the surface layer of some extrudates with severe low speed surface cracking, as described in Section 8.1. It was found that voids were more frequently present at the ends of two closely spaced particles which were aligned in the extrusion direction. The void formation could be explained by the local stress state owing to the presence of the particles. Figure 8.4 shows the tensile stress (σ_x) distribution around the particles at a reduction of 10% under the plane strain condition. A high tensile stress zone is generated between two particles in the x-direction. A smaller spacing ($20\mu\text{m}$) between the two particles with a large aspect ratio leads to a higher value of the tensile stress in the interparticle zone (see contour line value of 'J' of 104 MPa in Fig. 8.4(b) and compared to the contour line 'G' of 28MPa in Fig. 8.4(a) for a particle spacing of $40\mu\text{m}$). A high tensile stress value is also predicted for the multiple-particle model at a reduction of 1% (see contour line 'E' of 60MPa in Fig. 8.4(c)). This implies that in the matrix material within closely spaced particles, such as within a cluster, it is easier to initiate voids. The predictions are consistent with the results obtained by Poole et al.^[113-114]. It is interesting to note that the tensile stress component in the x-direction in the center zone of the monolithic material with no particles present is less than 6MPa, although all the other simulation conditions are the same, as shown in Fig. 8.5.



(a) Twin-particle model with a unity aspect ratio at a reduction of 10%



(b) Twin-particle model with an aspect ratio of 2 at a reduction of 10%



(c) Multiple-particle model with a unit aspect ratio at a reduction of 1%
Figure 8.4 Tensile stress distribution in the matrix and around particles

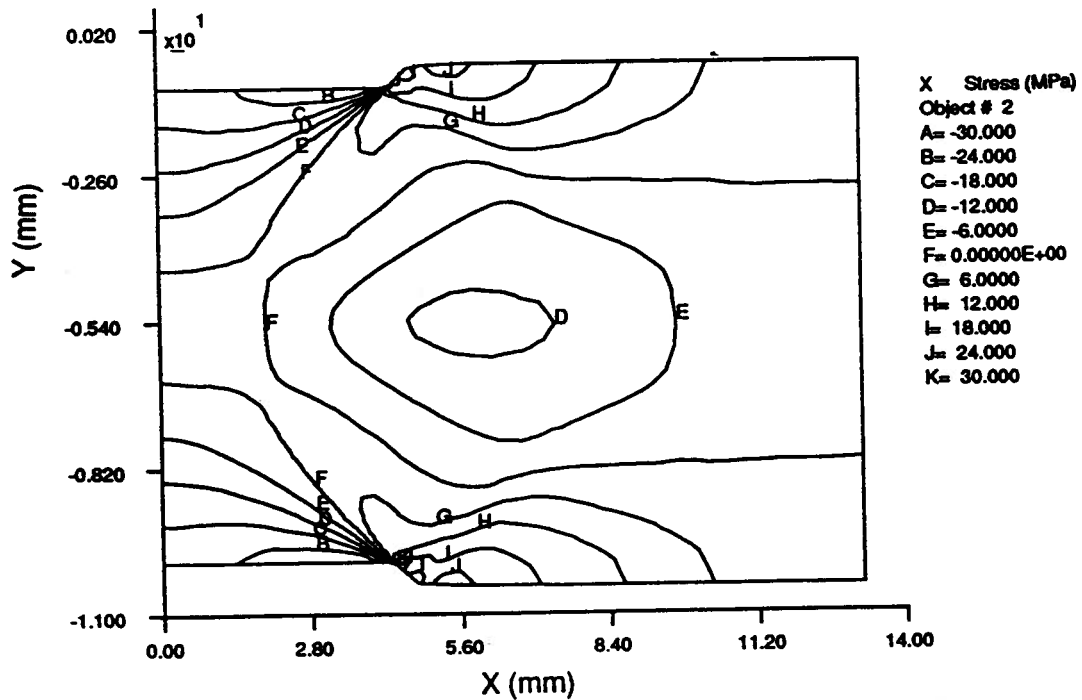


Figure 8.5 Tensile stress distribution in the monolithic material
at a reduction of 10% under plane strain condition

Therefore, even though the monolithic stress state is compressive, a local tensile stress component around particles may exist. It is the local tensile stress behind a particle in the flow direction which leads to void formation, as observed in the extrudates. The hydrostatic pressure helps to stop void formation and growth during extrusion which explain why the elastic modulus of the extrudates does not decline as the extrusion ratio increases.

8.3 Effect of Processing Parameters on Low Speed Cracking

From the microscopic analysis in the above section, it is known that low speed cracking is related to the presence of a tensile stress both in the particle and in the matrix, which might lead to particle fracture and void formation, respectively. However, the microscopic behavior must be related to the macroscopic extrusion parameters, such as extrusion temperature, speed and the material itself. The temperature is, however, affected by many factors such as ram speed, initial billet and die temperature and die material, etc.. An effort has been made to explore the origin of low speed cracking during extrusion with the aid of the finite element model, DEFORM[®].

The temperature distribution of both the billet of 6061/Al₂O₃/20p and the die near the die exit zone, during extrusion at steady state, is shown in Fig. 8.6. The simulation conditions are listed in Table 8.2. It is evident that the billet temperature is increased to about 460°C from the initial value of 425°C due to the heat of deformation for an extrusion ratio of 34; and the die interface also heats up due to heat conduction. Obviously, the thermal diffusivity of the die material is also very important to the temperature distribution in both the extrudate and the die interface. Figure 8.7 shows the tensile stress builds up at the die land area in the extrudate during extrusion. All the other zones in the billet are in a compressive stress, which

may help prevent void growth or crack formation. Apparently, both the temperature and tensile stress in this die land zone are crucial to the low speed cracking. As described in the last section, the fracture behavior of the composite is controlled by exhaustion of matrix ductility due to the constraints on matrix plastic flow by the elastic reinforcing particle^[122]. Therefore, the lower the billet temperature in the die land zone, the lower the matrix ductility. On the other hand, the larger the tensile stress generated in the surface layer in the die land zone, the higher the propensity for void formation due to local tensile stress near the ends of particles in the extrusion direction, especially for those closely distributed particles (e.g., particle cluster), based on the micromechanical analysis conducted in Chapter 6.

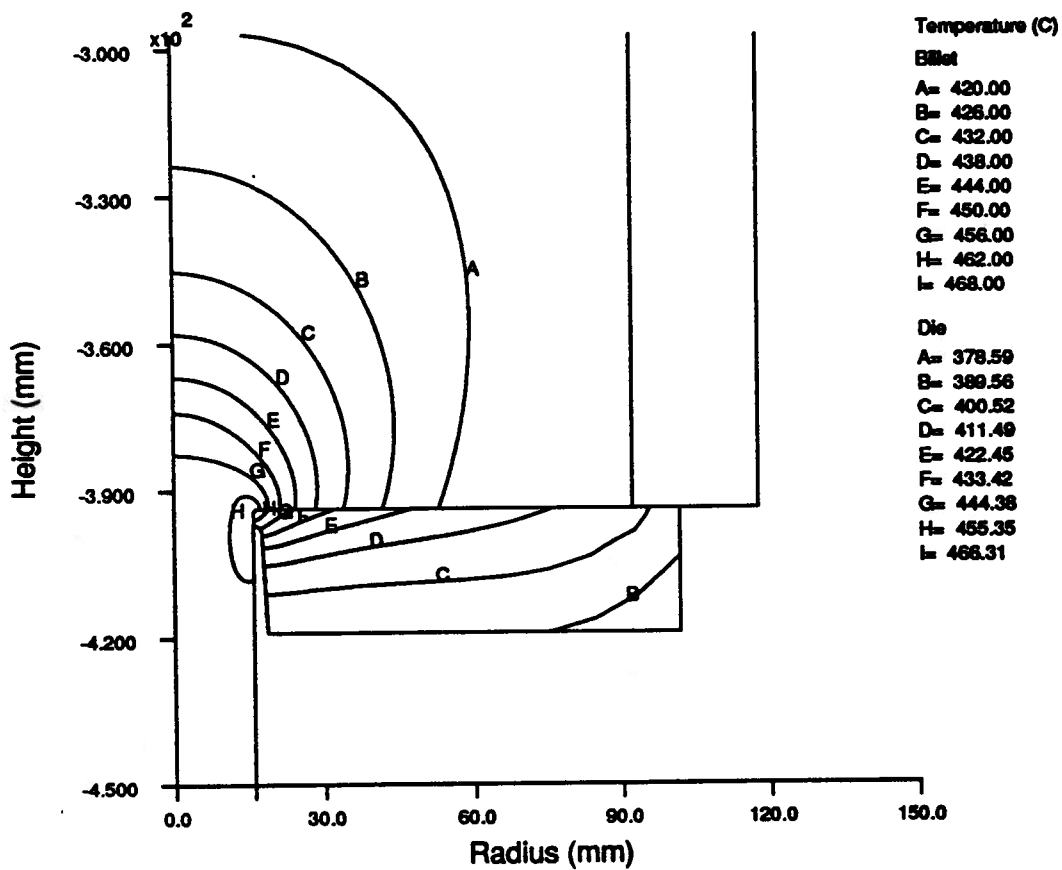
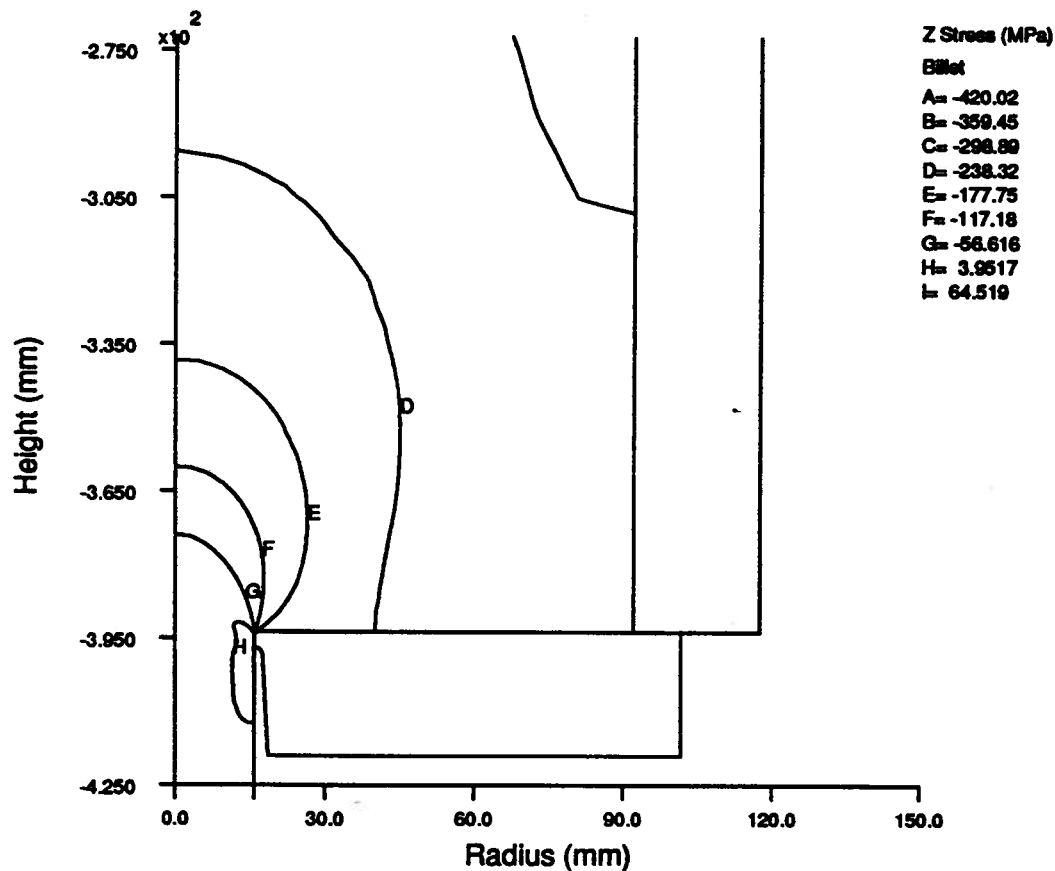


Figure 8.6 Temperature distribution of billet and die at steady state extrusion

Table 8.2 Standard conditions for parametric study

Ram speed:	1mm/s
Initial billet temperature:	425°C
Friction shear factor at the container and die interface:	m=1 (sticking)
Friction shear factor at pressure pad interface:	m=0.7
Initial die temperature:	395°C
Billet diameter:	178mm (7")
Contain inside diameter:	184 (7.25")
Extrusion ratio:	34

Figure 8.7 Tensile stress (σ_z) distribution at the die interface zone

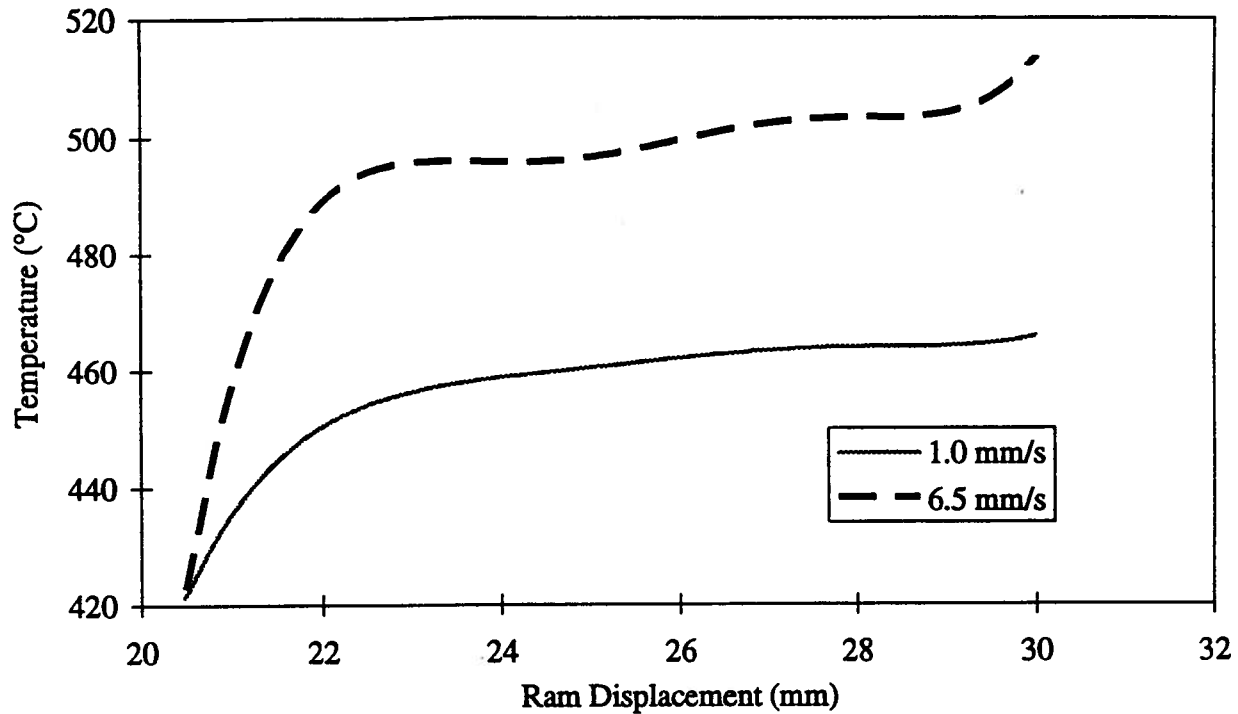
To determine the effect of extrusion variables on the temperature and the tensile stress in the die land zone, a systematic study of the extrusion of 6061/Al₂O₃/20p was conducted for

all the process parameters, such as ram speed, initial billet temperature, initial die temperature, frictional condition at the die interface, extrusion ratio and the billet materials. The standard simulation conditions are listed in Table 8.2.

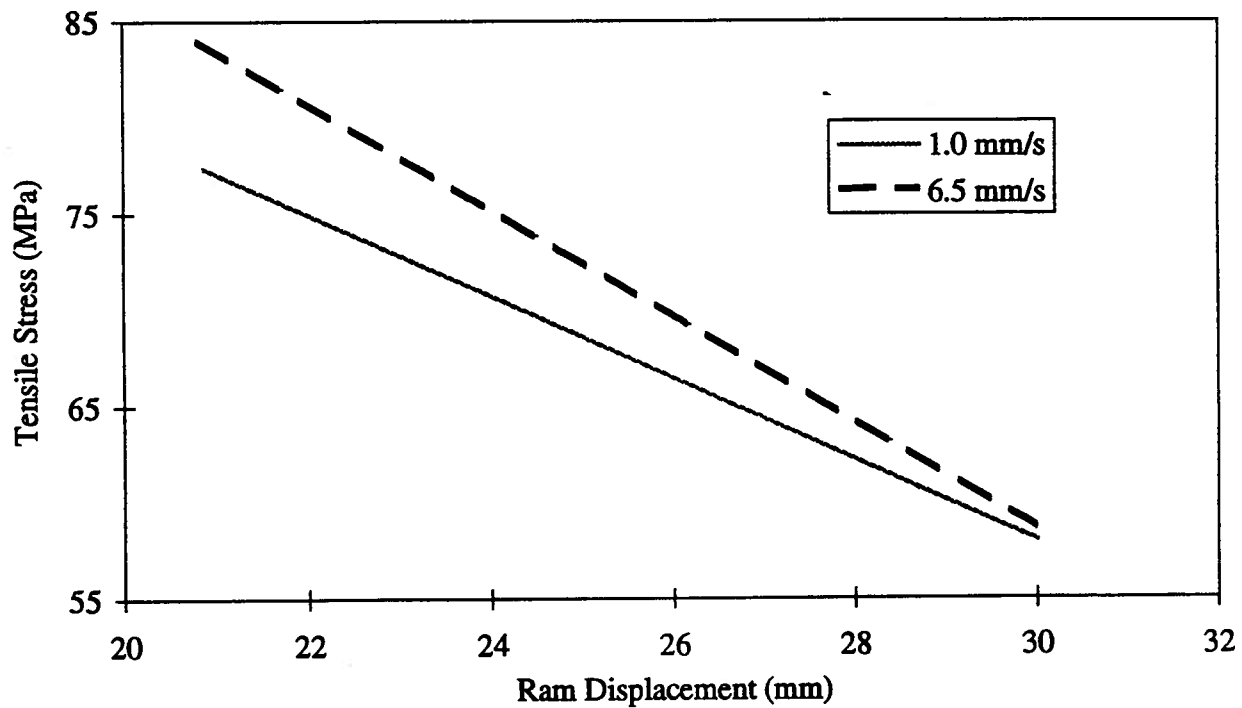
Effect of Ram Speed

Figure 8.8(a) and (b) show the effect of ram speed on the variation of the maximum billet temperature and the maximum tensile stress in the extrudate in the die land zone during extrusion. Figure 8.8(a) shows that the temperature increases much faster at the speed of 6mm/s than at 1mm/s. This is because a higher speed results in a higher heat generation rate, and also the higher speed reduces the time of heat transfer from the extrudate to the die, which generates a steeper thermal gradient near the die interface, as shown in Fig. 8.9. Tensile stress, σ_z , (where Z denotes the extrusion direction) in the die land zone decreases during extrusion, because of the temperature rise (Fig. 8.8(b)). A higher ram speed results in a sharper decrease in the stress value because of the higher heat generation rate. Apparently, the tensile stress value is quite sensitive to the extrusion temperature.

Figure 8.9 shows that the temperature distribution through the whole radius of the extrudate is higher for the ram speed of 6mm/s, and also that the thermal gradient is greater at the interface, due to the shorter heat transfer time. On the other side of the die interface, the thermal gradient is even greater because of the lower thermal diffusivity (the thermal diffusivity of H13 is about 7 times lower than that of the composite material). Again, because of the shorter heat transfer time, the thermal gradient is greater for the ram speed of 6mm/s and the inside temperature of the die is even lower than that of the ram speed of 1mm/s.



(a) Maximum temperature in the die land zone during extrusion



(b) Maximum tensile stress in the die land zone during extrusion

Figure 8.8 Effect of ram speed

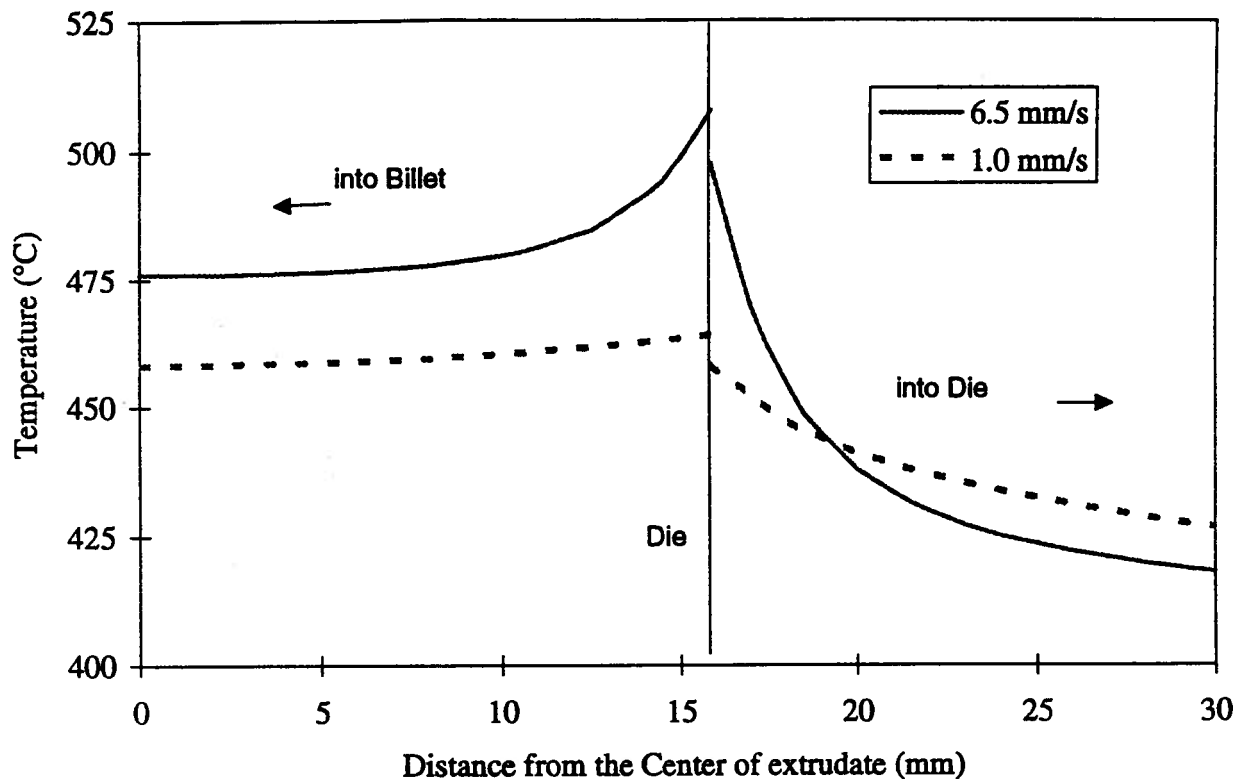


Figure 8.9 Temperature distribution on both side of the die interface at a ram displacement of 30mm

Figure 8.10 shows the effective strain distribution through the whole radius of the extrudate at the die exit. It is seen that the strain distribution is not sensitive to the ram speed, because the strain is more dependent on extrusion ratio. The distribution of stress component in the extrusion direction (σ_z) along the radius of extrudate, indicates that the stress is compressive near the center and gradually becomes tensile near the surface of the extrudate (Fig. 8.11). Obviously, in a surface layer of more than a quarter of the radius of the extrudate there exists a tensile stress in the extrusion direction. The existence of the tensile stress state in the surface layer may promote void formation if the temperature of the billet at the surface in the die land zone is low; this may finally lead to low speed cracking, as was observed.

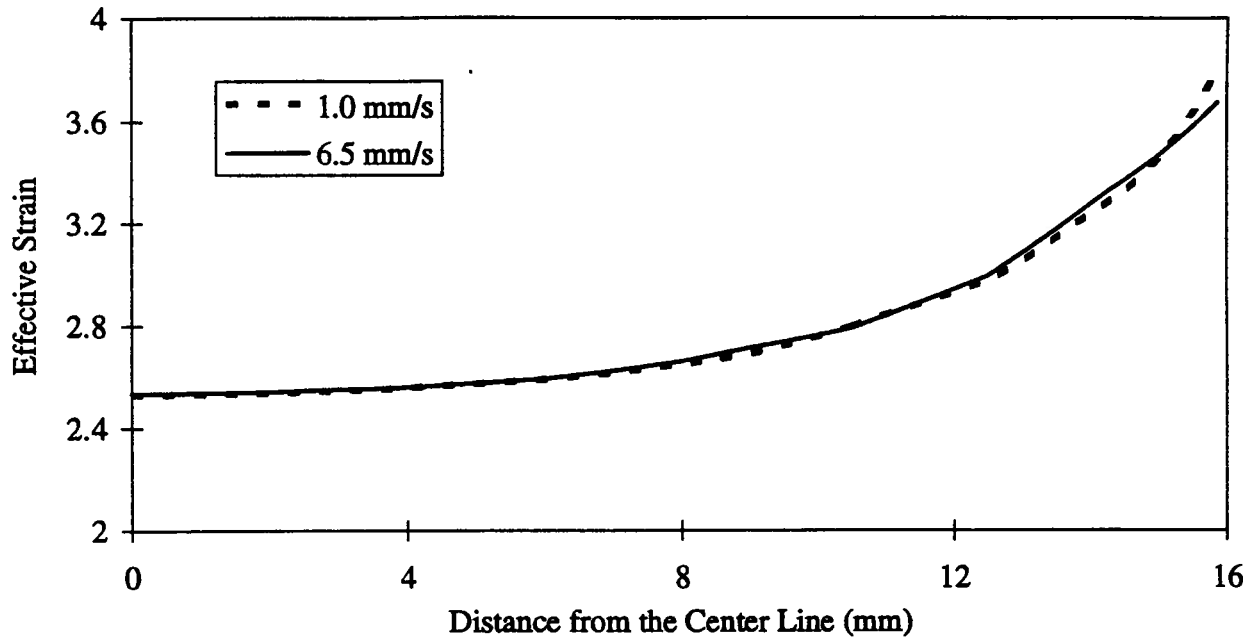


Figure 8.10 Effect of ram speed on strain distribution through radius direction

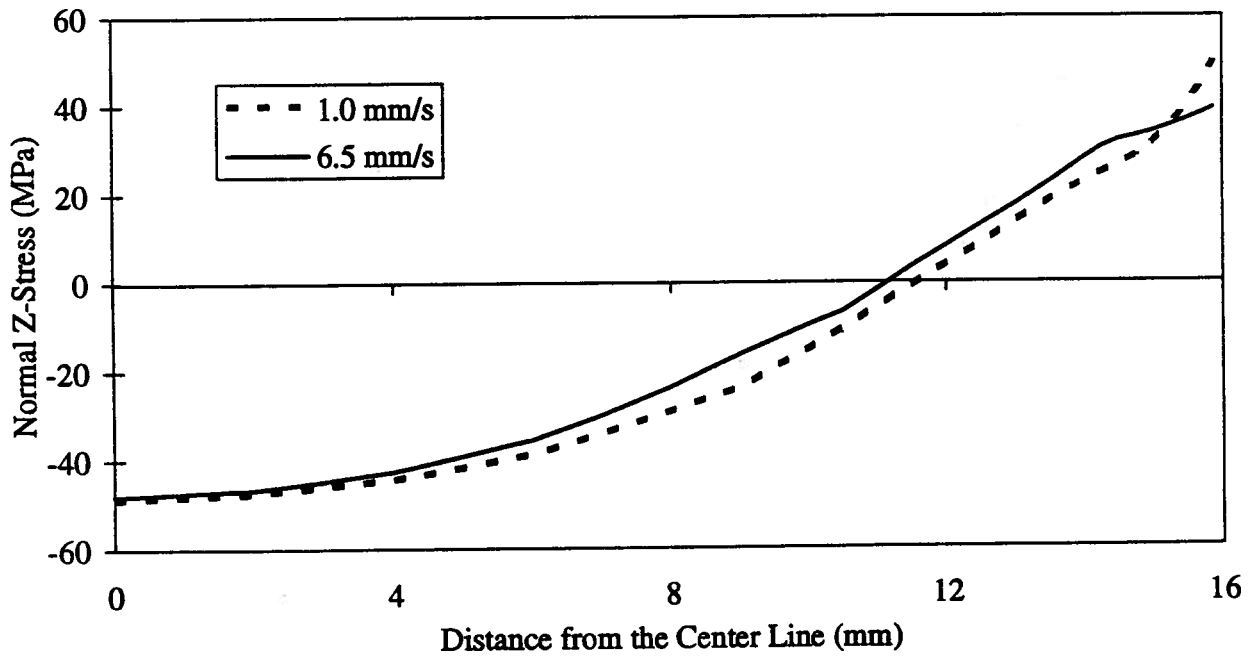


Figure 8.11 Effect of ram speed on stress distribution (σ_z) through radius direction

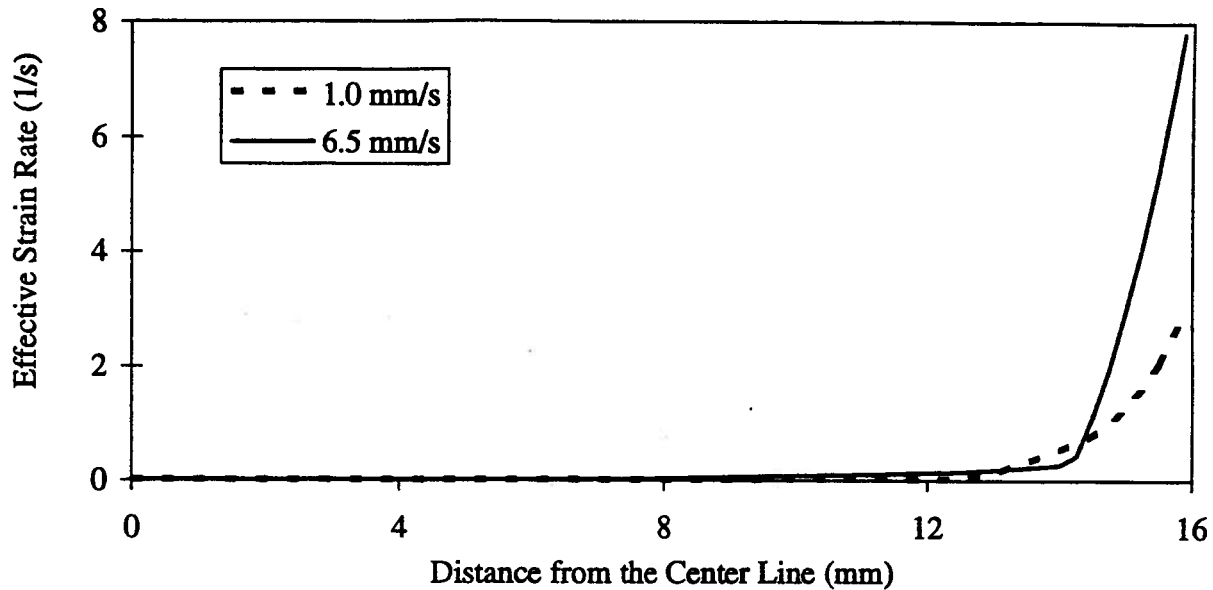
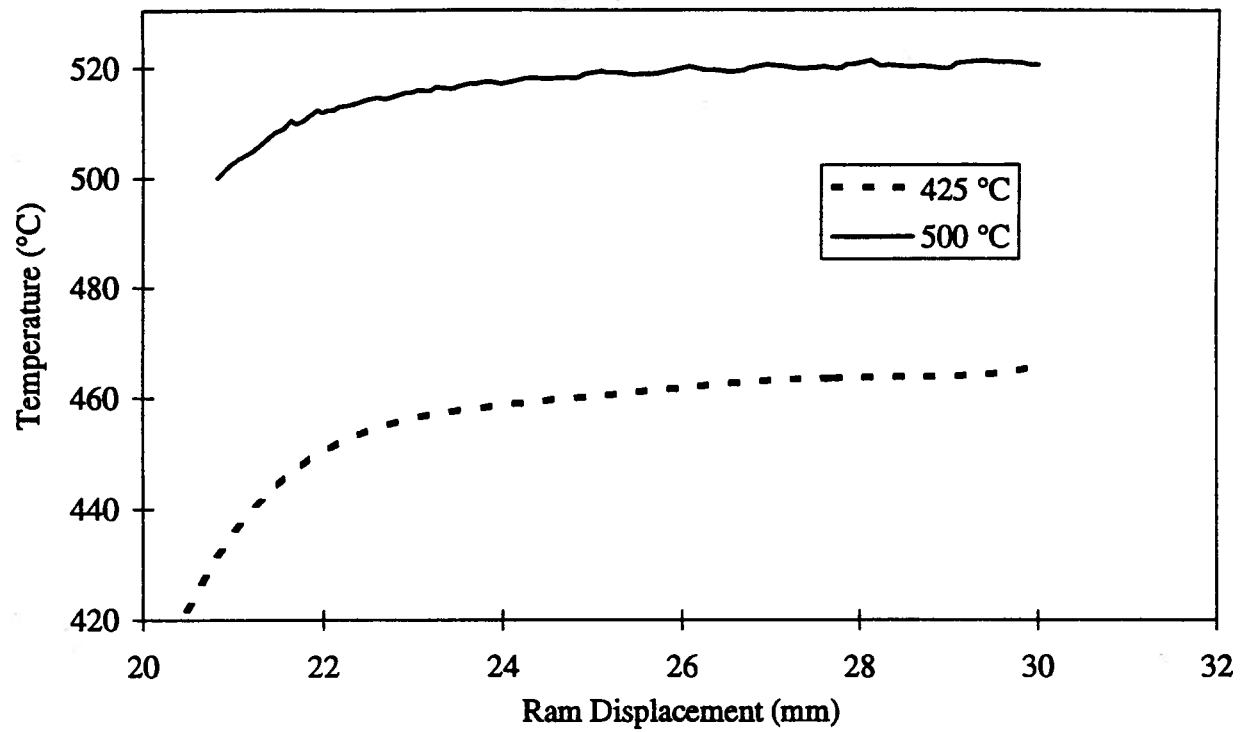


Figure 8.12 Effect of ram speed on effective strain rate variation in extrudate

A big difference in effective strain rate is expected because of the different ram speeds (Fig. 8.12) but near the exit of the die land, the strain rate is concentrated only within the surface layer.

Effect of Billet Temperature

With all the other conditions kept the same, the effect of initial billet temperature on the tensile stress in the extrusion direction and the temperature rise was studied (Fig. 8.13(a) and (b)). Thus the higher the initial temperature, the higher the extrusion temperature. However, the temperature rise is lower for the higher initial billet temperature ($\sim 20^\circ\text{C}$) than for the lower initial temperature ($\sim 40^\circ\text{C}$); because of the lower flow stress and the low heat generation obtained for the higher billet temperature. Correspondingly, the maximum tensile stress in the extrusion direction (σ_z) is lower, as shown in Fig. 8.13(b). A 75°C increase in



(a) Max. temperature in the die land zone during extrusion

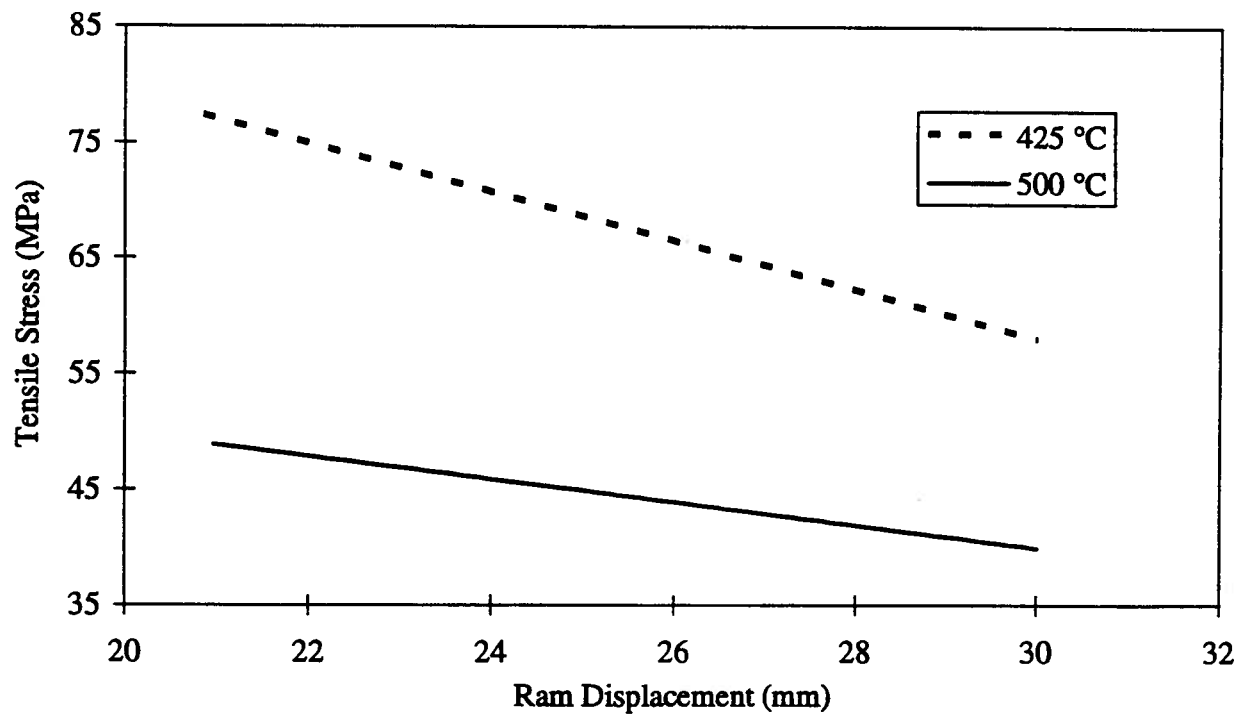


Figure 8.13 Effect of initial billet temperature: (b) Max. tensile stress in the die land zone

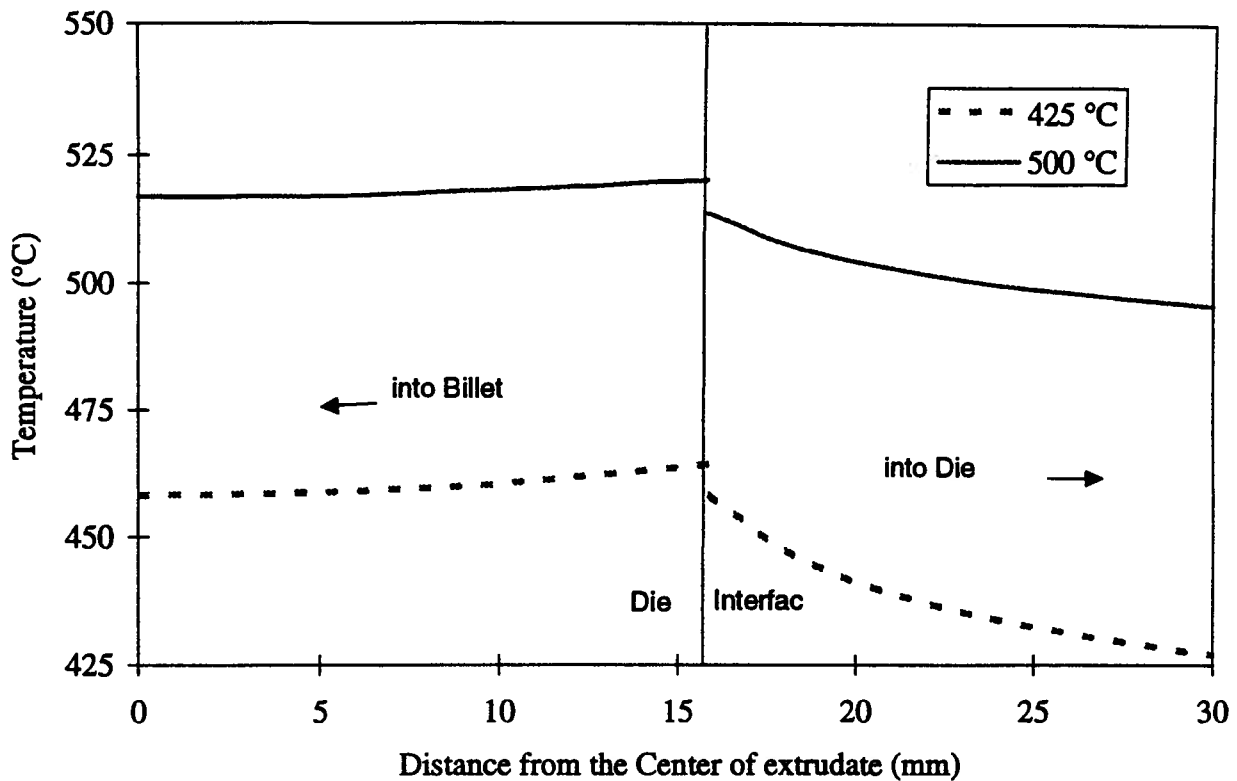
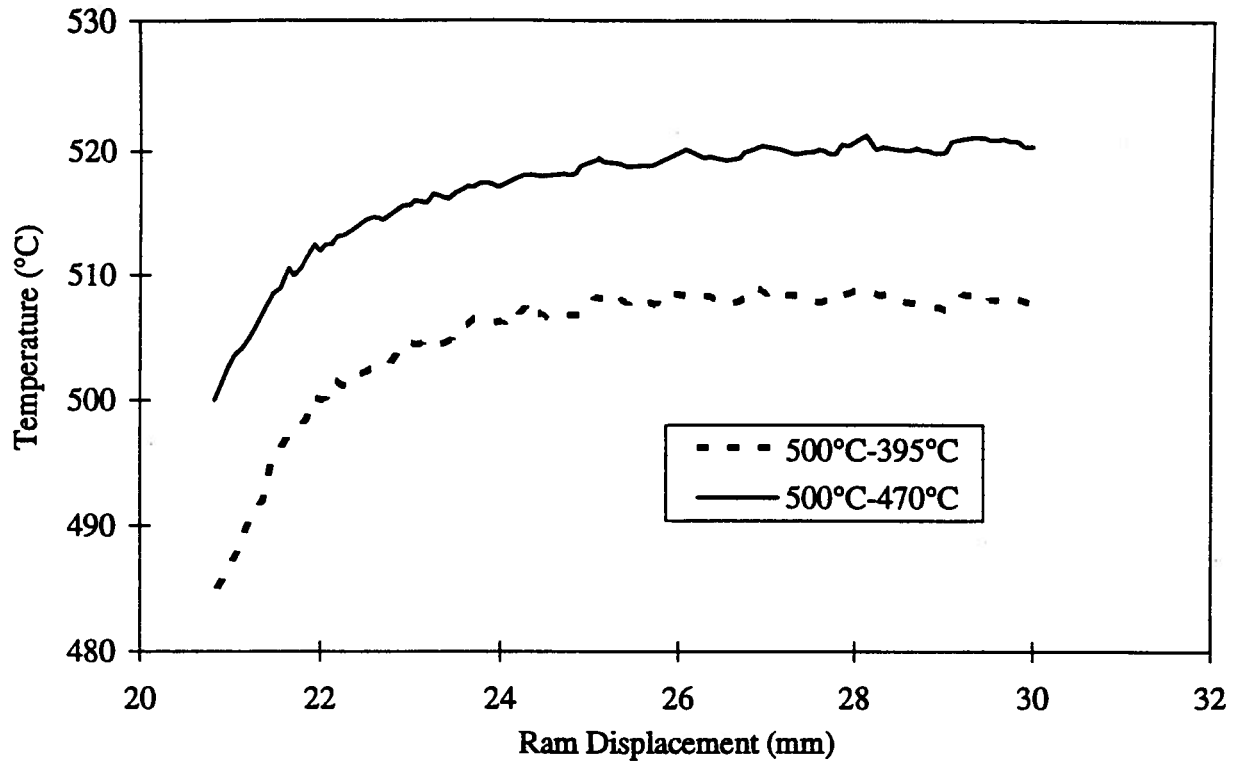


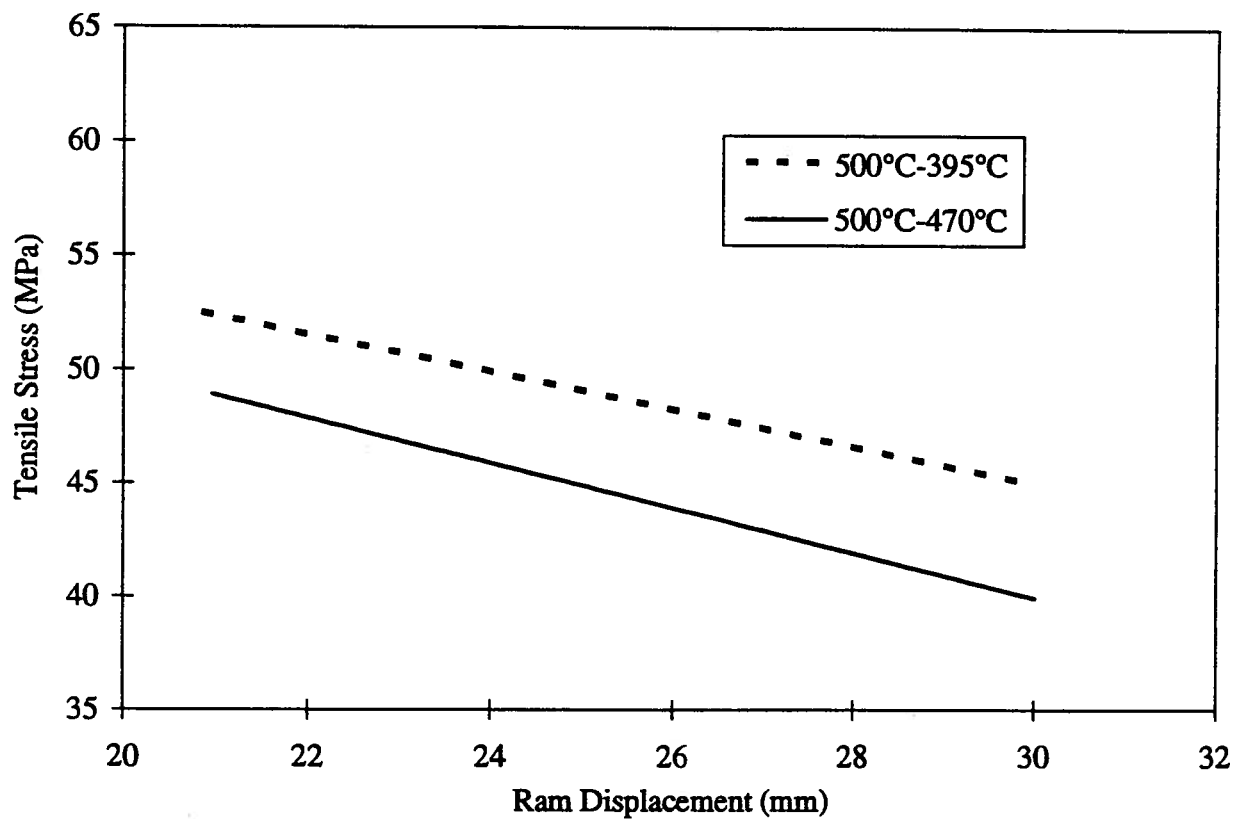
Figure 8.14 Thermal gradient on both sides of the die interface under different billet temperature

billet temperature results in a drop of maximum tensile stress of ~ 30 MPa. It is obvious that the effect of billet temperature on the maximum tensile stress is quite significant. It is known that a higher tensile stress may increase the propensity of void formation at high temperature in particulate reinforced MMCs^[101]. Therefore, temperature control is important to eliminate low speed cracking during extrusion. On the other hand, at a lower initial billet temperatures, the tensile stress in the extrusion direction in the surface layer of the extrudate decreases more rapidly because of the higher heat generation rate due to the high flow stress (Fig. 8.13(b)).

Because the ram speeds are the same for both cases, the thermal gradient in the extrudate is about the same (Fig. 8.14). However, on the die side, the thermal gradient is larger for the lower initial billet temperature of 425°C, because the temperature rise is higher.



(a) Maximum temperature in the die land zone during extrusion



(b) Maximum tensile stress in the die land zone during extrusion

Figure 8.15 Effect of initial die temperature

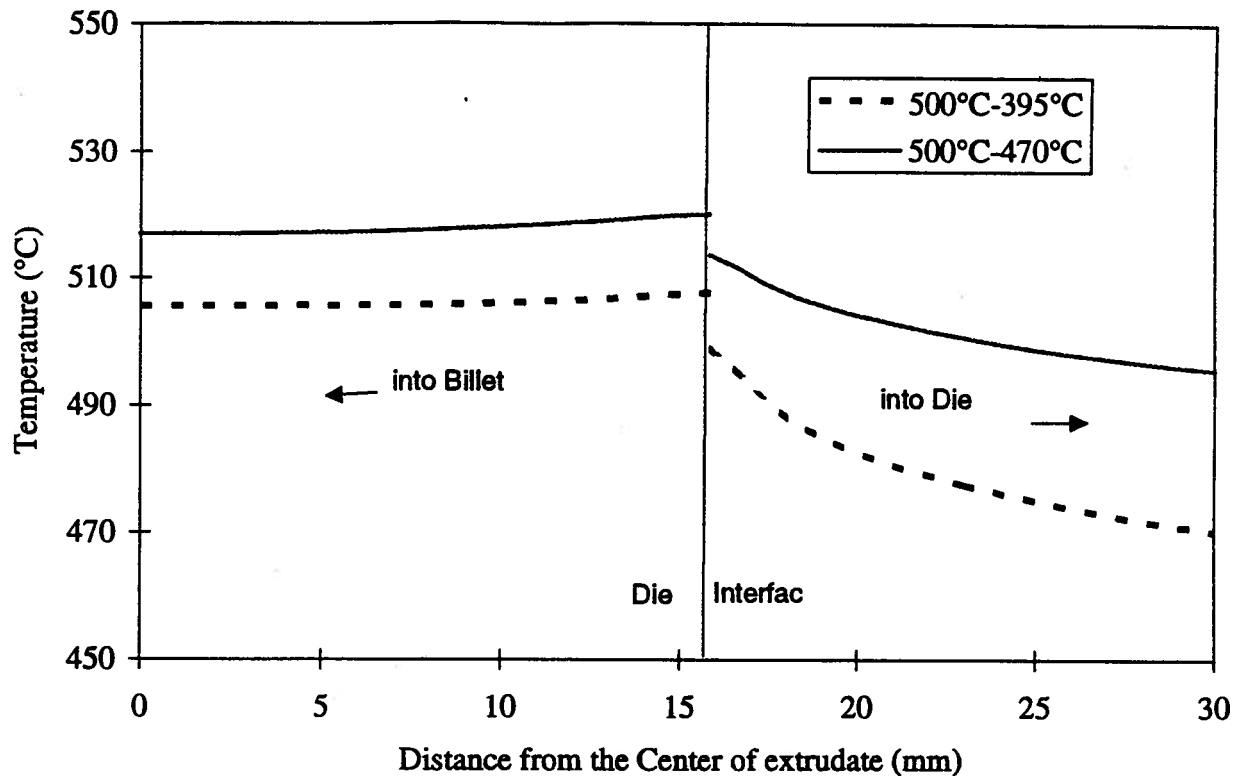


Figure 8.16 Thermal gradient on both sides of the die interface under different initial die temperatures

Effect of Die Temperature

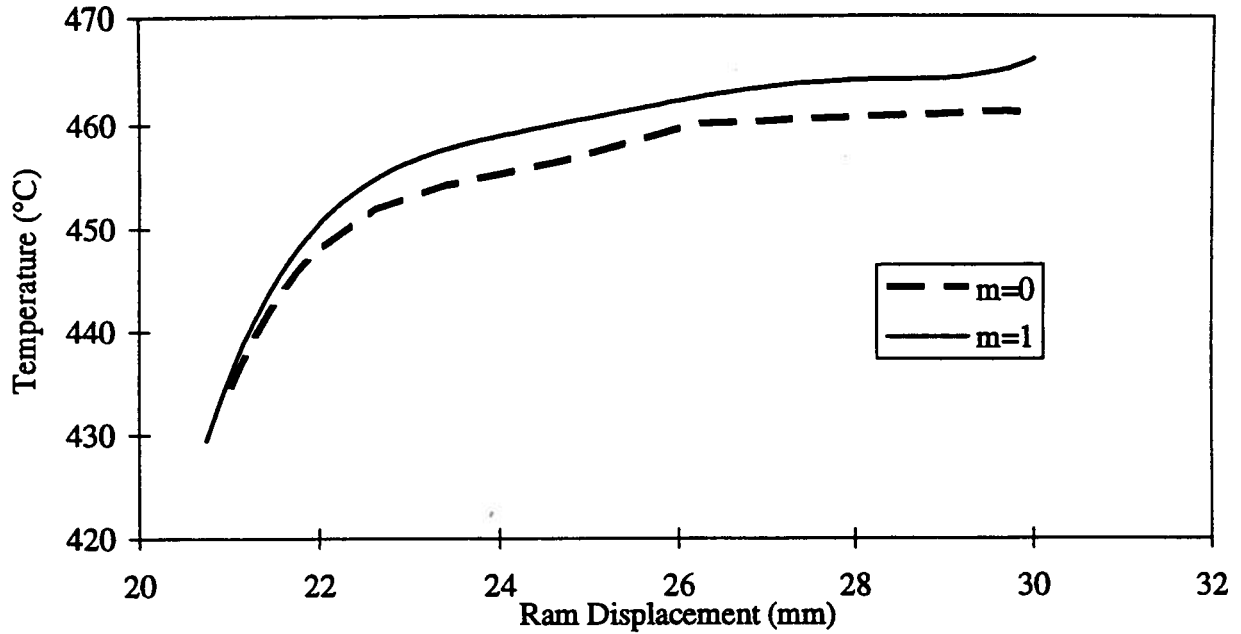
From the above analysis, it can be seen that the tensile stress is very sensitive to the temperature of the extrudate in the die land zone. Because the die temperature is not very well controlled in the plant trial at UAC, the sensitivity of die temperature was also analyzed (Fig. 8.15). Die temperatures of 395°C and 470°C were used with the same initial billet temperature of 500°C. From Fig. 8.15(a), it is seen that, because of the lower initial die temperature of 395°C, the maximum deformation temperature of the extrudate is about 15°C lower than that of the die temperature of 470°C, and the extrusion temperature is even below its initial temperature of 500°C at the end of the upsetting stage (at a ram displacement of

about 21mm) due to the cold die 'chilling' effect. As a result, the tensile stress of the extrudate in the surface layer within the die land zone is higher (Fig. 8.15(b)). The temperature distribution in the cross section of the extrudate is more uniform than that on the die side because of the higher thermal diffusivity. The lower initial die temperature results in a steeper thermal gradient on the die side (Fig. 8.15).

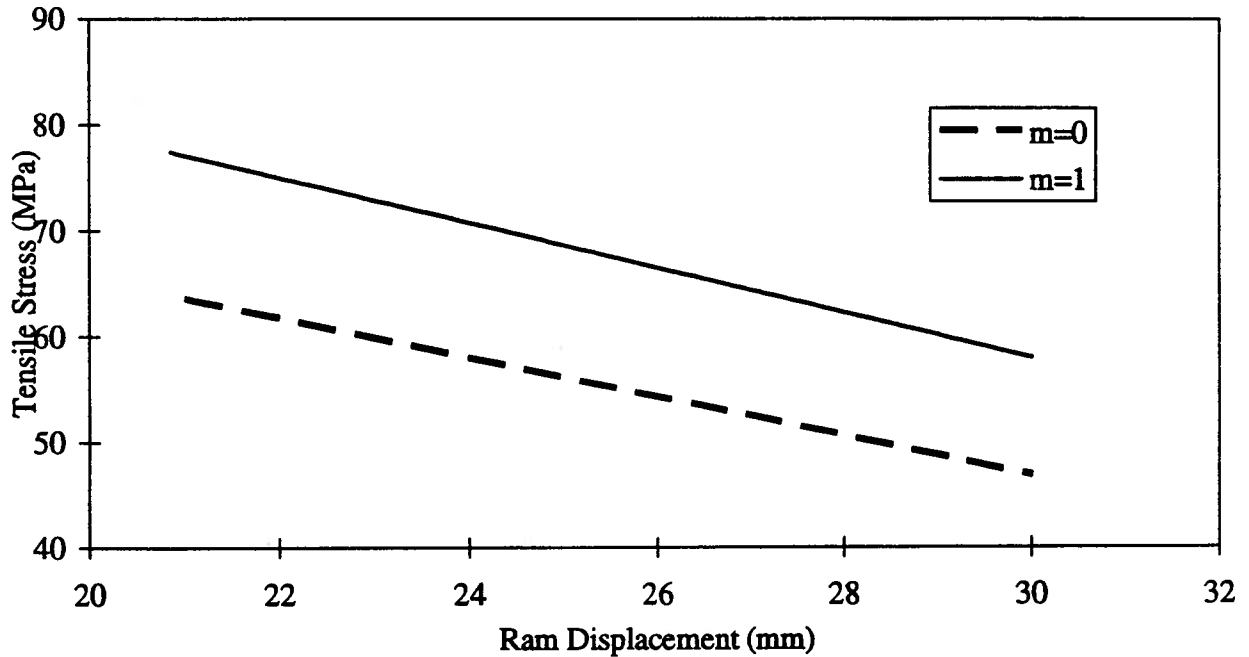
Effect of Friction at Die Interface

With sticking friction confined to the container interface, the sensitivity of two extreme friction conditions was studied with the friction shear factor being set at 0 and unity, respectively. It is worth pointing out that in DEFORM[®], when considering the sticking friction condition, the relative velocity between two objects in contact is not restricted; in contrast, a shear stress with an equivalent value of shear strength of the deformed material, is applied at the boundary^[83]. Therefore, although a sticking friction condition was specified, the nodes of the deforming finite element object (billet) in contact with the stationary object (tools) are still movable. Figure 8.17 shows the sensitivity of the friction condition at the die interface.

Without friction heating at the die interface, the maximum temperature of the extrudate during extrusion is lower than, but very close to, the value of the extrudate temperature with friction. This is because the die land length is only about 2 to 3mm; and thus the contribution of friction heating is very small. The small effect of friction on the temperature rise can also be seen from the thermal gradient on both sides of the die interface, as shown in Fig. 8.18. However, the difference in tensile stress related to the two different friction conditions is quite obvious (Fig. 8.17(b)). It is interesting to note that even with no friction condition applied at the die interface, the tensile stress still exists. This indicates that



(a) Maximum temperature in the die land zone during extrusion



(b) Maximum tensile stress in the die land zone during extrusion

Figure 8.17 Effect of friction condition at die interface

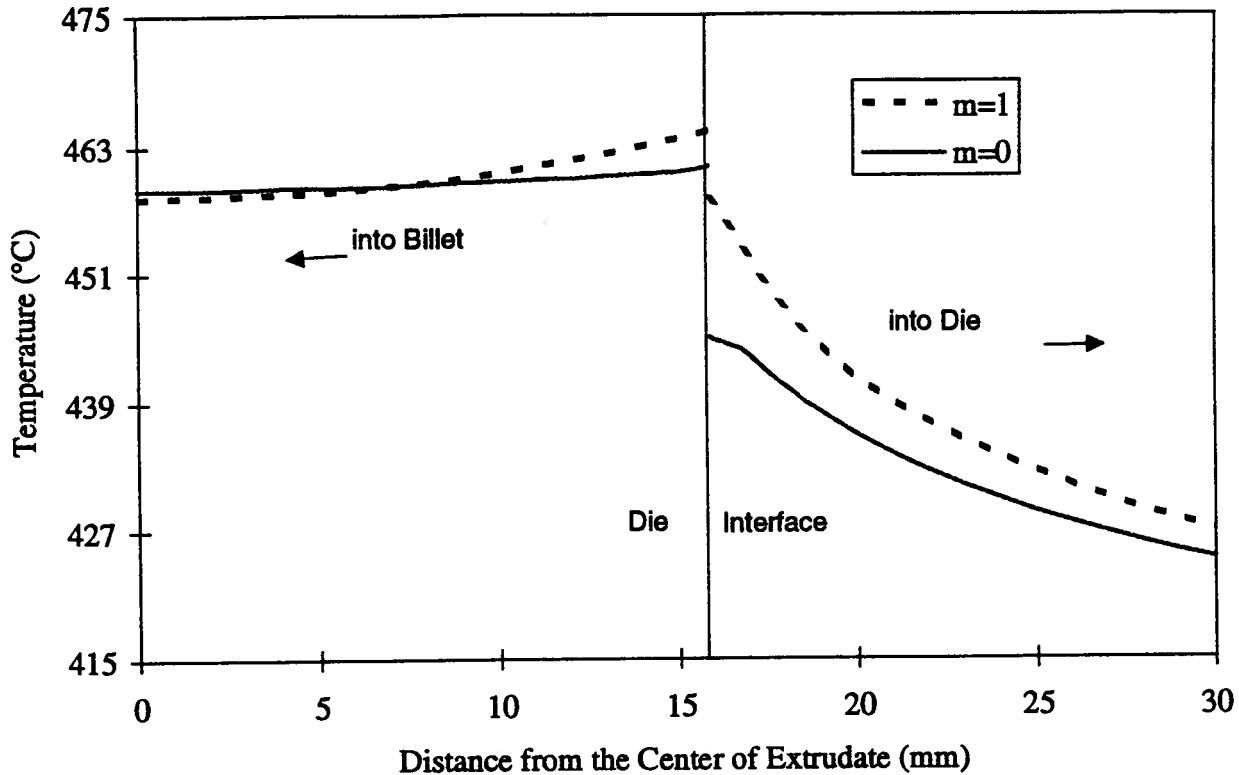
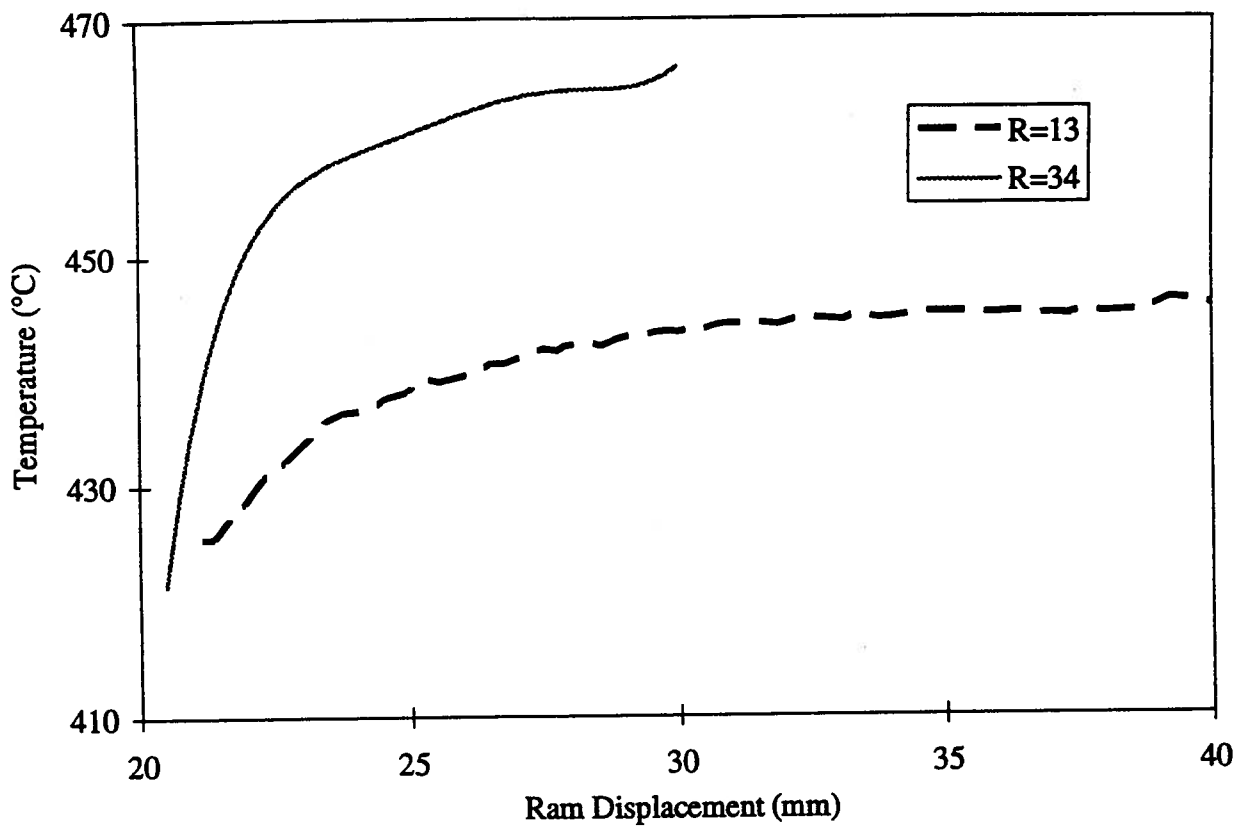


Figure 8.18 Thermal gradient on both sides of the die interface
under different friction condition at die interface

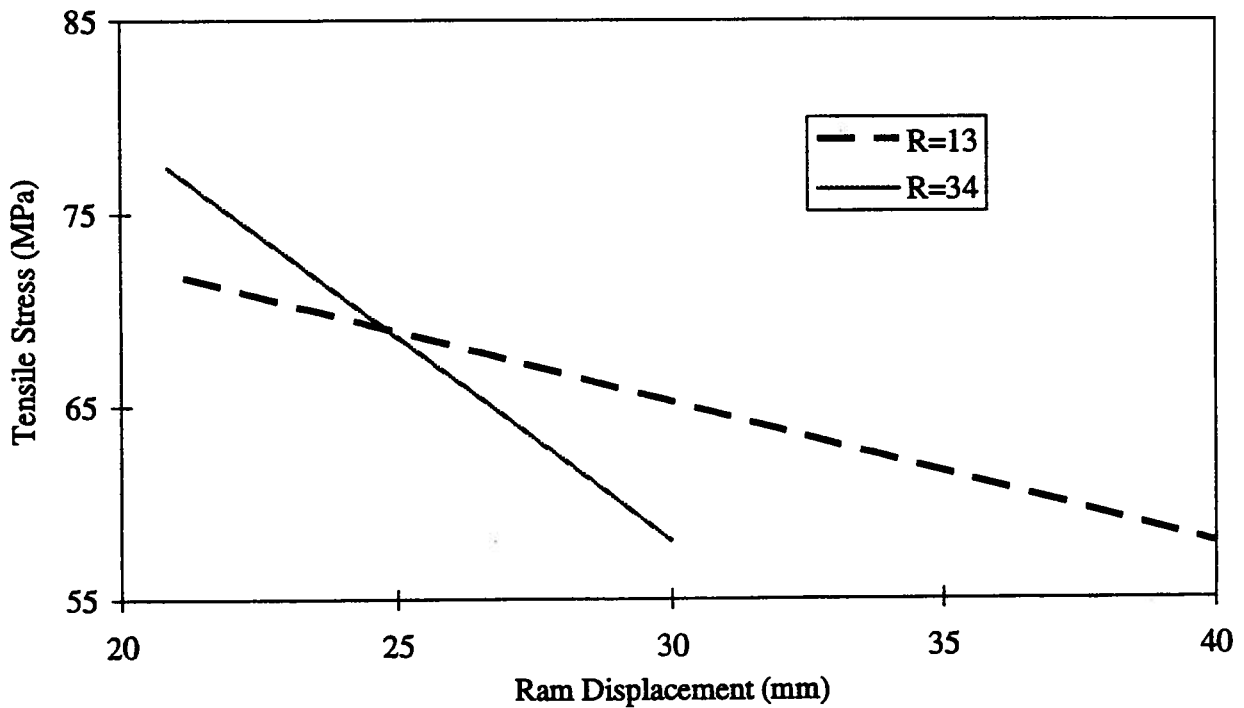
the tensile stress build-up in the die land zone is not only due to friction, but also due to material flow itself, because metal flows faster at the inside layer of the extrudate than at the outside layer and also there is no back pressure applied onto the front end of the extrudate. Therefore, it is this velocity difference that causes the tensile stress at the die exit. Severe friction conditions simply make the situation worse.

Effect of Extrusion Ratio

A temperature rise of the billet under smaller extrusion ratios is expected to be lower if all other conditions are kept the same. At an extrusion ratio of 13, the extrudate temperature rise is only about 15°C compared to 45°C for an extrusion ratio of 34. About 30°C difference has been predicted for the extrusion ratio of 13 and 34(Fig. 8.19(a)). Because of the relatively



(a) Maximum temperature in the die land zone during extrusion



(b) Maximum tensile stress in the die land zone during extrusion

Figure 8.19 Effect of extrusion ratio

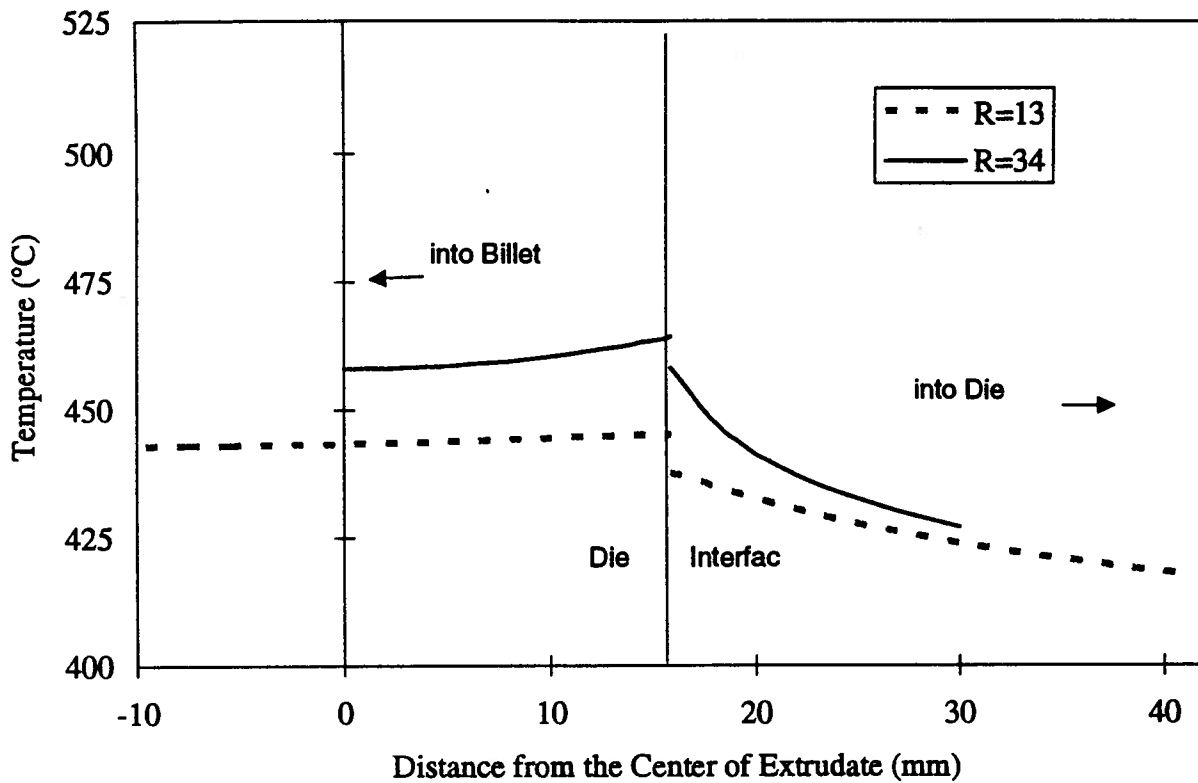
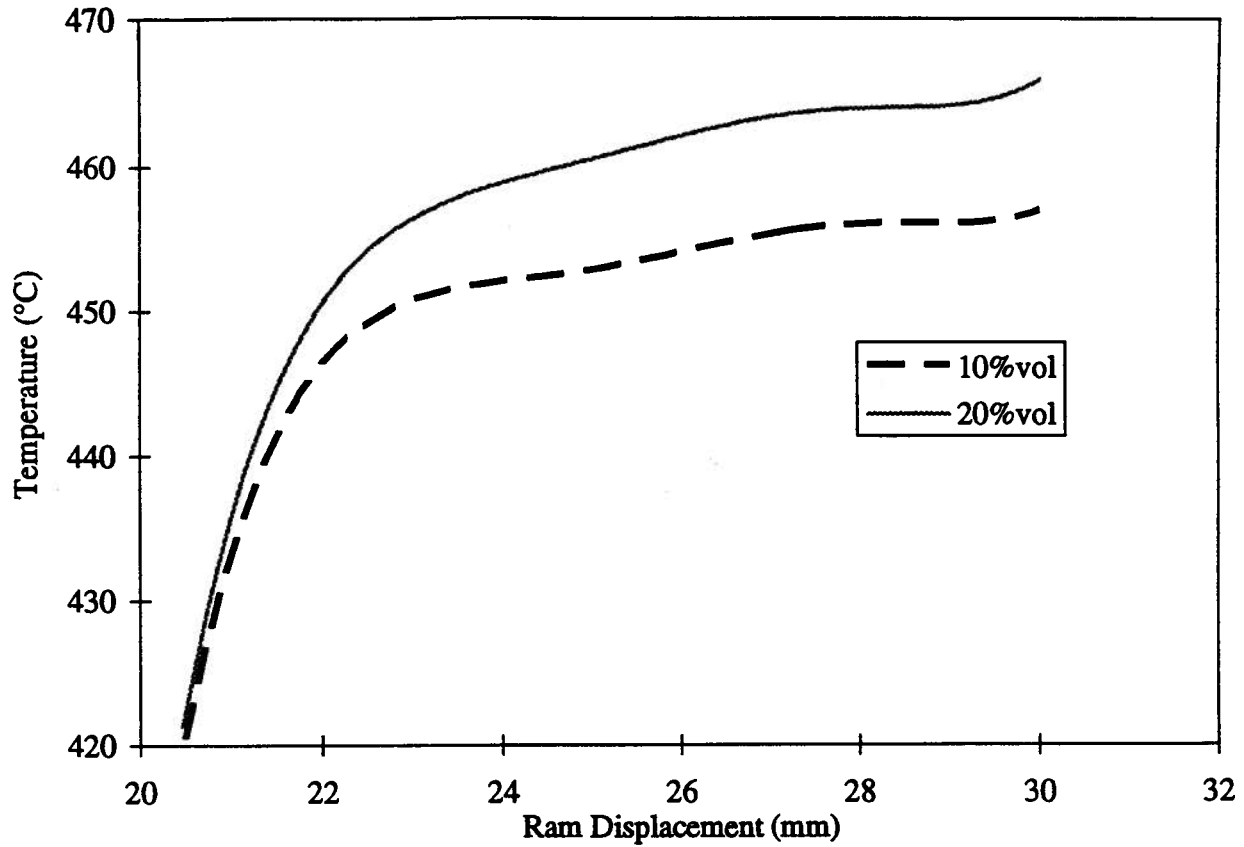


Figure 8.20 Thermal gradient on both sides of the die interface under different extrusion ratios

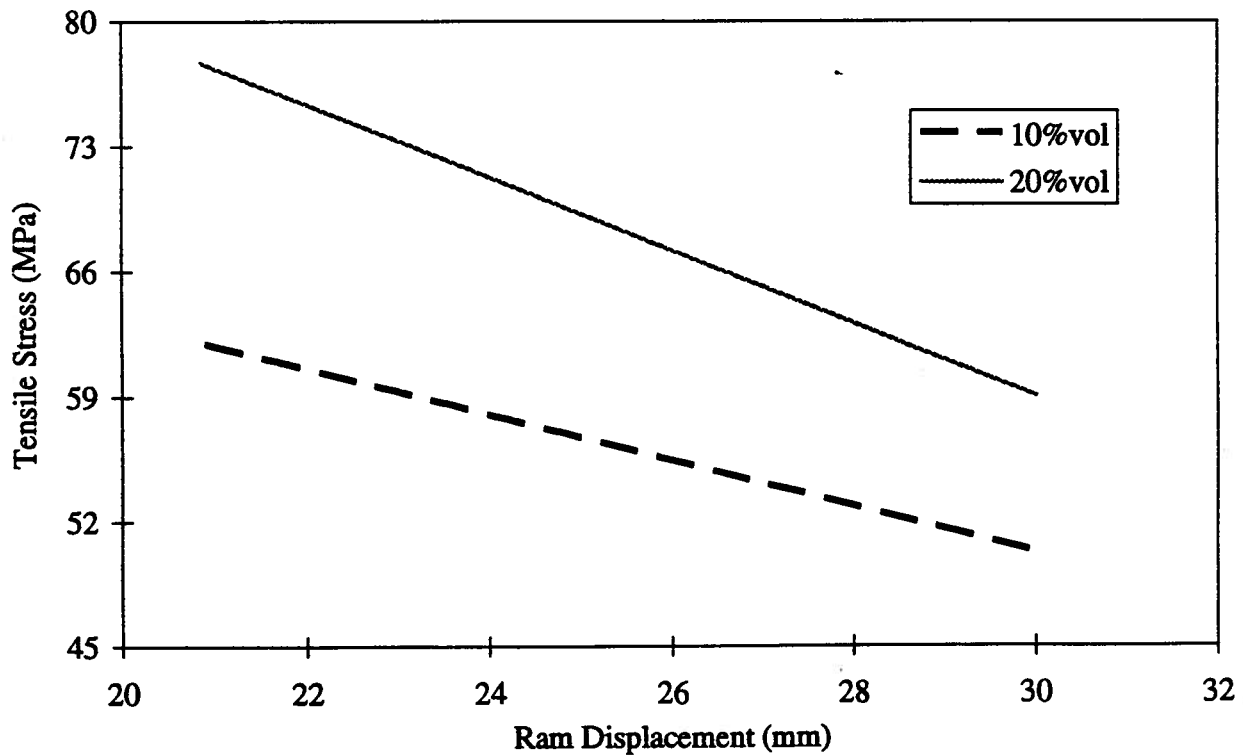
higher heat generation rate for the higher extrusion ratio, a greater thermal gradient is predicted for both sides of the billet and the die, as shown in Fig. 8.20. The tensile stress is higher initially for the higher extrusion ratio, but decrease rapidly because of the rapid temperature increase (Fig. 8.19(b)).

Effect of Volume Fraction of the Composites

The sensitivity analysis conducted above was for the 6061/Al₂O₃/20p. The effect of 10% and 20% volume fraction of the PRMMCs was also conducted for a similar sensitivity analysis (Fig. 8.21). As expected, a high volume fraction of particles results in a higher temperature rise due to the higher flow stress (Fig. 8.21(a)). The tensile stress is also greater



(a) Maximum temperature in the die land zone during extrusion



(b) Maximum tensile stress in the die land zone during extrusion

Figure 8.21 Effect of volume fraction

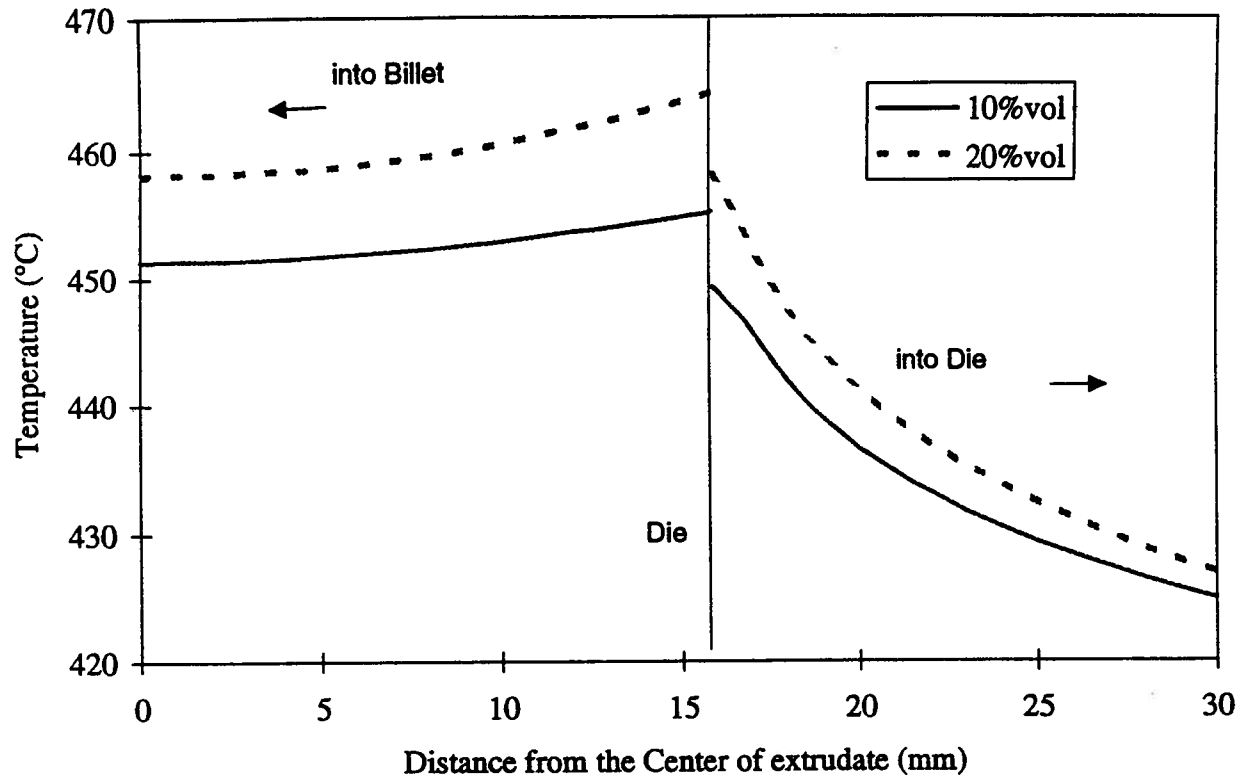


Figure 8.22 Thermal gradient on both sides of the die interface under different volume fraction

for the larger volume fraction material. This means that the decrease in flow stress due to temperature rise cannot compensate for the effect of a larger volume fraction of the reinforcement. The difference in thermal diffusivity of different composite materials can be seen from the thermal gradient in the extrudate, although it is quite small. The higher thermal diffusivity of 6061/Al₂O₃/10p results in a slightly flatter temperature distribution through the radius of the extrudate (Fig. 8.22).

8.4 Mechanism of Low Speed Cracking

Based on the analyses described in the above sections, it is believed that the low speed cracking is induced by both the low ductility of the composite and microstructural damage

(such as voids including decohesion and unhealed cracks) during extrusion as follows: 1) at the beginning of extrusion, the die temperature is lower than that of the billet, so a 'chilling' effect occurs at the front end of the billet when it is in contact with the 'cold' die. The lower temperature results in lower ductility of the composites; and 2) the extrudate surface is generated from two distinct regions of the composite: the deformation zone of intense shear, decorating the dead metal zone, which is the major contribution and the smaller deformation volume near the die throat, moving along the die face^[117]. With the presence of particles which constrain the surrounding matrix deformation, especially at low temperature, severe deformation near the die throat may lead to matrix failure at the particle interface (void formation) and particle fracture in particle clusters in the composite during extrusion. The tensile stress generated in the die land zone may not only leave the cracked particle unhealed, but also promote the void growth. When the fraction of the voids reaches a certain value, the voids may link each other to result in a tearing at the extrudate surface within the die land length, due to low ductility at low temperatures.

At high extrusion speed, because the heat generation rate of deformation is greater, and also because the thermal diffusivity of the die material (H13 and the ceramic die) is about 7 to 10 times lower than that of the composites, the temperature at the die interface increases very rapidly (See Fig. 8.8). However, at low speed, the heat generation rate is lower and the heat has time to diffuse through the die, due to the relatively longer extrusion time (Fig. 8.9). Therefore, if either the initial billet temperature or initial die temperature is low, the matrix within the particles is constrained much more than at higher temperature, because the flow stress is much higher at lower temperature (see also Figs. 8.13 and 8.15). Voids are easier to form and grow under tensile stress (see also Figs. 8.4 and 8.5). Therefore, low speed cracks

appear. Apparently, all the extrusion conditions that may result in lower billet temperature and higher tensile stress in the surface layer of the extrudate in the die land zone may lead to low speed cracking during extrusion, such as lower initial billet and die temperature, low ram speed, higher extrusion ratio, higher friction condition at the die interface, and also high volume fraction of the particle reinforcement. This is consistent with the plant trial observations at UAC and at KRDC, Kingston. At UAC, more severe low-speed cracking in the 6061/Al₂O₃/20p composite at higher extrusion ratio (1" and 1.25" die) has been found; and the low-speed cracking disappeared when the ram speed was increased. However, only one extrudate with low-speed cracking was found in the trials at KRDC, in which the ram speed was considerably lower than the set value of 0.9mm/s. This occurred when the press limit was exceeded due to low initial billet temperature of 400°C. At a ram speed of ~0.9mm/s, low speed cracking always appeared in the plant trials at UAC. However, no low speed cracking was observed in the plant trials at KRDC. This is because the die and the billet were heated at the same time in a furnace at KRDC, and the temperature of the container was even higher than that of the billet. The 'stick and slip' observed, is due to the fact that when voids link to form a crack, the tensile stress generated is released. This process repeats itself as long as the temperature of the billet remains low and also the tensile stress is sufficiently high to promote void formation in the extrusion process.

8.5 A Preliminary Criteria for Low Speed Cracking

It is clear now that the onset of low speed cracking is controlled by both the fracture stress and fracture strain (ductility) of the material. Therefore, a preliminary fracture criterion is proposed for the low speed cracking during extrusion based on the idea of the plastic-work criterion^[51]:

$$E = \sigma_z \bar{\epsilon}_{\max} \geq \sigma_F \epsilon_F = C_F \quad (8.1)$$

where σ_z is the maximum principle stress, and $\bar{\epsilon}_{\max}$ is the maximum tensile strain obtained during extrusion, which is defined as the strain induced under a tensile stress, while $\sigma_F \epsilon_F$ is the product of the fracture stress and tensile fracture strain of the material. The low speed cracking is induced by local failures of the composite, related to the local tensile stress and strain. However, because it is difficult to know the local tensile stress and strain, the monolithic tensile stress and strain are used in the criterion. Since the fracture strain of a material is also dependent on the process itself, a tensile strain is used, although it is hard to determine its value in an extrusion process. Apparently, if the product of the maximum tensile stress and the maximum tensile strain in the composites exceeds a critical value, which is the product of the fracture stress and strain, low speed cracking would occur. The reason to use a product instead of a single stress (*Stress Criterion*) or strain (*Strain Criterion*) is because the onset of low-speed cracking is induced by the combination of those two factors, i.e., the microdamage would be induced for a certain strain (fracture strain) within particles, and the tensile stress would promote the void growth to link voids to form the low speed cracks for a certain stress value (fracture stress).

According to Eq. (8.1), the effect of a variation of the product (E) of the maximum tensile stress and the maximum extrusion strain in the extrudate (rather than the difficult to obtain tensile strain) during extrusion under different conditions, but for the same extrusion ratio of 34, was shown in Fig. 8.23. J94-12 has the highest value of E , because it has the lowest temperature of 423°C. The higher starting value of E of J94-13, with higher initial

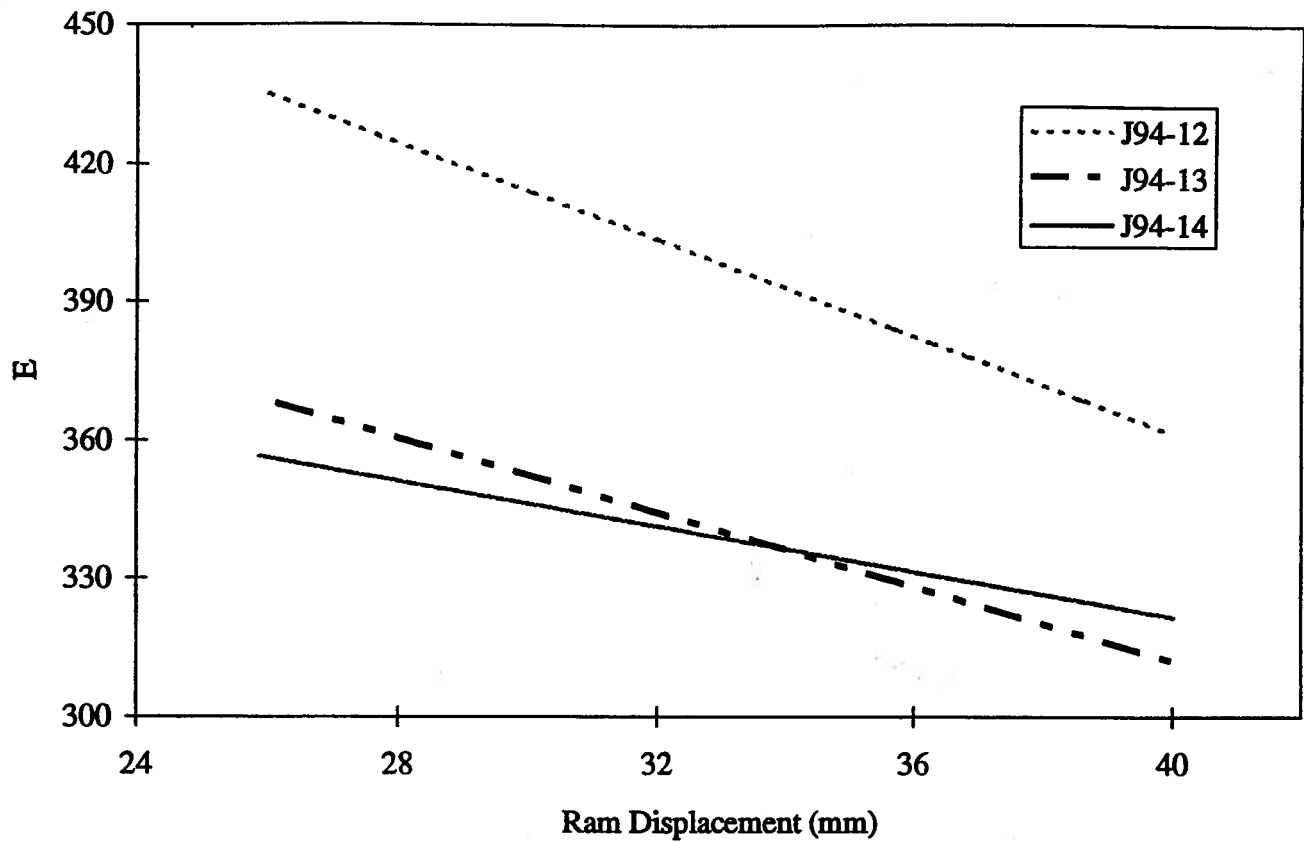


Figure 8.23 Variation of E value during different conditions but same extrusion ratio

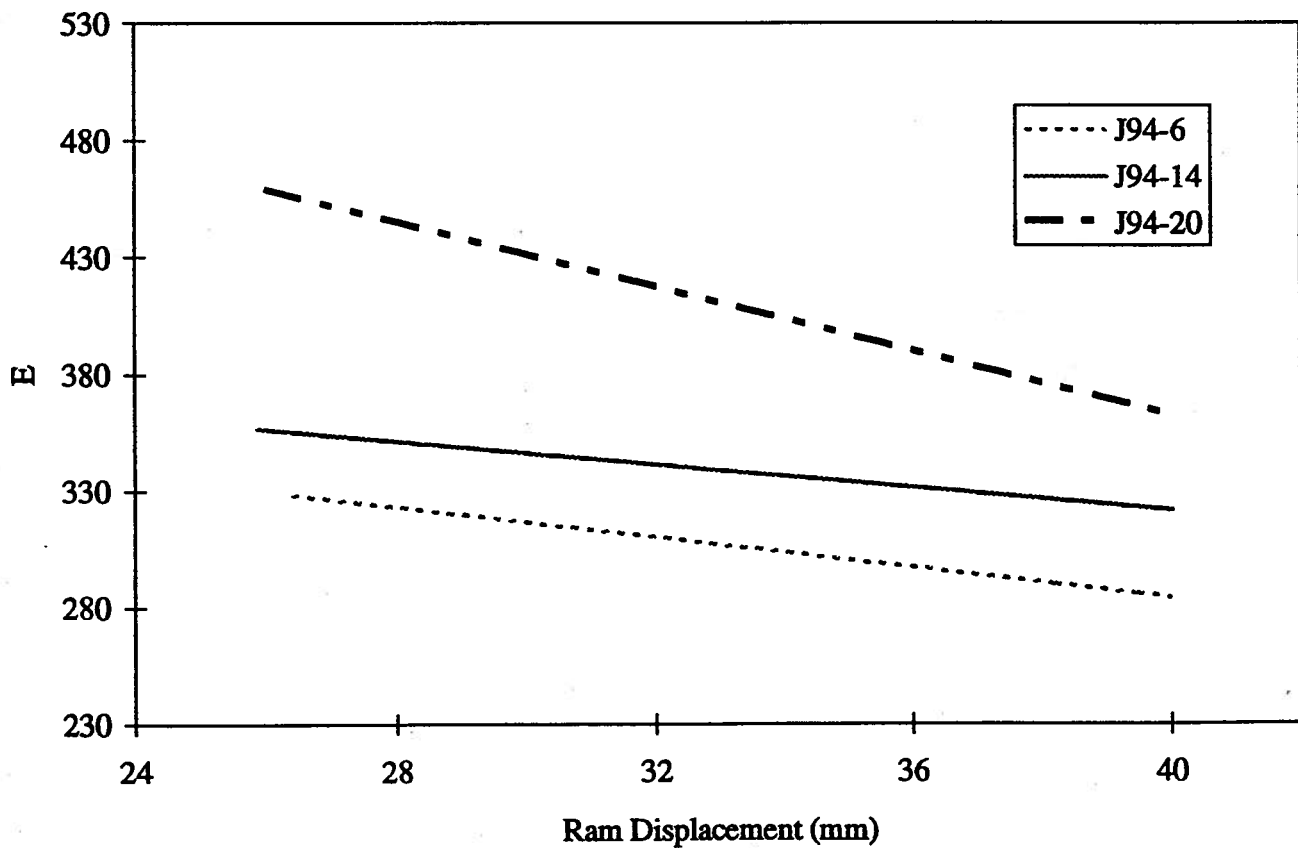


Figure 8.24 Variation of E value during extrusion at different extrusion ratios

billet temperature of 471°C, must be related to the lower initial die temperature. Although the starting values of E for both J94-12 and J94-13 are higher, they decrease more rapidly than those in J94-14. This implies that the low speed cracking would disappear in the extrudate earlier than noted in J94-14. This is consistent with the low speed cracking ranges at the front end of each extrudate, with J94-14 having the longest low speed cracking length and J94-13 the shortest (Table 4.7).

The variation of E during extrusion for different extrusion ratios, is shown in Fig. 8.24. Apparently, the highest extrusion ratio of J94-20 has the highest E value with the longest low speed cracking range in its extrudate. J94-6, with the smallest extrusion ratio, has the lowest E value and the shortest cracking range (Table 4.7). Although the E value variation corresponds qualitatively with the low speed cracking, the determination of the C_f value is difficult, because it is dependent on temperature, strain rate, and the process itself. However, in the plant trials at UAC, the large variation of ram speed would result in both strain rate and temperature fluctuations in the deformation zone. One way to determine the product of $\sigma_F \epsilon_F$ is to conduct a series of tests (e.g., collar tests) in the laboratory at different temperatures and strain-rates to measure the fracture stress and strain. However, it would still be difficult to specify the fracture stress and strain at the crack position; and moreover, the applicability of the laboratory test results to the industrial process would need to be verified.

Chapter 9 EXTRUSION OF THE PRMMCs

It is conceivable that the unique properties of particulate reinforced MMCs will ensure their place in automobiles and other applications by the year 2000 or before^[115]. As mentioned in the literature review, MMCs can be applied in the manufacture of the automobiles in several areas, such as drive shafts, brake rotors, engine blocks and cylinder liners, connecting rods and pistons, tire studs, etc. Although, of the mentioned parts, only the drive shafts and the connecting rods are produced through extrusion processing, the manufacturing technologies, involving control of consistent material quality and high-tolerance tube extrusion techniques, etc., are critical to the successful implementation of drive shafts in high-volume automotive applications. Quality aspects of the MMCs of concern to the customer for application in the auto industry include specific stiffness, fatigue life, wear resistance, tailorable properties (e.g., thermal expansion)^[8]. However, different parts have different quality requirements. Taking the drive shafts for example, the high specific modulus of MMCs is a very cost-effective improvement. Although the elastic modulus reduction occurs during low temperature deformation because of damage by particle fracture, especially for metal matrix composites with a high volume fraction (e.g., 20%)^[92-95,116], it has been confirmed that the hot extrusion process does not reduce the elastic modulus and tensile strength. Instead, it may increase the tensile properties due to an increase in the homogeneity of the particle distribution and particle size refinement. Fatigue life of the composites could also be affected by thermomechanical processing (e.g. hot extrusion). Improvements in the fatigue strength of MMCs, compared to parent alloys are reported, but a lower specific fatigue strength for 6061/Al₂O₃/20p compared to 6061 is also seen, which could depend

critically on both the method of testing and the quality of the composites^[8]. Therefore, acceptable process windows for reliably producing higher quality and high-volume production of the MMCs are yet to be defined.

9.1 Development of Extrusion Limit Diagram

9.1.1 Using Empirical Equations

The empirical equations used for the development of extrusion limit diagrams have been described in Section 2.3 in the literature review. For convenience, two main equations are listed below in Eq. (9.1) and (9.2). The extrusion pressure can be estimated using Eq. (9.1), which is related to the press parameters (e.g., R , L , D_C) and the extruded material properties (e.g., α , n , A). From the plant trial data at KRDC, and at UAC, the four constants in Equation (9.1) have been estimated for both the extrusion presses (Table 9.1).

$$P = \frac{1}{\alpha n} \left\{ B + C \ln R + E \ln \frac{Z}{A} + F \left(\ln \frac{Z}{A} \right) \left(\frac{L}{D_C} \right) \right\} \quad (9.1)$$

Table 9.1 Constants in Eq. (9.1) for the composites

	B	C	E	F	Correlation Coeff.
Small Press at KRDC for 6061/Al ₂ O ₃ /20p	36.0717	16.8147	-43.9526	40.6549	0.9882
Large Press at UAC for 6061/Al ₂ O ₃ /20p	291.0946	214.6415	-205.3810	218.3884	0.9804
Large Press at UAC for 6061/Al ₂ O ₃ /10p	443.0187	260.1046	-211.9300	205.3414	0.9381

A good correlation was obtained between the measured peak load and the prediction by the above equation. Hence the pressure limit line in a limit diagram can be delineated, at least tentatively, using Eq.(9.1), based on the press limit^[55-65].

With respect to the billet temperature rise during extrusion, the following equation (see also Eq. 2.9) is used, based on an assumption that there is little or no temperature difference between the billet and the surrounding tools^[63]. This assumption is valid for the plant trial at KRDC, because both the die and the billet were heated at the same time in the same furnace. However, the die temperature in the plant trial at UAC was significantly lower than that of the billet. For simplicity, in the calculation of temperature rise, the initial temperature difference between the billet and the tools was ignored, while the internal generation of heat establishes a temperature differential,

$$\Delta T = 0.9Pv_B t / C_1(t) = 0.9Pv_B t / (K_1 t^{1/2} + (K_2 + K_4)t^{2/3} + (K_3 + K_5)t^{1/3} + K_{11}t) \quad (9.2)$$

Based on Eqs. (9.1) and (9.2) for peak pressure and temperature rise, extrusion limit diagrams can be developed for the Duralcan[®] composite materials extruded in the small press at KRDC and the large press at UAC. Figure 9.1 shows a limit diagram at a constant extrusion ratio of 28 for 6061/Al₂O₃/20p for the press at KRDC. Due to the low capacity of the press (~1000kN), the operating window for extrusion processing is small.

Figure 9.2 shows a limit diagram for the same material at a constant ram speed of 12.5mm/s (maximum speed for the press at KRDC). A ram speed of 35mm/s for Duralcan[®] material processed at an extrusion ratio of 25 and 14mm/s for SiCp reinforced composites (matrix alloy: A357) at an extrusion ratio of 36 has been reported in industrial extrusion practice^[9,66]. A limit diagram for 6061/Al₂O₃/20p for the large press at UAC under an extrusion ratio of 34 is shown in Fig. 9.3. It is seen that, due to the large capacity of the press (3000 tons), the process window is much larger than that at KRDC. This indicates that the pressure limit for the large press at UAC is not a problem for extrusion of the composites at high temperature.

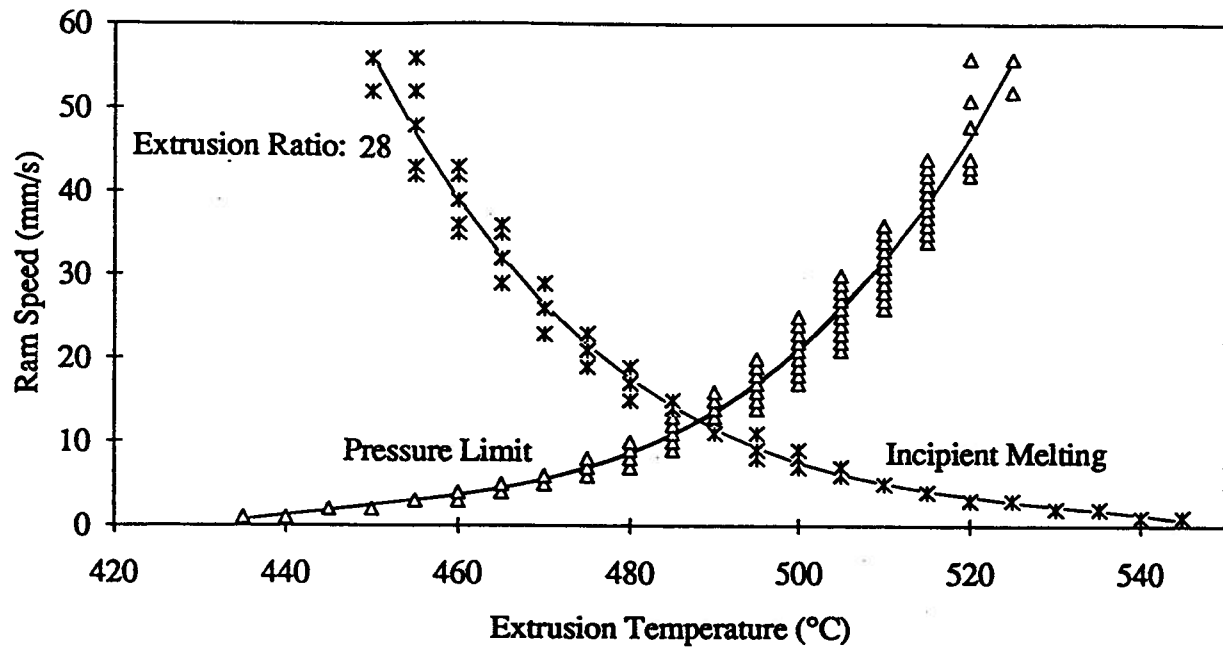


Figure 9.1 Extrusion limit diagram at an extrusion ratio of 28 for 6061/Al₂O₃/20p for the press at KRDC

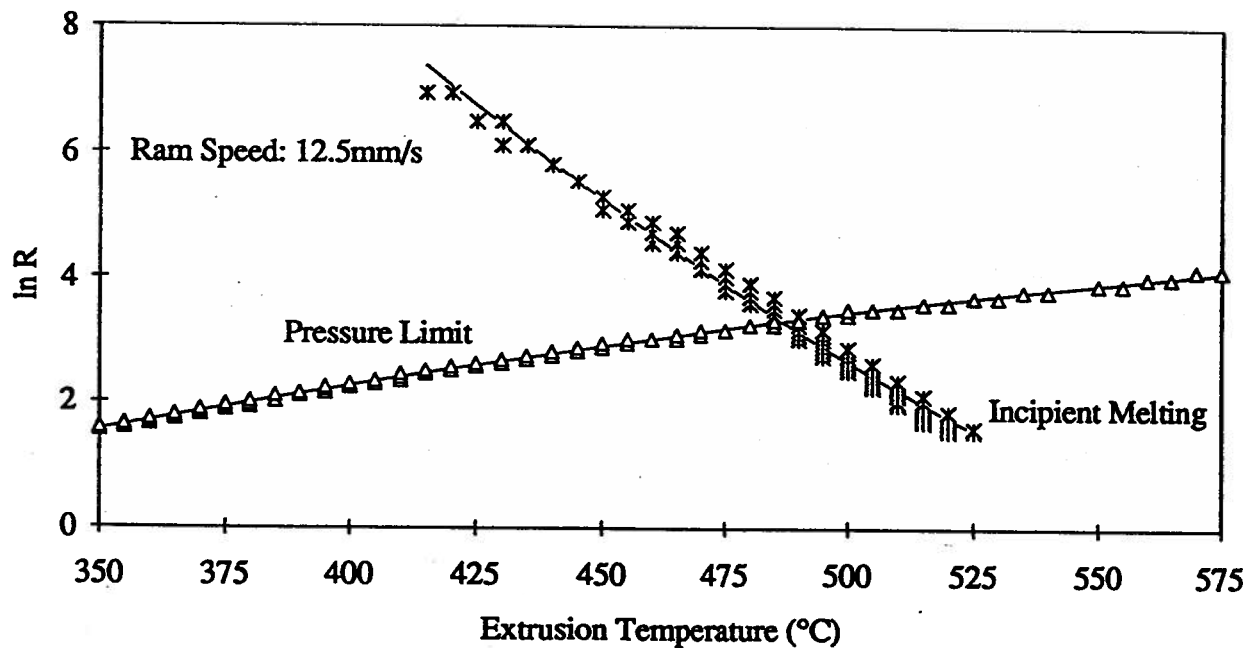


Figure 9.2 Extrusion limit diagram at a ram speed of 12.5mm/s for 6061/Al₂O₃/20p for the press at KRDC

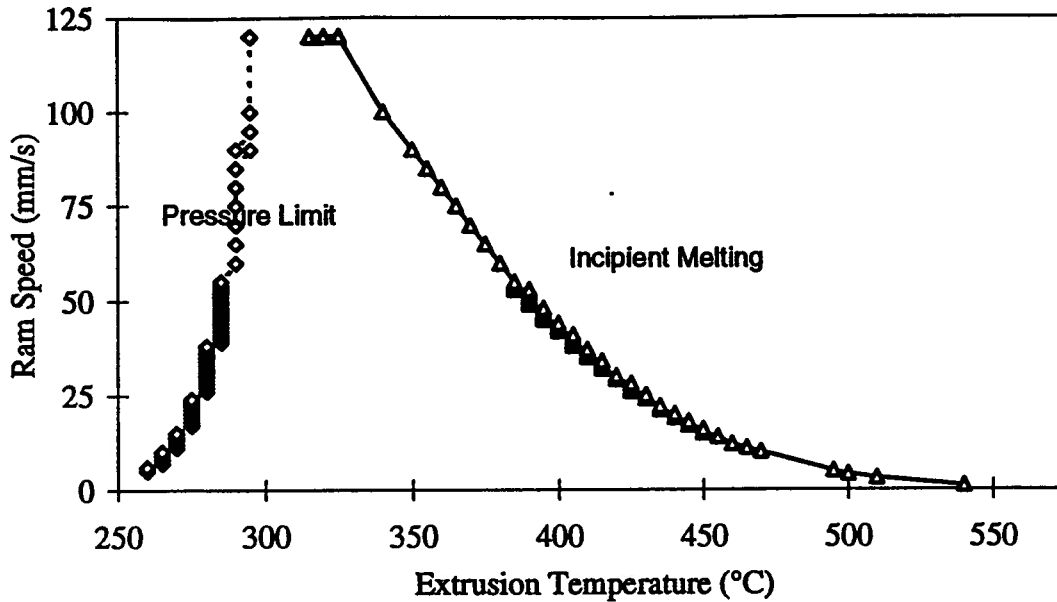


Figure 9.3 Extrusion limit diagram for 6061/Al₂O₃/20p at an extrusion ratio of 34 for the large press at UAC

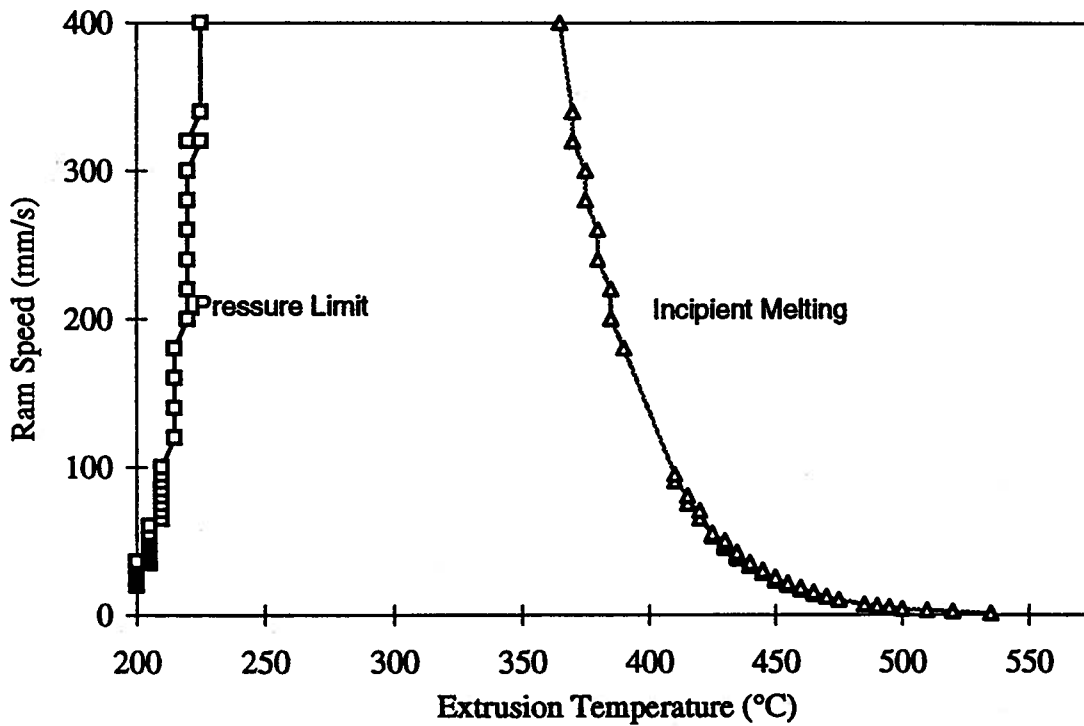


Figure 9.4 Extrusion limit diagram for 6061/Al₂O₃/10p at an extrusion ratio of 34 for the large press at UAC

An extrusion limit diagram for 6061/Al₂O₃/10p was also developed for the large press at UAC using the empirical equations (Fig. 9.4). It is evident that the process window of 6061/Al₂O₃/10p is even larger than that for 6061/Al₂O₃/20p due to its lower flow stress.

9.1.2 Using Finite Element Method

9.1.2.1 Application of the Finite Element Model

Extrusion limit diagrams are usually developed using the above empirical equations, based on extrusion plant trials. The assumptions and simplification of heat transfer analysis for derivation of the empirical equation for temperature rise during extrusion may lead to inaccuracy of the processing window. Moreover, to have an accurate load prediction, a small number of plant trials are necessary to determine the coefficients in Eq. (9.1). Obviously, this approach is not cost effective.

As computation technology advances, extrusion limit diagrams can also be developed using the finite element technique. Based on the finite element predictions, a relationship between temperature rise and billet temperature and extrusion speed may be obtained,

$$\Delta T = f_1(T, v_B) \quad (9.3)$$

Similarly, a relationship between peak pressure and the two variables can also be established:

$$P = f_2(T, v_B) \quad (9.4)$$

With the aid of DEFORM, extrusion of the composite material was simulated at different ram speeds and different initial billet temperatures. The ram speed varied from 1 to 50 mm/s for the press at KRDC and 1 to 75mm/s for the press at UAC; while the initial billet temperature changed from 400°C to 550°C for the press at KRDC (because of its low load capacity) and 300 °C to 570°C for the press at UAC. The initial die temperature was assumed to be 30°C less than that of the billet, while the container temperature was the same as that of

the die. The temperature of the pressure pad was 70°C. The interface friction was assumed to be sticking between the billet and the die, and between the billet and the container, while a friction shear factor of $m=0.7$ was assigned to the interface between the billet and the pressure pad, due to its lower temperature. The heat transfer coefficient at the interfaces was assumed to be $200\text{kW/m}^2\text{C}^{[86]}$. All the other boundary conditions were the same as described in Chapter 5. The incipient melting point of 582°C for the 6061/Al₂O₃/20p composite material was used^[55-57], and was taken as the limiting boundary for the incipient melting line in the extrusion limit diagram.

An extrusion limit diagram for 6061/Al₂O₃/20p for the small press at KRDC was thus developed, as shown in Fig. 9.5. Correspondingly, the extrusion limit diagram for 6061/Al₂O₃/20p for the press at UAC is shown in Fig. 9.6. Again, the processing window for the press at UAC is much larger than that for the press at KRDC.

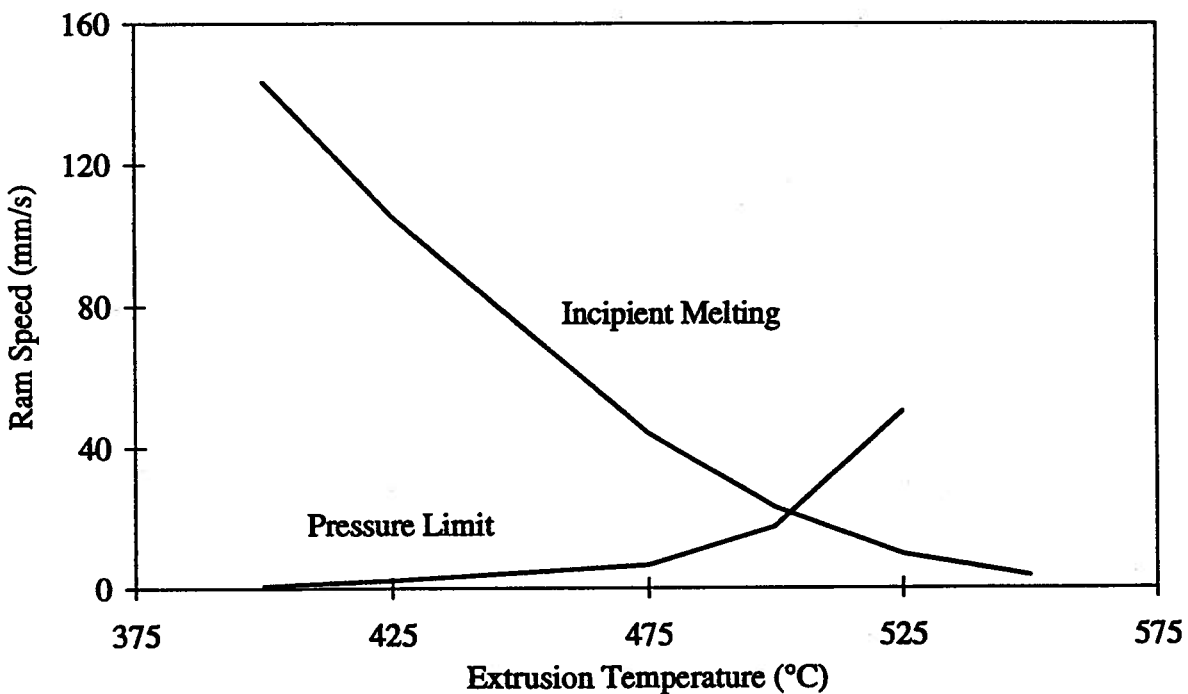


Figure 9.5 Extrusion limit diagram for 6061/Al₂O₃/20p for the press at KRDC

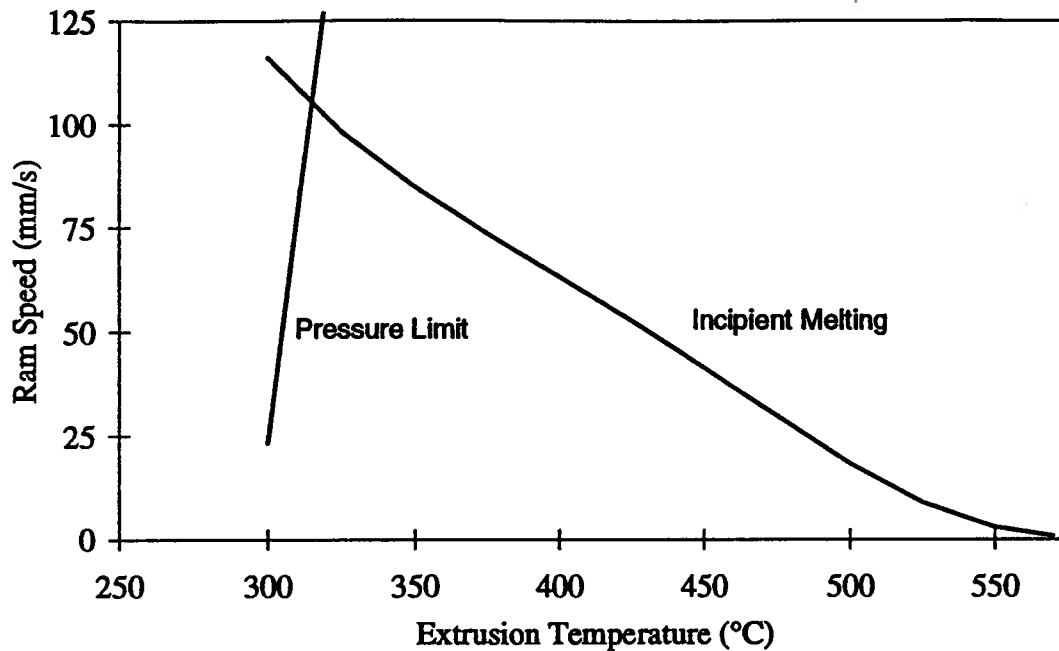


Figure 9.6 The limit diagram for 6061/Al₂O₃/20p for the press at UAC

9.1.2.2 Comparison of Extrusion Limit Diagrams

The extrusion limit diagrams for 6061/Al₂O₃/20p for the press at KRDC and UAC by both the empirical-equation technique and the finite element method are shown in Figs. 9.7 and 9.8. The pressure limit lines in the diagram from both techniques are quite close, especially in the limit diagram for the press at KRDC. This is expected because the empirical pressure equation (9.1) was determined using the plant trial data. The discrepancy between the pressure limit lines obtained by the two techniques in the diagram for the press at UAC is due to the low boundary temperature of about 250-300°C, because this temperature is beyond the valid extrusion temperature range of 390°C - 485°C used to determine the empirical equation (9.1). This might result in inaccuracy of the pressure prediction by the empirical equation (9.1). The difference between the two incipient melting lines is more obvious. This is mainly due to simplification of heat transfer analysis for the temperature rise estimation in

the empirical equation (9.2), because the FEM model considered coupled thermal and mechanical phenomena for both the billet itself and the surrounding tools during extrusion to steady state. The model predictions have been validated by comparison with the measured data in Chapter 5.

Limit diagrams for both the 6061/Al₂O₃/10p and the 6061/Al₂O₃/20p using the empirical equations are shown in Fig. 9.9. It is seen that the processing window for the 6061/Al₂O₃/20p is totally within the window of 6061/Al₂O₃/10p. This is due to the lower flow stress of 6061/Al₂O₃/10p. It thus can be concluded that the safe processing conditions for 6061/Al₂O₃/20p are also safe for the processing of 6061/Al₂O₃/10p.

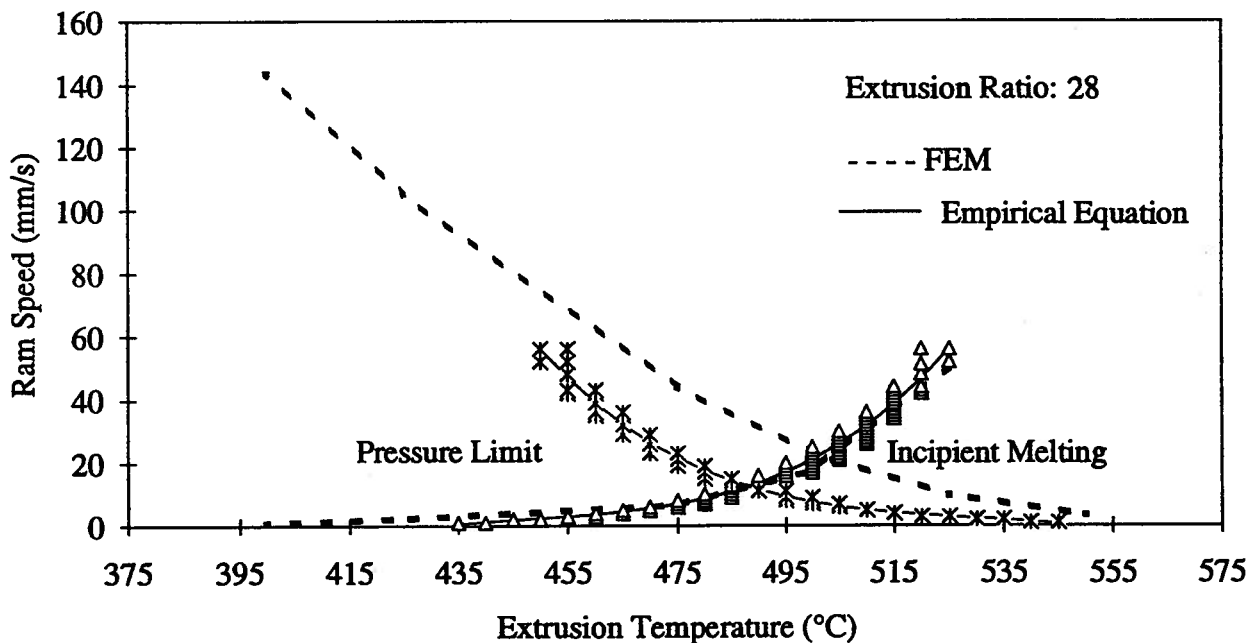


Figure 9.7 Comparison of the extrusion limit diagram of 6061/Al₂O₃/20p for the press at KRDC using different techniques

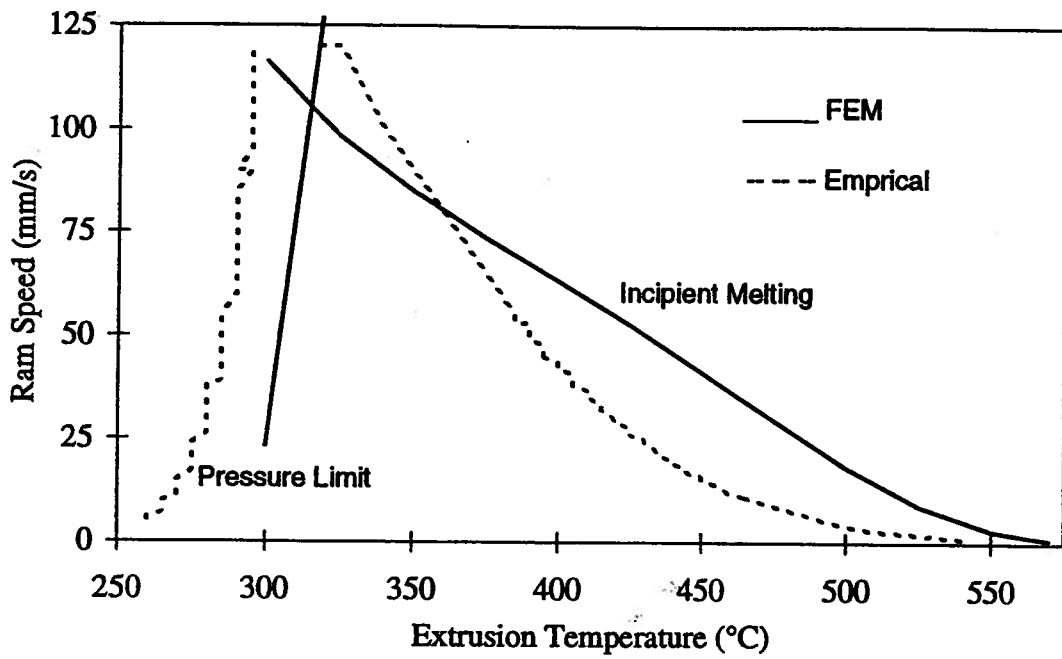


Figure 9.8 Comparison of the extrusion limit diagram of 6061/ $\text{Al}_2\text{O}_3/20\text{p}$ for the press at UAC using different techniques

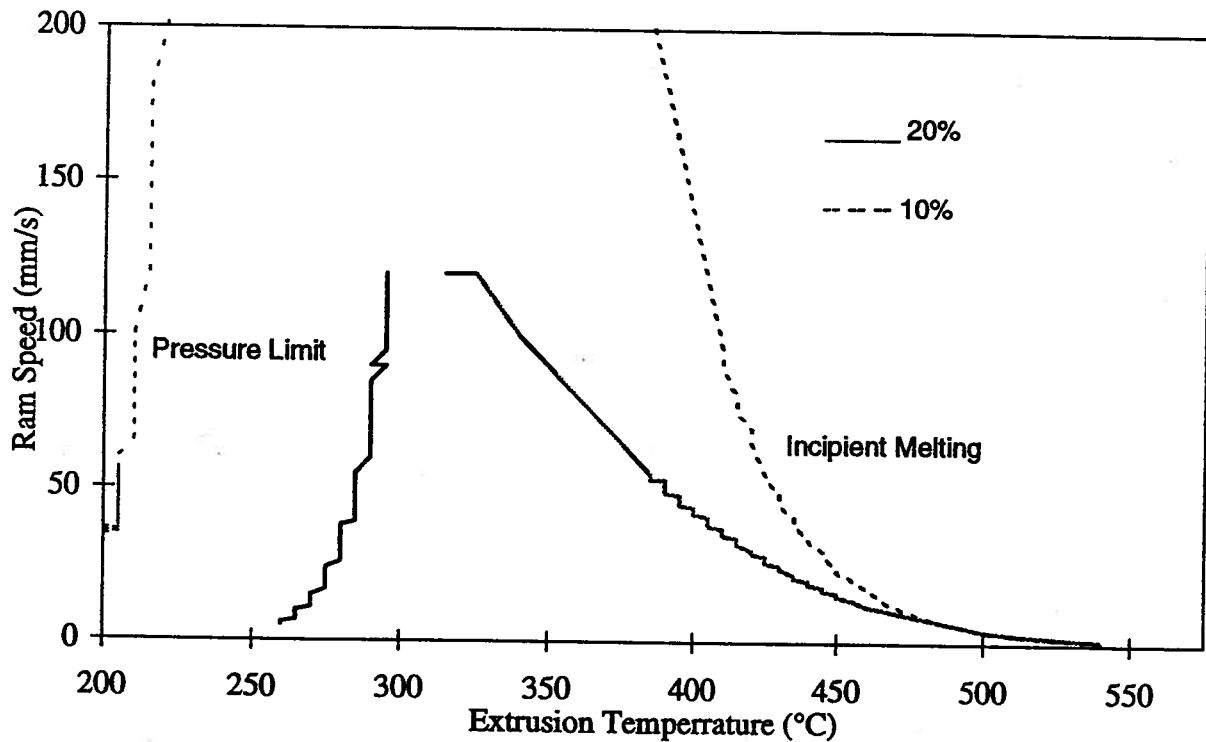


Figure 9.9 The extrusion limit diagram for both 6061/ $\text{Al}_2\text{O}_3/10\text{p}$ and 6061/ $\text{Al}_2\text{O}_3/20\text{p}$ using the empirical equation technique

9.2 Extrusion Limit Diagram with Low Speed Cracking Boundary

As observed in the plant trial at UAC, low speed cracking occurs at the front of extrudates in most of the trials. It is very important to delineate the boundaries of low speed cracking in the extrusion limit diagram for safe processing. Although a preliminary fracture criterion for the low speed cracking has been proposed in Chapter 8, it is still difficult to predict the low speed cracking by including a low speed criterion in the finite element model. Fortunately, substantial data on low speed cracking during the plant trial at different extrusion conditions has been generated, and the boundaries of low speed cracking can be delineated by processing the data.

9.2.1 Low Speed Cracking Boundary

During extrusion in the plant trial at UAC, the ram speed varied from less than 1mm/s to about 6mm/s, and the coverage of low-speed cracks on the surface of the extrudates changed from a few centimeters to more than 6 meters under different extrusion speeds and temperatures (Table 4.7). Because the billet temperature changes during extrusion, due to the heat of deformation, to track the billet temperature change, DEFORM was applied to the cases exhibiting long coverage of low-speed cracks through the extrudates (e.g., J94-6, J94-12, J94-13, J94-14, J94-20). The varying extrusion temperature and ram speed were traced from the front end of the extrudates exhibiting low speed cracks, toward the back end, until they disappeared. Then the data points traced from the recorded ram displacement were divided into two groups, the one associated with low speed cracking (termed as 'Fail'), and the other without low speed cracks (termed as 'Safe'). Thus the low speed cracking boundary of the extrudates of 6061/Al₂O₃/20p under the same extrusion ratio can be delineated, as shown in Figs. 9.10 to 9.12 for three different extrusion ratios.

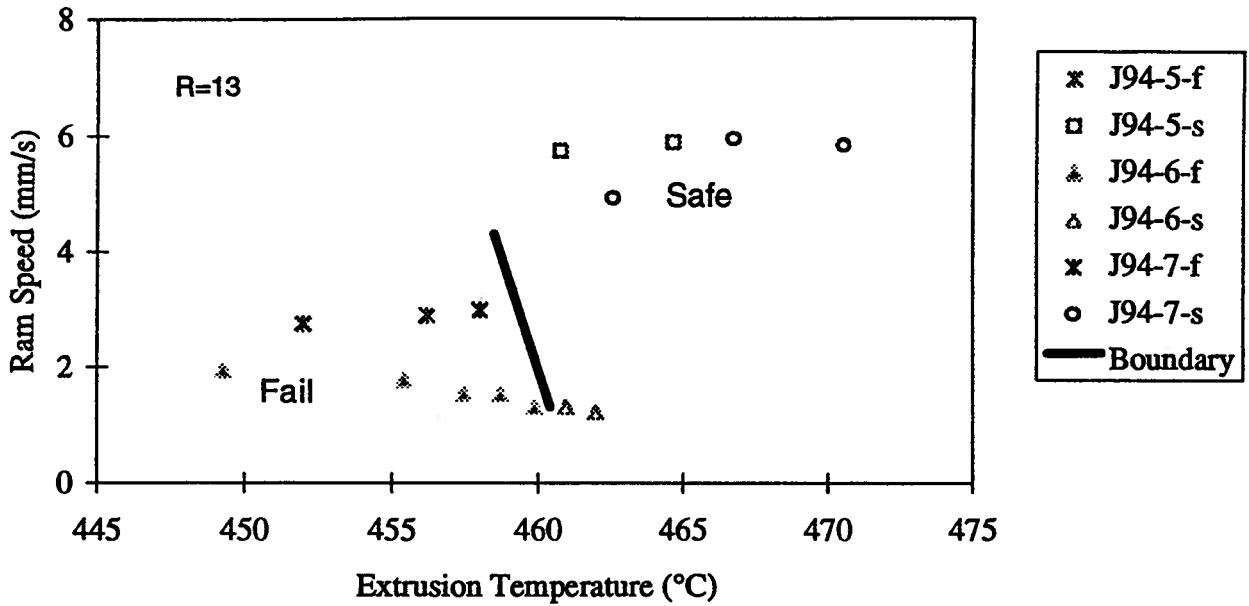


Figure 9.10 Low speed cracking boundary for the extrudate of 6061/Al₂O₃/20p at an extrusion ratio of 13

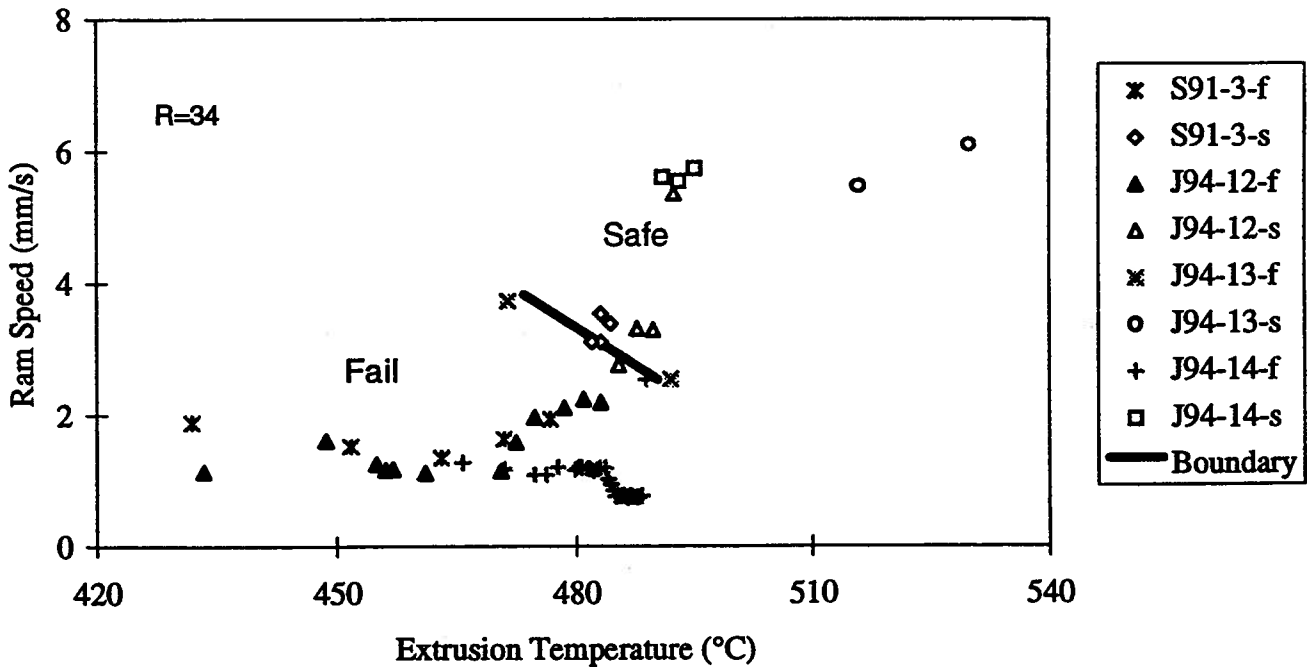


Figure 9.11 Low speed cracking boundary for the extrudate of 6061/Al₂O₃/20p at an extrusion ratio of 34

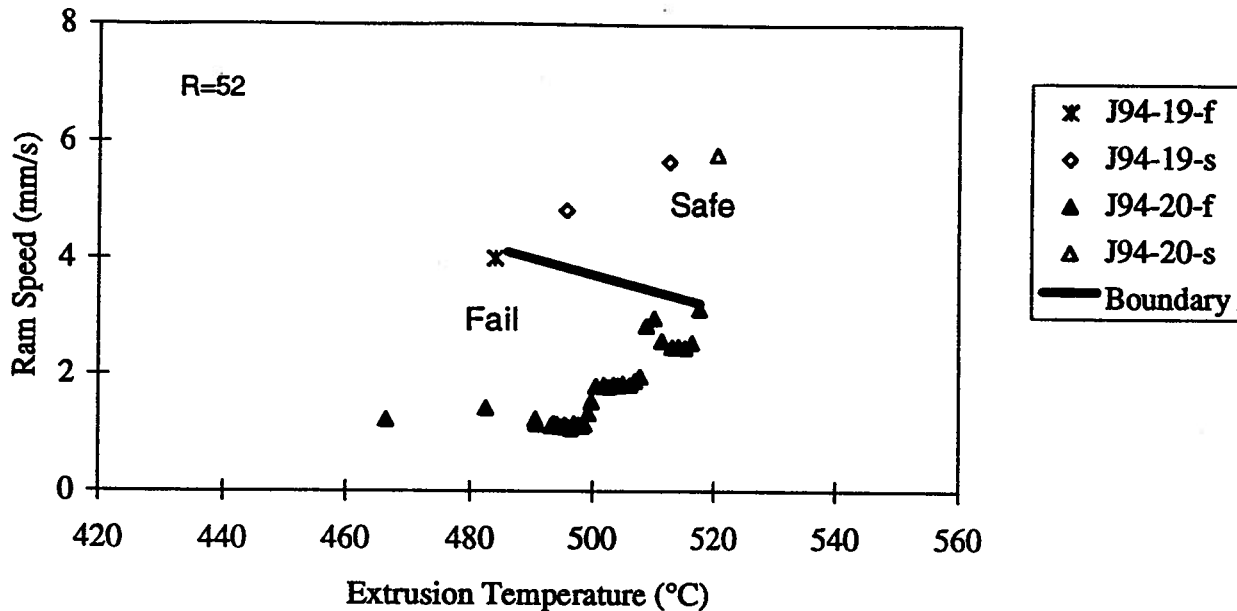


Figure 9.12 Low speed cracking boundary for the extrudate of 6061/Al₂O₃/20p at an extrusion ratio of 52

In the legend of Figs. 9.10 to 9.12, the symbol '-f' and '-s' denote 'fail' and 'safe', respectively for each extrudate. Due to less data being available for the 6061/Al₂O₃/10p, the low speed boundary could not be delineated.

9.2.2 Effect of Extrusion Ratios

The effect of extrusion ratio on the low speed cracking boundary is shown in Fig. 9.13. It is noted that to understand the effect of the extrusion ratio, the ram speed should be converted into extrusion exit speed, which is multiplied by the extrusion ratio. It is seen that as the extrusion ratio, R , increases, the low speed cracking boundary shifts toward high extrusion speed and higher temperature. This is consistent with the observation of the plant trial results, that is, more frequent low speed cracking occurred when the extrusion ratio was increased. The trend of the low speed cracking boundaries indicates that at a low extrusion

ratio, temperature has a larger effect than the ram speed, and vice versa at a high extrusion ratio. This is because at low extrusion ratio, the temperature rise of the billet due to the heat of deformation is low, and at a high extrusion ratio, because of higher exit speed, the adiabatic effect becomes more significant.

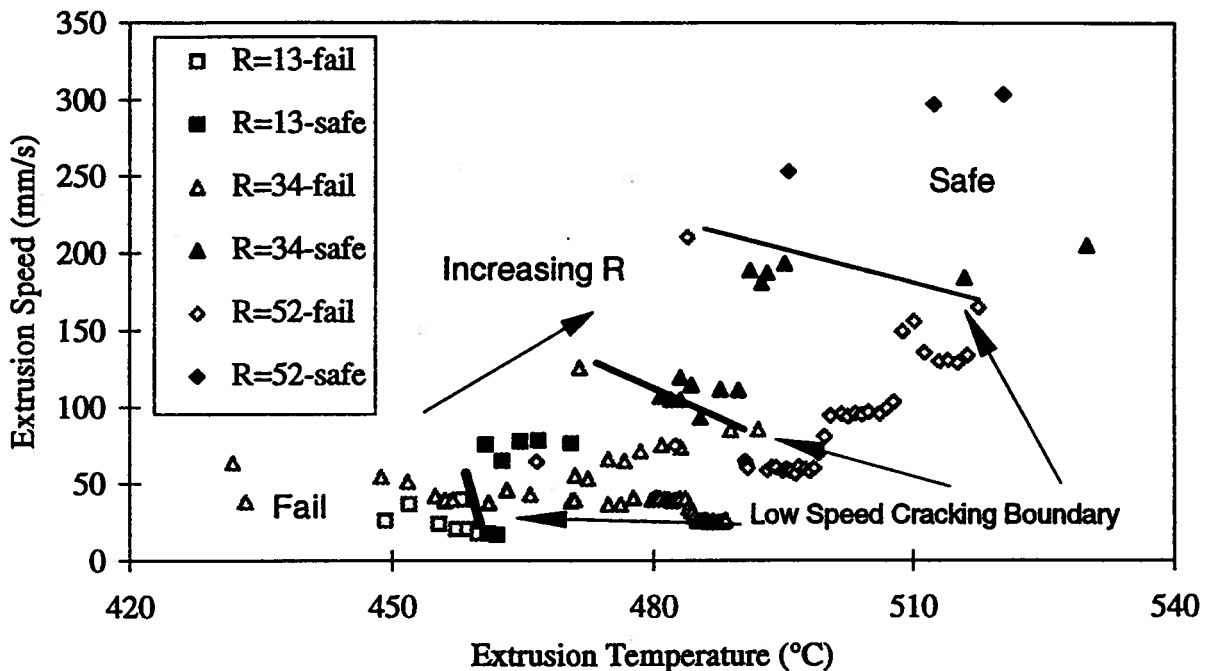


Figure 9.13 Effect on extrusion ratios on low speed cracking boundary during extrusion of 6061/Al₂O₃/20p

9.2.3 Extrusion Limit Diagram with Low Speed Cracking Boundary

The boundaries of low-speed cracking at different extrusion ratios are incorporated with the extrusion limit diagram developed using the FEM technique, as shown in Fig. 9.10. However, because of the limited range for the low speed cracking, only a part of the extrusion limit diagram is presented to clarify the low speed cracking boundaries. The high speed boundary refers to the incipient melting line obtained from Fig. 9.6. It is evident that an increase in either temperature or extrusion speed is beneficial to preventing occurrence of the

low-speed cracking. The boundary line shifts towards the high speed cracking line (high speed boundary) as the extrusion ratio increases to reduce the size of processing window. However, because no low speed cracking was observed at a ram speed of $\sim 6\text{mm/s}$ in the plant trials at UAC, 6mm/s is the minimum ram speed for the 7-inch press at UAC for extrusion of the PRMMCs at the extrusion ratio of 52.

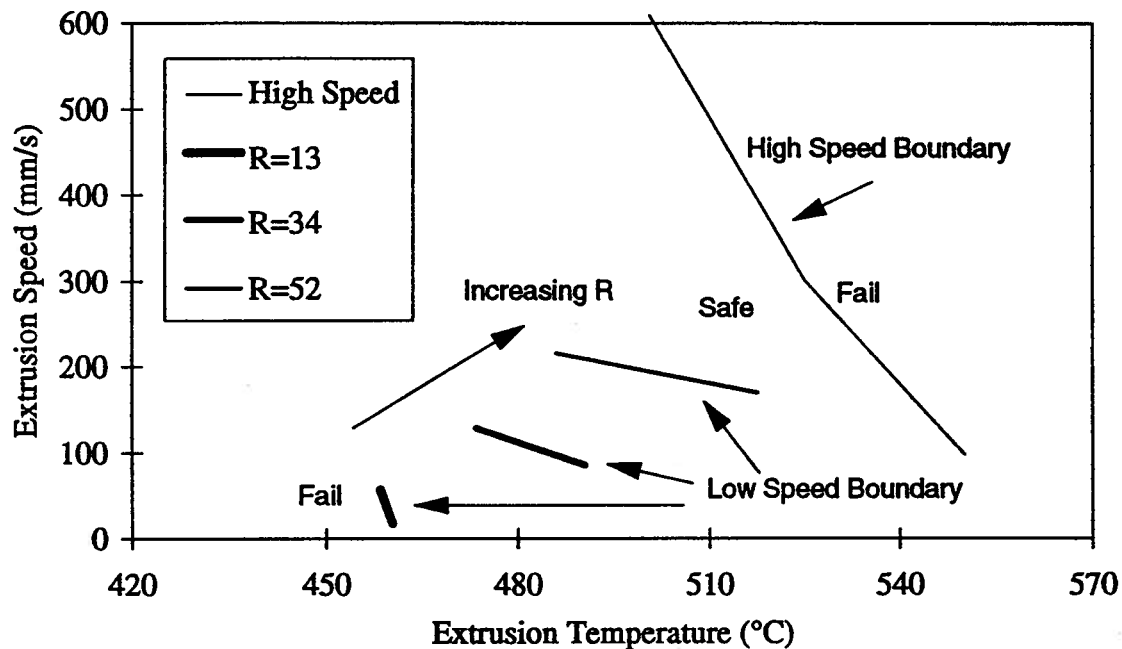


Figure 9.14 Extrusion limit diagram of 6061/Al₂O₃/20p for the press at UAC with low-speed cracking boundaries

9.3 Extrusion of the PRMMCs

Particle fracture, with its size refinement and particle redistribution during extrusion, has been examined in Chapter 7. The origin of low speed cracking observed in the plant trials has been explored with the aid of both macroscopic and microscopic finite element models in Chapter 8. It is therefore essential to minimize the potential microscopic damage, such as unhealed fractured particles and interface decohesion, which might lead to macroscopic low

speed cracking on the extrudate surface, and also to improve the quality of the PRMMCs by optimizing the extrusion processing conditions for maximum productivity.

9.3.1 Minimization of Microstructural Damage during Extrusion

The extrudates from two plant trials at KRDC and UAC were cut and polished. The specimen from the plant trial at KRDC was cut from the front end of the extrudate, K-6, and polished at KRDC following the procedure listed in Table 7.1; the specimens from the plant trial at UAC were also cut from the front end of the extrudates, J94-14, J94-20, with severe low speed cracks visible on the surface, and J94-11B, with slight low speed cracks, and polished at UBC following the procedure in Table 7.2. The extrusion conditions for the four specimens are listed in Table 9.2. The polishing samples were examined under an SEM for microstructure comparison. It seemed that some voids were present in the surface layer for all extrudates. The voids in the specimen from UAC were recognized as the origin of the low speed cracks, as shown in Fig. 9.15 from J94-14; while voids in K-6 specimen were associated with clusters, as shown in Fig. 9.16 for both the longitudinal and transverse sections.

Table 9.2 Extrusion conditions for the specimens examined under an SEM

Trial #	Material	Temp. (°C)	Extrusion Ratio	Billet Dia. (mm)	Remark
J94-14	20%	461 (Front)	34	178	Severe cracking
J94-20	20%	457 (Front)	52	178	Severe cracking
J94-11B	10%	434 (Front)	34	178	Slight cracking
K-6	10%	496(Front)	28	51	No cracking

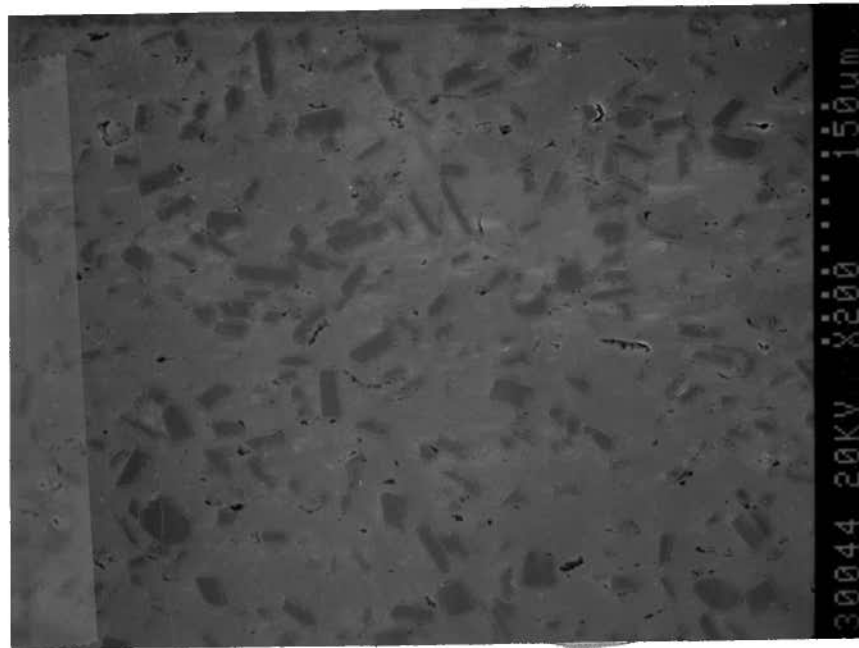
In the longitudinal section, again, most of the voids were formed at two ends of aligned particles in the extrusion direction, although some were also associated with particle fracture. The voids in the transverse section were randomly located around a particle or in a

cluster. The voids observed in the surface layer of the front-end extrudates could be due to the following reasons:

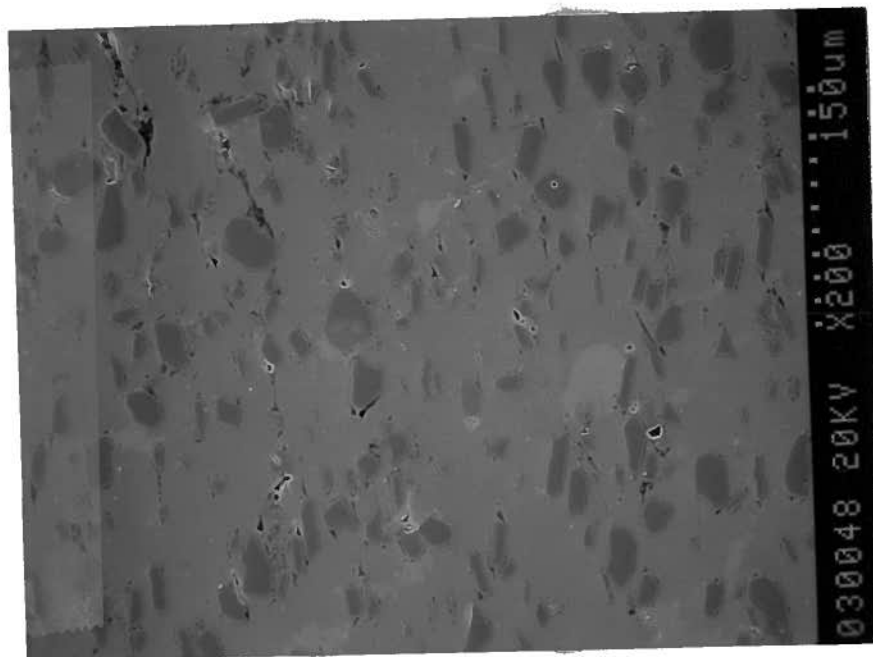
i) some voids could have been in the as-cast materials, not removed by extrusion, especially those in clusters. Any processing route in which the ceramic particles are not fully separated is susceptible to voids. In the cast materials, the voids are located between the particles (e.g., in clusters). Therefore, there is more likelihood of seeing voids in the as-cast 6061/Al₂O₃/10p because of the smaller particle size and its tendency towards particle clustering. This kind of void could be removed by either improving the particle distribution during the melt fabrication or breaking the clusters during extrusion.

ii) Voids form when a fractured particle was not healed by intruding the matrix material into the cracked gap. Most of these voids would be avoided by high hydrostatic pressure during extrusion at high temperature.

iii) Voids may also form by interface decohesion. Decohesion is encouraged by weak interfaces, such as obtained by spinel formation, MgAl₂O₄, at the particle interface^[123]. The generation of tensile stress in the surface layer of the extrudate in the die land area would lead to void formation, if either the tensile stress is higher or the interface was weak enough. Therefore, the tensile stress should be minimized by controlling all the possible extrusion parameters studied in Chapter 8, e.g., higher initial temperature of billet and die, high ram speed, low friction at the die interface. Elimination of spinel formation at the particle interface by increasing the magnesium content in the matrix alloy has been studied^[123], and new matrix alloys could also be sought with a better ductility^[122] and free of spinel formation^[123] during primary processing. In addition, a better die design, such as stream line die^[124] was recommended to minimize the fracture behavior during extrusion of MMCs. However, it is

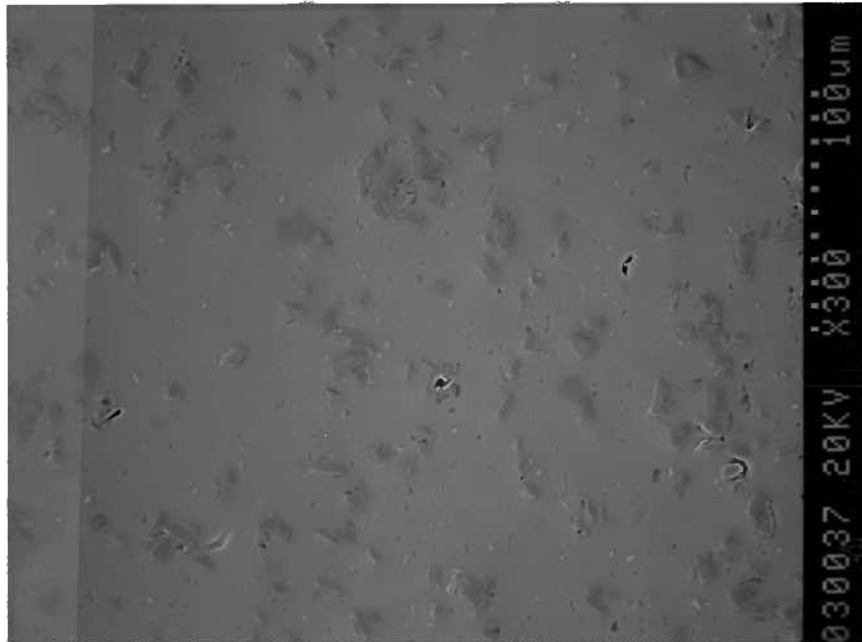


(a) Transverse

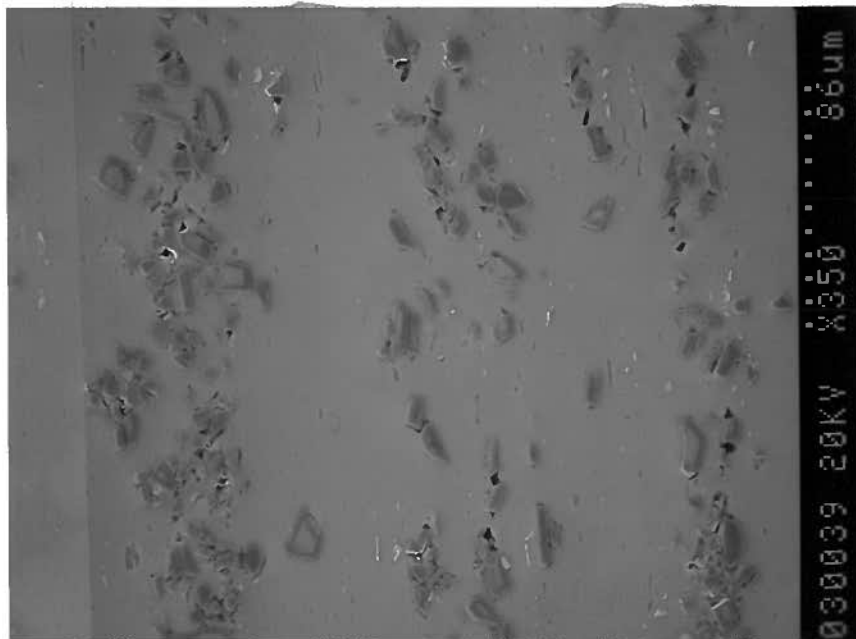


(b) Longitudinal

Figure 9.15 Voids in the surface layer of an extrudate of 6061/Al₂O₃/20p at an extrusion ratio of about 34 with low speed cracking (front end of J94-14)



(a) Transverse



(b) Longitudinal

Figure 9.16 Voids in the surface layer of an extrudate of 6061/Al₂O₃/10p at an extrusion ratio of about 28 with low speed cracking (front end of K-6)

unclear whether the use of a stream line die may sacrifice the improvement of particle distribution obtained by the flat face die extrusion, or increase the tendency of low speed cracking due to die interface friction. The adoption of a hydrostatic extrusion process^[11-12,76] is certainly helpful to suppress void formation, although the production cost could become a concern.

It is interesting to note that no obvious voids were present in the surface layer of the extrudates cut from the back end without visible low speed cracks on the surface, as shown in Fig. 9.17 for J94-14. This is mainly due to different extrusion temperatures and different ram speeds for the extrudates from the plant trials at UAC. Taking J94-14 for an example: at the front end, the extrusion temperature is about 460°C at a ram speed of about 1mm/s. However, at the back end, the extrusion temperature is about 55-60°C higher than that at the front end because of heat of deformation at a raised ram speed of about 6mm/s.

Because microstructural damage, such as particle fracture and/or void formation, may affect the elastic modulus of the composites^[92-95,122], the variation of values of the extrudates obtained under different extrusion conditions provide information on the effect of microstructural damage. The correlation between Young's modulus, E , of a hardened cement paste and the porosity P_0 was described as follows:

$$E = E_0 \exp(-xP_0) \quad (9.5)$$

where E_0 is the modulus of the solid phase without any pores and x is a material constant dependent on the internal structure^[104]. This may also be applicable to the composite materials during extrusion, where E is the elastic modulus of the composites after extrusion and E_0 is a standard elastic modulus which is a function of matrix alloy, reinforcement material and volume fraction of the reinforcement for a specific MMC. Hence the change in elastic

modulus of the composites for different extrusion conditions should reflect the existence of significant voids in the extrudates as a result of particle cracks, interface debonding, etc.

For the extrudates from KRDC, the elastic modulus as well as yield strength and the UTS for two different extrusion ratios (10 and 28) were tested, with little difference being found (See Fig. 4.18). This indicates that the void formation is not significant based on Eq. (9.5), although the elongation was sacrificed probably due to the presence of voids and/or the slight increase in the tensile strength. Obviously, the high hydrostatic pressure in the deformation zone helped suppress the void formation and growth during hot extrusion. However, it should be pointed out that at a higher temperature it seems likely that the lowest melting point phases could melt, leading to void formation. The low melting point phases must be associated with particles which were found at the dendrite extremities in the as-cast state.

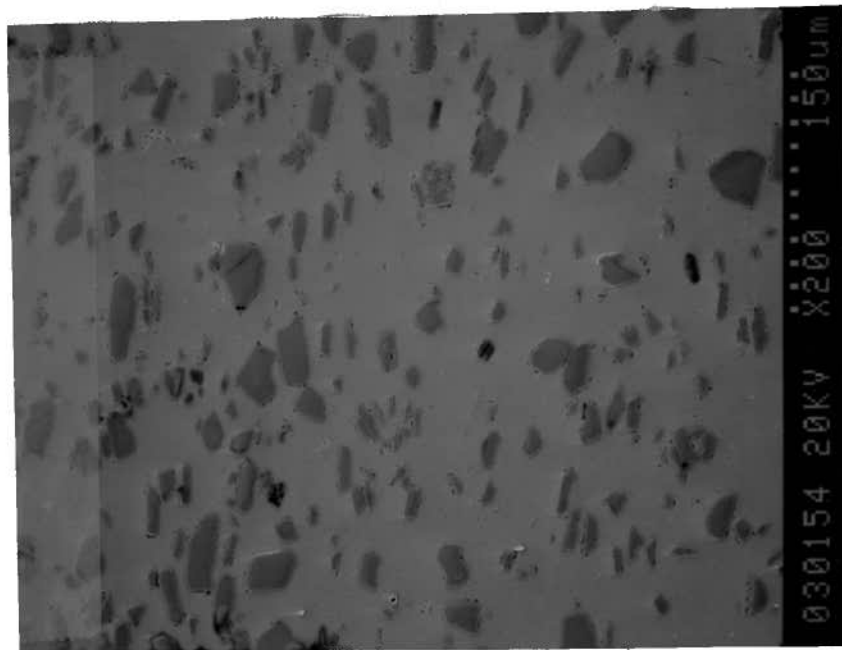


Figure 9.17 SEM image in the surface layer of the extrudate in longitudinal section at an extrusion ratio of about 34 without low speed surface cracking (back end of J94-14)

9.3.2 Improvement in Particle Distribution and Size Refinement

It is well known that at room temperature the elastic modulus deteriorates as strain increases, due to particle fracture^[75-76,93-94]. This is because the fractured particles were not healed at room temperature. However, in the hot extrusion process, the stress state in the deformation zone is tri-axial compressive, except in the surface layer of the extrudate in the die land area where the stress component in the extrusion direction is tensile. The compressive stress state results in two beneficial effects: firstly, void formation and growth is largely suppressed; secondly, most of the fractured particles were healed due to both severe shear and compressive deformation, because there is no oxidation in freshly formed surfaces^[11-12,75-76].

Reduction in particle size is known to be associated with an increase in the yield strength of composite materials. This decrease in size, in conjunction with the increased homogeneity of the particle distribution and reduction in aspect ratio, is expected to improve the fracture toughness. The healing of fractured particles will allow the material to attain its maximum potential elastic modulus. However, it could be balanced by the void formation if the secondary processing, e.g., extrusion, was not well controlled. A slight increase in the elastic modulus of the composites with an increase of the extrusion ratio (from the tensile tests) indicates that a large extrusion ratio should be beneficial to the improvement of mechanical properties, if and only if the voids can be minimized.

9.3.3 Quality and Productivity of the PRMMCs

Based on the above analysis, for a better quality control, a high extrusion temperature with a high absolute reduction would be suggested for the processing of the PRMMCs because of the following reasons:

- i) the increase in temperature improves the matrix flow due to lower flow stress, which, in turn, results in a series of beneficial effects: a) a lower tensile stress in the surface layer of the extrudate in the die land zone, which also leads to a lower local tensile stress at the ends of a particle, which could become a source of interface decohesion; b) a lower particle fracture probability based on the particle fracture model; c) easier to heal the gap between fracture particles due to matrix flow; d) more importantly, an increase in the ductility of the composite materials, which is the one of the controlling factor for fracture behavior of particulate reinforced MMCs^[122];
- ii) a higher absolute reduction is likely to result in a larger movement of particles in the deformation zone during extrusion which helps break clusters to improve the particle distribution; the clusters are always the source of potential damage, as presented in the micromechanical analysis of the PRMMCs in Chapter 6 and Chapter 8.

A higher extrusion speed is also recommended for extrusion of the PRMMCs. This is mainly due to:

- i) a higher extrusion speed will eliminate the low speed cracking, as described in Chapter 8;
- ii) it also helps the break-up of the particle clusters in the shear deformation zone; the cluster acts as a harder zone during deformation whose effect decreases as the strain rate increases^[124];
- iii) more importantly, the higher extrusion speed will result in a larger productivity of the composites, which reduces the production cost, and consequently makes the product more competitive.

Certainly, the high productivity is constrained by the high speed defects (such as void formation due to low melting phases, and high speed cracks on the surface). For this reason,

the composites should be processed within the high speed boundary of the extrusion limit diagram developed.

Chapter 10 CONCLUDING REMARKS

10.1 Summary and Conclusions

To convince customers to use Duralcan[®] materials, high quality product must be produced with a competitive price. A complete physical and chemical understanding of the product is essential for better quality and higher productivity. Hence, two extrusion plant trials were conducted on the Duralcan[®] materials; and the extrusion processes in two different presses have been simulated with the aid of a finite element model, DEFORM[®]. The plant trial data were used to validate the model predictions. Particle fracture and size refinement were observed in microstructural examination of the composites during extrusion. The finite element model predictions at both macroscopic and microscopic level were correlated with microstructure changes. Extrusion limit diagrams for both the 6061/Al₂O₃/10p and the 6061/Al₂O₃/20p were developed by both an empirical technique and the finite element technique, and modified with the low speed cracking boundary which is specific to the PRMMCs. The mechanism of low speed cracking was studied with the aid of the finite element model and the SEM analysis. The major findings from this study are summarized as follows:

- 1) Particles fractured during extrusion with accumulation of smaller particles in extrudates. Three particle fracture modes were proposed, i.e., comminution mode, shear mode, and tensile mode. Most of the fractured particles were healed under large hydrostatic pressure and shear deformation at high temperature.

2) Particles are aligned in the extrusion direction with formation of extrusion bands, especially in the 6061/Al₂O₃/10p. Voids were observed in the surface layer of the extrudates with low speed cracks, and also in those extrudates with severe particle clusters, especially the 6061/Al₂O₃/10p. The causes for void formation could be three-fold:

- i) retained from the as-cast material, especially for those in clusters;
- ii) unhealed particle fracture in the surface layer at relatively low temperature;
- iii) weak particle interface under high local tensile stress at the ends of the particles, especially for those in clusters in the surface layer of the extrudate.

These voids can be avoided by controlling the processing parameters in both the primary and secondly processing routes. The hydrostatic pressure generated during flat-face die extrusion may help suppress void formation and growth. This is why the elastic modulus and other tensile strengths (e.g., yield stress, and the ultimate tensile strength) do not decline under an extrusion ratio of about 30, although the elongation is sacrificed. The improvement in homogenization of particle distribution and the particle size refinement after extrusion allow the maximum potential increase of tensile properties and also the fracture toughness, if the void formation can be suppressed by generation of a high hydrostatic pressure and low tensile stress in the surface layer as obtained in higher temperature extrusion.

3) The safe processing window for the extrusion of the Duralcan materials was squeezed towards the high temperature side by the low speed cracking boundary. The low speed cracking, observed at the front end of extrudates, is believed to be induced by low ductility of the materials and void formation and growth at relative low temperature under tensile stress in the die land zone. Both the low speed cracking and the void formation can be suppressed by increasing the initial billet and die temperature and the extrusion speed within

the limit of the high speed cracking boundary (incipient melting line) with better quality and larger productivity of the PRMMCs.

10.2 Future Work

To better understand the physical and chemical nature of the composites, the following work is suggested based on the above study.

1) Because the origin of the low speed cracking is associated with void formation, a quantitative analysis of the fraction of voids formed under different temperature and strain rate is beneficial for a more accurate control of the processing parameters, such as temperature and extrusion speed, to improve quality (to minimize voids and obtain more homogenized particle distribution at a finer and a more uniform particle size level) and productivity;

2) A fracture criterion for low speed cracking or potential microstructural damage during extrusion needs to be developed and verified. The fracture criterion can then be incorporated into the finite element model to cost-effectively develop extrusion limit diagrams for different materials.

3) An effective technique is required at the fabrication stage to improve both the particle distribution and the bonding strength between the particles and the matrix to prevent potential interface decohesion. New choices of matrix alloys with higher ductility but free of spinel formation are needed. A better design of the die to have improved quality and higher productivity of the extruded products should also be studied. New processing technologies which produce defect free products with lower production costs should be explored.

REFERENCES

- [1] Chawla, K.K.: '*Composite Materials, Science and Engineering*', Material Research and Engineering (MRE), Springer-Verlag, 1987.
- [2] Caron, S.; Masounave, J.: A Literature Review on Fabrication Techniques of Particulate Reinforced Metal Composites, *Proc. of Int. Conf. on Particulate Reinforced Metal Composites*, Ed. by J. Masounave & F.G. Hamel, Montreal, Quebec, Canada, 17-29, Sept., 1990, pp. 79-86.
- [3] Hoover, W.R.: Commercialization of DURALCAN Aluminum Composites, *Private Communication*, Dural Aluminum Composites Corporation, San Diego, CA, USA, 1992, pp. 211-217.
- [4] Selseth, J.E. and Lefstad, M.: Extrusion of Aluminium Matrix Composites, *5th Scandinavian Symposium on Materials Science*, Copenhagen, May 22-25, 1989, pp. 1-8.
- [5] Jeffrey, P.W.; Holcomb, S.: Extrusion of Particulate-Reinforced Aluminium Matrix Composite, *Proc. of Int. Conf. on Particulate Reinforced Metal Composites*, Ed. by J. Masounave & F.G. Hamel, Montreal, Quebec, Canada, 17-29, Sept., 1990, pp. 181-186.
- [6] Brusethaug, S.; Reiso, O.; Ruch W.: Extrusion of Particulate-Reinforced Aluminium Billets made by D.C. Casting, *Proc. of Int. Conf. on Particulate Reinforced Metal Composites*. Ed. by J. Masounave & F.G. Hamel, Montreal, Quebec, Canada, 17-29, Sept., 1990, pp. 173-179.
- [7] Hains, R.W.; Morris, P.L.; Jeffrey, P.W.: Extrusion of Aluminium Metal Matrix Composites, *Proc. of Int. Symp. Advanced Structural material*, 1988, pp. 53-60.
- [8] Allison, J.E. and Cole, G.S.: Metal Matrix Composites in the Automotive Industry: Opportunities and Challenges, *JOM*, January 1993, Vol. 45, pp. 19-24.
- [9] Dixon William: Extrusion of Particulate-Reinforced Aluminium-Based Metal Matrix Composites, *5th International Aluminum Extrusion Technology Seminar*, Vol. 1, Chicago, Illinois, USA, 19-22 May 1992, pp. 429-436, The Aluminium Association.
- [10] Ghosh, S.: Finite Element Simulation of Some Extrusion Process Using the Arbitrary Lagrangian-Eulerian Description, *J. Mater. Shaping Technology*, (1990), 8:53-64.
- [11] Embury J.D. and Zok, F.: Forming of Metal-Matrix Composites under Superimposed Hydrostatic Pressure, *MMCs workshop at the University of B.C.*, Vancouver, B.C., Canada, May 19-20, 1994.
- [12] Embury J.D.; Tao S.; Newell J. and Zok, F.: Damage Accumulation in Metal-Matrix Composites and Its Role in Hydrostatic Extrusion, *Private Communication*, 1991.
- [13] Inoue, N. and Nishihara, M. (Eds): '*Hydrostatic Extrusion, Theory and Application*', Elsevier Applied Science Publishers, 1985.

- [14] Collier, J.R.; Gunasekera, J.S.; Sargand, S.M.: Streamlined Dies and Profiles Extrusion, *ANTEC'87*, pp. 203-206.
- [15] Gelin, J.C. and Predeleanu, M.: Finite Strain Elasto-Plasticity Including Damage-Application to Metal Forming Problems, *Numiform 89*, Thompson *et al.* (Eds.), 1989, Balkema, Rotterdam, pp. 151.
- [16] Ghosh, S.: A New Finite Element Description for Simulation of Metal Forming Processes, *Numiform 89*, Thompson *et al.* (Eds.), 1989, Balkema, Rotterdam, pp. 159.
- [17] Hussin, A.A.M.; Hartley, P.; Sturgess, C.E.N.; Rowe, G.W.: Elastic-Plastic Finite Element Modeling of A Cold-Extrusion Process Using a Microcomputer-Based System, *J. of Mechanical Working Technology*, 16 (1988), 7-19.
- [18] Wang, A.C.: Computer Modeling of Extrusion Elastic-Plastic Process, *Computer Eng.*, 1988, *Proc.*, Published by ASME, New York, USA, pp. 211-216.
- [19] Russel, P.N.: Problems and Progress in Extrusion Studies, *Num. Method in Ind. Forming Processes*, Pattman/Wood/Alexander/Zienkiewicz (eds), 1982, pp. 75.
- [20] Roll, K.; Neitzert, T.: On the Application of Different Numerical Methods to Calculate Cold Forming Processes, *Num. Method in Ind. Forming Processes*, Pattman/Wood/Alexander/Zienkiewicz (eds), 1982, pp. 97.
- [21] Wertheimer, T.B.: Thermal Mechanically Coupled Analysis in Metal Forming Processes, *Num. Method in Ind. Forming Processes*, Pattman /Wood /Alexander /Zienkiewicz (eds), 1982, pp. 425.
- [22] Abo-Elkhier, M., Orvas, G.A.; Dokainish, M.A.: A Consistent Eulerian Formulation for Large Deformation Analysis With Reference to Metal-Extrusion Process, *Int. J. Non-Linear Mechanics*, Vol. 23, No. 1, pp. 37-52, 1988.
- [23] Crochet, M.J.; Delvaux, V.; Marchal, J.M.: Numerical Prediction of Viscoelastic Extrudate Swell, *Numiform 89*, Thompson *et al.* (Eds.), 1989, Balkema, Rotterdam, pp. 17.
- [24] Yamada, Y.; Wifi, A.S. and Hirakawa, T.: Analysis of Large Deformation and Stress in Metal Forming Processes by Finite Element Method, *International Symposium on Metal Forming Plasticity*, Germany, 1978, pp. 158-189.
- [25] Rusia, D.K.; Gunasekera, J.S.: A Modified Viscoplastic Formulation for Large Deformation Using Bulk Modules, *Numiform 89*, Thompson *et al.* (eds), Fort Collins, Colorado, June 26-30, 1989.
- [26] Argyris, J.H.; Doltsinis, J. St; Luginsland, J., Shenze Hong: Numerical Simulation of Forward Extrusion by the Finite Element Method, *Numiform 89*, Thompson *et al.* (Eds.), 1989, Balkema, Rotterdam, pp. 529.
- [27] Srinivasan, R.; Gunasekera, J.S.; Gegel, H.L. and Doraivelu, S.M.: Extrusion Through Controlled strain Rate Dies, *J. Mater. Shaping Technol.*, Vol. 8 1990, pp. 133-141.

- [28] Chen, H.L.; Lehnhoff, T.F.; Doraivelu, S.M.: A Stress Ratio Parameter for Studying the Workability of Metals-Extrusion, *J. Mater. Shaping Technol.*, Vol. 8, No. 4, 1990, pp. 209-218.
- [29] Liu, T.S., Chung, N.L.: Extrusion Analysis and Workability Prediction Using Finite Element Method, *Computers & Structures*, Vol. 36, No. 2, pp. 369-377, 1990.
- [30] Shimazaki, Y.: A Penalty Function Method for Non-isothermal Axisymmetric Flow Problems, *Numiform 89*, Thompson *et al.* (Eds.), 1989, Balkema, Rotterdam, pp. 593.
- [31] Menges, G.; Masberg, U.; Gesenhues, B.; Berry, C.: Numerical Simulation of Three-Dimensional Non-Newtonian Flow in Thermoplastics Extrusion Dies with Finite Element Methods, *Numerical Analysis of Forming Process*, Edited by J.F.T. Pittman, O.C. Zienkiewicz, R.D. Wood, and J.M. Alexander, 1984, John Wiley and Sons Ltd, pp. 307-350.
- [32] Zienkiewicz, O.C.; Godbolt, P.N.: Flow of Plastic and Visco-Plastic Solids with Special Reference to Extrusion and Forming Processes, *Int. J for Numerical Methods in Engineering*, Vol. 8, pp. 3-16, 1974.
- [33] Zienkiewicz, O.C.; Jain, P.C.; Onate, E.: Flow of Solids during Forming and Extrusion: Some Aspects of Numerical Solutions, *Int. J. Solids Structures*, 1978, Vol. 14, pp. 15-38.
- [34] Zienkiewicz, O.C. and Huang, G.C.: Adaptive Modelling of Transient Coupled Metal Forming Processes, *Numiform 89*, Thompson *et al.* (Eds.), 1989, Balkema, Rotterdam.
- [35] Wang, K.C.; Carey, G.F.: Modelling Extrusion Using Adaptive Grid Refinement, *Numiform 89*, Thompson *et al.* (Eds.), 1989, Balkema, Rotterdam, pp. 229.
- [36] Gelten, C.J.M.; Konter, A.W.A: Application of Mesh-Rezoning in the Updated Lagrangian Method To Metal Forming Analysis, *Num. Method in Ind. Forming Processes*, Pattman/Wood/Alexander/Zienkiewicz (eds), 1982, pp. 511.
- [37] Wu, W.T.; Oh, S.I.; Altan, T.; Miller, R.A.: Automated Mesh Generation for Forming Simulation-I, *Private Communication*, Scientific Forming Technology Corporation, Columbus, Ohio, 1992.
- [38] Park, J.J. and Kobayashi, S.: Three-Dimensional Finite Element Analysis of Block Compression, *Int. J. of Mech. Sci.*, Vol. 26, No. 3, pp. 165-176.
- [39] Cheng J.-H.: Automatic Adaptive Remeshing for Finite Element Simulation of Forming Processes, *Int. J. of Numerical Methods in Engineering*, Vol. 26, No. 1, Jan, 1988, pp. 1-18.
- [40] Wu, J.F.; Shephard, M.S.; Dvorak, G.J. and Bahei-El-Din, Y.A.: A Material Model for the Finite Element Analysis of Metal Matrix Composite, *Composite Science and Technology*, Elsevier Science Publishers Ltd., England, 1989.

- [41] Bohm, H.J. and Rammerstorfer F.G.: Micromechanical investigation of the processing and loading of Fiber-reinforced metal matrix composites, *Materials Science and Engineering*, A135, (1991), pp. 185-188.
- [42] Levy, A.; Papazian, J.M.: Elastoplastic Finite Element Analysis of the Effects of Thermal Treatment on Discontinuously Reinforced SiC/Al Composites, *Metal & Ceramic Matrix Composites: Processing, Modeling & Mechanical Behavior*, 1990, pp. 319-326.
- [43]. Zhang H.Y.; Daehn, G.S. and Wagoner R.H.: The Temperature-Cycling Deformation of Particle Reinforced Metal Matrix Composites -- A Finite Element Study, *Scripta Metallurgica et Materialia*, Vol. 24, pp. 2151-2155, 1990.
- [44] Zahl, D.B. and McMeeking, R.M.: The Influence of Residual Stress on the Yielding of Metal Matrix Composite, *Acta Metall. Mater.*, Vol. 39, No. 6, pp. 1117-1122, 1991.
- [45] Aradhya, K.S.S. and Surappa, M.K.: Estimation of Mechanical Properties of 6061 Al-SiCp Composites Using Finite Element Method, *Scripta METALLURGICA*, Vol. 25, pp. 817-822, 1991.
- [46] Ramakrishnan, N.; Okada, H.; Atluri, S.N.: Computer Simulation of Transformation Induced Plasticity Using Finite Element Method, *Acta Metall. Mater.*, Vol. 39, No. 6, pp. 1297-1308.
- [47] Kopp Reiner: Multi-Level Simulation of Metal-Forming Processes, *2nd International Conference on Technology of Plasticity*, Stuttgart, 24-28 Aug., 1987.
- [48] Kopp Reiner and Cho, Myong-Lae: Influence of Boundary Conditions on Results of the Finite Element Simulation, *2nd International Conference on Technology of Plasticity*, Stuttgart, 24-28 Aug., 1987, pp. 165.
- [49] Sellars, C.M.; McG. Tegart, W.J.: Hot Workability, *International Metallurgical Review*, Review 158, Vol. 17, 1972, pp. 1-24.
- [50] Datsko, J. and Yang, C.T.: Correlation of Bendability of Materials with Their Tensile Properties, *J. of Engineering for Industry*, Vol. 82, Nov. 1960, pp. 309-314.
- [51] Lathem, D.J. and Cockcroft, M.G.: Ductility and the Workability of Metals, *J. Inst. Met.*, 1968, pp. 33.
- [52] Manoharan M.; and Kamat, S.V.: On the Fracture Toughness of Particulate Reinforced Metal Matrix Composites, *Scripta Metallurgica et Materialia*, Vol. 25, pp. 2121-2125, 1991.
- [53] Lloyd, D.J.: Particulate Reinforced Composites Produced by Molten Metal Mixing, *High Performance Composites for the 1990s*, Ed. by S.K. Das, C.P. Ballard and F. Marikar, The Minerals, Metals and Materials Society, 1991, pp. 33-45.
- [54] Kalu, P.N., McNelley, T.R.: Microstructural Refinement by Thermomechanical Treatment of a Cast and Extruded 6061 Al-Al₂O₃ Composite, *Scripta Metallurgica et Materialia*, Vol. 25, No. 4., April 1991, pp. 853-858.

- [55] Clode, M.P. and Sheppard, T.: Extrusion Limit Diagrams Containing Structural and Topological Information for AA6063 Aluminum Alloy, *Material Science and Technology*, April 1993, Vol. 9, pp. 313-318.
- [56] Sheppard, T.: The Extrusion of Aluminum Alloys: A Thermomechanical Process, *Aluminum Alloys '90*. Proceedings of the 2nd Int. Conf. of Aluminum Alloys--Their Physical and Mechanical Properties, Oct. 9-13, 1990, Beijing, China. Ed. C.Q. Chen, and E.A. Starke, Jr., pp. 744-754, International Academic Publishers.
- [57] Raybound, D. and Sheppard, T.: Axisymmetrical Extrusion: The Effect of Temperature Rise and Strain Rate on the Activation Energy and Material Constants of Some Aluminum Alloys and Their Relation to Recrystallization, Substructure, and Subsequent Mechanical Properties, *Journal of Institute of Metals*, Vol. 101, 1973, pp. 65-72.
- [58] Sheppard, T. and Raybound, D.: A New Approach to the Construction of Extrusion-Limit-Diagrams, Giving Structural Information with Application to Superpure Aluminum and Al-Zn-Mg Alloys, *Journal of Institute of Metals*, Vol. 101, 1973, pp. 72-78.
- [59] Oddvin Reiso: The Effect of Billet Preheating Practice on Extrudability of AlMgSi Alloys, *4th Int. Aluminum Extrusion Technology Seminar*, Chicago, Ill., 1988.
- [60] Zasadzinski, J.; Libura, W.; Richart, J. and Misiolak, W.Z.: Modeling of Temperature-Speed Parameters in Aluminum Extrusion, *Light Metal Age*, August, 1992, pp. 60-64.
- [61] Richardson, G. J.; Hawkins, D. N. and Sellars, C. M.: 'Worked Examples in Metalworking', The Institute of Metals, London, 1985, pp. 144-161.
- [62] Sheppard, T.: Extrusion of AA2024 Alloys, *Materials Science and Technology*, Vol. 9, May, 1993, pp. 430-440.
- [63] Meadows, B. J. and Culler, M. J.: A Theoretical Derivation of Stress/Strain Rate/Temperature Relationships in the Extrusion of Al-Mg-Si Type Alloys, *Journal of Institute of Metals*, Vol. 97, 1969, pp. 321-326.
- [64] McQueen, H.J. and Celliers, O.C.: Application of Hot Workability Studies to Extrusion Processing, I. Extrusion Control Parameters and Constitutive Equations, *Materials Forum*, Vol. 17, 1993, pp. 1-13.
- [65] Castle, A.F. and Sheppard, T.: Hot-Working Theory Applied to Extrusion of Some Aluminum Alloys, *Metals Technology*, Vol. 3, October 1976, pp. 454-475, .
- [66] Brusethaug, S. and Reiso, O.: Extrusion of SiCp Reinforced Al-Alloys, *12th Riso International Symposium on Materials Science*, 1991, Roskilde, Denmark, Riso National Laboratory.
- [67] Sheppard, T.: Press Quenching of Aluminum Alloys, *Materials Science and Technology* Vol. 4, July 1988, pp. 635-643.
- [68] Geltser, I. S.: *Master Thesis*, The University of British Columbia, 1992.

- [69] Sheppard, T.; Raybound, D.: On Load and Temperature Rise during the Extrusion of Superpure Al, Al-Zn, and Al-Zn-Mg Alloys, *J. Inst. Metals*, 1973, Vol. 101, pp. 33-44.
- [70] Grasmø, K.; Holthe, K.; Støren, S.; Valberg, H.; Flatval, R.; Hanssen, L.; Lefstad, M.; Lohne, O.; Welo, T.; Ørsund, R.; Herberg, J.: Modelling of Two-Dimensional Extrusion, in '5th International Aluminum Extrusion Technology Seminar', Chicago, Ill., May, 1992, pp. 367-376, Washington, The Aluminum Association.
- [71] Reinikainen, T.; Andersson, K.; Kivivuori, S.; Korhonen, A.S.: Finite-Element Analysis of Copper Extrusion Processes, *J. Mater. Proc. Tech.*, Vol. 34, 1992, pp. 101-108.
- [72] Alto, A.; Galantucci, L.M.; Tricarico, L.: A Parametric FEM Analysis of Extrusion Using a Personal Computer, *J. Mater. Proc. Tech.*, Vol. 31, 1992, pp. 335-345.
- [73] Devadas, C.; Celliers, O.C.: Metal Flow during the Extrusion Process, in '5th International Aluminum Extrusion Technology Seminar', Chicago, Ill., May, 1992, pp. 359-368, Washington, The Aluminum Association.
- [74] Davies, C.H.J.; Chen, W.C.; Samarasekera, I.V.; Hawbolt, E.B. and Brimacombe, J.K.: Extrusion of Metal Matrix Composites, -Modeling and Experimental, *Proceeding of 123rd TMS Annual Meeting*, San Francisco, Feb. 27-Mar. 3, 1994.
- [75] Brechet, Y.; Newell, J.; Tao, S. and Embury, J.D.: A Note on Particle Comminution at Large Plastic Strains in Al-SiC Composites, *Scripta Metallurgica et Materialia*, Vol. 28, No. 1, 1992, pp. 47-51.
- [76] Brechet, Y.; Embury, J.D.; Tao, S. and Luo, L.: Damage Initiation in Metal Matrix Composites, *Acta Metall. mater.*, Vol. 39, No. 8, pp. 1781-1786, 1991.
- [77] Humphreys, F.J.; Kalu, P.N.: Dislocation-Particle Interactions during High Temperature Deformation of Two-Phase Aluminum Alloys, *Acta Metall. Mater.*, Vol. 35, No. 12, 1987, pp. 2815-2859.
- [78] Jonas, J.J.; Sellars, C.M.; Tagart, W.J. McG.: Strength and Structure under Hot Working Conditions, *Metallurgical Review*, Vol. 14, 1969, Review No. 130, 1-24.
- [79] Rao, K.P.; Hawbolt, E.B.: Development of Constitutive Relationships Using Compression Testing of a Medium Carbon Steel, *J. Engrg. Mats. & Tech. (Trans. ASME)*, Vol. 114, Jan., 1992, 116-123.
- [80] Sheppard, T. and Wright, D.S.: Determination of Flow Stress: Part 1 Constitutive Equation for Aluminium Alloys at Elevated Temperature, *Metals Tech.*, Vol. 6, 1979, pp. 215-223.
- [81] Davies, C.H.J.; Chen, W.C.; Geltser, I.S.; Samarasekera, I.V.; Hawbolt, E.B. and Brimacombe, J.K.: Hot deformation of 6061/Alumina composite materials, *Proceedings of the 32nd CIM Metallurgist Conf.*, Quebec, Canada, Aug. 22-24, 1993.
- [82] Oh, S. I.; Wu, W.T.; Tang, J.P.; Vedhanayagam A.: Capabilities and applications of FEM codes DEFORM: the perspective of the developer, *J. Mater. Proc. Tech.*, 1991, Vol. 27, 25-42.

- [83] Kobayash, S.; Oh, S.I.; Altan T: '*Metal Forming and the Finite Element Method*', 1st Ed., pp. 111-130, 1989, O.U.P., Oxford, U.K..
- [84] Zienkiewicz, O.Z.; Taylor, R.L.: '*The Finite Element Method, Basic Formulation and Linear Problems*', Vol. 1, 4th edition, McGraw-Hill Book Company Europe, 1993.
- [85] Sheppard, T.: Extrusion of AA2024 Alloy, *Mater. Sci. Technol.*, Vol. 9, May 1993, pp. 430-440.
- [86] Hlady, C.O.: *Master Thesis of Applied Science*, The University of British Columbia, Vancouver, B.C., Canada, 1994.
- [87] Chevalier, L.; Dahan, N.: Metal-Forming Process Analysis by the Viscoplasticity Method: Application to Stationary and Non-Stationary Processes, *J. Mater. Proc. Tech.*, 1992, Vol. 31, 199-208.
- [88] McShane H.B.; Sheppard, T.; Raghunathan, N.; Subramaniyan: On Property Process Relationships When Extruding AA2024 Alloy, in '*Intl. Conf. on Aluminum Alloy 2*', Beijing, China, 1990, (ed. C.Q. Chen, E.A. Starke), pp. 325-336, International Academic Publishers.
- [89] Hunt, W.H.; Jr., Brockenbrough, J. and Magnusen, P.E.: An Al-Si-Mg Composite Model System: Microstructural Effects on Deformation and Damage Evolution, *Scripta Metall. Mater.*, Vol. 25, No. 1, 1991, pp. 15-20.
- [90] Liu, D.S.; Manoharan, M. and Lewandowski, J.J.: Effects of Microstructure on the Behavior of an Aluminum Alloy and an Aluminum Matrix Composite Tested under Low Levels of Superimposed Hydrostatic Pressure, *Met. Trans. A*, 20A, 2409-2417 (1989).
- [91] Lewandowski, J.J.; Liu, D.S. and Liu, C.: Observation on the Effects of Particulate Size and Superposed Pressure on Deformation of Metal Matrix Composites, *Scripta Metall. Mater.*, Vol. 25, No. 1, 1991, pp. 21-26.
- [92] Lloyd, D.J.: Aspects of Fracture in Particulate Reinforced Metal Matrix Composites, *Acta Metall. Mater*, Vol. 39, No. 1, 1991, pp. 59-71.
- [93] Mummery, P.M.; Derby, B. and Scruby, C.B.: Acoustic Emission from Particulate-Reinforced Metal Matrix Composites, *Acta metall. mater.*, Vol. 41, No. 5, pp. 1431-1445, 1993.
- [94] Mochida, T.; Taya, M.; and Obata, M.: Effect of Damaged Particles on the Stiffness of a Particle/Metal Matrix Composite, *JSME International Journal*, Series I, Vol. 34, No. 2, 1991.
- [95] Mochida, T.; Taya M. and Lloyd, D. J.: Fracture of Particles in a Particle/Metal Matrix Composite under Plastic Straining and Its Effect on the Young's Modulus of the Composites, *Materials Transactions, JIM*, Vol. 32, No. 10, 1991, pp. 931-942.
- [96] Metal Handbook, Metallography and Microstructure, 9th Edition, Metals Park, Ohio, ASM, Vol. 9, 1985, pp. 352.

- [97] Pickering, F.B.: *'The Basis of Quantitative Metallography'*, Institute of Metallurgical Technicians, Monography No. 1, July 1975, pp. 5.
- [98] Davies, C.H.J.; Chen, W.C.; Hawbolt, E.B.; Samarasekera, I.V. and Brimacombe, J.K.: Particle Fracture During Extrusion of 6061/ Alumina Composites, *Scripta Metallurgica et Materialia*, Vol. 32, 1995.
- [99] Ehrstrom, J.C.; Kool, W.H.: Migration of Particles during Extrusion of Metal Matrix Composites, *J. of Materials Science Letters*, Vol. 7, No. 6, 1988, pp. 578-580.
- [100] Newell, J.: *Master Thesis*, McMaster University, Hamilton, Ontario, Canada, 1992.
- [101] Zhao, D.; Tuler, F.R. and Lloyd, J.D.: Fracture at Elevated Temperature in a Particle Reinforced Composite, *Acta Metall. Mater.*, Vol. 42, No. 7, pp. 2525-2533, 1994.
- [102] Metal Handbook, Mechanical Test, 9th Edition, Metals Park, Ohio, ASM, Vol. 1, 1985.
- [103] Yokobori, T.; Yokobori, A.T. Jr. and Awaji, H.: Stochastic Approach to Statistical Aspects of Failure, *Probabilistic Methods in the Mechanics of Solids and Structures*, ed. S. Eggwertz, and N.C. Lind, IUTAM Symposium Stockholm/Sweden 1984, pp. 199-212.
- [104] Mihashi, H.: Stochastic Approach to Study the Fracture and Fatigue of Concrete, *Probabilistic Methods in the Mechanics of Solids and Structures*, ed. S. Eggwertz, and N.C. Lind, IUTAM Symposium Stockholm/Sweden, 1984, pp. 307-317.
- [105] Dixon, W.: Particle Fracture during Drawing and Extrusion, *Private Communication*, Duralcan USA, San Diego, C.A., USA, May 1992.
- [106] Xu, X.Q. and Watt, D.F.: Basic Role of a Hard Particle in a Metal Matrix Subjected to Tensile Loading, *Private Communication*, Department of Mechanical Engineering, University of Windsor, Windsor, Ontario, Canada, N9B 3P4.
- [107] Davis, L.C. and Allison, J.E.: Residual Stresses and Their Effects on Deformation in Particle Reinforced Metal Matrix Composites, *Metallurgical Transactions A*, Vol. 24A, November, 1993, pp. 2487-2496.
- [108] Finot, M.; Shen, Y.-L.; Needleman, A. and Suresh, S.: Micromechanical Modeling of Reinforcement Fracture in Particle-Reinforced Metal-Matrix Composites, *Metallurgical and Materials Trans. A*, Vol. 25A, Nov. 1994, pp. 2403-2420.
- [109] Kobayashi, S. and Lee, C. H.: Deformation Mechanics and Workability in Upsetting Solid Circular Cylinders, *Proc. NAMRC*, Vol. 1, p. 185.
- [110] Oh, S.I. and Kobayashi, S.: Workability of Aluminum Alloy 7075-T6 in Upsetting and Rolling, *Trans. ASME, J. of Engr. for Ind.*, 1976, p.1.
- [111] Ferry M. and Munroe P.R.: The Effect of Matrix Temper on Particulate Integrity in an Al/Al₂O₃ Metal Matrix Composite, *Scripta Metallurgica et Materialia*, Vol. 31, No. 2, pp. 143-148, 1994.
- [112] Syu, D.-G. C and Ghosh A.K.: Forging Limits for an Aluminum Matrix Composite: Part II. Analysis, *Metal. and Materials Trans A*, Vol. 25A, September, 1994, pp. 2039-2047.

- [113] Poole, W.J.; Embury, J.D.; MacEwen, S. and Kocks, U.F.: Large Strain Deformation of a Copper-Tungsten Composite System, I. Strain Distributions, *Philosophical Magazine A.*, 1994, Vol. 69, No. 4, pp. 645-665.
- [114] Poole, W.J.; Embury, J.D.; MacEwen, S. and Kocks, U.F.: Large Strain Deformation of a Copper-Tungsten Composite System, II. Applications, *Philosophical Magazine A.*, 1994, Vol. 69, No. 4, pp. 667-687.
- [115] Hunt, W. H., Jr.: Redefining the Limits of Aluminum-Based Materials, *JOM*, January 1993, p.18.
- [116] Derby, B.: Fracture and Damage in Metal Matrix Composites, *Los Alamos National Lab Workshop*, USA, Oct. 28-30, 1992.
- [117] Sheppard T. and Clode M.P.: The Origin of Surface Defects during Extrusion of AA6063 Alloy, *4th International Aluminum Extrusion Technology Seminar*, Vol. 2, Chicago, Illinois, USA, 11-14 April 1988, pp. 329-341.
- [118] Data Brochure on DURALCAN Composites for Wrought Products, Mechanical and Physical Property Data, Duralcan USA, Division of Alcan Aluminum Corporation, San Diego, California 92121, 1991.
- [119] Blecic, S.; Libura, W. and Zasadzinski, J.: Extrusion Technology of AlMgSi Alloys, in '*5th International Aluminum Extrusion Technology Seminar*', Vol. II, The Aluminum Association, Washington, 1992, 485-494.
- [120] Chen, C.C., Oh, S.I. and Kobayashi, S.: Ductile Fracture in Axisymmetric Extrusion and Drawing, Part 1: Deformation Mechanics of Extrusion and Drawing, *Trans. ASME, J. Eng. Ind.*, Vol. 101, pp. 23-35, 1979.
- [121] Laue, K. and Stenger, H.: '*Extrusion: Processing, Machinery Tooling*', Translators from the German Version, A.F. Castle, Gernot Lang, Metal Park, Ohio, American Society for Metals, c1981.
- [122] Lloyd, J.D.: Factors Influencing the Tensile Ductility of Melt Processed Particle Reinforced Aluminium Alloys, *Private Communication*, Kingston Research and Development Center, Alcan International Limited, 1994.
- [123] Lloyd, J.D.; Jin, I. and Weatherly, G.C. Controlling the Interface Reaction in Alumina Reinforced Aluminum Composites, *Scripta Metallurgica et Materialia*, Vol. 31, No. 4, pp. 393-396, 1994.
- [124] Ghosh, A. K: Solid-State Processing, Chapter 2, '*Fundamentals of Metal Matrix Composites*', Ed. by Subra Suresh, Andreas Mortensen, and Alan Needleman, Butterworth-Heinemann, 1993, pp. 23-41.